

Advanced Structured Materials

Volume 31

Series Editors

Andreas Öchsner

Lucas F. M. da Silva

Holm Altenbach

For further volumes:

<http://www.springer.com/series/8611>

Andreas Öchsner · Lucas F. M. da Silva
Holm Altenbach
Editors

Mechanics and Properties of Composed Materials and Structures

Editors

Andreas Öchsner
Department of Applied Mechanics
Faculty of Mechanical Engineering
Universiti Teknologi Malaysia—UTM
Johor
Malaysia

Holm Altenbach
Chair of Engineering Mechanics
Institute of Mechanics
Otto-von-Guericke-University
Magdeburg
Germany

Lucas F. M. da Silva
Department of Mechanical Engineering
Faculty of Engineering
University of Porto
Porto
Portugal

ISSN 1869-8433

ISSN 1869-8441 (electronic)

ISBN 978-3-642-31496-4

ISBN 978-3-642-31497-1 (eBook)

DOI 10.1007/978-3-642-31497-1

Springer Heidelberg New York Dordrecht London

Library of Congress Control Number: 2012945731

© Springer-Verlag Berlin Heidelberg 2012

This work is subject to copyright. All rights are reserved by the Publisher, whether the whole or part of the material is concerned, specifically the rights of translation, reprinting, reuse of illustrations, recitation, broadcasting, reproduction on microfilms or in any other physical way, and transmission or information storage and retrieval, electronic adaptation, computer software, or by similar or dissimilar methodology now known or hereafter developed. Exempted from this legal reservation are brief excerpts in connection with reviews or scholarly analysis or material supplied specifically for the purpose of being entered and executed on a computer system, for exclusive use by the purchaser of the work. Duplication of this publication or parts thereof is permitted only under the provisions of the Copyright Law of the Publisher's location, in its current version, and permission for use must always be obtained from Springer. Permissions for use may be obtained through RightsLink at the Copyright Clearance Center. Violations are liable to prosecution under the respective Copyright Law.

The use of general descriptive names, registered names, trademarks, service marks, etc. in this publication does not imply, even in the absence of a specific statement, that such names are exempt from the relevant protective laws and regulations and therefore free for general use.

While the advice and information in this book are believed to be true and accurate at the date of publication, neither the authors nor the editors nor the publisher can accept any legal responsibility for any errors or omissions that may be made. The publisher makes no warranty, express or implied, with respect to the material contained herein.

Printed on acid-free paper

Springer is part of Springer Science+Business Media (www.springer.com)

Preface

Common engineering materials reach in many engineering applications such as automotive or aerospace; their limits and new developments are required to fulfill increasing demands on performance and characteristics. The properties of materials can be increased, for example, by combining different materials to achieve better properties than a single constituent or by shaping the material or constituents in a specific structure. Many of these new materials reveal a much more complex behavior than traditional engineering materials due to their advanced structure or composition. The expression ‘composed materials’ should indicate here a wider range than the expression ‘composite material’ which is many times limited to classical fiber reinforced plastics.

The 5th International Conference on Advanced Computational Engineering and Experimenting, ACE-X 2011, was held in Algarve, Portugal, from July 3 to 6, 2011 with a strong focus on the above-mentioned materials. This conference served as an excellent platform for the engineering community to meet with each other and to exchange the latest ideas. This volume contains 12 revised and extended research articles written by experienced researchers participating in the conference. The book will offer the state-of-the-art of tremendous advances in engineering technologies of composed materials with complex behavior and also serve as an excellent reference volume for researchers and graduate students working with advanced materials. The covered topics are related to textile composites, sandwich plates, hollow sphere structures, reinforced concrete, as well as classical fiber reinforced materials.

The organizers and editors wish to thank all the authors for their participation and cooperation which made this volume possible. Finally, we would like to thank the team of Springer-Verlag, especially Dr. Christoph Baumann, for the excellent cooperation during the preparation of this volume.

June 2012

Andreas Öchsner
Lucas F. M. da Silva
Holm Altenbach

Contents

Numerical Model for Static and Dynamic Analysis of Masonry Structures	1
Jure Radnić, Domagoj Matešan, Alen Harapin, Marija Smilović and Nikola Grgić	
Wrinkling Analysis of Rectangular Soft-Core Composite Sandwich Plates	35
Mohammad Mahdi Kheirikhah and Mohammad Reza Khalili	
Artificial Neural Network Modelling of Glass Laminate Sample Shape Influence on the ESPI Modes	61
Zora Jančíková, Pavel Košťial, Soňa Rusnáková, Petr Jonšta, Ivan Ružiak, Jiří David, Jan Valíček and Karel Frydryšek	
Nonlinear Dynamic Analysis of Structural Steel Retrofitted Reinforced Concrete Test Frames	71
Ramazan Ozcelik, Ugur Akpınar and Baris Binici	
Acoustical Properties of Cellular Materials	83
Wolfram Pannert, Markus Merkel and Andreas Öchsner	
Simulation of the Temperature Change Induced by a Laser Pulse on a CFRP Composite Using a Finite Element Code for Ultrasonic Non-Destructive Testing	103
Elisabeth Lys, Franck Bentouhami, Benjamin Campagne, Vincent Métivier and Hubert Voillaume	
Macroscopic Behavior and Damage of a Particulate Composite with a Crosslinked Polymer Matrix	117
Luboš Náhlík, Bohuslav Máša and Pavel Hutař	

Computational Simulations on Through-Drying of Yarn Packages with Superheated Steam	129
Ralph W. L. Ip and Elvis I. C. Wan	
Anisotropic Stiffened Panel Buckling and Bending Analyses Using Rayleigh–Ritz Method	137
Jose Carrasco-Fernández	
Investigation of Cu–Cu Ultrasonic Bonding in Multi-Chip Package Using Non-Conductive Adhesive	153
Jong-Bum Lee and Seung-Boo Jung	
Natural Vibration Analysis of Soft Core Corrugated Sandwich Plates Using Three-Dimensional Finite Element Method	163
Mohammad Mahdi Kheirikhah, Vahid Babaghasabha, Arash Naeimi Abkenari and Mohammad Ehsan Edalat	
New High Strength 0–3 PZT Composite for Structural Health Monitoring.	175
Mohammad Ehsan Edalat, Mohammad Hadi Behboudi, Alireza Azarbayjani and Mohammad Mahdi Kheirikhah	
Free Vibration Analysis of Sandwich Plates with Temperature-Dependent Properties of the Core Materials and Functionally Graded Face Sheets	183
Y. Mohammadi and S. M. R. Khalili	

Numerical Model for Static and Dynamic Analysis of Masonry Structures

Jure Radnić, Domagoj Matešan, Alen Harapin, Marija Smilović
and Nikola Grgić

Abstract Firstly, the main problems of numerical analysis of masonry structures are briefly discussed. After that, a numerical model for static and dynamic analyses of different types of masonry structures (unreinforced, reinforced and confined) is described. The main nonlinear effects of their behaviour are modelled, including various aspects of material nonlinearity, the problems of contact and geometric nonlinearity. It is possible to simulate the soil-structure interaction in a dynamic analysis. The macro and micro models of masonry are considered. The equilibrium equation, discretizations, material models and solution algorithm are presented. Three solved examples illustrate some possibilities of the presented model and the developed software for static and dynamic analyses of different types of masonry structures.

Keywords Masonry structure · Numerical model · Static analysis · Dynamic analysis

J. Radnić · D. Matešan (✉) · A. Harapin · M. Smilović · N. Grgić
University of Split Faculty of Civil Engineering, Architecture and Geodesy,
Matice Hrvatske 15, 21000 Split, Croatia
e-mail: dmatesan@gradst.hr

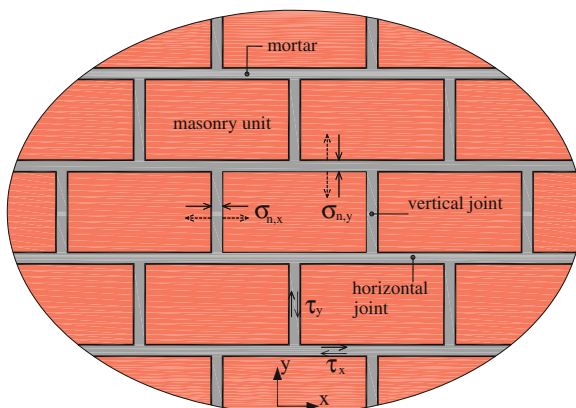
J. Radnić
e-mail: jradnic@gradst.hr

A. Harapin
e-mail: aharapin@gradst.hr

M. Smilović
e-mail: msmilovic@gradst.hr

N. Grgić
e-mail: ngrgic@gradst.hr

Fig. 1 Transfer of normal (σ_n) and shear (τ) stresses at the joint of masonry units and mortar



1 Introduction

Masonry buildings, and therefore masonry structures, are probably the most numerous in the history of architecture. One of their main advantages is simple and quick construction. Brickwork is usually performed with precast masonry units, bound by mortar. Masonry units are most frequently of baked clay, concrete, stone, etc. They are of different geometrical and physical properties, with a variety of brickwork bonds. Horizontal and vertical joints between the masonry units are often completely or partially filled with mortar. Various types of mortar are used (mostly lime, lime-cement and cement), with different thickness of mortar joints and material properties.

Apart from the quality of masonry units and mortar, the construction quality also has a great effect on the quality of masonry structures. The limit strength capacity and deformability of the masonry wall is affected by the quality of the bonds between the masonry unit and mortar, i.e. the level of transfer of normal and shear stresses in the contact surface (Fig. 1).

Compressive strength of masonry units or mortar is crucial for transfer of normal compressive stresses σ_n on the contact surface. There is usually a difference in the strength capacity between the horizontal and vertical joints. Vertical compressive stresses in masonry $\sigma_{n,y}$ are usually much higher than horizontal compressive stresses $\sigma_{n,x}$ due to gravity load. In addition, the compressive strength of horizontal joints is usually much higher than the compressive strength of vertical joints. They are usually only partially filled with mortar, which, due to the mode of placing, is usually of less strength than the mortar in horizontal joints.

The transfer of normal tensile stresses perpendicular to the joints is governed by the adhesion between mortar and masonry unit.

The transfer of shear stresses in horizontal (τ_x) and vertical (τ_y) joints are also different. The level of shear transfer in horizontal joints is greater than in vertical joints because of higher quality and better adhesion between the mortar and the masonry unit, especially due to the favourable effect of vertical compressive stress.

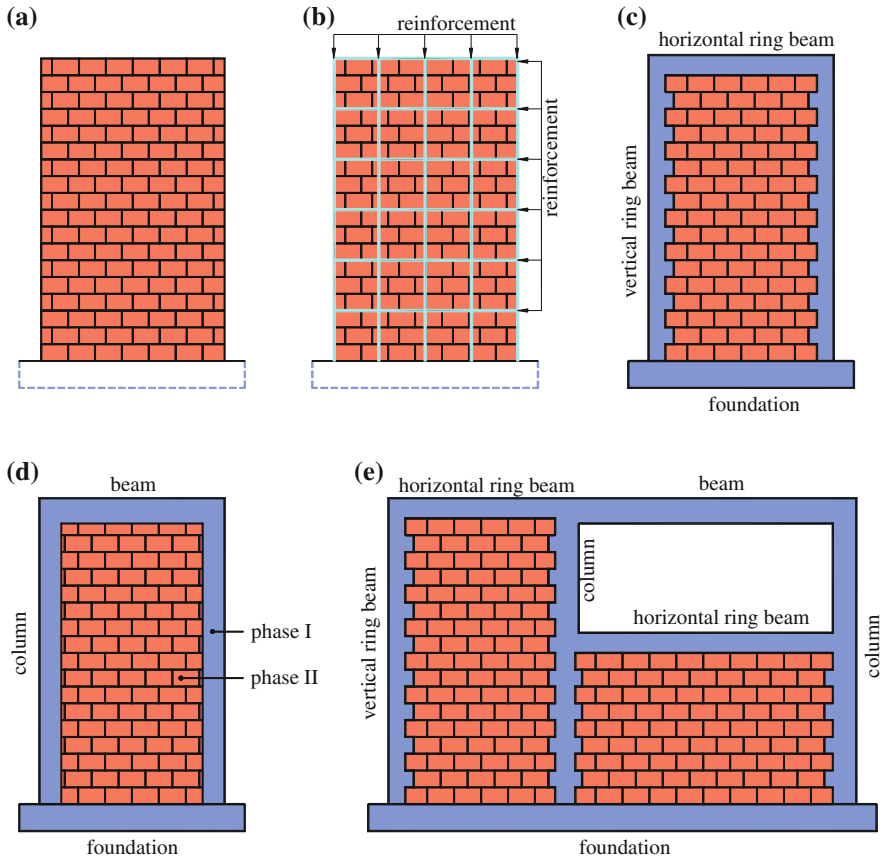


Fig. 2 Common types of masonry walls. **a** Unreinforced masonry. **b** Reinforced masonry. **c** Confined masonry. **d** Masonry infilled frame. **e** Complex masonry

The vertical holes through the masonry units contribute to masonry anisotropy. The usual types of masonry walls are (Fig. 2):

1. Unreinforced masonry walls (Fig. 2a).
2. Reinforced masonry walls (Fig. 2b), with horizontal reinforcement in horizontal joints and vertical reinforcement in the vertical holes through the masonry units.
3. Confined masonry walls (Fig. 2c) are unreinforced masonry walls confined by vertical and horizontal ring beams and foundation.
4. Subsequently constructed walls between the previously placed reinforced concrete beams and columns (Fig. 2d)—the infilled frames.

A special confined masonry wall can often be found in practice. Here, classic reinforced concrete columns and/or beams are constructed on part of the masonry walls instead of vertical and/or horizontal ring beams (Fig. 2e).

Masonry structures typically have a more complex behaviour and require more complex engineering calculations and numerical models than pure concrete structures.

Although there are many numerical models for static and dynamic analyses of masonry structures (see for example [1–5]), there still is not a generally accepted numerical model that would be sufficiently reliable and convenient for practical applications. For a more realistic analysis of masonry structures, it is necessary to include many nonlinear effects of the behaviour of the masonry, reinforced concrete and soil, such as:

- Yield of masonry in compression, opening of cracks in the masonry in tension, mechanism of opening and closing of cracks under cyclic load, transfer of shear stresses, anisotropic properties of strength and stiffness of masonry in horizontal and vertical direction, tensile and shear stiffness of cracked masonry,
- Concrete yielding in compression, opening of cracks in concrete in tension, mechanism of opening and closing of cracks in concrete under dynamic load, tensile and shear stiffness of cracked concrete,
- Strain rate effect of the material properties of masonry, reinforced concrete and soil,
- Soil yield under a foundation,
- Soil—structure dynamic interaction,
- Construction mode—the stages of masonry walls and infilled frames assembling.

This chapter presents a numerical model for static and dynamic analyses of planar (2D) masonry structures which include all previously mentioned nonlinear effects in their behaviour.

2 Equilibrium Equation and Structure Discretization

2.1 Spatial Discretization

By the spatial discretization and application of the finite element method, the equation of dynamic equilibrium of the masonry structure can be written as follows:

$$\mathbf{M}\ddot{\mathbf{u}} + \mathbf{C}(\dot{\mathbf{u}}) + \mathbf{R}(\mathbf{u}) = \mathbf{f} \quad (1)$$

where \mathbf{u} are the unknown nodal displacements, $\dot{\mathbf{u}}$ are velocities and $\ddot{\mathbf{u}}$ are acceleration; \mathbf{M} is the mass matrix, \mathbf{C} is the damping matrix and $\mathbf{R}(\mathbf{u})$ is a vector of internal nodal forces; \mathbf{f} is a vector of external nodal forces that can be generated by wind, engines etc. ($\mathbf{f} = \mathbf{F}(t)$) or by earthquakes ($\mathbf{f} = \mathbf{M}\ddot{\mathbf{d}}_0(t)$), see Fig. 3. Here, $\ddot{\mathbf{d}}_0$ is the base acceleration vector, and t is time. The inner forces vector $\mathbf{R}(\mathbf{u})$ can be expressed as:

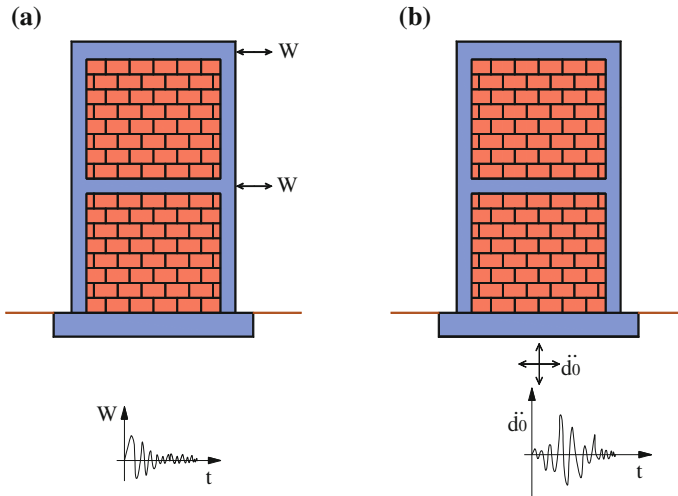


Fig. 3 Dynamic action on the masonry wall. **a** External force (wind, etc.). **b** Base acceleration (earthquake)

$$\mathbf{R}(\mathbf{u}) = \mathbf{K}\mathbf{u}; \quad \mathbf{K} = \partial\mathbf{R}/\partial\mathbf{u} \quad (2)$$

where \mathbf{K} is the stiffness matrix of the structure.

To solve the eigen-problem, which is necessary in the dynamic analysis (determination of the length of time increment for time integration of the equations of motion), Eq. (1) is reduced to:

$$\mathbf{K}\mathbf{x} = \lambda\mathbf{x} \quad (3)$$

where \mathbf{x} is the eigen vector and λ is the eigen value. The eigen-problem is solved by the WYD method [6] (developed by Wilson, Yuan, and Dickens in 1982).

For static problems, Eq. (1) is reduced to

$$\mathbf{R}(\mathbf{u}) = \mathbf{K}\mathbf{u} = \mathbf{f} \quad (4)$$

where \mathbf{f} is the vector of external static forces.

For spatial discretization of the structure, which is approximated by the state of plane stress, 8-node (“serendipity”) elements are used (Fig. 4a). The structure includes unreinforced or reinforced concrete, unreinforced or reinforced masonry, and the soil under the foundation. Reinforcement within the 2D element is simulated using a 1D bar element. It is assumed that there is no slip between the reinforcing bars and the surrounding concrete.

For contact modelling between the soil and foundations or between mortar and masonry units, contact elements are used (Fig. 4b). Flat 2D six-node contact finite elements of infinitely small thickness w (Fig. 4b1) can be used to simulate a continuous connection between the basic 8-node elements, or 1D (bar) two-node

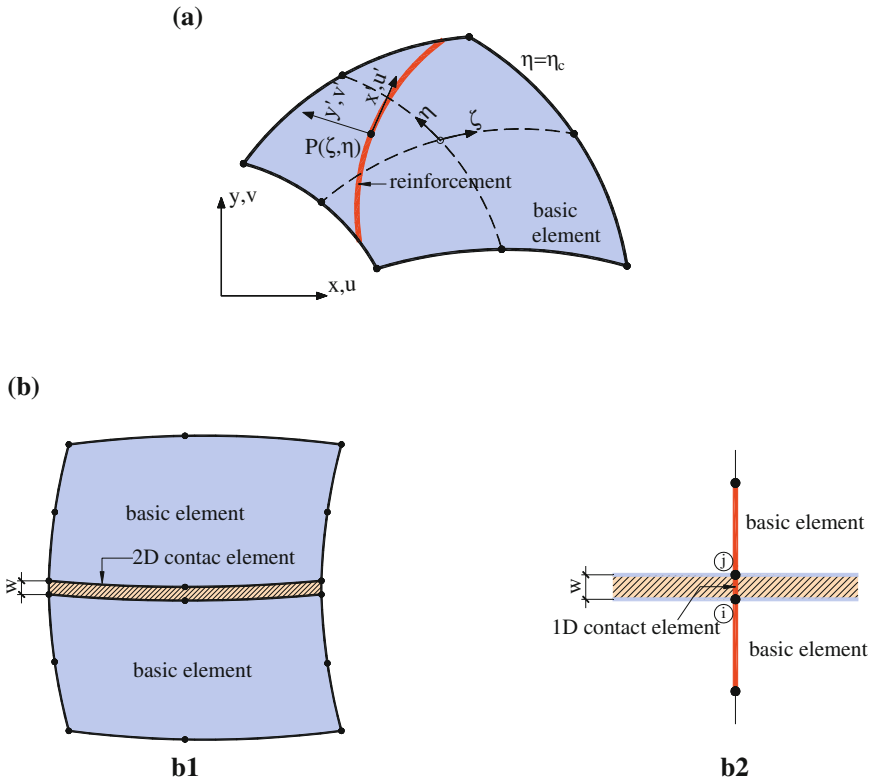


Fig. 4 Adopted finite elements for the masonry structure. **a** Basic 2D eight-node (“serendipity”) element for reinforced concrete, masonry and soil. **b** Contact elements between soil and foundation or between mortar and masonry unit, **b1** 2D contact six-node element, **b2** 1D contact two-node element

contact elements (Fig. 4b2) for the simulation of the reinforcement which passes across the contact surface.

2D contact elements can simulate sliding, separation and penetration of the contact surface, based on the adopted material model of contact elements. 1D contact elements can take the axial and shear forces, according to the adopted material model.

2.2 Time Discretization

For the solution of Eq. (1), implicit, explicit or implicit-explicit Newmark algorithms, developed in iterative form by Hughes [7], are used [8].

In the implicit algorithm, the equilibrium equation (1) is satisfied at the time $t_{n+1} = t_n + \Delta t$, i.e. in $(n + 1)$ time step.

$$\mathbf{M}\ddot{\mathbf{u}}_{n+1} + \mathbf{R}(\mathbf{u}_{n+1}, \dot{\mathbf{u}}_{n+1}) = \mathbf{f}_{n+1} \quad (5)$$

where:

$$\begin{aligned} \mathbf{u}_{n+1} &= \mathbf{u}_{n+1} + \beta \Delta t^2 \ddot{\mathbf{u}}_n \\ \dot{\mathbf{u}}_{n+1} &= \dot{\mathbf{u}}_{n+1} + \gamma \Delta t \ddot{\mathbf{u}}_n \end{aligned} \quad (6)$$

$$\begin{aligned} \mathbf{u}_{n+1} &= \mathbf{u}_n + \Delta t \dot{\mathbf{u}}_n + 0.5(1 - 2\beta) \Delta t^2 \ddot{\mathbf{u}}_n \\ \dot{\mathbf{u}}_{n+1} &= \dot{\mathbf{u}}_n + (1 - \gamma) \Delta t \ddot{\mathbf{u}}_n \end{aligned} \quad (7)$$

In the above expressions, Δt is the time increment and n is the time step; \mathbf{u}_{n+1} and $\dot{\mathbf{u}}_{n+1}$ are assumed, \mathbf{u}_{n+1} and $\dot{\mathbf{u}}_{n+1}$ are corrected values of displacement and velocity; β and γ are parameters that determine the stability and accuracy of the method [8].

By substituting (6) and (7) into (5), and by introducing an incremental-iterative procedure to solve the general nonlinear problem, the so-called effective static problem is obtained

$$\mathbf{K}_\tau^* \Delta \mathbf{u} = (\mathbf{f}^*)^i \quad (8)$$

where the effective tangent stiffness matrix \mathbf{K}_τ^* is calculated at time τ by:

$$\mathbf{K}_\tau^* = \frac{\mathbf{M}}{\beta \Delta t^2} + \gamma \frac{\mathbf{C}_\tau}{\beta \Delta t} + \mathbf{K}_\tau \quad (9)$$

and the effective load vector \mathbf{f}^* by:

$$\mathbf{f}^* = \mathbf{f}_{n+1} - \mathbf{M}\ddot{\mathbf{u}}_{n+1}^i - \mathbf{R}(\mathbf{u}_{n+1}^i, \dot{\mathbf{u}}_{n+1}^i) \quad (10)$$

In the above expressions, n indicates the time step, and i is the iterative step; $\Delta \mathbf{u}$ is the displacement increment vector. The Newmark implicit algorithm of the iterative problem solution is shown in Table 1 [8].

The Newmark explicit algorithm of the iterative problem solution can be written as follows:

$$\mathbf{M}\ddot{\mathbf{u}}_{n+1} + \mathbf{R}(\mathbf{u}_{n+1} + \mathbf{u}_{n+1}) = \mathbf{f}_{n+1} \quad (11)$$

This algorithm is shown in Table 2 [8]. In the explicit methods, the dynamic equilibrium equation is satisfied in the time t_n , and the unknown variables are calculated in the time $t_{n+1} = t_n + \Delta t$.

The main advantage of this method is the small number and simple numerical operations within each time step. Their main disadvantage is that they are not unconditionally stable. Therefore, the calculating advantage of explicit methods is often compensated by the fact that small time increments are required when solid (small) elements are present in the system. These methods are often not effective in the use of solid contact elements.

It is possible to use the implicit and explicit Newmark algorithms at the same time [8]. Specifically, the area of the structure with rigid elements is effectively

Table 1 Newmark implicit algorithm of the iterative problem solution

(1)	For time step (n+1), use iterative step $i = 1$
(2)	Calculate the vectors of the assumed displacement, velocity and acceleration at the beginning of time step using the known values from previous time step: $\mathbf{u}_{n+1}^1 = \mathbf{u}_{n+1}$ $\dot{\mathbf{u}}_{n+1}^1 = \dot{\mathbf{u}}_{n+1}$ $\ddot{\mathbf{u}}_{n+1}^1 = (\mathbf{u}_{n+1}^1 - \mathbf{u}_{n+1}) / (\beta \Delta t^2)$
(3)	Calculate effective residual forces $(\mathbf{f}^*)^i$: $(\mathbf{f}^*)^i = \mathbf{f}_{n+1} - \mathbf{M}\ddot{\mathbf{u}}_{n+1}^i - \mathbf{R}(\mathbf{u}_{n+1}^i, \dot{\mathbf{u}}_{n+1}^i)$
(4)	Calculate the effective stiffness matrix \mathbf{K}_τ^* (if required): $\mathbf{K}_\tau^* = \frac{\mathbf{M}}{\beta \Delta t^2} + \gamma \frac{\mathbf{C}_\tau}{\beta \Delta t} + \mathbf{K}_\tau$
(5)	Calculate the displacement increment vector $\Delta \mathbf{u}^i$: $\mathbf{K}_\tau^* \Delta \mathbf{u}^i = (\mathbf{f}^*)^i$
(6)	Correct the assumed values of displacement, velocity and acceleration: $\mathbf{u}_{n+1}^{i+1} = \mathbf{u}_{n+1}^i + \Delta \mathbf{u}_{n+1}^i$ $\ddot{\mathbf{u}}_{n+1}^{i+1} = (\mathbf{u}_{n+1}^{i+1} - \mathbf{u}_{n+1}) / (\beta \Delta t^2)$ $\dot{\mathbf{u}}_{n+1}^{i+1} = \dot{\mathbf{u}}_{n+1}^i + (\gamma \Delta t) \ddot{\mathbf{u}}_{n+1}^{i+1}$
(7)	Control the convergence procedure: <ul style="list-style-type: none"> • if $\Delta \mathbf{u}^i$ satisfies the convergence criterion $\ \Delta \mathbf{u}^i\ / \ \mathbf{u}_{n+1}^{i+1}\ \leq \epsilon_n$ proceed to the next time step (replace “n” with “n+1” and proceed to solution step (1)). The solution in time t_{n+1} is: $\mathbf{u}_{n+1} = \mathbf{u}_{n+1}^{i+1}$ $\dot{\mathbf{u}}_{n+1} = \dot{\mathbf{u}}_{n+1}^{i+1}$ $\ddot{\mathbf{u}}_{n+1} = \ddot{\mathbf{u}}_{n+1}^{i+1}$ • if the convergence criterion is not satisfied, the iteration procedure with correction of shear, velocity and acceleration continues (replace “i” with “i+1”, and proceed to solution step (3)).

integrated with the implicit algorithms, and the area of the structure with soft elements with the explicit algorithm.

3 Material Model

The application of an adequate material model for a realistic simulation of the behaviour of masonry structures under static and dynamic loads is of primary importance. The material models applied here for certain parts of masonry structures (reinforced concrete, masonry, soil) are described briefly hereinafter.

Table 2 Newmark explicit algorithm of the iterative problem solution

(1)	For time step (n+1), use iteration step $i = 1$
(2)	Calculate the vectors of the assumed displacement, velocity and acceleration at the beginning of time step using the known values from previous time step: $\mathbf{u}_{n+1}^1 = \mathbf{u}_{n+1}$ $\dot{\mathbf{u}}_{n+1}^1 = \dot{\mathbf{u}}_{n+1}$ $\ddot{\mathbf{u}}_{n+1}^1 = (\mathbf{u}_{n+1}^1 - \mathbf{u}_{n+1}) / (\beta \Delta t^2)$
(3)	Calculate effective residual forces $(\mathbf{f}^*)^i$: $(\mathbf{f}^*)^i = \mathbf{f}_{n+1} - \mathbf{R}(\mathbf{u}_{n+1}^i, \dot{\mathbf{u}}_{n+1}^i)$
(4)	Calculate the effective stiffness matrix \mathbf{K}^* (if required): $\mathbf{K}^* = \frac{\mathbf{M}}{\beta \Delta t^2}$ <p>Note: Since the matrix mass \mathbf{M} is constant, it is sufficient to calculate the effective stiffness matrix \mathbf{K}^* only once at the start of the solution. It is also obvious that it should be $\beta > 0$</p>
(5)	Calculate the displacement increment vector $\Delta \mathbf{u}^i$: $\mathbf{K}^* \Delta \mathbf{u}^i = (\mathbf{f}^*)^i$
(6)	Correct the assumed values of displacement, velocity and acceleration: $\mathbf{u}_{n+1}^{i+1} = \mathbf{u}_{n+1}^i + \Delta \mathbf{u}_{n+1}^i$ $\dot{\mathbf{u}}_{n+1}^{i+1} = (\mathbf{u}_{n+1}^{i+1} - \mathbf{u}_{n+1}) / (\beta \Delta t^2)$ $\ddot{\mathbf{u}}_{n+1}^{i+1} = \ddot{\mathbf{u}}_{n+1}^i + (\gamma \Delta t) \ddot{\mathbf{u}}_{n+1}^{i+1}$
(7)	Control the convergence procedure In the explicit procedure with a single correction of the results, convergence control is not required, but we directly proceed to the next time step With multiple correction results it is necessary to control the procedure convergence, as described in Table 1

3.1 Reinforced Concrete Model

The presented model is used to simulate the behaviour of parts of masonry structures made of concrete or reinforced concrete (ring beams, foundations, columns, beams, etc.). This model was previously developed for static and dynamic analyses of conventional reinforced concrete structures [8] and will be only briefly described.

3.1.1 Concrete Model

A simple concrete model, based on the basic parameters of concrete, has been adopted to simulate problems where nonlinearities are primarily caused by concrete cracking in tension and by concrete yielding in compression. A graphic presentation of the adopted concrete model is shown in Fig. 5.

A. Concrete model in compression

For the description of concrete behaviour in compression, the theory of plasticity is used with a defined yield criterion, flow rule and crushing criterion [8]. It

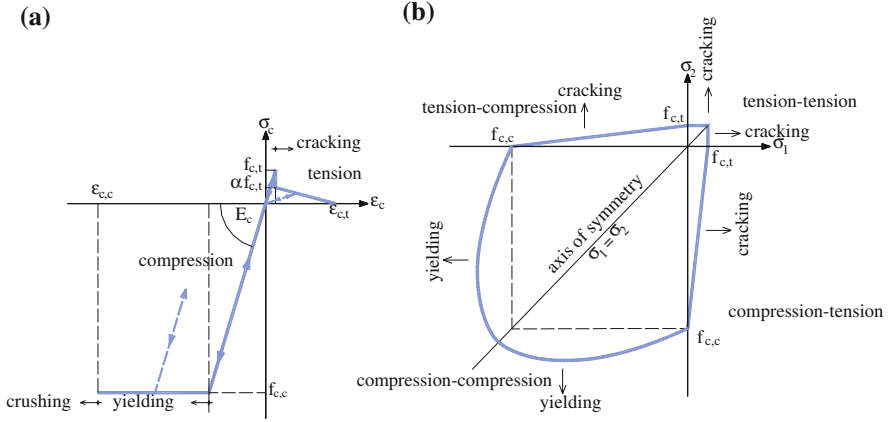


Fig. 5 Graphic presentation of the adopted concrete model. **a** 1D model. **b** 2D model

is assumed that concrete under low stress levels is homogeneous and isotropic and that the stress–strain relationship is linear-elastic. The relation between stress increment $\Delta\sigma_c$ and strain increment $\Delta\epsilon_c$ is expressed as:

$$\Delta\sigma_c = \mathbf{D}_c \Delta\epsilon_c \quad (12)$$

where \mathbf{D}_c is the matrix of elastic concrete parameters. Linear-elastic behaviour is valid until the yield condition is reached. Due to the simplicity, the Von Mises yield criterion is used which is expressed through the stress components

$$F(\sigma_c) = (\sigma_x^2 + \sigma_y^2 - \sigma_x\sigma_y + 3\tau_{xy}^2)^{1/2} - f_{c,c} = 0 \quad (13)$$

where $f_{c,c}$ is the equivalent uniaxial concrete compressive strength. After the yield criterion has been reached (13), an ideally plastic behaviour is adopted.

The concrete crushing criterion is defined as a function of strain components, as

$$F_\epsilon(\epsilon_c) = (\epsilon_x^2 + \epsilon_y^2 - \epsilon_x\epsilon_y + 0.75\gamma_{xy}^2)^{1/2} - \epsilon_{c,c} = 0 \quad (14)$$

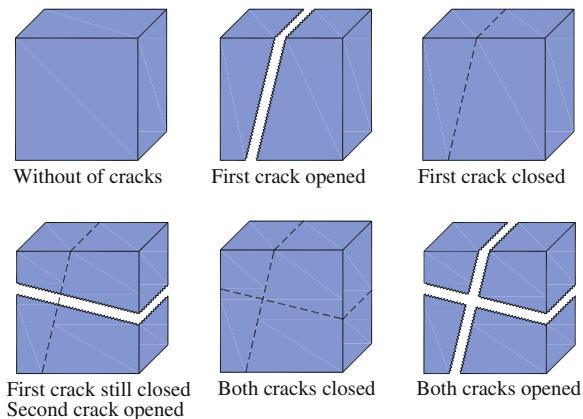
where $\epsilon_{c,c}$ is the equivalent uniaxial ultimate compressive strain of concrete (values between 0.0035 and -0.005 are usually used). When the crushing condition is reached, it is assumed that the concrete has no stiffness. The concrete failure in one or more integration points does not mean the failure of the whole structure.

B. Tension concrete model

Initially, the linear-elastic behaviour is assumed until the criterion of cracks initiation is reached

$$\sigma_1 \geq f_{c,t} \quad \text{and/or} \quad \sigma_2 \geq f_{c,t} \quad (15)$$

Fig. 6 Crack pattern in concrete



in the tension–tension area

$$(f_{c,t} - \sigma_1)/f_{c,t} \geq \sigma_2/f_{c,c} \quad \text{or} \quad \sigma_1/f_{c,c} + \sigma_2/f_{c,t} \leq f_{c,c}/f_{c,t} \quad (16)$$

in the tension–compression area. It is assumed that the cracks occur in the plane perpendicular to the direction of principal stresses σ_1 , σ_2 , and that after their occurrence the concrete remains continuum.

The cracks are modelled as smeared, which disregards the actual displacement discontinuity and the topology of the idealized structure remains unchanged after concrete cracking. After opening of cracks, it is assumed that the cracks position remains unchanged for the next loading and unloading. After opening of cracks, the concrete becomes anisotropic and the crack direction determines the main directions of concrete anisotropy. Partial or full closing of previously open cracks is modelled, as well as reopening of previously closed cracks. The transfer of compressive stress across a fully closed crack is modelled as for concrete without cracks. After crack reopening, the tensile stiffness of cracked concrete is not considered any more. Possible states of concrete cracks are shown in Fig. 6. The crack model is shown in Fig. 7.

The stress–strain relationship of cracked concrete can be expressed as:

$$\sigma_c^* = \mathbf{D}_c^* \varepsilon_c^* \quad (17)$$

where \mathbf{D}_c^* is the matrix of “elastic” constants of the cracked concrete. The components of the stress vector $\sigma_c^* = [\sigma_n^*, \sigma_t^*, \tau_{nt}^*]^T$ and strain vector $\varepsilon_c^* = [\varepsilon_n^*, \varepsilon_t^*, \gamma_{nt}^*]^T$ are in accordance with the local coordinate system (Fig. 7c).

For the plane stress state, the stress–strain relationship for concrete with one crack in the direction of the y^* axis is

$$\begin{bmatrix} \sigma_n^* \\ \sigma_t^* \\ \tau_{nt}^* \end{bmatrix} = \begin{bmatrix} 0 & 0 & 0 \\ 0 & E_c & 0 \\ 0 & 0 & G_c^* \end{bmatrix} \begin{bmatrix} \varepsilon_n^* \\ \varepsilon_t^* \\ \gamma_{nt}^* \end{bmatrix} \quad (18)$$

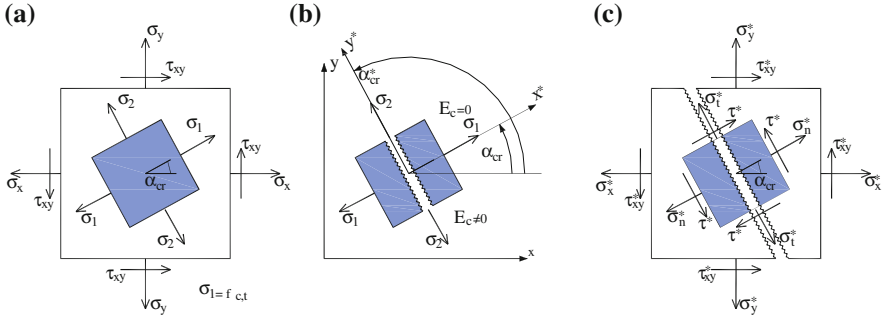


Fig. 7 Concrete cracks model. **a** Principal stress direction. **b** Crack direction. **c** Stresses after cracking

For concrete with two cracks, the matrix \mathbf{D}_c^* is

$$\mathbf{D}_c^* = \begin{bmatrix} 0 & 0 & 0 \\ 0 & 0 & 0 \\ 0 & 0 & \mathbf{G}_c^* \end{bmatrix} \quad (19)$$

where E_c is the elasticity modulus of concrete and \mathbf{G}_c^* is the modified shear modulus of cracked concrete.

B.1 Modelling of the tensile stiffness of the cracked concrete

The tensile stiffness of the cracked concrete is simulated by gradual decrease of the tensile stress components perpendicular to the crack, in accordance with the stress–strain relationship for the uniaxial stress state (Fig. 8). When the crack opens, where $\sigma_1 = f_{c,t} = E_c \varepsilon_{cr}$, the normal stress perpendicular to the crack decreases to $\sigma_n^* = \alpha f_{c,t}$. When the strain perpendicular to the crack exceeds $\varepsilon_{c,t}$, $\sigma_n^* = 0$ is adopted. The ultimate strain $\varepsilon_{c,t}$ is

$$\varepsilon_{c,t} = \bar{\alpha} \varepsilon_{cr} \quad (20)$$

where ε_{cr} is the strain at crack opening, and $\bar{\alpha}$ is an adopted parameter (usually 5–25).

B.2 Modelling of the shear stiffness of the cracked concrete

In accordance with the adopted smeared crack model, the shear modulus of concrete G_c is linearly reduced depending on the value of tensile concrete strain perpendicular to the crack ε_n^* . Specifically, the shear modulus of cracking concrete G_c^* is defined by (Fig. 9)

$$G_c^* = \bar{\beta} G_c \quad (21)$$

where $\bar{\beta}$ is a parameter defined by

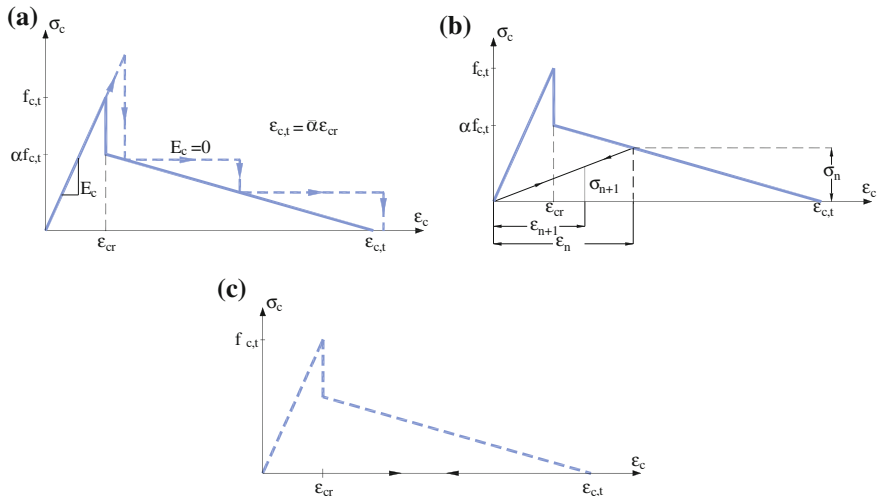
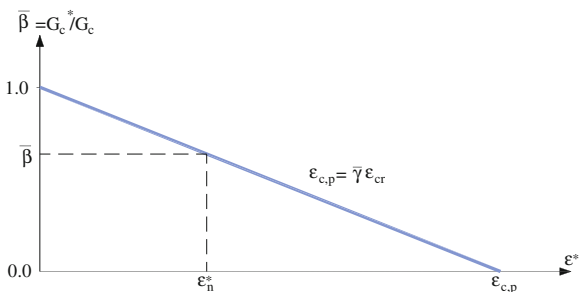


Fig. 8 Stress-strain relationship for concrete after crack opening. **a** Crack opening. **b** Crack closure. **c** Crack re-opening

Fig. 9 Shear stiffness model of the cracked concrete



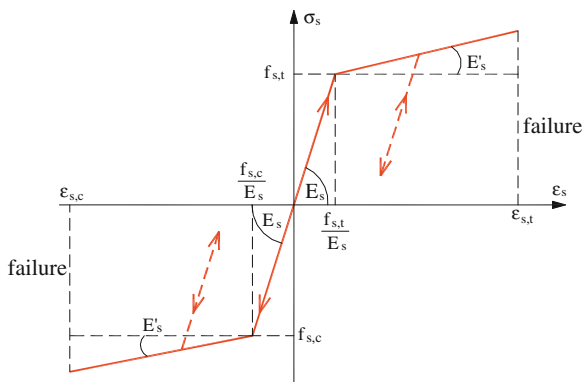
$$\begin{aligned} \bar{\beta} &= 1 - \varepsilon_n^*/\varepsilon_{c,p} \quad \text{for } \varepsilon_n^* \leq \varepsilon_{c,p} \\ \bar{\beta} &= 0 \quad \text{for } \varepsilon_n^* > \varepsilon_{c,p} \end{aligned} \tag{22}$$

where $\varepsilon_{c,p}$ is the ultimate strain perpendicular to the concrete crack over which there is no aggregate interlocking, i.e. over which there is no shear transfer. It can be written as

$$\varepsilon_{c,p} = \bar{\gamma}\varepsilon_{cr} \tag{23}$$

The empirical parameter $\bar{\gamma}$ is usually between 10 and 35, i.e. $\varepsilon_{c,p}$ is usually between 0.001 and 0.004 [8].

Fig. 10 Stress-strain relationship for the reinforcement



3.1.2 Reinforcement Model

The reinforcement is simulated by a bar element within the concrete element (Fig. 4a). The adopted stress–strain relationship for the reinforcement is shown in Fig. 10. Here $f_{s,c}$ and $f_{s,t}$ are the uniaxial compressive and tensile steel strengths; $\epsilon_{s,c}$ and $\epsilon_{s,t}$ are the uniaxial compressive and tensile limit steel strains; E_s and E'_s are the elasticity steel modules.

3.2 Masonry Model

3.2.1 Introduction

In the static and dynamic analyses of masonry structures, two numerical models for masonry are commonly used: macro model and micro model (Fig. 11).

- (i) Macro model of masonry (Fig. 11b). At the macro level, the masonry is approximated by a representative material whose physical–mechanical properties describe the actual complex masonry properties. Such an approach allows large finite elements (rough discretization) and significantly reduces the number of unknown variables, and also rapidly accelerates the structure analysis.
- (ii) Micro model of masonry (Fig. 11c). At the micro level, the spatial discretization of masonry can be performed at the level of masonry units and mortar (joints). For a more accurate analysis, the connection between mortar and masonry units can be simulated by contact elements. It is possible to use various micro models of masonry, with various precision and duration of analysis. In relation to the masonry macro model, the masonry micro models can provide a more accurate description of the damage and failure of masonry, but with much more complex analysis. It is used mainly for smaller spatial problems, and for verification of experimental tests of the masonry structures.

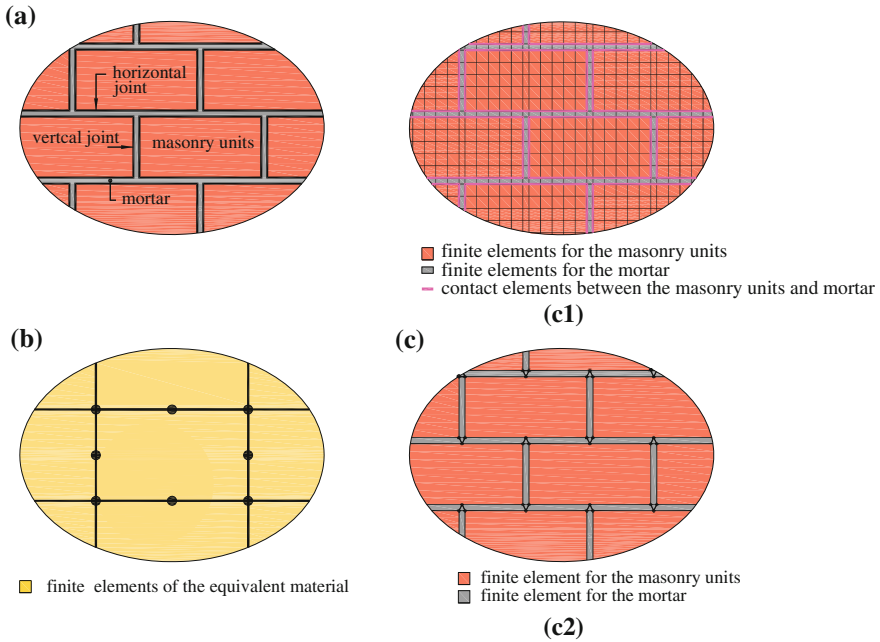


Fig. 11 Macro and micro models of masonry. **a** Fragment of masonry. **b** Macro model of masonry. **c** Micro models of masonry, **c1** Micro model of masonry 1, **c2** Micro model of masonry 2

The adopted macro model and micro models of masonry are briefly described hereinafter.

3.2.2 Macro Model of Masonry

In this model, attention should be given to defining the adequate physical–mechanical parameters of a representative idealized material. This material should describe the complex structures of masonry units, mortar in the joints and the connection characteristics between the mortar and masonry units.

The adopted constitutive model can simulate anisotropic properties of masonry, with different elasticity modulus E_m , strength (compressive $f_{m,c}$, tensile $f_{m,t}$, shear $f_{m,p}$) and limit strains (compressive $\epsilon_{m,c}$, tensile $\epsilon_{m,t}$) for horizontal (h) and vertical (v) directions (Fig. 12). The correspondent parameters for the representative material are determined based on analysis of relevant data for masonry units, mortar and connections between mortar and masonry units.

A. Modelling of masonry in compression and tension

A graphic presentation of the adopted orthotropic constitutive masonry model in compression and tension is given in Fig. 13. The masonry parameters in the horizontal (h) and vertical (v) directions are: σ_m^h and σ_m^v are normal stresses, $f_{m,c}^h$ and

Fig. 12 Parameters of orthotropic masonry.

a Fragment of real masonry with parameters for masonry units and mortar. **b** Macro model of masonry with the parameters of the equivalent material

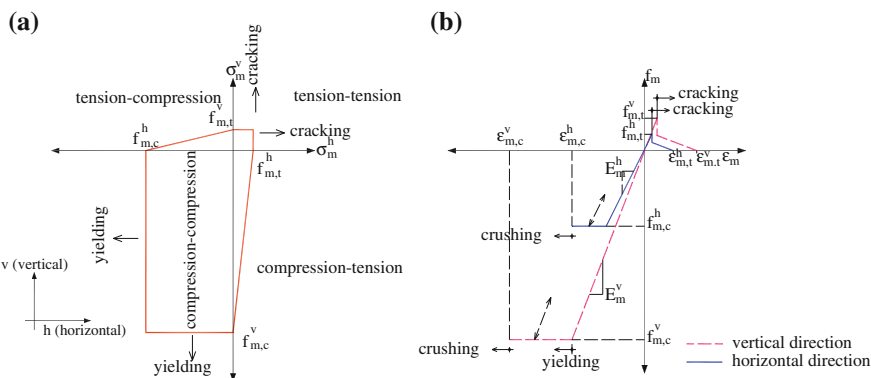
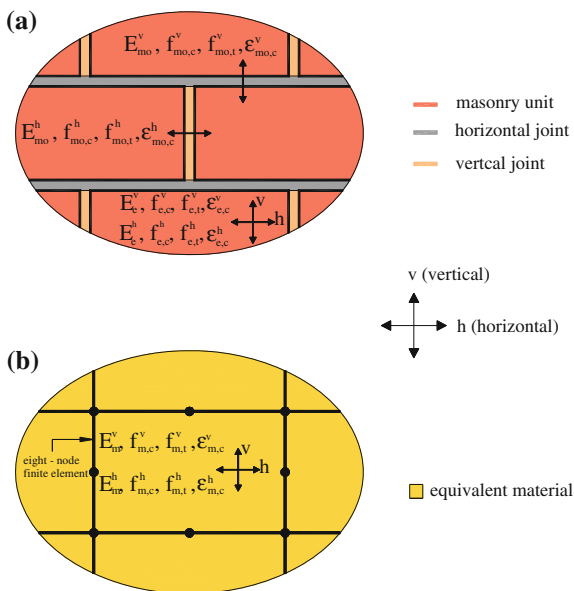


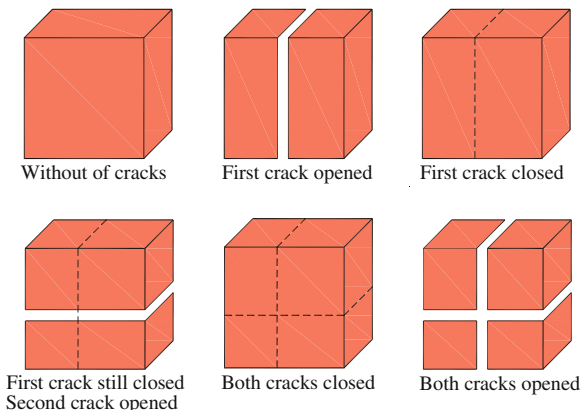
Fig. 13 Adopted orthotropic masonry model. **a** 2D model. **b** 1D model

$f_{m,c}^v$ are the compressive strengths, $f_{m,t}^h$ and $f_{m,t}^v$ are the tensile strengths, E_m^h and E_m^v are the elasticity modules, $\epsilon_{m,c}^h$ and $\epsilon_{m,c}^v$ are the crushing compressive strains.

As shown in Fig. 13, the effect of biaxial stresses to the limit compressive strength of masonry walls is disregarded. This effect could be easily included if the experimental results of the strength of walls with different proportions of normal stresses were known. In real masonry structures, the basic parameters of the masonry in the vertical direction have higher values than in the horizontal direction.

If there are no experimental values for the compressive masonry strength, then the smaller value of the respective compressive strengths of the masonry unit or mortar in vertical and horizontal directions can be used. Also, if there are no

Fig. 14 Cracks pattern of masonry



experimental values for the tensile masonry strength, then the adhesion strength between mortar and masonry units in vertical and horizontal joints can be used.

The masonry model in tension after cracking is used as in concrete (Fig. 8). It is possible to simulate the tensile stiffness of cracked masonry. The value of parameter $\bar{\alpha}$ for the masonry, which determines the maximum tensile strain perpendicular to the crack over which there is no tensile stiffness of the masonry, should be determined experimentally.

Cracks modelling of masonry are analogous to that for concrete, where, according to the adopted assumption, the cracks in the masonry are horizontal and/or vertical (Fig. 14). The transmission of compression stresses over the closed crack is modelled as in homogeneous masonry. After re-opening of the previously closed crack, the stiffness of the masonry is not taken into account. After crushing in compression, it is assumed that the masonry has no stiffness.

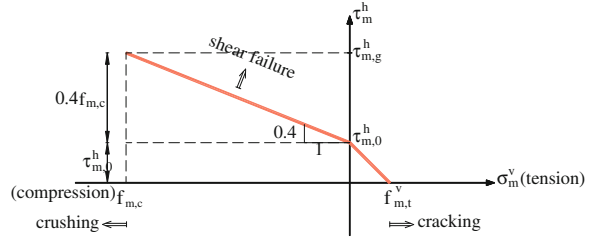
B. Modelling of masonry shear failure

Apart from tension (cracking) and/or compression (crushing), the collapse of the masonry due to the shear stress in the horizontal plane (horizontal joint) is modelled. Shear failure in the vertical joint is not currently modelled. The criterion of the masonry shear failure in the horizontal plane is defined according to Fig. 15, or as

$$\tau_{xy} \leq \tau_m^h \tag{24}$$

where τ_{xy} is the masonry shear stress from the numerical calculation, and τ_m^h is the masonry shear strength defined with (compressive stress has a negative sign)

Fig. 15 Adopted shear failure of masonry



(i) $\sigma_v \leq 0$ (compression)

$$\begin{aligned}\tau_m^h &= \tau_{m,0}^h - 0.4\sigma_m^v \\ \tau_{m,g}^h &= \tau_{m,0}^h - 0.4f_{m,c}^t\end{aligned}\quad (25)$$

(ii) $\sigma_v > 0$ (tension)

$$\tau_m^h = \tau_{m,0}^h \left(1 - \frac{\sigma_m^v}{f_{m,t}^v} \right) \geq 0 \quad (26)$$

In the previous expressions, $\tau_{m,0}^h$ is the basic masonry shear strength (without normal compressive stresses transversal to the horizontal joints), and σ_m^v is the vertical stress.

The shear stiffness of cracked masonry is simulated similarly to the shear stiffness of cracked concrete. Specifically, assuming that after cracking masonry remains a continuum, the initial shear modulus G_m of the masonry is reduced according to the value of the tensile strain perpendicular to the crack $\varepsilon_{n,m}^*$, according to (Fig. 16)

$$G_m^* = \bar{\bar{\beta}} G_m \quad (27)$$

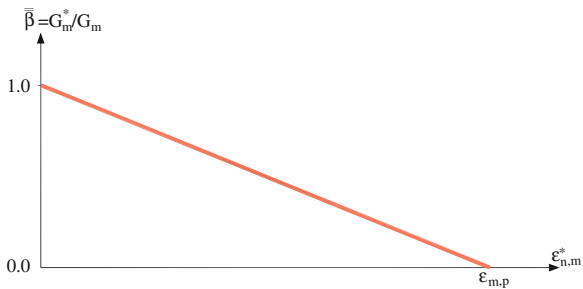
where G_m^* is the shear modulus of cracked masonry and $\bar{\bar{\beta}}$ is a parameter defined by

$$\begin{aligned}\bar{\bar{\beta}} &= 1 - \frac{\varepsilon_{n,m}^*}{\varepsilon_{m,p}} \quad \text{for } \varepsilon_{n,m}^* \leq \varepsilon_{m,p} \\ \bar{\bar{\beta}} &= 0 \quad \text{for } \varepsilon_{n,m}^* > \varepsilon_{m,p}\end{aligned}\quad (28)$$

where $\varepsilon_{m,p}$ is the limit strain perpendicular to the crack where there is no transfer of shear stress. It can be written as follows:

$$\varepsilon_{m,p} = \bar{\bar{\gamma}} / \varepsilon_{mr} \quad (29)$$

Fig. 16 Adopted shear stiffness of cracked masonry



Parameter $\bar{\gamma}$ should be experimentally determined for various types of masonry and load types. In case of shear failure of the masonry in a certain integration point, i.e. when $\tau_{x,y} > \tau_{m,g}^h$, $G_m = 0$ is adopted.

3.2.3 Micro Model of Masonry

The masonry can be more precisely and reliably modelled by the micro model than by the macro model. It is possible to use various micro models of masonry (some of them are presented in Fig. 11), with various precision and duration of analysis.

In micro model 1 in Fig. 11, the masonry units and mortar are discretized by 8-node elements, while at the contact of mortar and masonry units, thin 6-node contact elements are used. The constitutive material models of all these elements can well describe all effects of materials and contact surfaces.

In micro model 2 in Fig. 11, masonry units are discretized by 8-node elements, and vertical and horizontal joints with 6-node contact elements.

Also, other micro models can be used, i.e. different discretization of masonry.

3.3 Contact Element Model

2D contact elements transmit normal stress σ_n at the contact surface according to Fig. 17, which allows simulation of sliding, separation and penetration at the contact surface between the foundation and soil, or between the mortar and the masonry units. It is possible to define different types of $\sigma_n - \epsilon_n$ relationships, where σ_n is the stress and ϵ_n is the strain perpendicular to the contact surface.

In compression, $\sigma_{k,c}$ denotes the compressive strength at the contact surface, $\epsilon_{k,c}$ is the ultimate compressive strain at failure, E_k is the elasticity modulus perpendicular to the contact surface and E_1 is the hardening modulus.

In tension, $\sigma_{k,t}$ denotes the tensile strength over which cracks occur, E_2 is the hardening modulus, $\epsilon_{k,t}$ is the tensile strain perpendicular to the contact surface when cracks occur, and $\epsilon_{k,g}$ is the maximum tensile strain perpendicular to the contact surface over which there is no tensile stiffness. The model of tensile

Fig. 17 Modelling of normal stress transmission for 2D contact elements

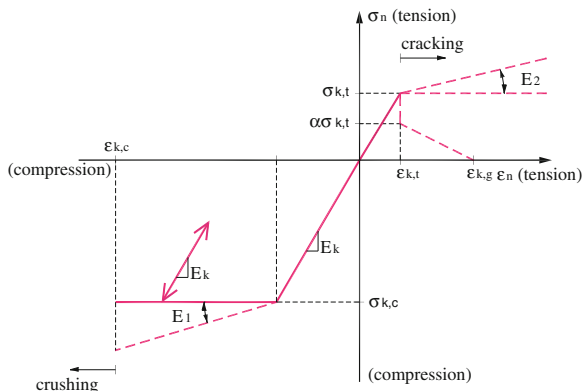
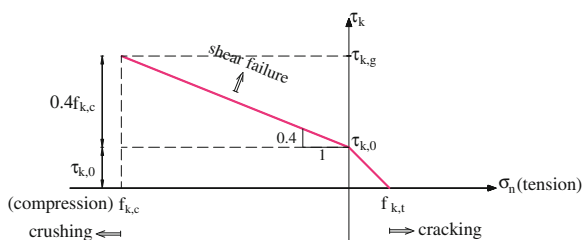


Fig. 18 Adopted shear strength model of the 2D contact element



stiffness and other characteristics of the diagram in Fig. 17 are similar to those for concrete, with additional material modelling possibilities.

The 2D contact element transmits shear stress at the contact surface, i.e. it enables simulation of sliding and shear failure of the joint. The adopted model of shear strength capacity of the joint is given in Fig. 18. The modelling of shear failure is similar to that of the masonry, i.e.

$$\tau_s \leq \tau_k \quad (30)$$

where τ_s is the shear stress in the contact element, and τ_k is the shear stress capacity defined by

(i) in compression ($\sigma_n \leq 0$)

$$\tau_k = \tau_{k,0} - 0.4\sigma_n \leq \tau_{k,0} - 0.4f_{k,c} \quad (31)$$

(ii) in tension ($\sigma_n > 0$)

$$\tau_k = \tau_{k,0} \left(1 - \frac{f_{k,t}}{\tau_{k,0}} \right) \geq 0 \quad (32)$$

where $\tau_{k,0}$ is the shear strength of the joint exposed to pure shear (without pressure), and σ_n is the normal stress in the contact surface.

3.3.1 A. 2D contact element

The shear strength of the cracked contact element is simulated in the similar way as in concrete and masonry. Specifically, the shear modulus of the contact element with cracks G_k^* is taken so that the initial shear modulus G_k is multiplied by parameter $\bar{\beta}$ (≤ 1), which is determined in an analogous manner as for masonry and concrete, i.e.

$$G_k^* = \bar{\beta} G_k \quad (33)$$

3.3.2 B. 1D contact element

1D contact elements simulate the reinforcement bars that pass through the 2D contact elements, and transmit normal and shear stresses.

Normal stresses in the direction of the bar elements are transferred in accordance with the adopted stress–strain diagram for steel. In this context, for example, the diagram in Fig. 10 can be used, or it is possible to set any polygonal line of stress–strain relationship. When the line in the σ – ε diagram is descending or fracture strains are exceeded, the steel elasticity modulus $E_s = 0$ is used.

3.4 Soil Model

A special constitutive soil model has not been developed. Only the concrete model described in Sect. 3.1, or masonry macro model described in Sect. 3.2, can be used with corresponding material parameters. Which model is more reliable, depends on soil properties. The material parameters should be properly defined based on the available soil parameters. The presented models can simulate the soil yielding and crushing in compression, the soil cracking in tension, anisotropic soil properties and other nonlinear soil effects according to Sects. 3.1 and 3.2.

3.5 Modelling of the Strain Rate Effect in the Material Properties

It is a known that the strain rate affects the mechanical properties of materials, i.e. for dynamic load and especially impact load. Generally, with increasing strain rate

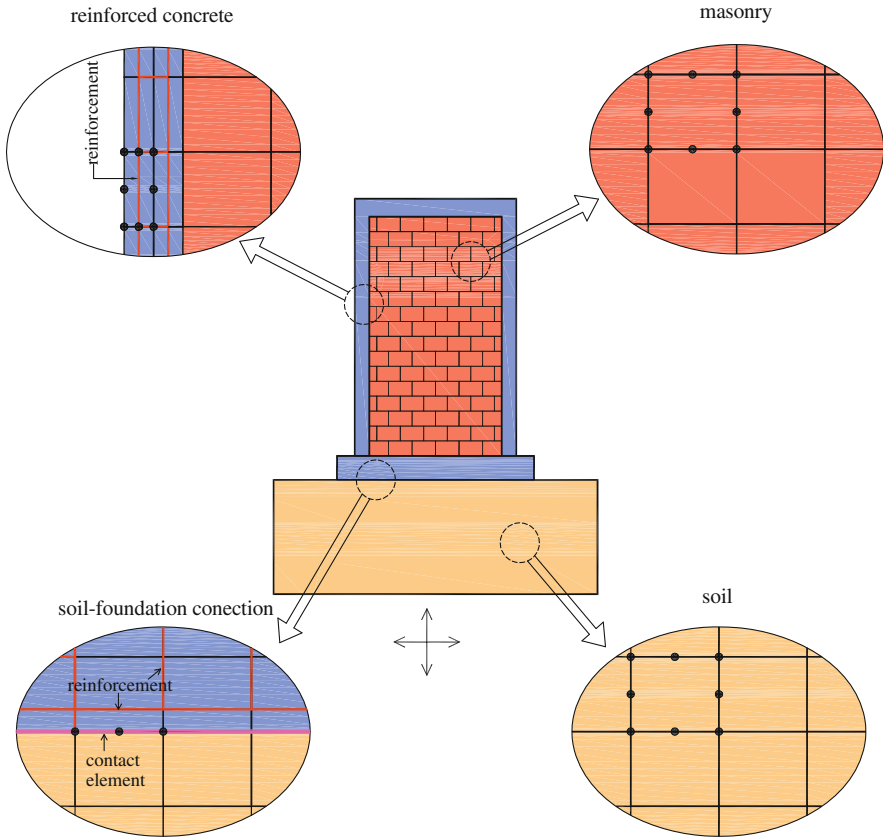


Fig. 19 An example of masonry wall spatial discretization

$\dot{\epsilon}$ the strength and elastic modulus of the material increase and its strain (ductility) at failure reduces.

This model includes the strain rate effects on the mechanical properties of reinforced concrete (concrete and steel) as described in [9]. The strain rate effects on the masonry and the soil have not been included.

4 Some Notes for Masonry Structures Modelling in Practice

As already stated, the presented numerical model is intended for static and dynamic analyses of masonry structures which can be satisfactory simulated by a planar model.

A spatial discretization of a masonry wall is shown in Fig. 19. In the case of whole masonry building simulation in one direction by planar model (analysis of the building in two separate directions), the masonry walls should be

interconnected at the floor level (common translational displacement of the walls). If the longitudinal wall is connected with a lateral wall, the effect of the lateral wall should be modelled by corresponding element width, mass and load. If the spatial structure model in the static and particularly dynamic analyses includes the sub-soil, it should be adequately simulated in the longitudinal and lateral directions.

5 Examples

Some possibilities for application of the presented numerical model and corresponding software are illustrated by the static and dynamic analyses of a two storey: confined masonry wall (Example 1), unreinforced masonry wall (Example 2), and masonry infilled concrete frame (Example 3).

5.1 Example 1

The basic data of the analyzed two storey confined masonry wall can be seen in Fig. 20. The macro model of masonry with isotropic material properties was adopted. The wall was founded on a rigid base, with the possibility of uplifting.

In the static analysis, the wall was loaded by self weight, other sustained vertical load q , and variable horizontal forces H_1 , H_2 at floor level up to wall collapse. Specifically, the different load factors f_0 of forces H_1 and H_2 were gradually changed, where $H_1 = 11$ kN and $H_2 = 11$ kN are the service load forces. The horizontal displacement of the wall top as a function of load factor f_0 is shown in Fig. 21a, the cracks of the wall just before the collapse in Fig. 21b, and reinforcement stress in point A and B in Fig. 21c. The behaviour of the wall is nearly linear-elastic up to the load factor of about $f_0 = 7$, i.e., by about half of the limit forces $H_1 = H_2$. After that, greater nonlinearity (cracks) occurred in the wall and the tensile stresses in the vertical reinforcement of the ring beam rapidly increased. Just before the collapse of the wall, there was a wide area of cracks.

In the dynamic analysis, the wall was subjected to horizontal harmonic base acceleration, where the excitation period corresponded to the first period of free oscillations. The horizontal displacement of the wall top is shown in Fig. 22a, the final state of cracks just before the collapse in Fig. 22b, and reinforcement stress in point A in Fig. 22c. There was a great difference of the results for the cases of the linear-elastic model and the nonlinear model. For the nonlinear model, there was a wide area of cracks, the remaining horizontal displacement and the remaining stresses in the vertical reinforcement of the ring beam at the end of the analysis.

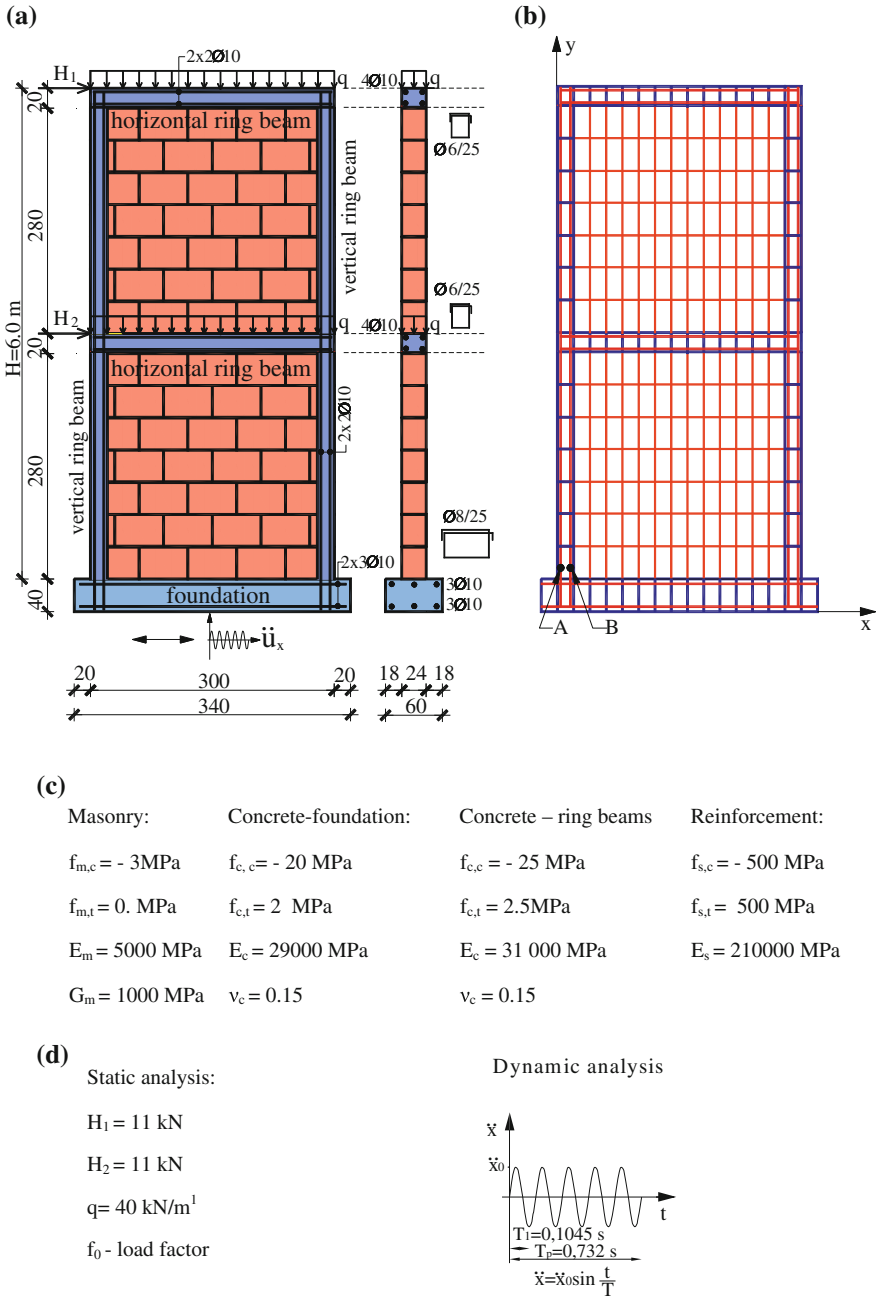
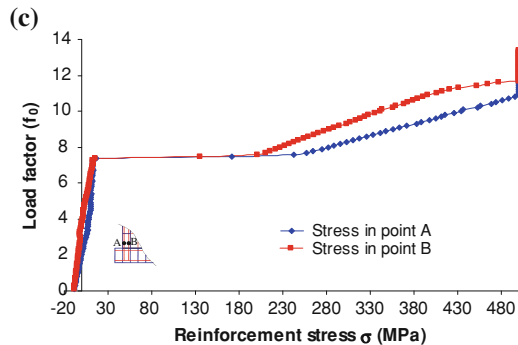
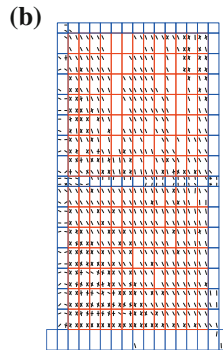
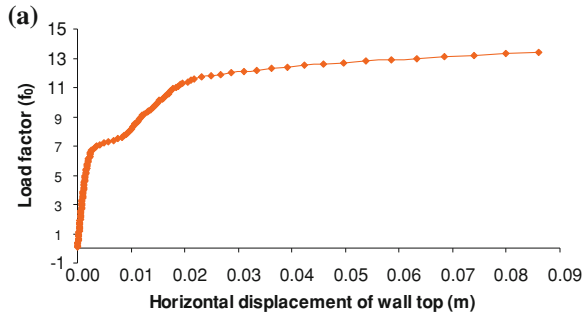


Fig. 20 Analyzed confined masonry wall from Example 1. **a** Geometry and load, **b** spatial discretization, **c** main material parameters, **d** load

Fig. 21 Some static analysis results of confined wall from Example1. **a** Horizontal displacement of wall top. **b** Cracks before collapse. **c** Reinforcement stress



5.2 Example 2

The basic data on the geometry, material properties, loads and spatial discretization of the two storey unreinforced wall are shown in Fig. 23. The macro model of masonry with isotropic material properties was also adopted.

In static analysis, the wall was also loaded by self weight and other sustained vertical load q , and variable horizontal forces H_1, H_2 at floor level up to wall collapse. The horizontal displacement of the wall top as a function of load factor f_0 is shown in Fig. 24a, and the cracks of the wall just before the collapse in Fig. 24b.

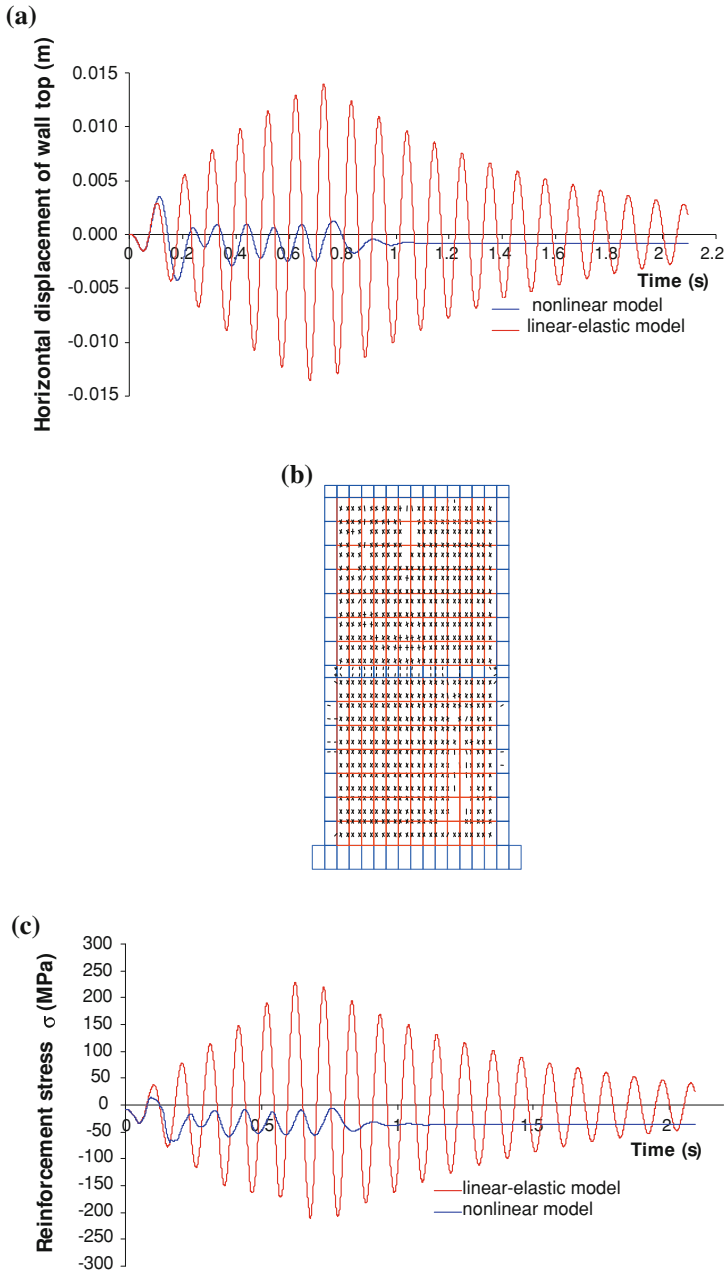
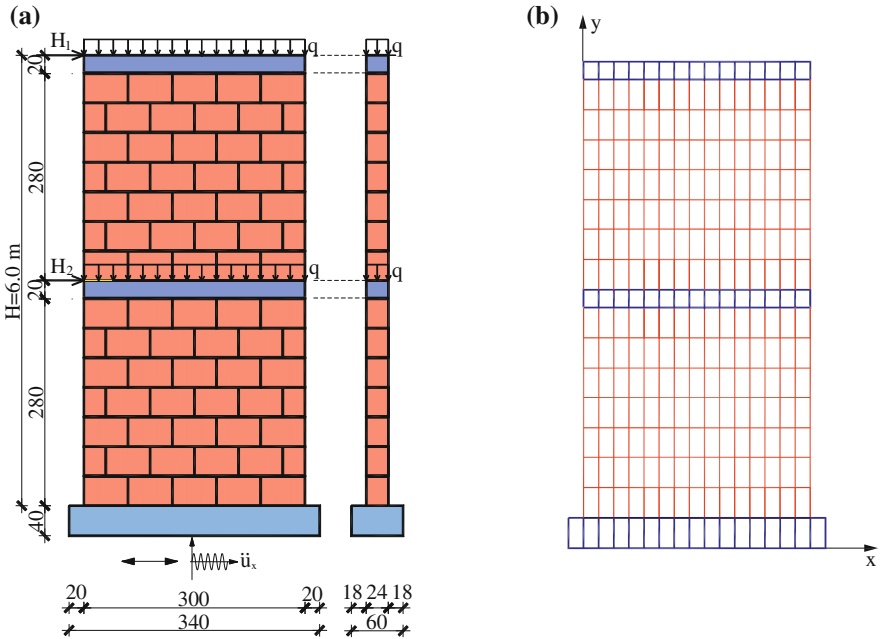


Fig. 22 Some dynamic analysis results of confined wall from Example 1. **a** Horizontal displacement of frame top. **b** Final state of cracks (nonlinear model). **c** Reinforcement stress in point A



(c)

Masonry:	Concrete-foundation:	Concrete-ring beams:
$f_{m,c} = -3 \text{ MPa}$	$f_{c,c} = -20 \text{ MPa}$	$f_{c,c} = -25 \text{ MPa}$
$f_{m,t} = 0.1 \text{ MPa}$	$f_{c,t} = 2 \text{ MPa}$	$f_{c,t} = 2.5 \text{ MPa}$
$E_m = 5000 \text{ MPa}$	$E_c = 29000 \text{ MPa}$	$E_c = 31000 \text{ MPa}$
$G_m = 1000 \text{ MPa}$	$\nu_c = 0.15$	$\nu_c = 0.15$

(d) Static analysis:

$H_1 = 11 \text{ kN}$

$H_2 = 11 \text{ kN}$

$q = 40 \text{ kN/m}^1$

f_0 - load factor

Dynamic analysis

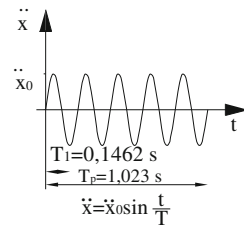


Fig. 23 Analyzed unreinforced masonry wall from Example 2. **a** Geometry and load. **b** Spatial discretization. **c** Main material parameters. **d** Load

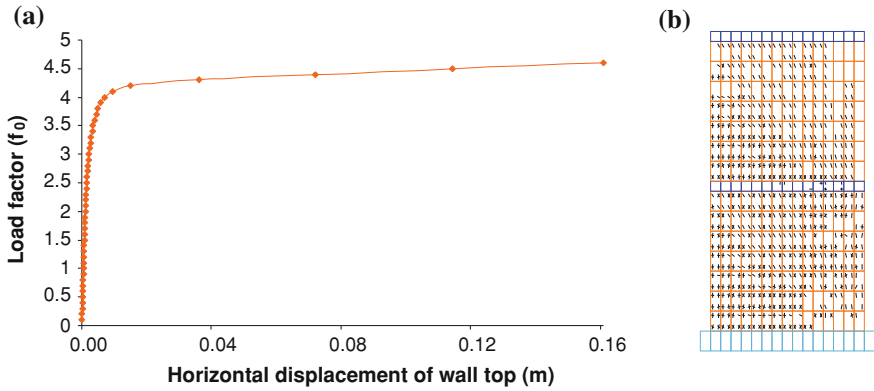


Fig. 24 Static analysis results of unreinforced wall from Example 2. **a** Horizontal displacement of wall top. **b** Cracks before collapse

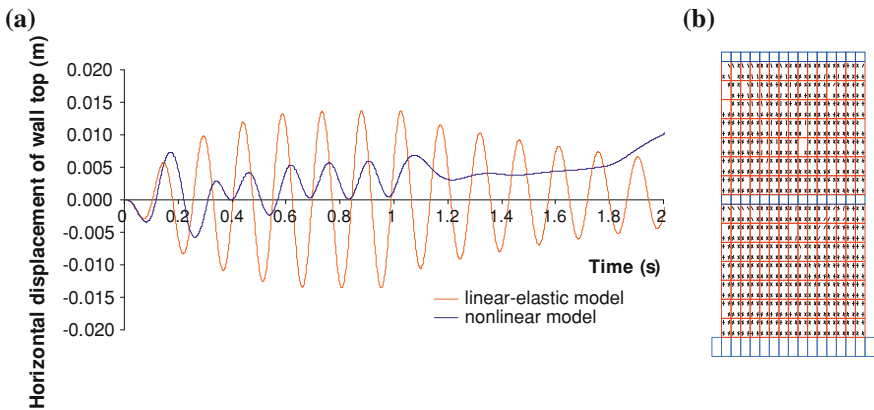
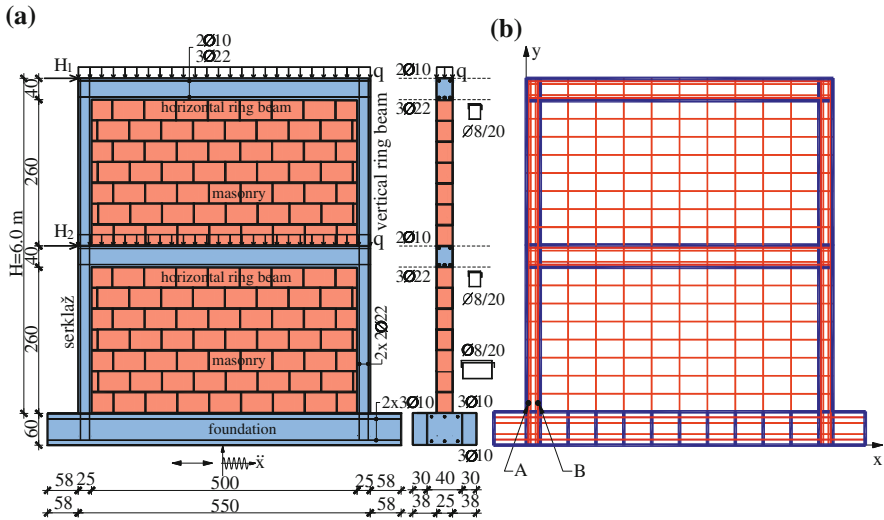


Fig. 25 Dynamic analysis results of unreinforced wall from Example2. **a** Horizontal displacement of wall top. **b** Final state of cracks (nonlinear model)

The behaviour of the wall was nearly linear-elastic up to just before the collapse, which occurred exceeding the tensile strength of masonry, with a wide area of cracks in the wall.

In the dynamic analysis, the wall was also subjected to horizontal harmonic base acceleration, where the excitation period also corresponded to the first period of free oscillations. The horizontal displacement of the wall top in time is shown in Fig. 25a, and the final state of the wall cracks just before collapse in Fig. 25b. Also, notable was the great difference in the horizontal displacement of the top of the wall for the linear-elastic model and the nonlinear model. For the nonlinear model, an irreversible horizontal displacement of the top of the wall was remained, which was rapidly increased at the end of the analysis (wall probably lose stability), with cracks on the entire surface of the wall.



(c) Masonry:	Concrete-foundation:	Concrete-ring beams	Reinforcement:
$f_{m,c} = -3 \text{ MPa}$	$f_{c,c} = -20 \text{ MPa}$	$f_{c,c} = -25 \text{ MPa}$	$f_{s,c} = -500 \text{ MPa}$
$f_{m,t} = 0.1 \text{ MPa}$	$f_{c,t} = 2 \text{ MPa}$	$f_{c,t} = 2.5 \text{ MPa}$	$f_{s,t} = 500 \text{ MPa}$
$E_m = 5000 \text{ MPa}$	$E_c = 29000 \text{ MPa}$	$E_c = 31\,000 \text{ MPa}$	$E_s = 210000 \text{ MPa}$
$G_m = 1000 \text{ MPa}$	$\nu_c = 0.15$	$\nu_c = 0.15$	

- (d) Static analysis:
- $H_1 = 10 \text{ kN}$
 - $H_2 = 10 \text{ kN}$
 - $q = q_I + q_{II} = 12 \text{ kN/m}^1 + 10 \text{ kN/m}^1$
 - $Q = 22 \text{ kN/m}^1$
 - f_0 - load factor

Dynamic analysis

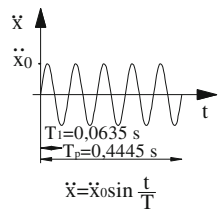


Fig. 26 Analyzed masonry infilled concrete frame from Example 3. a Geometry and load. b Spatial discretization. c Main material parameters. d Load

5.3 Example 3

The basic data of the geometry, material properties, loads and spatial discretization of analyzed masonry infilled concrete frame are shown in Fig. 26. The analysis of the structure was performed in two phases. A masonry macro model with isotropic material properties was also adopted.

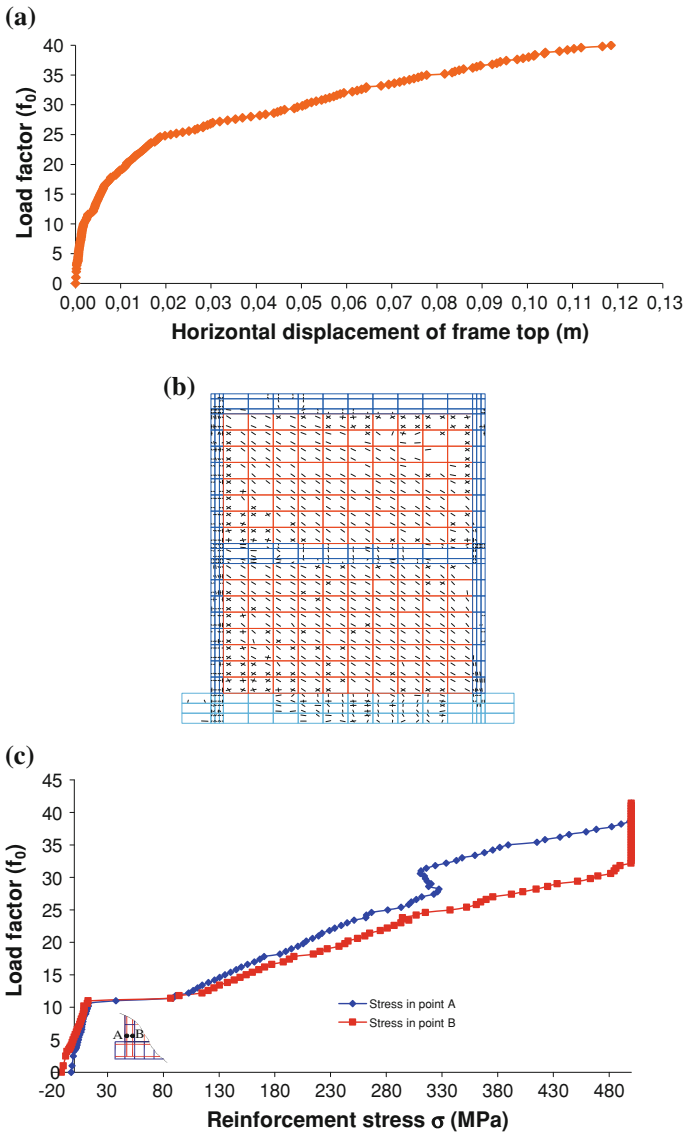


Fig. 27 Static analysis results of masonry infilled concrete frame from Example 3. **a** Horizontal displacement of frame top. **b** Cracks before collapse. **c** Reinforcement stress

In the static analysis of the first phase, only the concrete frame was loaded by appropriate sustained load. In the second phase, the infilled masonry elements were included with other sustained loads and variable horizontal load H_1 , H_2 (with various load factor f_0). The horizontal displacement of the top of the frame is shown in Fig. 27a, the state of cracks in Fig. 27b, and the reinforcement stress at the bottom of the column before collapse in Fig. 27c. The structure behaviour was

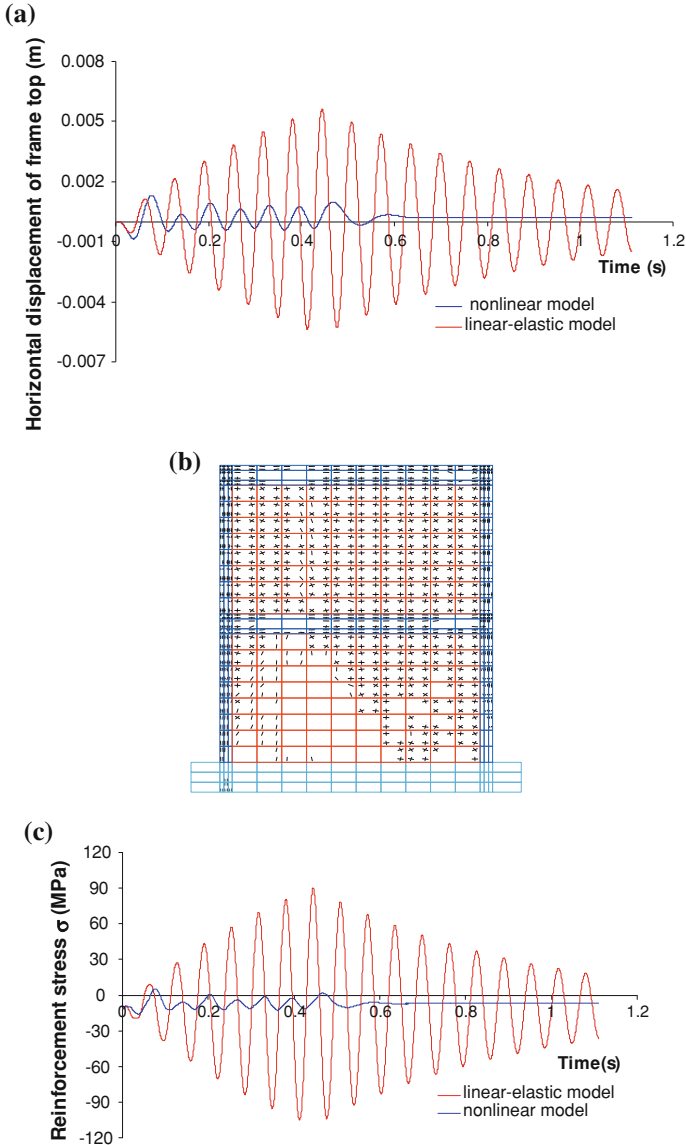


Fig. 28 Dynamic analysis results of masonry infilled concrete frame from Example 3. **a** Horizontal displacement of frame top. **b** Final state of cracks (nonlinear model). **c** Reinforcement stress in point A

linear-elastic up to about $f_0 = 11$, after which the cracks occurred and the tensile stresses in the column reinforcement rapidly increased. Just before the collapse of the structure, there was a wide area of cracks of the frame and the masonry.

The dynamic analysis considers the masonry infilled concrete frame exposed to horizontal harmonic base acceleration, where the excitation period corresponded to the first period of free oscillations. The horizontal displacement of the frame top is shown in Fig. 28a, the final state of cracks just before collapse in Fig. 28b, and the reinforcement stress in point A in Fig. 28c. There was also a great difference in the results for the cases of the linear-elastic model and the nonlinear model. The horizontal displacement of the top of the frame and the stress in the vertical reinforcement of the column were small for the nonlinear model. The area of the cracks on the wall of the first floor was wider than the area of the cracks of the second floor.

6 Conclusion

The presented numerical model can simulated many nonlinear effects of masonry, reinforced concrete and soil, such as yielding in compression, cracking in tension, opening and closing of cracks, tensile and shear stress of cracking material, etc. The macro and micro model of masonry can be used with the orthotropic constitutive material model. Shear failure of masonry can also be modelled. It is believed that the presented numerical model can provide a reliable non-linear static and dynamic analysis of different types of planar masonry structures (unreinforced, reinforced and confined). The solved examples illustrate some features of the model. Further testing of the presented model and the developed software on experimental tests and real structures are necessary.

Acknowledgments This work was supported by the funds of the Ministry of Science, Education and Sport of Croatia.

References

1. Brencich, A., de Felice, G.: Brickwork under eccentric compression: Experimental results and macroscopic models. *Constr. Build. Mater.* **23**, 1935–1946 (2009)
2. Brasile, S., Casciaro, R., Formica, G.: Multilevel approach for brick masonry walls-Part I: A numerical strategy for nonlinear analysis. *Compu. Methods Appl. Mech. Engrg.* **196**, 4934–4951 (2007)
3. Brasile, S., Casciaro, R., Formica, G.: Finite element formulation for nonlinear analysis of masonry walls. *Comp. Struct.* **88**, 135–143 (2010)
4. Chaimoon, K., Attard, M.: Modelling for unreinforced masonry walls under shear and compression. *Eng. Struct.* **29**, 2056–2068 (2007)
5. Zucchini, A., Lourenco, P.B.: A micro-mechanical model for the homogenisation of masonry. *Int. J. Solids Struct.* **39**, 3233–3255 (2002)
6. Harapin, A., Radnić, J., Brzović, D.: WYD method for an eigen solution of coupled problems. *Int. J. Multiphysics.* **3**, 167–176 (2009)

7. Hughes, T.J.R., Pister, K.S., Taylor, R.L.: Implicit-explicit finite elements in nonlinear transient analysis. *Comput. Methods Appl. Mech. Engrg.* **17–18**, 159–182 (1979)
8. Radnić, J., Damjanić, F.: Numerical model for static and dynamic analysis of RC structures. *Izgradnja* **10**, 5–14 (1989)
9. Radnić, J.: Modelling of the strain rate effects in dynamic analysis of R/C structures. *Eng. Model* **1–2**, 13–20 (1990)

Wrinkling Analysis of Rectangular Soft-Core Composite Sandwich Plates

Mohammad Mahdi Kheirikhah and Mohammad Reza Khalili

Abstract In the present chapter, a new improved higher-order theory is presented for wrinkling analysis of sandwich plates with soft orthotropic core. Third-order plate theory is used for face sheets and quadratic and cubic functions are assumed for transverse and in-plane displacements of the core, respectively. Continuity conditions for transverse shear stresses at the interfaces as well as the conditions of zero transverse shear stresses on the upper and lower surfaces of plate are satisfied. The nonlinear von Kármán type relations are used to obtain strains. Also, transverse flexibility and transverse normal strain and stress of the orthotropic core are considered. An analytical solution for static analysis of simply supported sandwich plates under uniaxial in-plane compressive load is presented using Navier's solution. The effect of geometrical parameters and material properties of face sheets and core are studied on the face wrinkling of sandwich plates. Comparison of the present results with those of plate theories confirms the accuracy of the proposed theory.

Keywords Overall Buckling • Wrinkling • Sandwich plate • Analytical solution • Soft core

M. M. Kheirikhah (✉)

Faculty of Industrial and Mechanical Engineering, Qazvin Branch, Islamic Azad University, Qazvin, Iran
e-mail: kheirikhah@qiau.ac.ir

M. R. Khalili

Centre of Excellence for Research in Advanced Materials & Structures,
Faculty of Mechanical Engineering, K.N. Toosi University of Technology, Tehran, Iran
e-mail: smrkhalili2005@gmail.com

1 Introduction

Sandwich plates are widely used in many engineering applications such as aerospace, automobile, and shipbuilding because of their high strength and stiffness, low weight and durability. These plates consist generally of two stiff face sheets and a soft core, which are bonded together. In most cases, the core consist of a thick foam polymer or honeycomb material, while thin composite laminates are commonly used as the face sheets. Sandwich plates experience some failure modes not occurring in metallic sheets or laminated plates. Face wrinkling is one of the important behaviors of these plates subjected to in-plane compressive loads. In this phenomenon, the faces buckle in shorter wavelength than those associated with overall buckling of the plate [1].

There are three different modes of wrinkling. The mode I which is named ‘rigid base’ may occur when only one of the face sheets buckle. The mode II or ‘anti-symmetric Wrinkling’ may happen when the mode-shape of the face sheets are the same. In this mode the mid-plane of the core deforms. In the mode III which is called ‘symmetric wrinkling’, the mode-shape of the face sheets is symmetric about mid-plane of sandwich plate. Such symmetrical modes can only occur in sandwich plates with a soft core material [2].

The first studies on wrinkling analysis of soft-core sandwich panels began in 1930s decade. Gough et al. [3] used the Winkler elastic foundation model to study sandwich panels with a compliant core material. They neglected the compressive stresses of the core in the direction of the applied load. The symmetric and anti-symmetric wrinkling for sandwich struts with isotropic facings and solid cores were investigated by Hoff and Mautner [4] using a new model. In this model, the through thickness deformation decays linearly from the face sheet into the core. Plantema [5] proposed an exponential decay for the through thickness deformation in his book. Allen [6] studied the 2D wrinkling problem of sandwich beams or plates in cylindrical bending. He solved the governing differential equation and assumed that the core stress field has to satisfy the Airy’s stress function under 2D conditions. Also, Zenkert [7] and Vinson [8] summarized sandwich wrinkling statements in their textbooks.

Benson and Mayers [9] presented a unified theory for the overall buckling and face wrinkling of sandwich panels with isotropic facings. This theory was expanded by Hadi and Matthews [10] for the wrinkling of anisotropic sandwich panels. Their approach was able to simultaneously calculate the anti-symmetric and symmetric wrinkling loads. Niu and Talreja [11] studied the wrinkling of composite sandwich plates. They presented a unified wrinkling model which combined three modes of wrinkling and also showed that the critical mode of wrinkling is the anti-symmetrical mode.

Frostig [12] developed a theory using the classical laminated plate theory (CLPT) for the face sheets and postulated a stress distribution in the core for overall and local buckling analysis of soft core sandwich plates. Analytical solutions were presented for simply supported soft-core sandwich plates, but the

transverse stress continuity conditions were neglected. In two papers, Dawe and Yuan [13, 14] provided a model which uses a quadratic and linear expansion of the in-plane and transverse displacements of the core and represented the face sheets as either FSDT or CLPT. A B-spline finite stripe method (FSM) was used for buckling and wrinkling of rectangular sandwich plates subjected to in-plane compressive and shears loads applied to the face sheets. Vonach and Rammerstorfer [15] studied the problem of the wrinkling of orthotropic sandwich panels under general loading. They assumed infinite thickness for the core and a sinusoidal wrinkling wave at the interface of the face sheet and the core. A high-order layer-wise model was proposed by Dafedar et al. [16] for buckling analysis of multi-core sandwich plates. They assumed cubic polynomial functions for all displacement components in any layer. As a large number of unknowns were involved, they proposed a simplified model and calculated critical loads based on the geometric stiffness matrix concept.

Leotoing et al. [17] proposed a single model for local and global buckling of sandwich beams with facings and core made of homogeneous isotropic linear elastic materials. In this model, a linear distribution was assumed for the transverse shear stress through the beam thickness. Biaxial wrinkling of sandwich panels with composite face sheets was investigated by Birman and Bert [1]. They used three different models for the core: a simple Winkler elastic foundation model, the Hoff and Mautner [4] model which assumed a linear decay for the through thickness deformation from the face sheet into the core, and the Plantema [5] model with exponential decay. Birman [18] also analyzed wrinkling of a large aspect ratio simply supported sandwich panel with cross-ply facings subjected to an elevated temperature or heat flux on one of the surfaces. Fagerberg and Zenkert [19] studied imperfection-induced wrinkling material failure in sandwich panels based on Allen's model [6]. Also, effects of anisotropy and biaxial loading on the wrinkling of sandwich panels were considered by Fagerberg and Zenkert [20]. Elastic and elastic-plastic skin wrinkling of graded and layered foam core sandwich panels were studied Grenestedt and Danielsson [21]. Kardomateas [22] presented a 2D elasticity solution for the wrinkling analysis of sandwich beams or wide sandwich panels subjected to axially compressive loading. The sandwich section was assumed symmetric and the facings and the core were considered to be orthotropic. Solutions for global buckling and face wrinkling of sandwich plates under transient loads were presented by Hohe [23] using the Galerkin method. He used the first-order shear deformable plate theory (FSDT) for the face sheets and linear and quadratic functions for transverse and in-plane displacements of the core. Meyer-Piening [24] presented two linear wrinkling formulations for sandwich plates with thin and thick orthotropic facings based on the analytical formulations of Zenkert [7]. He modified the models to account for unequal facings and orthotropic properties in the face layers and compared the obtained results with the finite element method (FEM).

Aiello and Ombres [25] presented an analytical approach for evaluating the buckling load of sandwich panels made of hybrid laminated faces and a transversely flexible core. A priori assumption of the displacement field through the

thickness was applied which was a superposition of symmetric and anti-symmetric components besides a pure compressive mode. Lopatin and Morzov [2] presented the solution of the face wrinkling problem for a sandwich panel with composite facings and an orthotropic core based on the energy method. They developed a new model of the elastic core which allowed for the transverse compression and shear of the core material as well as nonlinear through-the-thickness decay of the lateral normal displacements at wrinkling. Shariyat [26] studied nonlinear dynamic thermo-mechanical buckling and wrinkling of the imperfect sandwich plates using the finite element method. He introduced a generalized global–local plate theory (GLPT) that guarantees the continuity conditions of all displacements and transverse stress components and considered the transverse flexibility of sandwich plates.

Some researchers studied the face wrinkling problem of sandwich plates experimentally. Pearce and Webber [27] presented the overall buckling and wrinkling loads for different four-edges simply supported sandwich plates by experiments. Wadee [28] investigated localized cylindrical buckling of sandwich panels experimentally and compared the obtained results with the theoretical solutions. Also, Wadee [29] studied the effect of localized imperfections on the wrinkling of sandwich panels. Gdoutos et al. [30] measured face wrinkling failure loads of sandwich columns under compression, beams in three- and four-point bending and cantilever beams under end loading.

Noor et al. [31] presented three-dimensional elasticity solutions for global buckling of simply supported sandwich panels with composite face sheets. But, they did not present a wrinkling analysis of the sandwich plates. Kardomateas [32] presented a 2D elasticity solution for the wrinkling analysis of sandwich beams or wide sandwich panels subjected to axially compressive loading. The sandwich section was assumed symmetric and the facings and the core were considered to be orthotropic. Ji and Waas [33] studied the elastic stability of a sandwich panel (wide beam) using 2D classical elasticity. They obtained global buckling and wrinkling loads of 2D sandwich panels.

Based on the above discussions, it can be concluded that initial works on wrinkling of sandwich plates [3–6] modeled the supporting action of the core by a simple Winkler elastic foundation. In these models, the effect of the other face sheet is neglected and face sheets are assumed isotropic. Also, in this approach, the sandwich plate wrinkle in a 2D manner such as a sandwich beam or a sandwich plate in cylindrical bending. Based on this approach, some authors [1, 18–20] studied the wrinkling of sandwich plates with anisotropic or orthotropic face sheets. 2D wrinkling analysis of sandwich beams or sandwich plates in cylindrical bending was only presented using an elasticity solution [22] or an energy method [2]. Some investigators [12–14, 16, 23 and 26] assumed the layered sandwich plates consisting of two laminated composite face sheets and a soft flexible core and postulated polynomial functions for in-plane and transverse displacements of each layer. Frostig [12], Dafedar et al. [16] and Hohe [23] presented analytical solutions for wrinkling analysis of sandwich plates, but they used some simplifications which resulted in a lower accuracy. The higher-order global–local theory

of Shariyat [26] is sufficient and accurate for the solution of sandwich plates. But, his solution for buckling and wrinkling problem was not presented analytically.

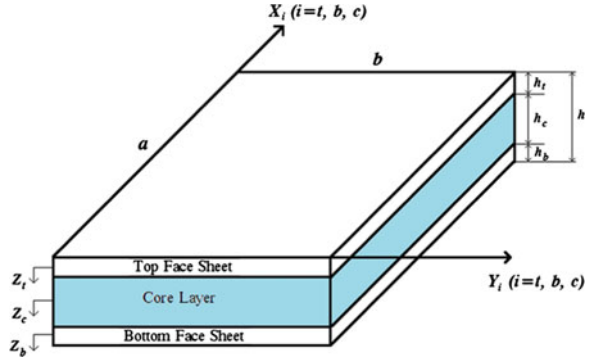
Therefore, it seems there are no published papers on an analytical solution for wrinkling analysis of composite-faced sandwich plates using an accurate 3D theory. The purpose of this chapter is to present a higher-order plate theory for the wrinkling analysis of composite-faced sandwich plates with a soft orthotropic core. There are some important points to be noted for more accuracy in the modeling and analysis of sandwich structures. The continuity conditions of the displacements and the inter-laminar transverse shear stresses should be satisfied to accurately model the mechanical behavior of these plates. But, variation of material properties between the core and the face sheets causes slopes of displacements and transverse shear stresses to change in the face sheet-core interfaces. In addition, the conditions of zero transverse shear stresses on the upper and lower surfaces must be enforced. Polymer foam cores are very flexible relative to the face sheets. As such, this behavior leads to un-identical displacement patterns through the depth of the panel and also the displacements of the upper face sheet differ from those of the lower one [34].

In the present chapter, third-order plate theory is used for the face sheets and quadratic and cubic functions are assumed for the transverse and in-plane displacements of the core. The nonlinear von Kármán type relations are used to obtain strains. Continuity conditions of transverse shear stresses at the interfaces as well as the conditions of zero transverse shear stresses on the upper and lower surfaces of the plate are satisfied. Also, transverse flexibility and transverse normal strain and stress of the core are considered. The equations of motion and boundary conditions are derived via the principle of minimum potential energy. An analytical solution for static analysis of simply supported sandwich plates under in-plane compressive loads is presented using Navier's solution. Wrinkling loads are obtained for various sandwich plates. The effect of geometrical parameters of face sheets and core are studied on the wrinkling behavior of sandwich plates.

2 Mathematical Formulations

A rectangular sandwich plate with plane dimensions $a \times b$ and total thickness of h is considered, as shown in Fig. 1. The sandwich is composed of three layers: the top and the bottom face sheets and the core layer. All layers are assumed with a uniform thickness and the z -coordinate of each layer is measured downward from its mid-plane. The face sheets are generally unequal in thickness i.e. h_t and h_b are the thicknesses of the top and bottom face sheets respectively. The face sheets are assumed to be laminated composites. The core is also assumed as a soft orthotropic material with thickness h_c .

Fig. 1 A typical sandwich plate and its dimensions



2.1 Kinematic Relations

In the present structural model for sandwich plates, the third-order shear deformable theory is adopted for the face sheets. Hence, the displacement components of the top and bottom face sheets ($j = t, b$) are represented as [34]:

$$\begin{aligned} u_j(x, y, z_t) &= u_{0j}(x, y) + z_j u_{1j}(x, y) + z_j^2 u_{2j}(x, y) + z_j^3 u_{3j}(x, y) \\ v_j(x, y, z_t) &= v_{0j}(x, y) + z_j v_{1j}(x, y) + z_j^2 v_{2j}(x, y) + z_j^3 v_{3j}(x, y) \\ w_j(x, y, z_t) &= w_{0j}(x, y) \end{aligned} \quad (1)$$

where u_{kj} and v_{kj} ($k = 0, 1, 2, 3$) are the unknowns of the in-plane displacements of each face sheet and w_{0j} are the unknowns of its vertical displacements, respectively.

The core layer is much thicker and softer than the face sheets. Thus, the displacements fields for the core are assumed as a cubic pattern for the in-plane displacement components and as a quadratic one for the vertical component:

$$\begin{aligned} u_c(x, y, z_c) &= u_{0c}(x, y) + z_c u_{1c}(x, y) + z_c^2 u_{2c}(x, y) + z_c^3 u_{3c}(x, y) \\ v_c(x, y, z_c) &= v_{0c}(x, y) + z_c v_{1c}(x, y) + z_c^2 v_{2c}(x, y) + z_c^3 v_{3c}(x, y) \\ w_c(x, y, z_c) &= w_{0c}(x, y) + z_c w_{1c}(x, y) + z_c^2 w_{2c}(x, y) \end{aligned} \quad (2)$$

where u_{kc} and v_{kc} ($k = 0, 1, 2, 3$) are the unknowns of the in-plane displacement components of the core and w_{lc} ($l = 0, 1, 2$) are the unknowns of its vertical displacements, respectively. Therefore, the face sheets are assumed as in-plane flexible and transversely rigid plates. Also, the core is assumed as in-plane and transversely flexible layer. Finally, in this model there are twenty-nine displacement unknowns: nine unknowns for each face sheet and eleven unknowns for the core.

2.2 Compatibility Conditions

In the present sandwich plate theory, the core is perfectly bonded to the face sheets. Hence, there are three interface displacement continuity requirements in each face sheet-core interface which can be obtained as follows:

$$\begin{aligned}
 u_t \left(z_t = \frac{h_t}{2} \right) &= u_c \left(z_c = \frac{-h_c}{2} \right), u_b \left(z_b = \frac{-h_b}{2} \right) = u_c \left(z_c = \frac{h_c}{2} \right) \\
 v_t \left(z_t = \frac{h_t}{2} \right) &= v_c \left(z_c = \frac{-h_c}{2} \right), v_b \left(z_b = \frac{-h_b}{2} \right) = v_c \left(z_c = \frac{h_c}{2} \right) \\
 w_t \left(z_t = \frac{h_t}{2} \right) &= w_c \left(z_c = \frac{-h_c}{2} \right), w_b \left(z_b = \frac{-h_b}{2} \right) = w_c \left(z_c = \frac{h_c}{2} \right)
 \end{aligned} \tag{3}$$

2.3 Strains

The nonlinear von Kármán strain–displacement relations for the face sheets ($j = t, b$) can be expressed as:

$$\begin{aligned}
 \varepsilon_{xx}^j &= u_{0j,x} + z_j u_{1j,x} + z_j^2 u_{2j,x} + z_j^3 u_{3j,x} + \frac{1}{2} (w_{0j,x})^2 \\
 \varepsilon_{yy}^j &= v_{0j,y} + z_j v_{1j,y} + z_j^2 v_{2j,y} + z_j^3 v_{3j,y} + \frac{1}{2} (w_{0j,y})^2 \\
 \varepsilon_{zz}^j &= 0 \\
 \gamma_{xy}^j &= v_{0j,x} + z_j v_{1j,x} + z_j^2 v_{2j,x} + z_j^3 v_{3j,x} + u_{0j,y} + z_j u_{1j,y} + z_j^2 u_{2j,y} + z_j^3 u_{3j,y} + w_{0j,x} w_{0j,y} \\
 \gamma_{xz}^j &= u_{1j} + 2z_j u_{2j} + 3z_j^2 u_{3j} + w_{0j,x} \\
 \gamma_{yz}^j &= v_{1j} + 2z_j v_{2j} + 3z_j^2 v_{3j} + w_{0j,y}
 \end{aligned} \tag{4}$$

and the nonlinear von Kármán strain–displacement relations for the core can be defined as:

$$\begin{aligned}
 \varepsilon_{xx}^c &= u_{0c,x} + z_c u_{1c,x} + z_c^2 u_{2c,x} + z_c^3 u_{3c,x} + \frac{1}{2} (w_{0c,x})^2 \\
 \varepsilon_{yy}^c &= v_{0c,y} + z_c v_{1c,y} + z_c^2 v_{2c,y} + z_c^3 v_{3c,y} + \frac{1}{2} (w_{0c,y})^2 \\
 \varepsilon_{zz}^c &= w_{1c} + 2z_c w_{2c} \\
 \gamma_{xy}^c &= v_{0c,x} + z_c v_{1c,x} + z_c^2 v_{2c,x} + z_c^3 v_{3c,x} + u_{0c,y} + z_c u_{1c,y} + z_c^2 u_{2c,y} + z_c^3 u_{3c,y} + w_{0c,x} w_{0c,y} \\
 \gamma_{xz}^c &= u_{1c} + 2z_c u_{2c} + 3z_c^2 u_{3c} + w_{0c,x} + z_c w_{1c,x} + z_c^2 w_{2c,x} \\
 \gamma_{yz}^c &= v_{1c} + 2z_c v_{2c} + 3z_c^2 v_{3c} + w_{0c,y} + z_c w_{1c,y} + z_c^2 w_{2c,y}
 \end{aligned} \tag{5}$$

2.4 Transverse Shear Stresses

For an orthotropic lamina of laminated composite plates such as the top and bottom face sheets, the reduced stress–strain relationships can be defined as follows [34]:

$$\begin{Bmatrix} \sigma_{xx} \\ \sigma_{yy} \\ \tau_{yz} \\ \tau_{xz} \\ \tau_{xy} \end{Bmatrix} = \begin{bmatrix} Q_{11} & Q_{12} & 0 & 0 & Q_{16} \\ Q_{12} & Q_{22} & 0 & 0 & Q_{26} \\ 0 & 0 & Q_{44} & Q_{45} & 0 \\ 0 & 0 & Q_{45} & Q_{55} & 0 \\ Q_{16} & Q_{26} & 0 & 0 & Q_{66} \end{bmatrix} \begin{Bmatrix} \varepsilon_{xx} \\ \varepsilon_{yy} \\ \gamma_{yz} \\ \gamma_{xz} \\ \gamma_{xy} \end{Bmatrix} \quad (6)$$

where Q_{mn} ($m, n = 1, 2, 6$) are the reduced stiffness coefficients and Q_{kl} ($k, l = 4, 5$) are the transverse shear stiffness coefficients. The transverse shear stresses on the upper surface of the sandwich plate are zero [32]. Hence:

$$\begin{cases} Q_{44}^u \gamma_{yz}^t \left(z_t = \frac{-h_t}{2} \right) + Q_{45}^u \gamma_{xz}^t \left(z_t = \frac{-h_t}{2} \right) = 0 \\ Q_{45}^u \gamma_{yz}^t \left(z_t = \frac{-h_t}{2} \right) + Q_{55}^u \gamma_{xz}^t \left(z_t = \frac{-h_t}{2} \right) = 0 \end{cases} \quad (7)$$

where Q_{mn}^u ($m, n = 4, 5$) and γ_{kz}^t ($k = x, y$) are the transverse shear stiffness coefficients and transverse shear strains of the upper lamina of the top face sheet, respectively. From the above equations, it can be simply drawn that:

$$\gamma_{yz}^t \left(z_t = \frac{-h_t}{2} \right) = \gamma_{xz}^t \left(z_t = \frac{-h_t}{2} \right) = 0 \quad (8)$$

Similarly, for the lower lamina of the bottom face sheet:

$$\gamma_{yz}^b \left(z_b = \frac{h_b}{2} \right) = \gamma_{xz}^b \left(z_b = \frac{h_b}{2} \right) = 0 \quad (9)$$

In addition, the continuity of transverse shear stresses at the top and bottom face sheet-core interfaces must be satisfied. The stress–strain relationships for the orthotropic core can be read as follows [34]:

$$\begin{Bmatrix} \sigma_{xx}^c \\ \sigma_{yy}^c \\ \sigma_{zz}^c \\ \tau_{yz}^c \\ \tau_{xz}^c \\ \tau_{xy}^c \end{Bmatrix} = \begin{bmatrix} C_{11}^c & C_{12}^c & C_{13}^c & 0 & 0 & 0 \\ C_{21}^c & C_{22}^c & C_{23}^c & 0 & 0 & 0 \\ C_{31}^c & C_{32}^c & C_{33}^c & 0 & 0 & 0 \\ 0 & 0 & 0 & C_{44}^c & 0 & 0 \\ 0 & 0 & 0 & 0 & C_{55}^c & 0 \\ 0 & 0 & 0 & 0 & 0 & C_{66}^c \end{bmatrix} = \begin{Bmatrix} \varepsilon_{xx}^c \\ \varepsilon_{yy}^c \\ \varepsilon_{zz}^c \\ \gamma_{yz}^c \\ \gamma_{xz}^c \\ \gamma_{xy}^c \end{Bmatrix} \quad (10)$$

where C_{mn}^c ($m, n = 1, \dots, 6$) are the stiffness coefficients of the core. Therefore, at the top face sheet-core interface, the transverse shear stress continuity conditions can be read as:

$$\begin{cases} Q_{44}^{tl} \gamma_{yz}^t \left(z_t = \frac{h_t}{2} \right) + Q_{45}^{tl} \gamma_{xz}^t \left(z_t = \frac{h_t}{2} \right) = C_{44}^c \gamma_{yz}^c \left(z_c = \frac{-h_c}{2} \right) \\ Q_{45}^{tl} \gamma_{yz}^t \left(z_t = \frac{h_t}{2} \right) + Q_{55}^{tl} \gamma_{xz}^t \left(z_t = \frac{h_t}{2} \right) = C_{55}^c \gamma_{xz}^c \left(z_c = \frac{-h_c}{2} \right) \end{cases} \quad (11)$$

In the above equations, $Q_{mn}^{tl} (m, n = 4, 5)$ and $\gamma_{kz}^t (k = x, y)$ are the transverse shear stiffness coefficients and the transverse shear strains of the lower lamina of the top face sheet, respectively. $C_{mn}^c (m = 4, 5)$ are the transverse shear stiffness coefficients of the core and $\gamma_{kz}^c (k = x, y)$ are the transverse shear strains of the core. Similarly, at the bottom face sheet-core interface:

$$\begin{cases} Q_{44}^{bu} \gamma_{yz}^b \left(z_b = \frac{-h_b}{2} \right) + Q_{45}^{bu} \gamma_{xz}^b \left(z_b = \frac{-h_b}{2} \right) = C_{44}^c \gamma_{yz}^c \left(z_c = \frac{h_c}{2} \right) \\ Q_{45}^{bu} \gamma_{yz}^b \left(z_b = \frac{-h_b}{2} \right) + Q_{55}^{bu} \gamma_{xz}^b \left(z_b = \frac{-h_b}{2} \right) = C_{55}^c \gamma_{xz}^c \left(z_c = \frac{h_c}{2} \right) \end{cases} \quad (12)$$

where $Q_{mn}^{bu} (m, n = 4, 5)$ and $\gamma_{kz}^b (k = x, y)$ are the transverse shear stiffness coefficients and transverse shear strains of the upper lamina of the bottom face sheet, respectively. Finally, eight Eqs. (8, 9, 11, 12) are obtained for satisfying the continuity conditions of transverse shear stresses at the interfaces as well as the conditions of zero transverse shear stresses on the upper and lower surfaces of the sandwich plate. In the case of cross-ply laminated face sheets, these equations can be reduced by applying $Q_{45}^{tu} = Q_{45}^{tl} = Q_{45}^{bu} = Q_{45}^{bl} = 0$. In addition, for an orthotropic core $C_{44}^c = G_{yz}^c$ and $C_{55}^c = G_{xz}^c$.

2.5 Governing Equations

The governing equations of motion for the face sheets and the core are derived through the principle of minimum potential energy:

$$\delta \Pi = \delta U + \delta V = 0 \quad (13)$$

where U is the total strain energy, V is the potential of the external loads and δ denotes the variation operator. The variation of the external work equals to:

$$\delta V = - \int_0^a \int_0^b \left[\bar{n}_{xt} \delta u_{0t} + \bar{n}_{yt} \delta v_{0t} + q_t \delta w_{0t} + \bar{n}_{xb} \delta u_{0b} + \bar{n}_{yb} \delta v_{0b} + q_b \delta w_{0b} \right] dx dy \quad (14)$$

where u_{0j} , v_{0j} and $w_{0j} (j = t, b)$ are the displacements of the mid-plane of the face sheets in the longitudinal, transverse and vertical directions, respectively; \bar{n}_{xj} and $\bar{n}_{yj} (j = t, b)$ are the in-plane external loads of the top and bottom face sheets and q_t and q_b are the vertical distributed loads applied on the top and bottom face sheets, respectively.

The first variation of the total strain energy can be expressed in terms of all stresses and strains of the face sheets and the core. In addition, six compatibility conditions at the interfaces, four conditions of zero transverse shear stresses on the upper and lower surfaces of the plate and four continuity conditions of transverse shear stresses at the interfaces are fulfilled by using fourteen Lagrange multipliers. Thus, the variation of the strain energy for the sandwich plate with cross-ply laminated face sheets and an orthotropic core can be modified by using the following equation [12]:

$$\begin{aligned}
\delta U = & \int_{v_t} \left(\sigma_{xx}^t \delta \varepsilon_{xx}^t + \sigma_{yy}^t \delta \varepsilon_{yy}^t + \tau_{xy}^t \delta \gamma_{xy}^t + \tau_{xz}^t \delta \gamma_{xz}^t + \tau_{yz}^t \delta \gamma_{yz}^t \right) dv \\
& + \int_{v_b} \left(\sigma_{xx}^b \delta \varepsilon_{xx}^b + \sigma_{yy}^b \delta \varepsilon_{yy}^b + \tau_{xy}^b \delta \gamma_{xy}^b + \tau_{xz}^b \delta \gamma_{xz}^b + \tau_{yz}^b \delta \gamma_{yz}^b \right) dv \\
& + \int_{v_c} \left(\sigma_{zz}^c \delta \varepsilon_{zz}^c + \tau_{xz}^c \delta \gamma_{xz}^c + \tau_{yz}^c \delta \gamma_{yz}^c + \sigma_{xx}^c \delta \varepsilon_{xx}^c + \sigma_{yy}^c \delta \varepsilon_{yy}^c + \tau_{xy}^c \delta \gamma_{xy}^c \right) dv \\
& + \delta \left\{ \int_0^a \int_0^b \int_0^t \left[\lambda_x^t \left(u_t \left(z_t = \frac{h_t}{2} \right) - u_c \left(z_c = \frac{-h_c}{2} \right) \right) + \lambda_y^t \left(v_t \left(z_t = \frac{h_t}{2} \right) - v_c \left(z_c = \frac{-h_c}{2} \right) \right) \right. \right. \\
& + \lambda_z^t \left(w_t \left(z_t = \frac{h_t}{2} \right) - w_c \left(z_c = \frac{-h_c}{2} \right) \right) + \lambda_x^b \left(u_b \left(z_b = \frac{-h_b}{2} \right) - u_c \left(z_c = \frac{h_c}{2} \right) \right) \\
& \left. + \lambda_y^b \left(v_b \left(z_b = \frac{-h_b}{2} \right) - v_c \left(z_c = \frac{h_c}{2} \right) \right) + \lambda_z^b \left(w_b \left(z_b = \frac{-h_b}{2} \right) - w_c \left(z_c = \frac{h_c}{2} \right) \right) \right] dx dy \Big\} \\
& + \delta \left\{ \int_0^a \int_0^b \int_0^t \left[\lambda_{xz}^t \left(\gamma_{xz}^t \left(z_t = \frac{-h_t}{2} \right) \right) + \lambda_{yz}^t \left(\gamma_{yz}^t \left(z_t = \frac{-h_t}{2} \right) \right) + \lambda_{xz}^b \left(\gamma_{xz}^b \left(z_b = \frac{h_b}{2} \right) \right) \right. \right. \\
& + \lambda_{yz}^b \left(\gamma_{yz}^b \left(z_b = \frac{h_b}{2} \right) \right) + \lambda_{yz}^{tc} \left(Q_{44}^t \gamma_{yz}^t \left(z_t = \frac{h_t}{2} \right) - G_{yz}^c \gamma_{yz}^c \left(z_c = \frac{-h_c}{2} \right) \right) \\
& + \lambda_{xz}^{tc} \left(Q_{55}^t \gamma_{xz}^t \left(z_t = \frac{h_t}{2} \right) - G_{xz}^c \gamma_{xz}^c \left(z_c = \frac{-h_c}{2} \right) \right) + \lambda_{yz}^{bc} \left(Q_{44}^b \gamma_{yz}^b \left(z_b = \frac{-h_b}{2} \right) - G_{yz}^c \gamma_{yz}^c \left(z_c = \frac{h_c}{2} \right) \right) \\
& \left. + \lambda_{xz}^{bc} \left(Q_{55}^b \gamma_{xz}^b \left(z_t = \frac{-h_b}{2} \right) - G_{xz}^c \gamma_{xz}^c \left(z_c = \frac{h_c}{2} \right) \right) \right] dx dy \Big\}
\end{aligned} \tag{15}$$

where $\lambda_i^j (i = x, y, z), (j = t, b)$ are the six Lagrange multipliers for compatibility conditions at the top and bottom interfaces; $\lambda_{iz}^j (i = x, y), (j = t, b)$ are the four Lagrange multipliers for conditions of zero transverse shear stresses on the upper and lower surfaces of the plate and $\lambda_{iz}^{jc} (i = x, y), (j = t, b)$ are the four Lagrange multipliers for continuity conditions of transverse shear stresses at the interfaces. The stress resultants for the two face sheets and the core ($j = t, b, c$) can be defined as:

$$\left\{ \begin{array}{ccc} N_{xx}^j & N_{yy}^j & N_{xy}^j \\ M_{xx}^j & M_{yy}^j & M_{xy}^j \\ P_{xx}^j & P_{yy}^j & P_{xy}^j \\ R_{xx}^j & R_{yy}^j & R_{xy}^j \end{array} \right\} = \frac{h_j}{2} \int_{-\frac{h_j}{2}}^{\frac{h_j}{2}} \left[\begin{array}{ccc} \sigma_{xx}^j & \sigma_{yy}^j & \tau_{xy}^j \end{array} \right] \left\{ \begin{array}{c} 1 \\ z_j \\ z_j^2 \\ z_j^3 \end{array} \right\} dz_j \tag{16}$$

$$\begin{Bmatrix} Q_{xz}^j \\ S_{xz}^j \\ T_{xz}^j \end{Bmatrix} \begin{Bmatrix} Q_{yz}^j \\ S_{yz}^j \\ T_{yz}^j \end{Bmatrix} = \int_{\frac{-h_j}{2}}^{\frac{h_j}{2}} \begin{bmatrix} \tau_{xz}^j & \tau_{yz}^j \end{bmatrix} \begin{Bmatrix} 1 \\ z_j \\ z_j^2 \end{Bmatrix} dz_j \quad (17)$$

Also, the transverse normal stress resultants for the core can be defined as:

$$\begin{Bmatrix} N_{zz}^c \\ M_{zz}^c \end{Bmatrix} = \int_{\frac{-h_c}{2}}^{\frac{h_c}{2}} \sigma_{zz}^c \begin{Bmatrix} 1 \\ z_c \end{Bmatrix} dz_c \quad (18)$$

Integrating by part and doing some mathematical operations, the equations of motion for the top face sheet can be calculated as:

$$\begin{aligned} -N_{xx,x}^t - N_{xy,y}^t + \lambda_x^t - \bar{n}_{xt} &= 0 \\ -M_{xx,x}^t - M_{xy,y}^t + Q_{xz}^t + \frac{h_t}{2} \lambda_x^t + \lambda_{xz}^t + \frac{h_t}{2} \bar{n}_{xt} &= 0 \\ -P_{xx,x}^t - P_{xy,y}^t + 2S_{xz}^t + \frac{h_t^2}{4} \lambda_x^t - h_t \lambda_{xz}^t + \lambda_{xz}^{tc} - \frac{h_t^2}{4} \bar{n}_{xt} &= 0 \\ -R_{xx,x}^t - R_{xy,y}^t + 3T_{xz}^t + \frac{h_t^3}{8} \lambda_x^t + \frac{3h_t^2}{4} \lambda_{xz}^t + \frac{h_t^3}{8} \bar{n}_{xt} &= 0 \\ -N_{yy,y}^t - N_{xy,x}^t + \lambda_y^t - \bar{n}_{yt} &= 0 \\ -M_{yy,y}^t - M_{xy,x}^t + Q_{yz}^t + \frac{h_t}{2} \lambda_y^t + \lambda_{yz}^t + \frac{h_t}{2} \bar{n}_{yt} &= 0 \\ -P_{yy,y}^t - P_{xy,x}^t + 2S_{yz}^t + \frac{h_t^2}{4} \lambda_y^t - h_t \lambda_{yz}^t + \lambda_{yz}^{tc} - \frac{h_t^2}{4} \bar{n}_{yt} &= 0 \\ -R_{yy,y}^t - R_{xy,x}^t + 3T_{yz}^t + \frac{h_t^3}{8} \lambda_y^t + \frac{3h_t^2}{4} \lambda_{yz}^t + \frac{h_t^3}{8} \bar{n}_{yt} &= 0 \\ -Q_{xz,x}^t - Q_{yz,y}^t - \mathcal{N}(w_{0t}) + \lambda_z^t - \lambda_{xz,x}^t - \lambda_{yz,y}^t - q_t &= 0 \end{aligned} \quad (19)$$

and for the bottom face sheet as:

$$\begin{aligned} -N_{xx,x}^b - N_{xy,y}^b + \lambda_x^b - \bar{n}_{xb} &= 0 \\ -M_{xx,x}^b - M_{xy,y}^b + Q_{xz}^b - \frac{h_b}{2} \lambda_x^b + \lambda_{xz}^b - \frac{h_b}{2} \bar{n}_{xb} &= 0 \\ -P_{xx,x}^b - P_{xy,y}^b + 2S_{xz}^b + \frac{h_b^2}{4} \lambda_x^b + h_b \lambda_{xz}^b + \lambda_{xz}^{bc} - \frac{h_b^2}{4} \bar{n}_{xb} &= 0 \\ -R_{xx,x}^b - R_{xy,y}^b + 3T_{xz}^b - \frac{h_b^3}{8} \lambda_x^b + \frac{3h_b^2}{4} \lambda_{xz}^b - \frac{h_b^3}{8} \bar{n}_{xb} &= 0 \\ -N_{yy,y}^b - N_{xy,x}^b + \lambda_y^b - \bar{n}_{yb} &= 0 \\ -M_{yy,y}^b - M_{xy,x}^b + Q_{yz}^b - \frac{h_b}{2} \lambda_y^b + \lambda_{yz}^b - \frac{h_b}{2} \bar{n}_{yb} &= 0 \\ -P_{yy,y}^b - P_{xy,x}^b + 2S_{yz}^b + \frac{h_b^2}{4} \lambda_y^b + h_b \lambda_{yz}^b + \lambda_{yz}^{bc} - \frac{h_b^2}{4} \bar{n}_{yb} &= 0 \\ -R_{yy,y}^b - R_{xy,x}^b + 3T_{yz}^b - \frac{h_b^3}{8} \lambda_y^b + \frac{3h_b^2}{4} \lambda_{yz}^b - \frac{h_b^3}{8} \bar{n}_{yb} &= 0 \\ -Q_{xz,x}^b - Q_{yz,y}^b - \mathcal{N}(w_{0b}) + \lambda_z^b - \lambda_{xz,x}^b - \lambda_{yz,y}^b - q_b &= 0 \end{aligned} \quad (20)$$

and also for the core as:

$$\begin{aligned}
& -N_{xx,x}^c - N_{xy,y}^c - \lambda_x^t - \lambda_x^b = 0 \\
& -M_{xx,x}^c - M_{xy,y}^c + Q_{xz}^c + \frac{h_c}{2} \lambda_x^t - \frac{h_c}{2} \lambda_x^b - \frac{G_{xz}^c}{2h_t Q_{55}^t} \lambda_{xz}^{tc} + \frac{G_{xz}^c}{2h_b Q_{55}^b} \lambda_{xz}^{bc} = 0 \\
& -P_{xx,x}^c - P_{xy,y}^c + 2S_{xz}^c - \frac{h_c^2}{4} \lambda_x^t - \frac{h_c^2}{4} \lambda_x^b + \frac{G_{xz}^c h_c}{2h_t Q_{55}^t} \lambda_{xz}^{tc} + \frac{G_{xz}^c h_c}{2h_b Q_{55}^b} \lambda_{xz}^{bc} = 0 \\
& -R_{xx,x}^c - R_{xy,y}^c + 3T_{xz}^c + \frac{h_c^3}{8} \lambda_x^t - \frac{h_c^3}{8} \lambda_x^b - \frac{3G_{xz}^c h_c^2}{8h_t Q_{55}^t} \lambda_{xz}^{tc} + \frac{3G_{xz}^c h_c^2}{8h_b Q_{55}^b} \lambda_{xz}^{bc} = 0 \\
& -N_{yy,y}^c - N_{xy,x}^c - \lambda_y^t - \lambda_y^b = 0 \\
& -M_{yy,y}^c - M_{xy,x}^c + Q_{yz}^c + \frac{h_c}{2} \lambda_y^t - \frac{h_c}{2} \lambda_y^b - \frac{G_{yz}^c}{2h_t Q_{44}^t} \lambda_{yz}^{tc} + \frac{G_{yz}^c}{2h_b Q_{44}^b} \lambda_{yz}^{bc} = 0 \\
& -P_{yy,y}^c - P_{xy,x}^c + 2S_{yz}^c - \frac{h_c^2}{4} \lambda_y^t - \frac{h_c^2}{4} \lambda_y^b + \frac{G_{yz}^c h_c}{2h_t Q_{44}^t} \lambda_{yz}^{tc} + \frac{G_{yz}^c h_c}{2h_b Q_{44}^b} \lambda_{yz}^{bc} = 0 \\
& -R_{yy,y}^c - R_{xy,x}^c + 3T_{yz}^c + \frac{h_c^3}{8} \lambda_y^t - \frac{h_c^3}{8} \lambda_y^b - \frac{3G_{yz}^c h_c^2}{8h_t Q_{44}^t} \lambda_{yz}^{tc} + \frac{3G_{yz}^c h_c^2}{8h_b Q_{44}^b} \lambda_{yz}^{bc} = 0 \quad (21) \\
& -Q_{xz,x}^c - Q_{yz,y}^c - \mathcal{N}(w_{0c}) - \lambda_z^t - \lambda_z^b + \frac{G_{xz}^c}{2h_t Q_{55}^t} \lambda_{xz,x}^{tc} + \frac{G_{yz}^c}{2h_t Q_{44}^t} \lambda_{yz,y}^{tc} \\
& \quad - \frac{G_{xz}^c}{2h_b Q_{55}^b} \lambda_{xz,x}^{bc} - \frac{G_{yz}^c}{2h_b Q_{44}^b} \lambda_{yz,y}^{bc} = 0 \\
& -S_{xz,x}^c - S_{yz,y}^c + N_{zz}^c + \frac{h_c}{2} \lambda_z^t - \frac{h_c}{2} \lambda_z^b - \frac{G_{xz}^c h_c}{4h_t Q_{55}^t} \lambda_{xz,x}^{tc} - \frac{G_{yz}^c h_c}{4h_t Q_{44}^t} \lambda_{yz,y}^{tc} \\
& \quad - \frac{G_{xz}^c h_c}{4h_b Q_{55}^b} \lambda_{xz,x}^{bc} - \frac{G_{yz}^c h_c}{4h_b Q_{44}^b} \lambda_{yz,y}^{bc} = 0 \\
& -T_{xz,x}^c - T_{yz,y}^c + 2M_{zz}^c - \frac{h_c^2}{4} \lambda_z^t - \frac{h_c^2}{4} \lambda_z^b + \frac{G_{xz}^c h_c^2}{8h_t Q_{55}^t} \lambda_{xz,x}^{tc} + \frac{G_{yz}^c h_c^2}{8h_t Q_{44}^t} \lambda_{yz,y}^{tc} \\
& \quad - \frac{G_{xz}^c h_c^2}{8h_b Q_{55}^b} \lambda_{xz,x}^{bc} - \frac{G_{yz}^c h_c^2}{8h_b Q_{44}^b} \lambda_{yz,y}^{bc} = 0
\end{aligned}$$

where for $j = t, b, c$:

$$\mathcal{N}(w_{0j}) = \frac{\partial}{\partial x} \left(w_{0j,x} N_{xx}^j + w_{0i,y} N_{xy}^i \right) + \frac{\partial}{\partial y} \left(w_{0j,y} N_{yy}^j + w_{0j,x} N_{xy}^j \right) \quad (22)$$

The resultants in the Eqs. (19)–(21) can be related to the total strains by the following equations. For each face sheet ($i = t, b$):

$$\begin{aligned}
\begin{Bmatrix} N_{xx}^i \\ M_{xx}^i \\ P_{xx}^i \\ R_{xx}^i \end{Bmatrix} &= \begin{bmatrix} K_{i,11}^0 & K_{i,11}^1 & K_{i,11}^2 & K_{i,11}^3 \\ K_{i,11}^1 & K_{i,11}^2 & K_{i,11}^3 & K_{i,11}^4 \\ K_{i,11}^2 & K_{i,11}^3 & K_{i,11}^4 & K_{i,11}^5 \\ K_{i,11}^3 & K_{i,11}^4 & K_{i,11}^5 & K_{i,11}^6 \end{bmatrix} \begin{Bmatrix} u_{0i,x} + \frac{1}{2}(w_{0i,x})^2 \\ u_{1i,x} \\ u_{2i,x} \\ u_{3i,x} \end{Bmatrix} \\
&+ \begin{bmatrix} K_{i,12}^0 & K_{i,12}^1 & K_{i,12}^2 & K_{i,12}^3 \\ K_{i,12}^1 & K_{i,12}^2 & K_{i,12}^3 & K_{i,12}^4 \\ K_{i,12}^2 & K_{i,12}^3 & K_{i,12}^4 & K_{i,12}^5 \\ K_{i,12}^3 & K_{i,12}^4 & K_{i,12}^5 & K_{i,12}^6 \end{bmatrix} \begin{Bmatrix} v_{0i,y} + \frac{1}{2}(w_{0i,y})^2 \\ v_{1i,y} \\ v_{2i,y} \\ v_{3i,y} \end{Bmatrix} \\
\begin{Bmatrix} N_{yy}^i \\ M_{yy}^i \\ P_{yy}^i \\ R_{yy}^i \end{Bmatrix} &= \begin{bmatrix} K_{i,21}^0 & K_{i,21}^1 & K_{i,21}^2 & K_{i,21}^3 \\ K_{i,21}^1 & K_{i,21}^2 & K_{i,21}^3 & K_{i,21}^4 \\ K_{i,21}^2 & K_{i,21}^3 & K_{i,21}^4 & K_{i,21}^5 \\ K_{i,21}^3 & K_{i,21}^4 & K_{i,21}^5 & K_{i,21}^6 \end{bmatrix} \begin{Bmatrix} u_{0i,x} + \frac{1}{2}(w_{0i,x})^2 \\ u_{1i,x} \\ u_{2i,x} \\ u_{3i,x} \end{Bmatrix} \\
&+ \begin{bmatrix} K_{i,22}^0 & K_{i,22}^1 & K_{i,22}^2 & K_{i,22}^3 \\ K_{i,22}^1 & K_{i,22}^2 & K_{i,22}^3 & K_{i,22}^4 \\ K_{i,22}^2 & K_{i,22}^3 & K_{i,22}^4 & K_{i,22}^5 \\ K_{i,22}^3 & K_{i,22}^4 & K_{i,22}^5 & K_{i,22}^6 \end{bmatrix} \begin{Bmatrix} v_{0i,y} + \frac{1}{2}(w_{0i,y})^2 \\ v_{1i,y} \\ v_{2i,y} \\ v_{3i,y} \end{Bmatrix} \\
\begin{Bmatrix} N_{xy}^i \\ M_{xy}^i \\ P_{xy}^i \\ R_{xy}^i \end{Bmatrix} &= \begin{bmatrix} K_{i,66}^0 & K_{i,66}^1 & K_{i,66}^2 & K_{i,66}^3 \\ K_{i,66}^1 & K_{i,66}^2 & K_{i,66}^3 & K_{i,66}^4 \\ K_{i,66}^2 & K_{i,66}^3 & K_{i,66}^4 & K_{i,66}^5 \\ K_{i,66}^3 & K_{i,66}^4 & K_{i,66}^5 & K_{i,66}^6 \end{bmatrix} \begin{Bmatrix} u_{0i,y} + v_{0i,x} + w_{0i,x}w_{0i,y} \\ u_{1i,y} + v_{1i,x} \\ u_{2i,y} + v_{2i,x} \\ u_{3i,y} + v_{3i,x} \end{Bmatrix} \\
\begin{Bmatrix} Q_{xz}^i \\ S_{xz}^i \\ T_{xz}^i \end{Bmatrix} &= \begin{bmatrix} K_{i,55}^0 & 2K_{i,55}^1 & 3K_{i,55}^2 \\ K_{i,55}^1 & 2K_{i,55}^2 & 3K_{i,55}^3 \\ K_{i,55}^2 & 2K_{i,55}^3 & 3K_{i,55}^4 \end{bmatrix} \begin{Bmatrix} u_{1i} + w_{0i,x} \\ u_{2i} \\ u_{3i} \end{Bmatrix} \\
\begin{Bmatrix} Q_{yz}^i \\ S_{yz}^i \\ T_{yz}^i \end{Bmatrix} &= \begin{bmatrix} K_{i,44}^0 & 2K_{i,44}^1 & 3K_{i,44}^2 \\ K_{i,44}^1 & 2K_{i,44}^2 & 3K_{i,44}^3 \\ K_{i,44}^2 & 2K_{i,44}^3 & 3K_{i,44}^4 \end{bmatrix} \begin{Bmatrix} v_{1i} + w_{0i,y} \\ v_{2i} \\ v_{3i} \end{Bmatrix}
\end{aligned} \tag{23}$$

and for the core:

$$\begin{aligned}
\begin{Bmatrix} N_{xx}^c \\ M_{xx}^c \\ P_{xx}^c \\ R_{xx}^c \end{Bmatrix} &= C_{11}^c \begin{bmatrix} K_c^0 & K_c^1 & K_c^2 & K_c^3 \\ K_c^1 & K_c^2 & K_c^3 & K_c^4 \\ K_c^2 & K_c^3 & K_c^4 & K_c^5 \\ K_c^3 & K_c^4 & K_c^5 & K_c^6 \end{bmatrix} \begin{Bmatrix} u_{0c,x} + \frac{1}{2}(w_{0c,x})^2 \\ u_{1c,x} \\ u_{2c,x} \\ u_{3c,x} \end{Bmatrix} \\
&+ C_{12}^c \begin{bmatrix} K_c^0 & K_c^1 & K_c^2 & K_c^3 \\ K_c^1 & K_c^2 & K_c^3 & K_c^4 \\ K_c^2 & K_c^3 & K_c^4 & K_c^5 \\ K_c^3 & K_c^4 & K_c^5 & K_c^6 \end{bmatrix} \begin{Bmatrix} v_{0c,y} + \frac{1}{2}(w_{0c,y})^2 \\ v_{1c,y} \\ v_{2c,y} \\ v_{3c,y} \end{Bmatrix} + C_{13}^c \begin{bmatrix} K_c^0 & 2K_c^1 \\ K_c^1 & 2K_c^2 \\ K_c^2 & 2K_c^3 \\ K_c^3 & 2K_c^4 \end{bmatrix} \begin{Bmatrix} w_{1c} \\ w_{2c} \end{Bmatrix} \\
\begin{Bmatrix} N_{yy}^c \\ M_{yy}^c \\ P_{yy}^c \\ R_{yy}^c \end{Bmatrix} &= C_{21}^c \begin{bmatrix} K_c^0 & K_c^1 & K_c^2 & K_c^3 \\ K_c^1 & K_c^2 & K_c^3 & K_c^4 \\ K_c^2 & K_c^3 & K_c^4 & K_c^5 \\ K_c^3 & K_c^4 & K_c^5 & K_c^6 \end{bmatrix} \begin{Bmatrix} u_{0c,x} + \frac{1}{2}(w_{0c,x})^2 \\ u_{1c,x} \\ u_{2c,x} \\ u_{3c,x} \end{Bmatrix} \\
&+ C_{22}^c \begin{bmatrix} K_c^0 & K_c^1 & K_c^2 & K_c^3 \\ K_c^1 & K_c^2 & K_c^3 & K_c^4 \\ K_c^2 & K_c^3 & K_c^4 & K_c^5 \\ K_c^3 & K_c^4 & K_c^5 & K_c^6 \end{bmatrix} \begin{Bmatrix} v_{0c,y} + \frac{1}{2}(w_{0c,y})^2 \\ v_{1c,y} \\ v_{2c,y} \\ v_{3c,y} \end{Bmatrix} + C_{23}^c \begin{bmatrix} K_c^0 & 2K_c^1 \\ K_c^1 & 2K_c^2 \\ K_c^2 & 2K_c^3 \\ K_c^3 & 2K_c^4 \end{bmatrix} \begin{Bmatrix} w_{1c} \\ w_{2c} \end{Bmatrix} \\
\begin{Bmatrix} N_{zz}^c \\ M_{zz}^c \end{Bmatrix} &= C_{31}^c \begin{bmatrix} K_c^0 & K_c^1 & K_c^2 & K_c^3 \\ K_c^1 & K_c^2 & K_c^3 & K_c^4 \end{bmatrix} \begin{Bmatrix} u_{0c,x} \\ u_{1c,x} \\ u_{2c,x} \\ u_{3c,x} \end{Bmatrix} \\
&+ C_{32}^c \begin{bmatrix} K_c^0 & K_c^1 & K_c^2 & K_c^3 \\ K_c^1 & K_c^2 & K_c^3 & K_c^4 \end{bmatrix} \begin{Bmatrix} v_{0c,y} \\ v_{1c,y} \\ v_{2c,y} \\ v_{3c,y} \end{Bmatrix} + C_{33}^c \begin{bmatrix} K_c^0 & 2K_c^1 \\ K_c^1 & 2K_c^2 \end{bmatrix} \begin{Bmatrix} w_{1c} \\ w_{2c} \end{Bmatrix} \\
\begin{Bmatrix} N_{xy}^c \\ M_{xy}^c \\ P_{xy}^c \\ R_{xy}^c \end{Bmatrix} &= G_{xy}^c \begin{bmatrix} K_c^0 & K_c^1 & K_c^2 & K_c^3 \\ K_c^1 & K_c^2 & K_c^3 & K_c^4 \\ K_c^2 & K_c^3 & K_c^4 & K_c^5 \\ K_c^3 & K_c^4 & K_c^5 & K_c^6 \end{bmatrix} \begin{Bmatrix} u_{0c,y} + v_{0c,x} + w_{0c,x}w_{0c,y} \\ u_{1c,y} + v_{1c,x} \\ u_{2c,y} + v_{2c,x} \\ u_{3c,y} + v_{3c,x} \end{Bmatrix} \\
\begin{Bmatrix} Q_{xz}^c \\ S_{xz}^c \\ T_{xz}^c \end{Bmatrix} &= G_{xz}^c \begin{bmatrix} K_c^0 & K_c^1 & K_c^2 \\ K_c^1 & K_c^2 & K_c^3 \\ K_c^2 & K_c^3 & K_c^4 \end{bmatrix} \begin{Bmatrix} u_{1c} + w_{0c,x} \\ 2u_{2c} + w_{1c,x} \\ 3u_{3c} + w_{2c,x} \end{Bmatrix} \\
\begin{Bmatrix} Q_{yz}^c \\ S_{yz}^c \\ T_{yz}^c \end{Bmatrix} &= G_{yz}^c \begin{bmatrix} K_c^0 & K_c^1 & K_c^2 \\ K_c^1 & K_c^2 & K_c^3 \\ K_c^2 & K_c^3 & K_c^4 \end{bmatrix} \begin{Bmatrix} v_{1c} + w_{0c,y} \\ 2v_{2c} + w_{1c,y} \\ 3v_{3c} + w_{2c,y} \end{Bmatrix}
\end{aligned}$$

(24)

The coefficients $K_{i,jk}^n$ and K_c^n can be defined as:

$$K_{i,jk}^n = \sum_{l=1}^{l_i} Q_{jk}^l \int_{z_i^{l-1}}^{z_i^l} z_i^n dz_i \quad (25)$$

$$K_c^n = \int_{\frac{-hc}{2}}^{\frac{hc}{2}} z_c^n dz_c = \begin{cases} 0 & n = \text{even} \\ \frac{h^{n+1}}{(n+1)2^n} & n = \text{odd} \end{cases} \quad (26)$$

where $l_i (i = t, b)$ are the number of composite layers in each face sheet and Q_{jk}^l are the reduced stiffness coefficients of the l th composite layer of each face sheet. Also, z_i^{l-1} and z_i^l are the upper and lower vertical distance of the l th composite layer from the mid-plane of each face sheet.

3 Analytical Solution

Exact analytical solutions of Eqs. (19)–(21) exist for a simply-supported rectangular sandwich plate with cross-ply face sheets. Both face sheets are considered as a cross-ply laminated composite.

For simply-supported plates, the tangential displacements on the boundary are admissible, but the transverse displacements are not as such. Therefore, the boundary conditions of simply-supported plates can be expressed as:

At edges $x = 0$ and $x = a$;

$$\begin{aligned} v_{0j} = 0, v_{1j} = 0, v_{2j} = 0, v_{3j} = 0, j = t, b, c \\ w_{0t} = 0, w_{0b} = 0, w_{0c} = 0, w_{1c} = 0, w_{2c} = 0 \end{aligned} \quad (27)$$

At edges $y = 0$ and $y = b$;

$$\begin{aligned} u_{0j} = 0, u_{1j} = 0, u_{2j} = 0, u_{3j} = 0, j = t, b, c \\ w_{0t} = 0, w_{0b} = 0, w_{0c} = 0, w_{1c} = 0, w_{2c} = 0 \end{aligned} \quad (28)$$

Equation (22) can be rewritten as:

$$\mathcal{N}(w_{0j}) = \frac{\partial}{\partial x} \left(w_{0j,x} \hat{N}_{xx}^j + w_{0i,y} \hat{N}_{xy}^j \right) + \frac{\partial}{\partial y} \left(w_{0j,y} \hat{N}_{yy}^j + w_{0j,x} \hat{N}_{xy}^j \right) \quad (29)$$

where $\hat{N}_{xx}^j, \hat{N}_{yy}^j, \hat{N}_{xy}^j$ ($j = t, b$ and c) are external in-plane loads exerted to the top and bottom face sheets and the core. Therefore:

$$\mathcal{N}(w_{0j}) = w_{0j,xx} \hat{N}_{xx}^j + 2w_{0j,xy} \hat{N}_{xy}^j + w_{0j,yy} \hat{N}_{yy}^j \quad (30)$$

For sandwich plate subjected to uniaxial compressive loading:

$$\hat{N}_{xx} = -\hat{N}_0, \hat{N}_{yy} = \hat{N}_{xy} = \overline{n_{xt}} = \overline{n_{yt}} = \overline{n_{xb}} = \overline{n_{yb}} = q_t = q_b = 0 \quad (31)$$

The in-plane compressive loads at edges $x = 0$ or $x = a$ are illustrated in Fig. 2. At these edges, the equilibrium equations can be defined as:

$$\begin{aligned} \hat{N}_{xx}^t + \hat{N}_{xx}^b + \hat{N}_{xx}^c &= -\hat{N}_0 \\ \hat{N}_{xx}^t \left(\frac{h_t + h_c}{2} \right) &= \hat{N}_{xx}^b \left(\frac{h_b + h_c}{2} \right) \end{aligned} \quad (32)$$

where \hat{N}_{xx}^t , \hat{N}_{xx}^b and \hat{N}_{xx}^c are the parts of total load which are exerted to the top face sheet, bottom face sheet and the core along x -direction, respectively. Thus, by setting the nonlinear terms of strains to zero and $z_t = z_b = z_c = 0$ at the mid-plane of the top and bottom face sheets and the core:

$$\begin{aligned} \hat{N}_{xx}^t &= K_{t,11}^0 u_{0t,x} + K_{t,12}^0 v_{0t,y} \\ \hat{N}_{xx}^b &= K_{b,11}^0 u_{0b,x} + K_{b,12}^0 v_{0b,y} \\ \hat{N}_{xx}^c &= C_{11}^c K_c^0 u_{0c,x} + C_{12}^c K_c^0 v_{0c,y} \end{aligned} \quad (33)$$

The sandwich plates can be analyzed for the following two loading conditions [16]:

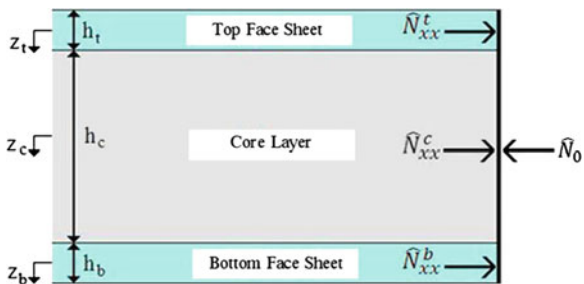
Case I: uniform state of stress in which all the layers are subjected to equal edge stresses.

Case II: uniform state of strain in which the individual layers are subjected to stresses in proportion to their elastic modulus.

In the buckling analysis, if a uniform state of strain is assumed, the relative edge stresses in the individual layers are proportional to the respective elastic modulus. The in-plane flexural rigidity of the soft cores is comparatively very small and hence the condition of uniform strain state is more realistic for sandwich plates [16]. Therefore, in this analysis the uniform strain state is assumed. Hence, the external in-plane loads exerted to the top and bottom face sheets and the core along x -direction can be defined as:

$$\begin{aligned} \hat{N}_{xx}^t &= \frac{\hat{N}_0(h_b + h_c) \left(K_{t,12}^0 K_{b,11}^0 - K_{t,11}^0 K_{b,12}^0 \right)}{(h_t + h_b + 2h_c) \left(K_{t,12}^0 K_{b,11}^0 - K_{t,11}^0 K_{b,12}^0 \right) + K_c^0(h_b + h_c) \left(K_{b,11}^0 C_{12}^c - K_{b,12}^0 C_{11}^c \right) + K_c^0(h_t + h_c) \left(K_{t,12}^0 C_{11}^c - K_{t,11}^0 C_{12}^c \right)} \\ \hat{N}_{xx}^b &= \frac{\hat{N}_0(h_t + h_c) \left(K_{t,12}^0 K_{b,11}^0 - K_{t,11}^0 K_{b,12}^0 \right)}{(h_t + h_b + 2h_c) \left(K_{t,12}^0 K_{b,11}^0 - K_{t,11}^0 K_{b,12}^0 \right) + K_c^0(h_b + h_c) \left(K_{b,11}^0 C_{12}^c - K_{b,12}^0 C_{11}^c \right) + K_c^0(h_t + h_c) \left(K_{t,12}^0 C_{11}^c - K_{t,11}^0 C_{12}^c \right)} \\ \hat{N}_{xx}^c &= \frac{K_c^0 \hat{N}_0 \left[(h_b + h_c) \left(K_{b,11}^0 C_{12}^c - K_{b,12}^0 C_{11}^c \right) + (h_t + h_c) \left(K_{t,12}^0 C_{11}^c - K_{t,11}^0 C_{12}^c \right) \right]}{(h_t + h_b + 2h_c) \left(K_{t,12}^0 K_{b,11}^0 - K_{t,11}^0 K_{b,12}^0 \right) + K_c^0(h_b + h_c) \left(K_{b,11}^0 C_{12}^c - K_{b,12}^0 C_{11}^c \right) + K_c^0(h_t + h_c) \left(K_{t,12}^0 C_{11}^c - K_{t,11}^0 C_{12}^c \right)} \end{aligned} \quad (34)$$

Fig. 2 Distributions of external in-plane loads exerted to the top and bottom face sheets and the core



The partial loads along y -direction can be calculated using the procedure presented along Eqs. (32)–(34). Therefore, Eq. (30) can be rewritten as:

$$\mathcal{N}(w_{0i}) = w_{0i,xx} \hat{N}_{xx}^i \quad (35)$$

Using Navier's procedure, the solution of the displacement variables satisfying the above boundary conditions can be expressed in the following forms:

$$\begin{aligned} u_{ij}(x, y) &= \sum_{n=1}^N \sum_{m=1}^M U_{ij}^{mn} \cos(\alpha_m x) \cdot \sin(\beta_n y) \\ v_{ij}(x, y) &= \sum_{n=1}^N \sum_{m=1}^M V_{ij}^{mn} \sin(\alpha_m x) \cdot \cos(\beta_n y) \\ w_{0j}(x, y) &= \sum_{n=1}^N \sum_{m=1}^M W_{0j}^{mn} \sin(\alpha_m x) \cdot \sin(\beta_n y) \\ u_{ic}(x, y) &= \sum_{n=1}^N \sum_{m=1}^M U_{ic}^{mn} \cos(\alpha_m x) \cdot \sin(\beta_n y) \\ v_{ic}(x, y) &= \sum_{n=1}^N \sum_{m=1}^M V_{ic}^{mn} \sin(\alpha_m x) \cdot \cos(\beta_n y) \\ w_{kc}(x, y) &= \sum_{n=1}^N \sum_{m=1}^M W_{kc}^{mn} \sin(\alpha_m x) \cdot \sin(\beta_n y) \end{aligned} \quad (36)$$

By using Navier's procedure, the Lagrange multipliers can be expressed in the following forms:

$$\begin{aligned}
\lambda_x^j(x, y) &= \sum_{n=1}^N \sum_{m=1}^M X_j^{mn} \cos(\alpha_m x) \cdot \sin(\beta_n y) \\
\lambda_y^j(x, y) &= \sum_{n=1}^N \sum_{m=1}^M Y_j^{mn} \sin(\alpha_m x) \cdot \cos(\beta_n y) \\
\lambda_z^j(x, y) &= \sum_{n=1}^N \sum_{m=1}^M Z_j^{mn} \sin(\alpha_m x) \cdot \sin(\beta_n y) \\
\lambda_{xz}^j(x, y) &= \sum_{n=1}^N \sum_{m=1}^M L_{xj}^{mn} \cos(\alpha_m x) \cdot \sin(\beta_n y) \\
\lambda_{yz}^j(x, y) &= \sum_{n=1}^N \sum_{m=1}^M L_{yj}^{mn} \sin(\alpha_m x) \cdot \cos(\beta_n y) \\
\lambda_{xz}^{jc}(x, y) &= \sum_{n=1}^N \sum_{m=1}^M L_{xjc}^{mn} \cos(\alpha_m x) \cdot \sin(\beta_n y) \\
\lambda_{yz}^{jc}(x, y) &= \sum_{n=1}^N \sum_{m=1}^M L_{yjc}^{mn} \sin(\alpha_m x) \cdot \cos(\beta_n y)
\end{aligned} \tag{37}$$

where $i = t, b, i = 0, 1, 2, 3$, $k = 0, 1, 2$ and $\alpha_m = \frac{m\pi}{a}$, $\beta_n = \frac{n\pi}{b}$ in which m and n are the wave numbers. By substituting Eqs. (34), (35), (36) and (37) into (19), (20) and (21), the final equations of motion in the matrix form can be determined as:

$$[A]_{43 \times 43} \{X\}_{43 \times 1} = \{0\}_{43 \times 1} \tag{38}$$

where $[A]$ is the coefficients matrix and $\{X\}$ is defined as:

$$\begin{aligned}
\{X\} = \{ & U_{0t}^{mn} \quad U_{1t}^{mn} \quad U_{2t}^{mn} \quad U_{3t}^{mn} \quad V_{0t}^{mn} \quad V_{1t}^{mn} \quad V_{2t}^{mn} \quad V_{3t}^{mn} \quad W_{0t}^{mn} \quad X_t^{mn} \quad Y_t^{mn} \quad Z_t^{mn} \\
& L_{xt}^{mn} \quad L_{yt}^{mn} \quad L_{xtc}^{mn} \quad L_{ytc}^{mn} \quad U_{0c}^{mn} \quad U_{1c}^{mn} \quad U_{2c}^{mn} \quad U_{3c}^{mn} \quad V_{0c}^{mn} \quad V_{1c}^{mn} \quad V_{2c}^{mn} \quad V_{3c}^{mn} \\
& W_{0c}^{mn} \quad W_{1c}^{mn} \quad W_{2c}^{mn} \quad X_b^{mn} \quad Y_b^{mn} \quad Z_b^{mn} \quad L_{xb}^{mn} \quad L_{yb}^{mn} \quad L_{xbc}^{mn} \quad L_{ybc}^{mn} \\
& U_{0b}^{mn} \quad U_{1b}^{mn} \quad U_{2b}^{mn} \quad U_{3b}^{mn} \quad V_{0b}^{mn} \quad V_{1b}^{mn} \quad V_{2b}^{mn} \quad V_{3b}^{mn} \quad W_{0b}^{mn} \}
\end{aligned} \tag{39}$$

The nonzero result and buckling load is obtained when the determinant of $[A]$ is set to be zero.

4 Numerical Results and Discussion

In this section, several examples of the overall buckling and face wrinkling problems of the sandwich plates are studied to verify the accuracy and applicability of the present higher order theory. The results obtained by present theory are

Table 1 Dimensionless overall buckling load for symmetric square sandwich plate [(0/90)₅/Core/(90/0)₅]

h_f/h	a/h	Elasticity [31]	Present	GLPT [26]	MLW [16]	ESL [16]
0.025	20	2.5543	2.5658	2.5391	2.5390	2.6386
	10	2.2376	2.2621	2.1914	2.1904	2.2942
	20/3	1.8438	1.8882	1.7961	1.7952	1.8980
	5	1.5027	1.5316	1.4449	1.4427	1.5393
0.05	20	4.6590	4.6804	4.6387	4.6386	4.7857
	10	3.7375	3.7611	3.6770	3.6759	3.8475
	20/3	2.7911	2.8320	2.7509	2.7506	2.9222
	5	2.0816	2.1017	2.0431	2.0426	2.1977
0.075	20	6.4224	6.4414	6.3915	6.3914	6.5644
	10	4.7637	4.8256	4.7432	4.7433	4.9580
	20/3	3.3729	3.4026	3.3387	3.3385	3.5466
	5	2.3973	2.4067	2.3674	2.3672	2.5461
0.1	20	7.8969	7.9171	7.8632	7.8631	8.0544
	10	5.6081	5.6215	5.5471	5.5463	5.7946
	20/3	3.7883	3.7931	3.7430	3.7424	3.9752
	5	2.6051	2.6077	2.5791	2.5789	2.7719

compared with the results in the previous literature. The following dimensionless buckling load used in the present analysis is defined as [16, 26]:

$$\bar{N} = \frac{a^2 \hat{N}_0}{E_2 h^3} \quad (40)$$

where E_2 is the transverse elastic modulus of the face sheets. Two types of buckling modes are studied for sandwich plates: overall buckling and wrinkling modes. Generally, the overall buckling load corresponds to both wave numbers equal to unity ($m = n = 1$). If the buckling load of a higher wave number is less than the overall buckling load, the sandwich plate fails in the wrinkling mode, although, it is not a general case. For assessing the wrinkling possibility, the wave number m should be increased in steps of one, when the wave number n is considered to be unity.

Example 1: Overall buckling of a square sandwich plate

A square symmetric sandwich plate with stack-up sequence of $[(0^\circ/90^\circ)_5/\text{Core}/(90^\circ/0^\circ)_5]$ with a total thickness of h is considered. The sandwich plate consists of equal thickness cross-ply laminated face sheets with 10 layers and a soft orthotropic core. The analysis is performed for different thickness ratios ($a/h = 20, 10, 20/3$ and 5) and different face sheet thickness ratios ($h_f/h = 0.025, 0.05, 0.075$ and 0.1). The dimensionless overall buckling loads obtained by 3D elasticity solution [31], global high-order equivalent single layer theory (ESL) [16], higher-order global-local plate theory (GLPT) [26], mixed layer-wise (MLW) theory [16] and the present high-order analytical theory are

given in Table 1. All results are presented for case (II) loading which is uniform state of strain. The material constants used in this example are assumed as follows:

For each composite layer of the face sheets [16]:

$$\begin{aligned} E_1 = 19E, E_2 = E_3 = E, G_{12} = G_{13} = 0.52E, G_{23} = 0.338E, \\ \nu_{12} = \nu_{13} = 0.32, \nu_{23} = 0.49 \end{aligned} \quad (41)$$

For the orthotropic core [16]:

$$\begin{aligned} E_x = 3.2 \times 10^{-5} E, E_y = 2.9 \times 10^{-5} E, E_z = 0.4E, G_{xy} = 2.4 \times 10^{-3} E \\ G_{yz} = 6.6 \times 10^{-2} E, G_{xz} = 7.9 \times 10^{-2} E, \nu_{xy} = 0.99, \nu_{xz} = \nu_{yz} = 3 \times 10^{-5} \end{aligned} \quad (42)$$

It can be seen that the present results are in good agreement with 3D elasticity solutions [31]. Also, it can be concluded that the results of the ESL theory are very far from the 3D elasticity solutions and are not accurate.

Example 2: Wrinkling of a square sandwich plate

The dimensionless wrinkling loads of the above square symmetric sandwich plate with stacking sequence of $[(0^\circ/90^\circ)_5/\text{Core}/(90^\circ/0^\circ)_5]$ are obtained by the present higher-order theory. All geometrical parameters and material properties are the same as the Example 1. The results obtained by global high-order equivalent single layer theory (ESL) [16], high-order global-local plate theory (GLPT) [26], mixed layer-wise theory (MLW) [16] and the present high-order analytical theory are presented and compared in Table 2. Also, if wrinkling mode is possible, the mode number of wrinkling loads (m) is presented in parenthesis. A 3D elasticity solution for wrinkling loads of sandwich plates was not presented by Noor et al. [31]. Kardomateas [32] presented a 2D elasticity solution for the wrinkling analysis of sandwich beams or wide sandwich panels which is not applicable for this 3D example.

The results presented in Table 2 indicate that based on all the theories, for thin sandwich plates ($alh = 20$), wrinkling behavior does not occur. It can be seen that the present results are in good agreement with GLPT [26] and MLW [16] results, but the ESL theory [16] could not predict the wrinkling modes as well as the overall buckling, accurately. For a constant thickness ratio (alh), the wrinkling loads increase with an increase in face sheet thickness ratio (h_f/h), because the stiffness of the face sheets is much greater than the stiffness of the core.

Example 3: Wrinkling of a rectangular sandwich plate

A rectangular symmetric sandwich plate with stack-up sequence of $[0^\circ/90^\circ/\text{Core}/90^\circ/0^\circ]$ and equal thickness cross-ply laminated face sheets and a soft orthotropic core is considered. The analysis is performed for different thickness ratios ($alh = 20, 10, 20/3$ and 5) and different aspect ratios ($alb = 0.5, 1, 2$ and 5). The face sheet thickness ratio is considered constant and equal to $h_f/h = 0.05$. The dimensionless overall buckling and wrinkling loads obtained by the

Table 2 Dimensionless wrinkling load for symmetric square sandwich plate [(0/90)_s/Core/(90/0)_s]

h_r/h	a/h	Present	GLPT [26]	MLW [16]	ESL [16]
0.025	20	- ^a	-	-	-
	10	1.3350 (54)	1.3601	1.2766 (57)	1.4395 (54)
	20/3	0.5942 (36)	0.5837	0.5680 (38)	0.6407 (36)
	5	0.3348 (27)	0.3486	0.3200 (28)	0.3611 (27)
0.05	20	-	-	-	-
	10	2.9358 (42)	2.9653	2.8002 (43)	3.4713 (37)
	20/3	1.3059 (28)	1.2826	1.2456 (29)	1.5440 (25)
	5	0.7355 (21)	0.7305	0.7016 (22)	0.8697 (19)
0.075	20	-	-	-	-
	10	-	4.6843	4.6321 (39)	-
	20/3	2.1843 (25)	2.1304	2.0595 (26)	2.6357 (21)
	5	1.2301 (19)	1.2163	1.1597 (19)	1.4839 (15)
0.1	20	-	-	-	-
	10	-	-	-	-
	20/3	3.1418 (24)	2.8792	2.9284 (25)	-
	5	1.7686 (18)	1.6249	1.6483 (19)	2.1324 (14)

^a Wrinkling mode is not possible

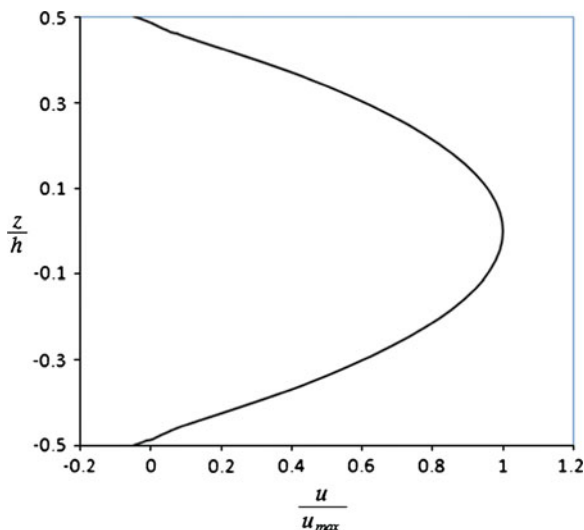
Table 3 Dimensionless overall buckling and wrinkling load for symmetric rectangular sandwich plate [0/90/Core/90/0] ($h_r/h = 0.05$)

a/b	a/h	Overall buckling	Wrinkling
0.5	20	9.8395	- ^a
	10	8.2161	-
	20/3	6.4504	3.9533 (29)
	5	4.9626	2.2253 (22)
1	20	4.6808	-
	10	3.7619	2.2247 (43)
	20/3	2.8328	0.9899 (29)
	5	2.1021	0.5579 (22)
2	20	7.3479	-
	10	4.2763	0.5577 (43)
	20/3	2.5438	0.2490 (29)
	5	1.6267	0.1410 (22)
5	20	17.3411	-
	10	5.6626	0.0910 (43)
	20/3	2.6151	0.0416 (29)
	5	1.4518	0.0243 (22)

^a Wrinkling mode is not possible

present high-order analytical theory are given in Table 3. Also, if the wrinkling mode is possible, the mode numbers of wrinkling loads (m) is presented in parenthesis. All material constants are the same as the Example 1.

Fig. 3 Distributions of in-plane displacement through the thickness of symmetric sandwich plate [0/90/Core/90/0] subjected to wrinkling load ($a/b = 2$, $alh = 5$, $h_c/h = 0.05$)



Results show that for a constant aspect ratio (alb), the overall buckling and wrinkling loads increase with increase in thickness ratio (alh). Also, it can be seen that for thin sandwich plates ($alh = 20$), the wrinkling behavior does not occur.

In Table 3, it can be seen that the symmetric rectangular sandwich plate with $a/b = 2$, $h_c/h = 0.05$ and $alh = 5$ wrinkled in mode number $m = 22$. The through-thickness distributions of some dimensionless parameters for this symmetric sandwich plate subjected to wrinkling load ($m = 22$) are plotted in Figs. 3–6. Figs. 3 and 4 show the distributions of in-plane and transverse displacements through the thickness of the points ($x = 0$, $y = b/2$) and ($x = a/2$, $y = b/2$) of the sandwich plate, respectively. As shown in these figures, the displacements continuity between each face sheet-core interface is satisfied. The distribution of in-plane normal stress through the thickness of the mid-point ($x = a/2$, $y = b/2$) of the sandwich plate is shown in Fig. 5. This figure shows that the in-plane stress is discontinue at the face sheet-core interfaces. Also, it can be observed that the in-plane stresses in the core are very small in comparison with those obtained in the face sheets. Figure 6 shows the through thickness distribution of transverse shear stress τ_{yz} of the edge-point ($x = a/2$, $y = 0$) for the sandwich plate. As shown in this figure, the transverse shear stress distribution is continues in the face sheet-core interfaces and is zero on the upper and lower surfaces of the sandwich plate.

5 Conclusions

In this chapter, a new improved higher-order theory was presented for overall buckling and wrinkling analysis of soft-core sandwich plates. An analytical solution for buckling and wrinkling analysis of simply supported sandwich plates

Fig. 4 Distributions of transverse displacement through the thickness of symmetric sandwich plate [0/90/Core/90/0] subjected to wrinkling load ($a/b = 2$, $alh = 5$, $h_c/h = 0.05$)

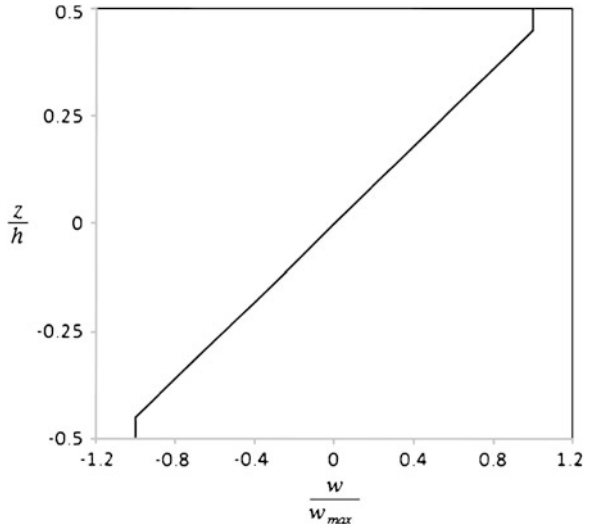
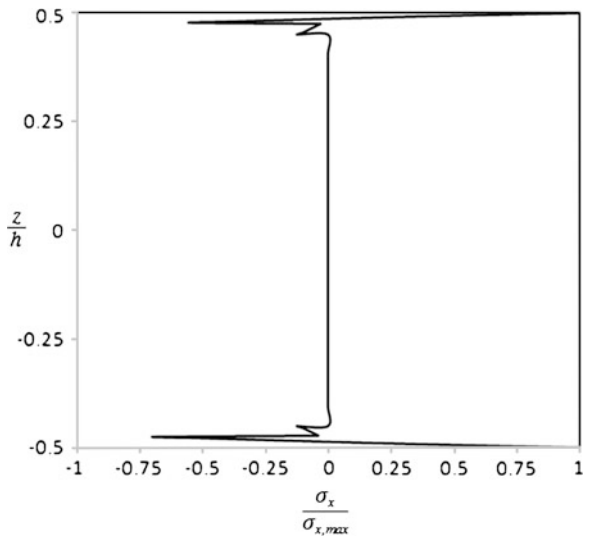
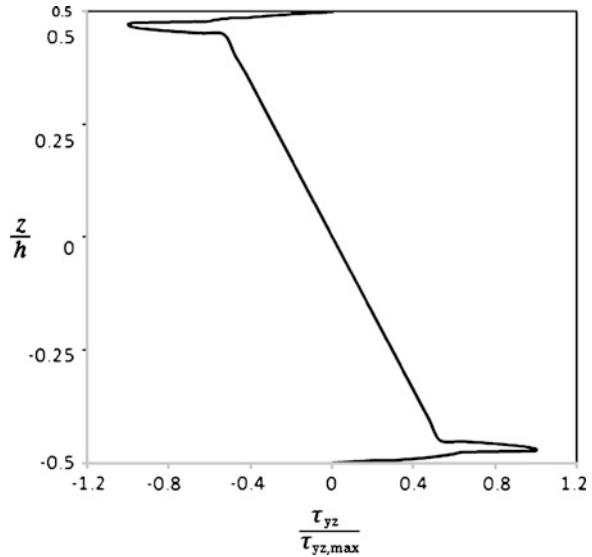


Fig. 5 Distributions of in-plane normal stresses through the thickness of symmetric sandwich plate [0/90/Core/90/0] subjected to wrinkling load ($a/b = 2$, $alh = 5$, $h_c/h = 0.05$)



under various in-plane compressive loads were presented using Navier’s solution. The presented theory satisfies the continuity conditions of transverse shear stresses at the interfaces as well as the conditions of zero transverse shear stresses on the upper and lower surfaces of the plate. The nonlinear von Kármán type relations were used to obtain strains and also transverse flexibility and transverse normal strain and stress of the core considered in the analysis. It can be concluded from the results that the overall buckling loads obtained by the present theory are in good agreement with elasticity solutions and other accurate numerical results. The

Fig. 6 Distributions of transverse shear stress through the thickness of symmetric sandwich plate [0/90/Core/90/0] subjected to wrinkling load ($a/b = 2$, $alh = 5$, $h_c/h = 0.05$)



in-plane flexural rigidity of the soft cores is comparatively very small and hence the condition of uniform strain state is more realistic for sandwich plates.

Also, it can be concluded that the present theory can estimate the wrinkling loads as well as the mode number accurately. The overall buckling loads calculated by ESL theories are higher than that of the present analysis.

References

1. Birman, V., Bert, C.W.: Wrinkling of composite-facing sandwich panels under biaxial loading. *J. Sandwich Struct. Mater.* **6**, 217–237 (2004)
2. Lopatin, A.V., Morzov, E.V.: Symmetrical facing wrinkling of composite sandwich panels. *J. Sandwich Struct. Mater.* **10**, 475–497 (2008)
3. Gough, C.S., Elam, C.F., De Bruyne, N.A.: The Stabilization of a thin sheet by a continuous support medium. *J. R. Aeronaut. Soc.* **44**, 12–43 (1940)
4. Hoff, N.J., Mautner, S.E.: The buckling of sandwich-type panels. *J. Aeronaut. Sci.* **12**, 285–297 (1945)
5. Plantema, F.J.: *Sandwich Construction*. Wiley, New York (1966)
6. Allen, H.C.: *Analysis and design of structural sandwich panels*. Pergamon Press, Oxford (1969)
7. Zenkert, D.: *An Introduction to Sandwich Construction*. Chameleon Press Ltd, London (1995)
8. Vinson, J.R.: *The Behavior of Sandwich Structures of Isotropic and Composite Materials*. Lancaster, Technomic (1999)
9. Benson, A.S., Mayers, J.: General instability and face wrinkling of sandwich plates—unified theory and applications. *AIAA J.* **5**(4), 729–739 (1967)
10. Hadi, B.K., Matthews, F.L.: Development of benson-mayers theory on the wrinkling of anisotropic sandwich panels. *Compos. Struct.* **49**, 425–434 (2000)

11. Niu, K., Talreja, R.: Modeling of wrinkling in sandwich panels under compression. *J. Eng. Mech.* **125**(8), 875–883 (1999)
12. Frostig, Y.: Buckling of sandwich panels with a transversely flexible core: high-order theory. *Int. J. Solids Struct.* **35**, 183–204 (1998)
13. Dawe, D.J., Yuan, W.X.: Overall and local buckling of sandwich plates with laminated faceplates part I: analysis. *Comput. Methods Appl. Mech. Eng.* **190**, 5197–5213 (2001)
14. Yuan, W.X., Dawe, D.J.: Overall and local buckling of sandwich plates with laminated faceplates part II: applications. *Comput. Methods Appl. Mech. Eng.* **190**, 5215–5231 (2001)
15. Vonach, W.K., Rammerstorfer, F.G.: A general approach to the wrinkling instability of sandwich plates. *Struct Eng Mech* **12**, 363–376 (2001)
16. Dafedar, J.B., Desai, Y.M., Mufti, A.A.: Stability of sandwich plates by mixed, higher-order analytical formulation. *Int. J. Solids Struct.* **40**, 4501–4517 (2003)
17. Leotoing, L., Drapier, S., Vautrin, A.: Using new closed-form solutions to set up design rules and numerical investigations for global and local buckling of sandwich beams. *J. Sandwich Struct. Mater.* **6**, 263–289 (2004)
18. Birman, V.: Thermally induced bending and wrinkling in large aspect ratio sandwich panels. *Compos. A* **36**, 1412–1420 (2005)
19. Fagerberg, L., Zenkert, D.: Imperfection-induced wrinkling material failure in sandwich panels. *J. Sandwich Struct. Mater.* **7**, 195–219 (2005)
20. Fagerberg, L., Zenkert, D.: Effects of anisotropy and loading on wrinkling of sandwich panels. *J. Sandwich Struct. Mater.* **7**, 177–194 (2005)
21. Grenestedt, J.L., Danielsson, M.: Elastic–plastic wrinkling of sandwich panels with layered cores. *J. Appl. Mech.* **72**, 276–281 (2005)
22. Kardomateas, G.A.: Wrinkling of wide sandwich panels/beams with orthotropic phases by an elasticity approach. *J. Appl. Mech.* **72**, 818–825 (2005)
23. Hohe J (2005) Global buckling and face wrinkling response of sandwich panels under transient loads. 46th AIAA/ASME/ASCE/AHS/ASC structures, structural dynamics & materials conference, Austin, USA
24. Meyer-Piening, H.R.: Sandwich plates: stresses, deflection, buckling and wrinkling loads—a case study. *J. Sandwich Struct. Mater.* **8**, 381–394 (2006)
25. Aiello, M.A., Ombres, L.: Buckling load design of sandwich panels made with hybrid laminated faces and transversely flexible core. *J. Sandwich Struct. Mater.* **9**, 467–485 (2007)
26. Shariyat, M.: Non-linear dynamic thermo-mechanical buckling analysis of the imperfect sandwich plates based on a generalized three-dimensional high-order global–local plate theory. *Compos. Struct.* **92**, 72–85 (2010)
27. Pearce, T.R.A., Webber, J.P.H.: Experimental buckling loads for sandwich panels. *Aeronaut. Q.* **24**, 295–312 (1973)
28. Wadee, M.A.: Experimental evaluation of interactive buckle localization in compression sandwich panels. *J. Sandwich Struct. Mater.* **1**, 230–254 (1999)
29. Wadee, M.A.: Effects of periodic and localized imperfections on struts on nonlinear foundations and compression sandwich panels. *Int. J. Solids Struct.* **37**, 1191–1209 (2000)
30. Gdoutos, E.E., Daniel, I.M., Wang, K.A.: Compression facing wrinkling of composite sandwich structures. *Mech. Mater.* **35**, 511–522 (2003)
31. Noor, A.K., Peters, J.M., Burton, W.S.: Three-dimensional solutions for initially stressed structural sandwiches. *J. Eng. Mech. ASCE* **120**(2), 284–303 (1994)
32. Kardomateas, G.A.: Wrinkling of wide sandwich panels/beams with orthotropic phases by an elasticity approach. *J. Appl. Mech.* **72**, 818–825 (2005)
33. Ji, W., Waas, A.M.: 2D elastic analysis of the sandwich panel buckling problem: benchmark solutions and accurate finite element formulations. *ZAMP* **61**, 897–917 (2010)
34. Reddy, J.N.: *Mechanics of laminated composite plates and shells, theory and analysis*, 2nd edn. CRC Press, New York (2004)

Artificial Neural Network Modelling of Glass Laminate Sample Shape Influence on the ESPI Modes

Zora Jančíková, Pavel Košťál, Soňa Rusnáková, Petr Jonšta, Ivan Ružiak, Jiří David, Jan Valíček and Karel Frydryšek

Abstract The present work is devoted to the applications of artificial neural networks (ANN) for material design prediction. We have investigated the dependence of the generated mode frequency as a function of a sample thickness and a sample shape of glass laminate samples by electronic speckle interferometry (ESPI). The obtained experimental results for differently shaped (thickness, canting and rounding) glass laminate samples are compared with those of ANN. The coincidence of both experimental and simulated results is very good.

Keywords Artificial neural networks · Glass laminate · Resonance frequencies · Electronic speckle pattern interferometry · Finite element method

1 Introduction

The basis of the mathematical model of the neural network is a formal neuron, which describes by a simplified way a function of a biological neuron by means of mathematic relations.

Learning is a basic and essential feature of ANN. Knowledge is recorded especially through the strength of linkages between particular neurons. Linkages between neurons leading to a “correct answer” are strengthened and linkages leading to a

Z. Jančíková (✉) · P. Košťál · P. Jonšta · I. Ružiak · J. David · J. Valíček · K. Frydryšek
VŠB-Technical University of Ostrava, 17. listopadu 15/2172,
70833 Ostrava-Poruba, Czech Republic
e-mail: zora.jancikova@vsb.cz

S. Rusnáková
Tomas Bata University in Zlín, Faculty of Technology, T. G. Masaryka 275,
762 72Zlín, Czech Republic

“wrong answer” are weakened by means of the repeated exposure of examples describing the problem area. These examples create a so-called training set.

For all types of predictions, ANN are suitable to be used for their learning Back propagation algorithm. This algorithm is convenient for multilayer feed forward network learning, which is created minimally by three layers of neurons: input, output and at least one inner (hidden) layer. Between the two adjoining layers there is always a so-called total connection of neurons, thus each neuron of the lower layer is connected to all neurons of the higher layer. Learning in the neural network is realized by setting the values of synaptic weights between neurons, biases or inclines of activation functions of neurons. The adaptation at Back propagation types of networks is also called “supervised learning”, when the neural network learns by comparing the actual and the required output and by setting the values of the synaptic weights so that the difference between the actual and the required output decreases [1, 2].

The rate of inaccuracy between predicted and actual output represent a prediction error. In technical applications the error is mainly represented by following relations:

relation for RMS error (Root Mean Squared)—it does not compensate used units

$$\text{RMS} = \sqrt{\frac{\sum_{i=0}^{i=n-1} (y_i - o_i)^2}{n - 1}}. \quad (1)$$

relation for REL_RMS error—it compensates used units

$$\text{REL_RMS} = \sqrt{\frac{\sum_{i=0}^{i=n-1} (y_i - o_i)^2}{\sum_{i=0}^{i=n-1} (y_i)^2}} \quad (2)$$

where:

n number of patterns of a training or test set,

y_i predicted outputs,

o_i measured outputs

Polymeric composites have large scale industrial applications. Glass fabric laminates are widely used when large strength to weight ratios is required. Relevant inorganic—organic polymeric composites are increasingly applicable in industry. Fillers in polymers change their physical properties and in some cases also environmental acceptability [3, 4].

Fibre-reinforced components of various shapes and different boundary conditions (free, clamped, and hinged) commonly occur in practice. Designers need to

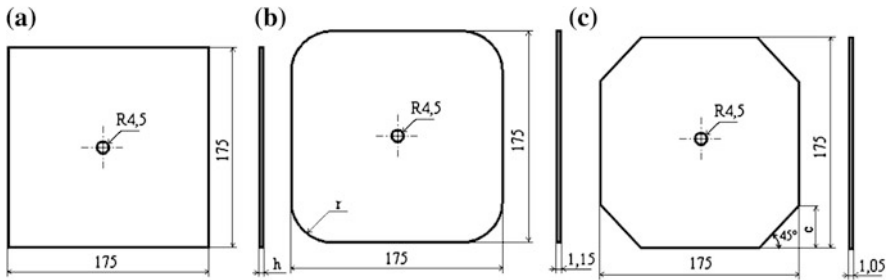


Fig. 1 Sample shaping: **a** sample thickness values **b** sample rounding values **c** sample canting values

be able to predict the stiffness parameters and damping values of components for conditions such as aeroelasticity, acoustic fatigue, and so on [5, 6].

Electronic speckle pattern interferometry can serve as a tool of an easy determination of Poisson’s ratio, Young’s modulus E and shear modulus G from the measured resonant frequencies. Subsequently for example it is possible to make various computer models on the basis of values determined by *ESPI* [7, 8]. The paper [9] reviews the main developments in the field of electronic speckle pattern interferometry that have been published over the past 20–25 years.

In this paper a model of *ANN* for prediction of natural frequencies of glass laminates was designed and gradually tested. The influence of thickness, shaping (rounding and canting) of the glass laminate samples on their natural frequencies during dynamic excitation was measured and modelled. These geometric factors related with the shape of laminate products are utilized for design of car-body parts of transport.

2 Experimental Procedure

The measured samples were prepregs M34 containing glass fibres and epoxy resin (see <http://hexcel.com>). Sample dimensions were $75 \times 175 \text{ mm}^2$.

In the first step, we have tested the mode frequency generation as a function of the sample thickness equals to 0.8, 1.05, 1.35, 1.65 mm (Fig. 1a).

The different sample rounding equals to 0, 10, 20, 30, 40, 50, 60, 70, 87.5 mm. Sample with $r = 0$ is tetragonal and sample with $r = 87.5 \text{ mm}$ is a disc. Dimensions of rectangular samples were $175 \times 175 \times 1.05 \text{ mm}^3$ (Fig. 1b).

Finally the different sample canting (represented by an ordinate length against a canting angle) equals to 0, 10, 20, 30, 40, 50, 60, 70 mm. Dimensions of rectangular samples were $175 \times 175 \times 1.05 \text{ mm}^3$ (Fig. 1c).

Electron speckle interferometry experiments were realized according to Fig. 2 [10]. *ESPI* records surface displacement of an object in response to the applied force. *ESPI* can be used in arrangements where fringes will represent lines of

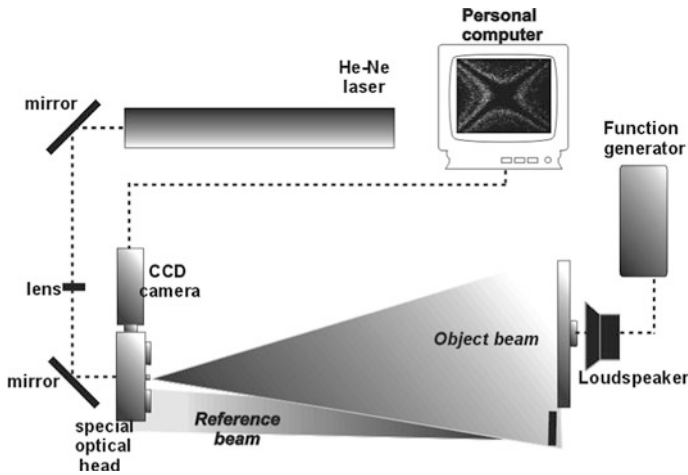


Fig. 2 Schema of *ESPI* apparatus

either in-plane or off-plane displacement. Periodic sample deformation was realized by a loudspeaker. Sample fixation (white plate) in a holder with exciting loudspeaker is described in Fig. 3. *ESPI* records the surface displacement of an object in response to an applied force. *ESPI* can be used in arrangements where fringes represent lines of either in-plane or out-of-plane displacement. To perform an *ESPI* inspection process, a speckle image of the unstressed object is first captured and saved in a computer. The object is then stressed, resulting into the object's surface being displaced.

Neural networks were created in the software *STATISTICA—Neural Networks*. This system enables among others a choice of most suitable *ANN* with the best performance, it contains efficient investigative and analytic techniques and enables to achieve summary descriptive statistics, to execute sensitive analysis and to create response graphs.

3 Experimental Results and Discussion

To discuss the results we start with the description of results concerning the thickness influence on the mode structure. For prediction of the resonance frequency in dependence of the sample thickness, data of sample thickness and mode type (7 types of modes) were used as an input vector (8 neurons in the input layer). The output vector represented the resonance frequency (1 neuron in the output layer). The best results of prediction provided a multilayer feed forward neural network with topology 8-3-1. Above mentioned prediction errors for this neural network are: $RMS = 13.668$ Hz, $REL_RMS = 0.0226$, $R^2 = 0.9983$.

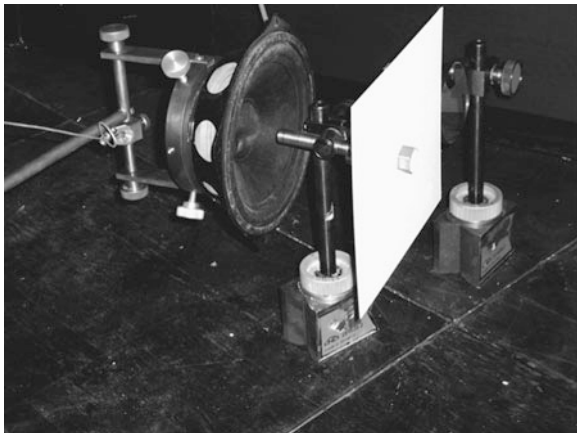


Fig. 3 Sample fixation in holder with exciting loudspeaker

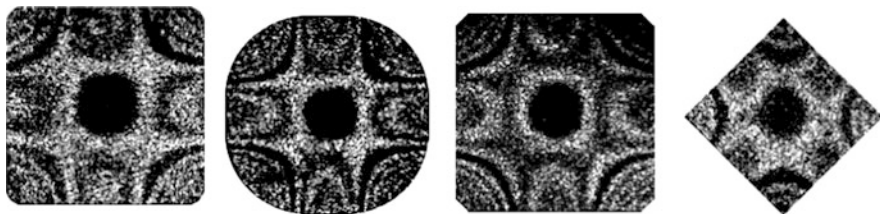


Fig. 4 Changes of mode 4 for different rounding (*left*) and canting (*right*) obtained from *ESPI* measurements

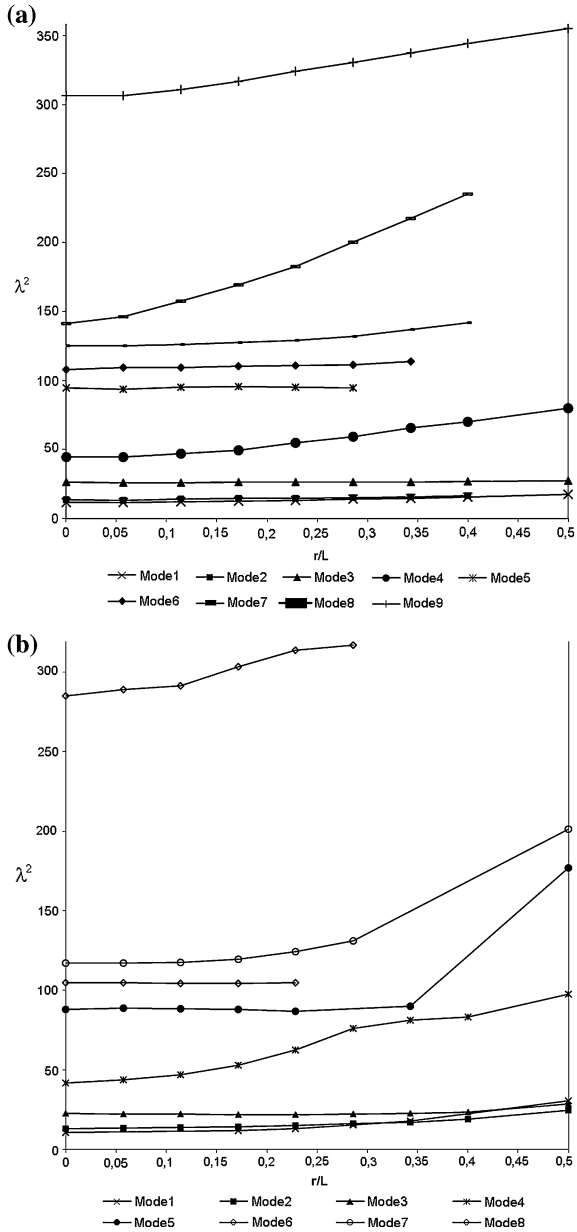
In the next paragraph we describe both sample rounding and canting influence on the mode shape and mode frequency. According to [11, 12] for the study of rounding and canting influence on the resonance frequency, it is possible to introduce the dimensionless parameter

$$\lambda^2 = 2\pi f L^2 \sqrt{\frac{12\rho(1-\nu^2)}{Eh^2}}, \quad (3)$$

where L is the maximum distance between opposite sample edges, h is the sample thickness, f is the frequency, E is the Young's modulus, ρ is the density and ν is the Poisson's ratio. For $r/L = 0$, we have a rectangular plate, a ratio $r/L = 0.5$ corresponds to a circular sample.

Visualized *ESPI* mode four changes caused by rounding and canting are presented in the Fig. 4. From Fig. 4, where λ^2 versus r/L is plotted, it is possible to see weak frequency dependence versus rounding for modes 3, 5, 6. On the other hand, a stronger dependence occurs for modes 4, 8, 9.

Fig. 5 a λ^2 versus r/L dependence for different modes of rounding. **b** λ^2 versus r/L dependence for different modes of canting



The results obtained for sample rounding λ^2 versus r/L dependence for different modes are presented in Fig. 5a. For prediction of the resonance frequency in dependence of the sample rounding, data of sample rounding and mode type (9 types of modes) were used as an input vector (10 neurons in the input layer). The output vector represented the resonance frequency (1 neuron in the output layer).

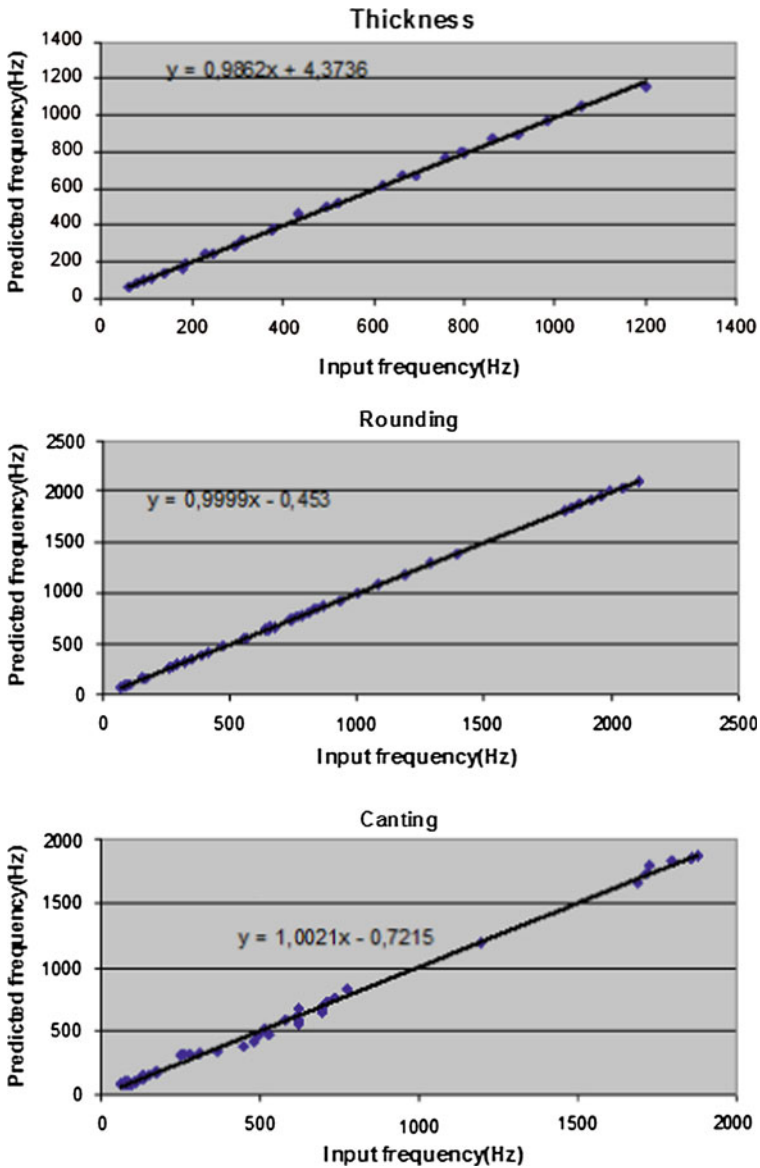


Fig. 6 ANN prediction of resonance frequencies for different plate thickness, rounding and canting

The best results of prediction provided a multilayer feed forward neural network with topology 10-7-1. Prediction errors for this neural network are: $RMS = 2.743$ Hz, $REL_RMS = 0.0031$, $R^2 = 0.9999$.

The results obtained for sample canting λ^2 versus r/L dependence for different modes are presented in Fig. 5b. For prediction of the resonance frequency in dependence of the sample canting, data of sample canting and mode type (8 types of modes) were used as an input vector (9 neurons in the input layer). The output vector represented the resonance frequency (1 neuron in the output layer). The best results of prediction provided a multilayer feed forward neural network with topology 9-3-1. For this neural network the prediction errors are: RMS = 31.6 Hz, REL_RMS = 0.0438, $R^2 = 0.9962$.

Comparison of measured and predicted values of the resonance frequencies in dependence of plate shaping is represented in Fig. 6. From these graphs is clearly seen a very good coincidence of measured and predicted data.

4 Conclusions

The relatively rich experimental material obtained by *ESPI* was compared with that by *ANN* application to find the proper way for designers who have to optimize the product or component shape with physical product properties such as vibrations.

Models of artificial neural networks for prediction of resonance frequencies of glass laminates were created. These models enable to predict glass laminates resonance frequencies with a sufficiently small error. The coincidence of both experimental and simulated results was very good.

References

1. Heger, M., Špička, I., Franz, J.: Time Prediction of Cooling Down Low Range Specimen with Neural Network Exploitation. *Hutnik-Wiadomości Hutnicze* **LXXV**, 478–480 (2008)
2. Špička, I., Heger, M., Franz, J.: The mathematical-physical models and the neural network exploitation for time prediction of cooling down low range specimen. *Arch. Metall. Mater.* **55**, 921–926 (2010)
3. Skalková, P., Jakubíková, Z., Mošková, D.J.: Štúdium mechanických a termických vlastností PE-LD/CMS zmesí. *Plasty a kaučuk* **3–4**, 3–4 (2010)
4. Skalková, P., Csomorová, K., Mošková, D., Košťál, P.: Monitoring thermal properties of various LDPE/polysaccharides blends. *Proceedings of VŠB-TU Ostrava, Metallurgical series*, ISBN 978-80-248-1964-8, 78–81 (2009)
5. Caldersmith, G.W.: Vibrations of orthotropic rectangular plates. *J. Acoustica* **56**, 144–152 (1984)
6. Gaul, L., Willner, K., Hurlenhaus, S.: Determination of material properties of plates from modal *ESPI* measurements. *Proceedings of the 17th IMAC Orlando, Florida*, (1999)
7. Ma, C.C., Lin, C.C.: Experimental investigation of vibrating laminated composite plates by optical interferometry method. *AIAA J* **39**, 491–497 (2001)
8. Lin, D.X., Ni, R.G., Adams, R.D.: Decomposition of coupling effects on damping of laminated composites under flexural vibration. *J. Compos. Mater.* **18**, 132–152 (1984)
9. Mujeeb, A., Nayar, V.U., Ravindran, V.R.: Electronic Speckle Pattern Interferometry techniques for non-destructive evaluation: a review. *Insight: Non-Destructive Testing and Condition Monitoring* **48**, 275–281 (2006)

10. Rusnáková, S., Slabeycius, J., Rusnák, V.: Determination of Resonant Frequencies of Composite Plates by Electronic Speckle Pattern Interferometry. In: TRANSCOM 2005, Žilina: ŽU, ISBN 80-8070-418-X, s.165–168, (2005)
11. Huang, C.H.: Experimental measurements by an optical method of resonant frequencies and mode shapes for square plates with rounded corners and chamfers. *J. Sound Vib.* **253**, 571–583 (2002)
12. Wang, W.C., Hwang, C.H., Lin, S.Y.: Vibration measurement by the time-average electronic speckle pattern interferometry methods. *Appl. Opt.* **35**, 4502–4509 (1996)

Nonlinear Dynamic Analysis of Structural Steel Retrofitted Reinforced Concrete Test Frames

Ramazan Ozcelik, Ugur Akpınar and Baris Binici

Abstract This chapter presents the analysis of deficient and retrofitted reinforced concrete test frames subjected to simulated earthquake excitations. First, the results of the pseudo dynamic (PsD) tests conducted on three two story-three bay reinforced concrete (RC) frames are presented. One of the test frames was a reference frame with infill walls, while the others were strengthened with chevron brace and internal steel frame. For PsD tests, Duzce motion record was applied. A nonlinear time history analysis was performed to observe the ability of estimating the dynamic response of the test frame. Force based fiber elements were utilized to model RC beams and columns by considering the confined and unconfined concrete parts of these members' sections. The infill wall was conducted by compression struts with the capability of simulating collapse with an element removal algorithm. The simulations revealed that collapse simulation of the infill wall plays a crucial role in estimating large seismic deformation demands. It was also observed that post installed connections of the structural steel members may exhibit some flexibility, hence need to be taken into account in the numerical models.

Keywords RC frame · Nonlinear time history analysis · Pseudo dynamic test · Chevron brace · Internal steel frame

R. Ozcelik (✉)
Department of Civil Engineering, Akdeniz University,
06800, Antalya, Turkey
e-mail: rozcelik@akdeniz.edu.tr

U. Akpınar · B. Binici
Department of Civil Engineering, Middle East Technical University,
Dumlupınar Bulvarı, 06800 Ankara, Turkey
e-mail: akpınar@metu.edu.tr

B. Binici
e-mail: binici@metu.edu.tr

1 Introduction

The numerical simulations have gained importance in both design and assessment of existing buildings before and after retrofitting. During the numerical simulation of such buildings, structural members should be modeled properly in order to obtain reasonably accurate results for economical retrofits. Although neglecting the infill walls is not necessarily a conservative approach [1], the effects of the infill walls on the lateral strength and stiffness of the system are usually neglected. Furthermore, including infill walls in a nonlinear numerical model also increases the complexity of numerical simulations. In the literature, there are many studies that explore lateral load resisting systems consisting on unreinforced infill members (see for example [2–4]). This chapter examines the numerical simulation of RC frames with infill walls, steel braces and internal steel frames. For this purpose, three two bay-three story RC frames were constructed and tested by utilizing pseudo dynamic (PsD) testing procedures [5]. While one of the RC frames was reference frame with infill walls tested by [6], the others were retrofitted by using chevron braces and internal steel frames tested by [7].

2 Test Frames

Three two story-three bay RC frames were tested to determine the performance of these frames under the Duzce ground motion. Comprehensive information about the reference test frames is available elsewhere [6].

As shown in Fig. 1, the exterior and interior spans of the frame were 2500 and 1300 mm, respectively. The first and second story column height was 2000 and 1500 mm, respectively. The dimensions of the columns were 150×150 mm with four 8 mm diameter longitudinal reinforcement plain bars. 4 mm diameter plain bars were used for stirrups. Turkish Earthquake Code 2007 (TEC 2007) [8] requires stirrups to be anchored using 135° hooks, 90° hooks, on the other hand, were used for all columns and beam to simulate the detailing deficiency of the Turkish construction practice before the establishment of the modern seismic codes. To simulate the insufficient confinement details of the columns, the stirrup spacing of the columns was 100 mm. The 150×200 mm beam was cast with a 600 mm wide, 60 mm thick slab. A 100 mm transverse reinforcement spacing was used for the beams. The RC beam-column joint had no column stirrup. The yield strength of the 4 and 8 mm diameter reinforcement bars was determined as 270 and 330 MPa by conducting uniaxial tension coupon tests, respectively. The target 28 day cylinder compression strength was 7.5 MPa to simulate the existing deficient structures with low concrete strength determined in field investigations [9–11]. The concrete compressive strength of the reference and retrofitted frames are indicated in Table 1.

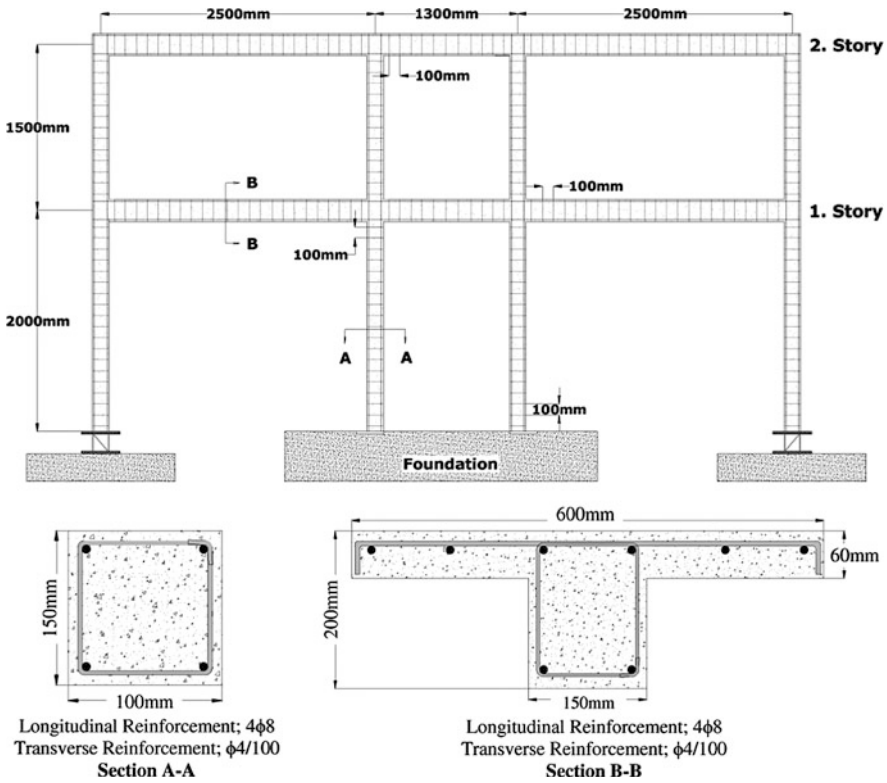


Fig. 1 Test frame and setup (Adapted from [6])

The reference frame had infill walls made from hollow clay brick into its interior span. Figure 2a indicates the test setup for the reference frame. The chevron braces had three connections between RC frame and brace members in a single story. The connection was conducted by using anchorage rods post-installed into the RC frame members. The test setup of the chevron braced frame is shown in Fig. 2b while more details are available elsewhere [7]. The steel frames were installed within bays of the deficient existing RC frames, and are thus referred to in this study as internal steel frames (ISFs). In the ISF frame, the interior columns and beams are constructed as composite members by installing the steel members to the existing RC members by using anchors [7, 12]. Figure 2c indicates the test setup for the RC frame strengthened with ISF while more details are available elsewhere [7].

The north–south component of the 1999 Duzce earthquake as seen in Fig. 3 was used for the pseudo dynamic test. This figure also shows the spectral acceleration vs. time plot of the Duzce earthquake and spectrum defined in TEC 2007 [8].

Table 1 Concrete strength

Ground motion scale (%)	Reference frame (MPa)	Chevron braced frame 1.story/ 2.story (MPa)	RC frame with ISF 1.story/ 2.story (MPa)
50	7.4	7.8/7.4	7.5/7.3
100	7.4	7.8/7.5	7.5/7.3
140	7.4	7.8/7.5	7.5/7.3

3 Numerical Modeling

A nonlinear time history analysis (NTHS) of test structures were performed by utilizing Open sees Simulation Platform [13] to observe the ability of estimating the dynamic response of the analyzed frame. Although the general modeling approach of the reference frame is mentioned in this chapter, comprehensive data about the reference test frame and test data are available elsewhere [1, 6, 14]. Figure 4 indicates the numerical modeling approach for the reference frame. Force based fiber frame elements were used to model beams and columns. The material model used for concrete (Concrete01 given in [13]) follows the rules of the confined and unconfined concrete models proposed by [15] with plastic offset rules [16]. Due to welding of longitudinal reinforcements to the foundation in the column ends, bond-slip was not observed during the test frame. Hence, reinforcing steel was modeled using a bilinear elastoplastic model (Steel 02 given in [13]) with a kinematic hardening slope of 1 %. The infill walls were modeled using compression only truss elements connected to the diagonal nodes of the boundary frame. Although the infill diagonal strut fails in one direction in the numerical simulations, the strut in the opposite direction at the first story had still significant capacity and stiffness. Hence, the frame could not deform in the opposite direction upon failure of only one diagonal strut. In order to model this phenomenon, an element removal algorithm as suggested by [4] was adopted. When the failure strain of the diagonal strut is exceeded in one direction, the struts in both directions are removed from the model. Upon element removal, internal forces are redistributed to achieve an equilibrium state at failure time. In this way, failure of the strut in one direction results in complete failure of the infill wall. As a result, there were two numerical models for the reference frame namely: the model with element removal algorithm and the model without element removal algorithm. The details of modeling and the properties of the effective truss model are given in Fig. 4.

Figure 5 shows the modeling strategy of the chevron braced frame. For the modeling of the brace sections, the aim was to have accurate buckling and post buckling predictions. For this purpose, the effective length of the braces was adjusted properly by introducing rigid end zones at the brace ends. These connections were modeled with simple elastic frames (elasticBeamCoulmn given in [13]) which had high rigidity with respect to the braces and the RC frame. However, the stiffness of the elements (used to account for the gusset plate lengths) at the base level were modified due to the uplift of the gusset plates that

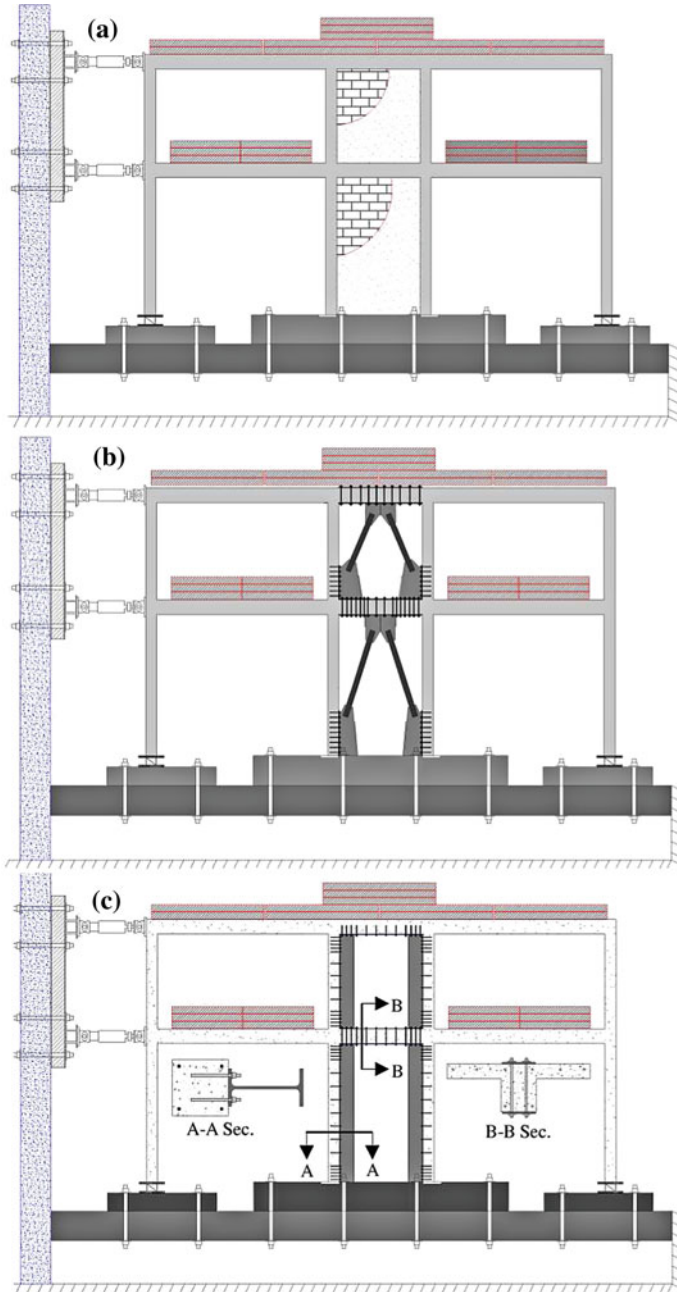


Fig. 2 Test setup: a Reference frame. b chevron braced frame. c RC frame with ISF

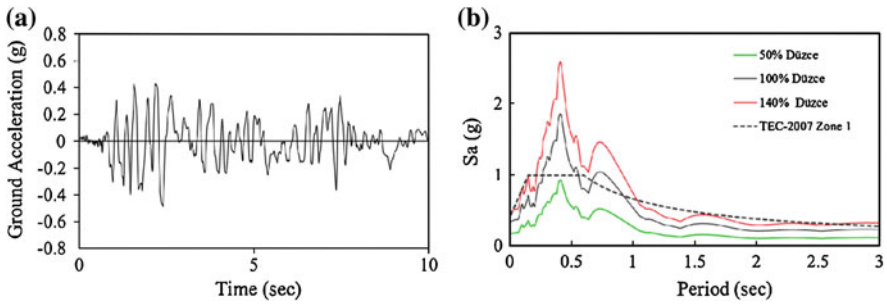


Fig. 3 a Duzce ground motion. b Spectrum

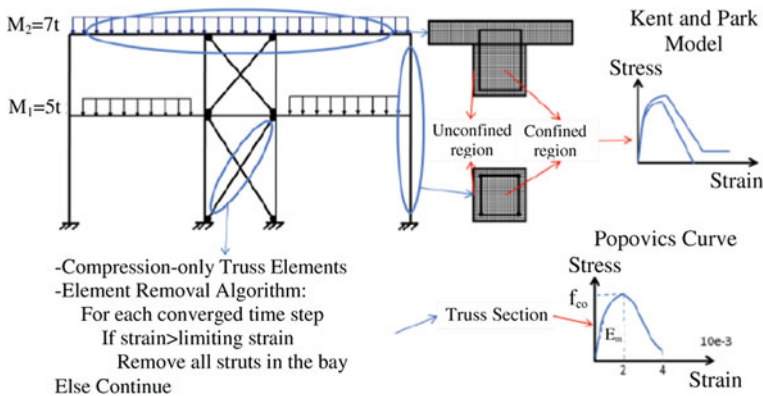


Fig. 4 Modelling strategy of the reference test frame

was observed during the test. Axial force on brace elements versus uplift displacements of gusset plates were sketched from the test data. The effective stiffness's of the link elements were calculated by using trend lines of measured uplift from different level ground motions. By including an element property change method, the corresponding stiffness's were modified at the termination of each ground motion and the analysis was conducted with the updated stiffness's prior to the beginning of each ground motion. Therefore, two numerical models namely model with flexible link (considering the gusset plate uplift) and model with rigid links (excluding the gusset plate uplift) were analyzed for the chevron braced frame. To capture the brace buckling, braces were divided into four equal elements as proposed by [17]. Instead of a straight brace member, a sinusoidal curved member was used with an initial imperfection at the mid-span of the brace.

In order to simulate the ISF, concrete and steel sections were defined with appropriate steel and concrete fibers as a simple section (Fig. 6). In this way, full composite action was ensured. Force based fiber frame elements (nonlinear-BeamColumn) were used to model the beam and the columns. As shown in Fig. 6, the composite section is formed from reinforced concrete and steel members. RC

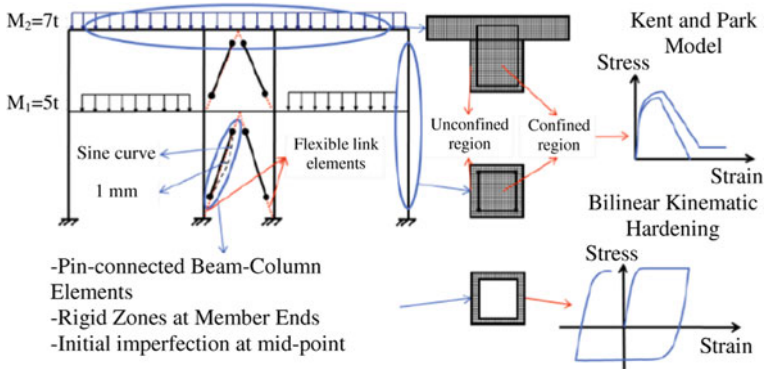


Fig. 5 Modelling strategy of the chevron braced frame

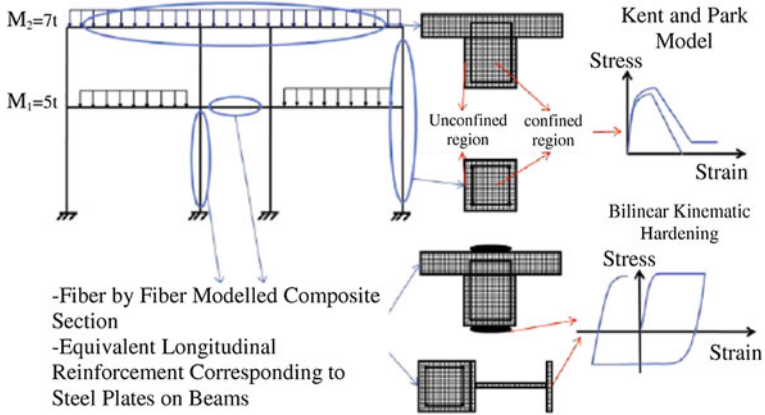


Fig. 6 Modeling strategy of the RC frame retrofitted with ISF

columns and steel frames were mounted to foundation with fixed connections. The material model of the internal steel frame members was assigned as hysteretic material model having a bilinear monotonic envelope with cyclic stiffness degradation in order to simulate severe pinching due to slippage of the two sections as observed in the experiments. Nodes were constrained to act as rigid diaphragms for all stories. The lumped mass approach with a Rayleigh critical damping of 5 % was utilized during the analyses, incorporating also the second order nonlinear geometric effects.

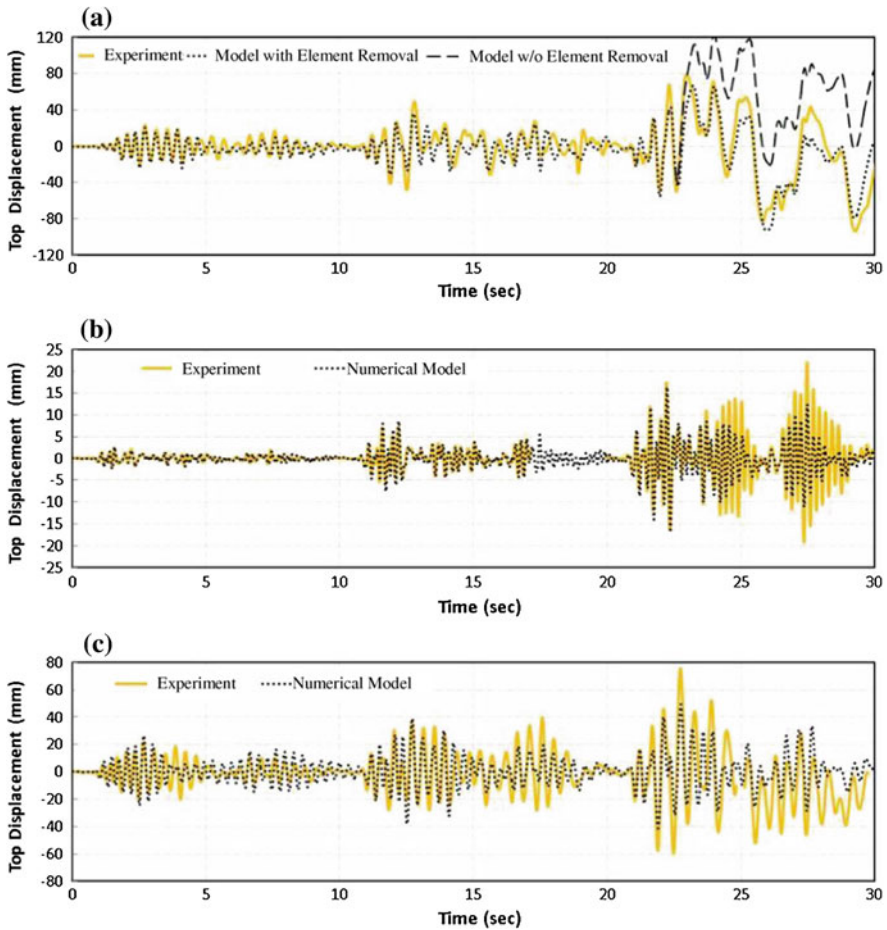


Fig. 7 Simulation results for the top displacement vs. time response: **a** reference frame, **b** chevron braced frame and **c** ISF system

4 Results of the Test Frames and Numerical Simulations

Figure 7 indicates the results of the test frame and numerical simulations for the reference frame, chevron braced frame and RC frame retrofitted with ISF in terms of time vs. top displacements. Errors in peak displacements and base shear force capacity of the frame models are given in Table 2.

The NTHA results of the reference frame indicate that the proposed model of the infill wall with the element removal algorithm was able to capture the load deformation behavior (Fig. 7a) in a fairly accurate manner. It can be observed that the inclusion of the element removal algorithm is necessary in order to capture the damage state of the test frame at the verge of collapse (Table 2).

Table 2 Error estimation of peak base shear and top displacement

Frame	Ground motion scale (%)	Test max. base shear demand (kN)	Analysis max. base shear (kN)	Error (%)	Story	Test max. disp. demand (mm)	Analysis max. disp. (mm)	Error (%)
<i>Reference frame</i>								
Model with element removal	50	60.35	55.8	7.5	1	15.0	17.0	13.3
					2	23.0	24.3	5.5
	100	62.24	57.7	7.3	1	31.2	23.3	25.5
					2	48.0	36.2	24.5
	140	54.54	55.09	1.0	1	85.3	88.3	3.5
					2	93.8	92.5	1.4
Model without element removal	50	60.35	55.8	7.5	1	15.0	17.0	13.3
					2	23.0	24.3	5.5
	100	62.24	57.6	7.3	1	31.2	23.3	25.5
					2	48.0	36.2	24.5
	140	54.54	56	2.8	1	85.3	116.9	37.0
					2	93.8	123.4	31.5
<i>Chevron brace frame</i>								
Model with flexible links	50	39.94	42.66	6.8	1	1.7	1.6	5.7
					2	2.5	2.4	1.0
	100	89.13	95.15	6.8	1	4.7	5.2	9.9
					2	7.3	8.6	18.5
	140	178.98	153.29	14.4	1	13.2	10.5	20.2
					2	22.1	16.9	23.3
Model with rigid links	50	39.94	42.66	6.8	1	1.7	1.6	5.7
					2	2.5	2.7	10.7
	100	89.13	85.81	3.7	1	4.7	3.2	32.4
					2	7.3	5.8	20.8
	140	178.98	102.84	42.5	1	13.2	4.5	65.5
					2	22.1	8.6	61.1
<i>ISF</i>								
	50	67.6	86	27.2	1	12.6	13.6	8.1
					2	21	24.4	12.1
	100	88.2	114.66	30.0	1	21.7	22.7	4.8
					2	39.7	39.1	1.5
	140	116.6	100.85	13.5	1	40.8	29.9	26.7
					2	75.6	49.5	34.5

For the case of the chevron braces, there was no buckling observed in the braces for any scale of applied ground motion. This condition resulted in events such as observing relatively low drift ratios, high initial stiffness and lack of softening in the system. The initial stiffness and displacement response of the numerical simulation (model with flexible links) results agree well with those of test measurements. However, the displacement response was underestimated at the end of

140 % Duzce test. According to the results of NTHA excluding the uplift of the gusset plates (model with rigid links) prevented the chevron braced frame to soften for 100 and 140 % Duzce tests. For these tests, the model underestimated the peak displacements and was unable to match the cyclic response of the test results. According to the error estimation of this case, the error increased with increasing earthquake scale and this effect became more critical.

For the results of the numerical simulation of the ISF, although the initial stiffness was estimated accurately, the numerical model underestimated the degradation of stiffness of the system. The peak lateral load capacity of the frame, on the other hand, was simulated with little error. For 50 and 100 % Duzce tests, the model was almost perfectly capable of capturing the displacement history achieved by the test. However, for the 140 % Duzce test, a significant error was observed in terms of maximum displacements between the simulation and the test results (Fig. 7).

5 Conclusions

The NTHA indicated that numerical models can estimate the behavior of the test frames tested by utilizing PsD testing methods. The infill wall model with the element removable algorithm was capable of simulating the reference frame with a reasonable accuracy. On the other hand, the numerical model without the element removable algorithm estimated the behavior of the test frame poorly. The numerical model with a flexible link estimated the behavior of the chevron braced frame better than that with a rigid link. This indicates that the numerical model may need to be modified with respect to test observations and measurements. The proposed numerical model of the ISF estimated the behavior of the ISF test frame system with a reasonable accuracy but this model needs further study.

Acknowledgments The research discussed in this chapter was conducted at Middle East Technical University (METU)-Structural Mechanics Laboratory. Funding provided by TÜBİTAK (project no: 106M493) and ÖYP program (supported by Akdeniz University) are greatly appreciated.

References

1. Akpınar, U., Ozcelik, R., Binici, B.: The Effect of Infill Wall on Seismic Performance of Deficient RC Structures. Proceedings of COMPDYN 2011 III ECCOMAS thematic conference on computational methods in structural dynamics and earthquake engineering, Corfu, Greece (2011)
2. Al-Chaar, G., Issa, M., Sweeney, S.: Behavior of masonry-infilled nonductile reinforced concrete frames. *J. Struct. Eng. ASCE* **128**(8), 1055–1064 (2002)
3. El-Dakhkhni, W., Elgaaly, F.M., Hamid, A.A.: Three-strut model for concrete masonry-infilled steel frames. *J. Struct. Eng. ASCE* **129**(2), 177–185 (2003)

4. Talaat, K., Mosalam, K.M.: Modeling progressive collapse in reinforced concrete buildings using direct element removal. *Earthquake Eng. Struct. Dynam.* **38**(5), 609–634 (2009)
5. Molina, F.J., Verzeletti, G., Magonette, G., Buchet, P.H., Geradin, M.: Bi-Directional pseudo dynamic test of a full-size three-storey building. *Earthquake Eng. Struct. Dynam.* **28**(12), 1541–1566 (1999)
6. Kurt, E.G.: Investigation of strengthening techniques using pseudo-dynamic testing, MS Thesis, Middle east technical University, Ankara, Turkey (2010)
7. Ozcelik, R. Seismic upgrading of reinforced concrete frames with structural steel elements. PhD Thesis, Middle east technical University, Ankara, Turkey (2011)
8. Turkish earthquake code (TEC 2007) specifications for structures to be built in seismic areas. Ministry of public works and settlement, Ankara, Turkey
9. Çağatay, I.H.: Experimental evaluation of buildings damaged in recent earthquakes in Turkey. *Eng. Fail. Anal.* **12**(3), 440–452 (2005)
10. Tezcan, S.S., Ipek, M.A.: A reconnaissance report: 1995 Dinar, Turkey, Earthquake. *Eng. Struct.* **18**(12), 906–916 (1996)
11. Doğangün, A.: Performance of reinforced concrete buildings during the May 1, 2003 Bingöl Earthquake in Turkey. *Eng. Struct.* **26**(6), 841–856 (2004)
12. Ozcelik, R., Akpınar, U., Binici, B.: Seismic retrofit of deficient RC structures with internal steel frames. *Adv. Struct. Eng.* **14**(6), 1205–1222 (2011)
13. Mazzoni, S., McKenna, H., Scott, M.H., Fenves, G.L.: Open sees manual. Pacific earthquake engineering research center, <http://opensees.berkeley.edu> (2009)
14. Kurt, E.G., Binici, B., Kurc, O., Canbay, E., Akpınar, U., Özcebe, G.: Seismic performance of a reinforced concrete test frame with infill walls. *Earthquake Spectra* **27**(3), 817–834 (2011)
15. Kent, D.C., Park, R.: Flexural members with confined concrete. *J. Struct. Div. ASCE*. **ST7**(97):1969–1990 (1971)
16. Karsan, I.D., Jirsa, J.O.: Behavior of concrete under compressive loading. *J. Struct. Div. ASCE*. **ST12**(95):2543–2563 (1969)
17. Uriz, P., Filippou, F.C., Mahin, S.A.: Model for cyclic inelastic buckling of steel braces. *J. Struct. Eng. ASCE* **134**, 619–629 (2008)

Acoustical Properties of Cellular Materials

Wolfram Pannert, Markus Merkel and Andreas Öchnser

Abstract While the acoustical behaviour of standard homogeneous materials like sheet metal can be described by a few basic statements, cellular materials show a more complex behaviour. Depending on the structure of the cells (open cells or closed cells) different acoustical behaviour can be seen. Transmission, absorption and reflection appear and vary in quantity depending on the shape and geometrical dimensions of the cells. Of course, the basic material of a single cell as well as the type of interconnection between the cells also have a strong influence on the acoustical properties. Within this contribution the acoustical properties of cellular materials are investigated by simulation and experiments. Hollow sphere structures serve as examples and plastic foams serve as references. The absorption coefficients as well as the complex wave number and the characteristic impedance are presented. The theoretical description is based on the theory of sound in porous media.

Keywords Acoustical property · Cellular material · Porous media

W. Pannert (✉) · M. Merkel
University of Applied Sciences Aalen, Department of Mechanical Engineering,
Aalen, Germany
e-mail: Wolfram.Pannert@htw-aalen.de

M. Merkel
e-mail: Markus.Merkel@htw-aalen.de

A. Öchnser
Universiti Teknologi Malaysia UTM, Faculty of Mechanical Engineering,
Johor, Malaysia
e-mail: Andreas.Oechsner@gmail.com

1 Introduction

As opposed to bulk material or closed-cell foams, which are poor sound absorbers, we study metallic hollow sphere structures which reveal porosity. Thus, it is expected that these materials show similar behaviour to open-celled metal foams, which have good absorption behaviour [1]. Metallic hollow sphere structures (MHSS) represent a relatively new group of advanced composite materials characterised by high geometry reproduction leading to relatively constant mechanical and physical properties. The MHSS combine the well-known advantages of cellular metals without major scattering of their material parameters. Various joining technologies such as sintering, soldering and adhering can be used to assemble single metallic hollow spheres to interdependent structures and allow adjusting different macroscopic properties [2].

Using open-cell polymer foam and glass or mineral wool fibers as sound absorbing material various housings are usually needed in order to improve stiffness and durability or to protect the absorber from contamination. In [3] sound absorption is discussed for metal foams, measured data are presented for the absorption behaviour of glass wool and Alporas[®]. In [4] measured data for the sound absorption coefficient are presented for Alporas[®], Alulight[®] and fibreglass. In [5] acoustical properties for ceramic materials are presented. Industrial application of MHSS as sound absorbing material are described in [6] and in [7], where noise reduction can be achieved for silencers and mufflers. In [8] the absorption coefficient is discussed as essential acoustical property of MHSS. Results are presented for specimen with hard back.

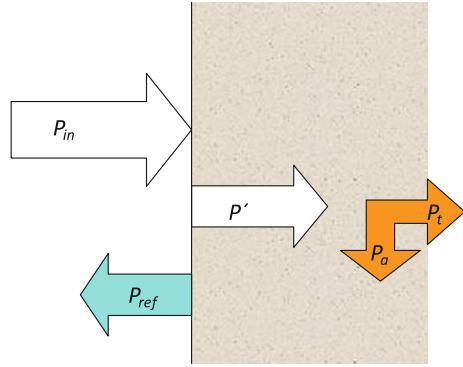
In this paper we discuss the reflection, transmission and absorption of cellular materials. Measurements data are gained by the 4-microphone method as well as by the 2-microphone method. The absorption coefficient, the wave number and the characteristic impedance are presented as essential acoustical properties.

2 Sound Propagation

Sound is a form of energy, which is transmitted by the collisions of atoms and molecules. It is important that there is no transfer matter in this case. The spreading of sound happens in form of longitudinal and transversal vibrations (waves) of the medium. In gases and liquids only longitudinal vibrations are possible, while in solids there are also transversal modes due to the shear forces. The speed of the longitudinal waves depends on the elastic properties (bulk modulus K) and the density ρ of the medium and is given by [9]

$$c \sim \sqrt{\frac{K}{\rho}}. \quad (1)$$

Fig. 1 Split of power for incoming plane wave



For this reason sound travels at velocities between 5000 m/s in steel and 340 m/s in air. The human ear responds to frequencies from about 20 to 20 kHz, which in air corresponds to wavelengths of 17 m–17 mm. The amplitude of the sound wave determines the loudness sensation. The amplitude of sound pressure is measured in Pascals (Pa), but it is more convenient to use a logarithmic scale in decibels (dB).

At the boundary between two different materials, an incoming plane wave is reflected due to the difference in the acoustic impedances Z_1 and Z_2 of the different materials. Parts of the incoming wave are absorbed in the material and a part is transmitted (see Fig. 1).

According to [9] the amplitude of the reflected wave p_{ref} is given by

$$p_{ref} = r p_{in} \tag{2}$$

with

$$r = \frac{Z_2 - Z_1}{Z_2 + Z_1} \tag{3}$$

where p_{in} is the amplitude of the incoming wave, r is the sound reflection factor. For the intensity I , this relation reads

$$I_{ref} = |r|^2 \times I_{in} \tag{4}$$

The coefficient $(1 - |r|^2) = \alpha$ is also called the absorption coefficient and is a very important functional property of any porous or cellular material. The coefficient t with

$$|t|^2 = \frac{I_t}{I_{in}}, \tag{5}$$

is called transmission coefficient and the coefficient d

$$d = \frac{I_{in} - I_{ref} - I_t}{I_{in}} = \alpha - |t|^2 \tag{6}$$

is called the dissipation coefficient.

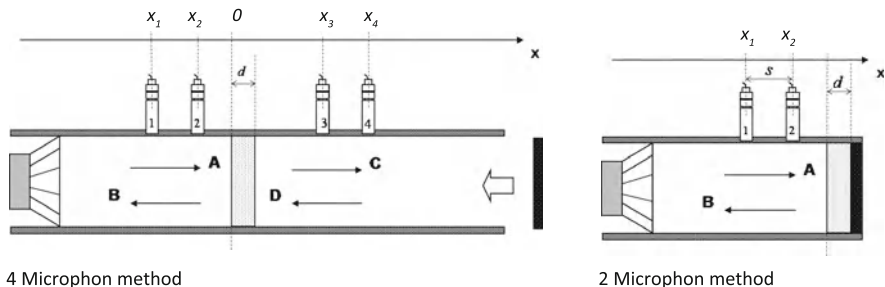


Fig. 2 Scheme **a** 4-microphone method **b** 2-microphone method

The coefficients depend on the frequency and angle of the incident wave and for a given cellular material they are a function of the material thickness, density and flow resistance. For small samples (up to 100 mm in diameter) the absorption coefficient of normally incident waves can easily be measured by an impedance tube. If the absorption coefficient for all angles of incidence is required, the measurement in a reverberation room is usually required. Much larger samples are needed in this case (up to 10 m²).

3 Experimental Method

3.1 Measurement Setup

The measuring equipment covers a signal generator for the generation of white noise, a loudspeaker, two impedance tubes (2-microphone and 4-microphone) with high quality microphones and a QUADRIGA[®] frontend for data acquisition (see Fig. 2). The analysis of the data was carried out using the program Matlab and the signal processing toolbox.

A number of preliminary tests with different materials were performed to minimize errors and find possible problems in the calculation procedure for the transfer function. The sound absorption coefficient of the steel back plate of the 2-microphone impedance tube was also measured and found to be less than 0.1 at all relevant frequencies.

The maximum frequency of the impedance tube is limited by its inner diameter.

3.2 Theoretical Background of Measurement

As mentioned above, there are two main methods for the determination of the acoustic absorption coefficient of materials—the reverberation room method and the impedance tube method. In this investigation we used the second method, since

it is faster and generally reproducible and only relatively small samples are required. Two different impedance tube methods are available—the 2-microphone method and the 4-microphone method. Both methods use the transfer function description which is a relatively recent development. In this method a broadband noise signal is used as sound source. The sound absorption coefficient and the impedance ratio of the tested materials can be measured much faster and easier, compared to other methods. Therefore the transfer function technique was adopted in this study.

A detailed description of the 2-microphone method is given in DIN EN ISO 10534-2. The 4-microphone method is e.g. discussed in [10].

3.2.1 2-Microphone Method

In the 2-microphone method the specimen is placed in front of an acoustically hard steel plate (see Fig. 2) and the incoming and reflected sound waves are analysed. With this method the sound absorption coefficient α can be calculated from the recorded data.

The transfer function method is based on the fact that the sound reflection factor r at normal incidence can be determined from the measured transfer function H_{12} between two microphones, which are positioned in front of the material under investigation.

The complex transfer function H_{12} is defined as [9]

$$H_{12} = \frac{p_2}{p_1} = \frac{e^{jk_0x_2} + r \cdot e^{-jk_0x_2}}{e^{jk_0x_1} + r \cdot e^{-jk_0x_1}} \quad (7)$$

where p_1 and p_2 are the complex sound pressure amplitudes at the two microphone positions x_1 and x_2 , which are measured from the reference plane $x = 0$. k_0 is the wave vector and is defined by

$$k_0 = 2 \times \pi / \lambda = 2 \times \pi \times f / c \quad (8)$$

The transfer function for the incident wave H_{in} and for the reflected wave H_{ref} can be calculated by

$$H_{\text{in}} = e^{-jk_0(x_1-x_2)}, H_{\text{ref}} = e^{jk_0(x_1-x_2)} \quad (9)$$

Combining these equations, the complex reflection factor r can be calculated by

$$r = \frac{H_{12} - H_{\text{in}}}{H_{\text{ref}} - H_{12}} \cdot e^{j2k_0x_1} \quad (10)$$

The sound absorption coefficient α can be determined in terms of r

$$\alpha = 1 - |r|^2 \quad (11)$$

3.2.2 4-Microphone Method

With the same technique as above, the 4-microphone-method is able to calculate the complex wave number and the characteristic impedance of the test sample directly from the measurement. The complex wave number and the characteristic impedance are quantities which do not depend on the geometry of the sample and therefore this pair of quantities characterizes the material of the test sample in a unique manner.

With the mathematical concept of the transfer matrix T , one can describe the transfer properties of the test sample as

$$\begin{bmatrix} p \\ v \end{bmatrix}_{x=0} = \begin{bmatrix} T_{11} & T_{12} \\ T_{21} & T_{22} \end{bmatrix} \cdot \begin{bmatrix} p \\ v \end{bmatrix}_{x=d}, \quad (12)$$

where p and v describe the pressure and normal velocity at the surface of the sample at $x = 0$ and $x = d$. The transfer matrix contains 4 elements—therefore 4 independent equations are required to determine the matrix elements.

The two-load-method based on 2 measurements with 2 different closures provides 2 equations. The one-load-method uses a special feature of the transfer matrix. In terms of electrical elements it describes a symmetrical 4-pole. The elements satisfy the following additional equations:

$$T_{11} = T_{22}, \quad (13)$$

$$T_{11}T_{22} - T_{12} \cdot T_{21} = 1. \quad (14)$$

The wave propagation inside the test sample gives the following expression for the 4 elements. They contain the complex wave number k_a and the characteristic impedance $Z_a = \rho_a \cdot c_a$ of the test material:

$$\begin{bmatrix} T_{11} & T_{12} \\ T_{21} & T_{22} \end{bmatrix} = \begin{bmatrix} \cos(k_a d) & j \cdot \sin(k_a \cdot d) \cdot \rho_a \cdot c_a \\ j \cdot \sin(k_a \cdot d) / \rho_a \cdot c_a & \cos(k_a d) \end{bmatrix} \quad (15)$$

Inverting the above relations, one can solve for k_a and Z_a :

$$k_a = \frac{1}{d} \cdot \cos^{-1} T_{11} \quad (16a)$$

or

$$k_a = \frac{1}{d} \cdot \sin^{-1} \sqrt{-T_{12} \cdot T_{21}} \quad (16b)$$

$$Z_a = \rho_a \cdot c_a = \sqrt{\frac{T_{12}}{T_{21}}}. \quad (17)$$

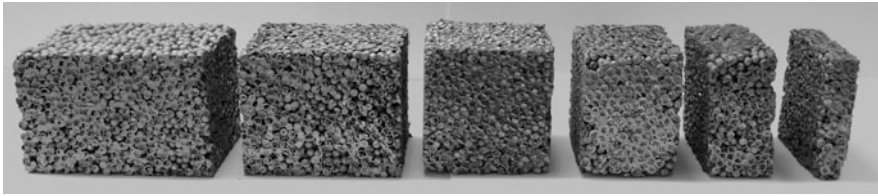


Fig. 3 Sample MHSS 113 with different thickness varying from 10 to 60 mm

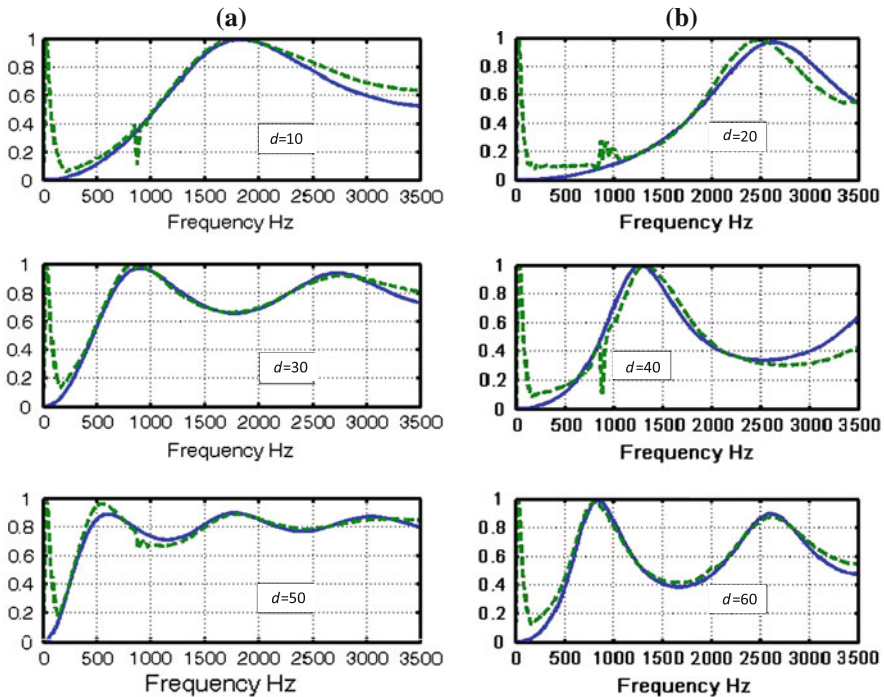


Fig. 4 Coefficient of absorption for samples with thickness of 20, 40 and 60 mm, measurement (dashed/green) and theory (full line/blue) (a) MHSS 86 (b) MHSS 113

3.3 Comparison with Theory of Sound in Porous Media

For our theoretical description we neglect all effects which are due to an interaction of the sound waves with the rigid frame of the porous absorber. These effects are included in the theory of Biot [11].

According to the simple Rayleigh-model of a porous absorber [9], the porous medium can be considered as an ensemble of many small tubes and the sound propagates in these small tubes. The flow in each tube can be calculated exactly and gives the known result in form of the “Hagen-Poiseuille—Law”. It is possible

Table 1 Parameter used for adjusting the theory to measured data

Parameter	MHSS 86	MHSS 113
α : porosity (measured)	0.84 (0.6)	0.37 (0.4)
Ξ : flow resistance [Ns/m ⁴]	17600	13500
χ : structure form factor	3.25	2.2
c_v : shape factor of the tubes; viscous effects	1.7	0.16
c_t : shape factor of the tubes; thermal effects	2.0	2.7

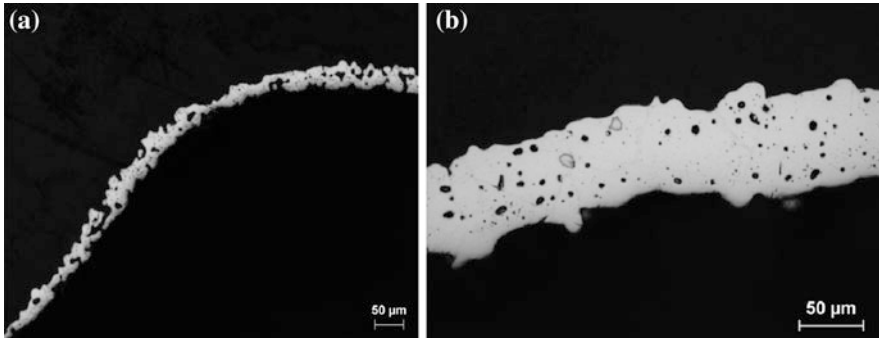


Fig. 5 **a** MHSS 86, wall thickness = 29 μm **b** MHSS 113, wall thickness = 67 μm

to introduce the flow-resistance Ξ , which is responsible for the absorption of energy in the porous material.

Solving the wave-equation with the appropriate boundary conditions (hard backing) for the 2-microphone method, one can find the following expression for the impedance $Z(\omega)$ of a sample of thickness d . $Z_a(\omega)$ is the characteristic impedance of the material and k_a is the wave number inside the material.

$$Z(\omega) = -j \frac{Z_a(\omega)}{\sigma} * \text{ctg}(k_a d) \tag{18}$$

For the definition of the parameters see the appendix.

From this model one can calculate the coefficient of absorption α :

$$\alpha = \frac{4\text{Re}\left(\frac{Z}{\rho_0 c}\right)}{\left[\text{Re}\left(\frac{Z}{\rho_0 c}\right) + 1\right]^2 + \left[\text{Im}\left(\frac{Z}{\rho_0 c}\right)\right]^2} \tag{19}$$

The results of the theoretical calculation can now be compared with measurements and one can test, if the same set of parameters can be used for all samples of one type of MHSS with different thickness. The shape of $\alpha(\omega)$ – curve is governed by a dimensionless parameter D .

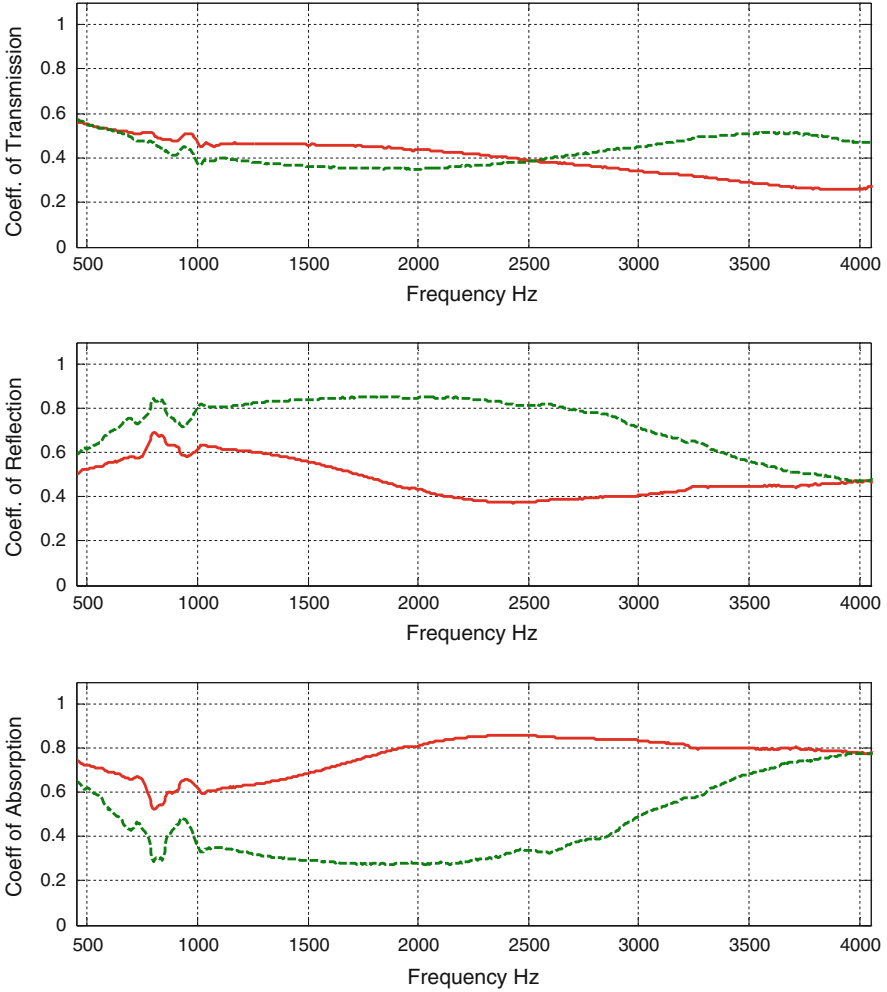


Fig. 6 The coefficients α , r , t : *full/red* = MHSS 86; *dashed/green* = MHSS 113

$$D = \frac{\Xi * d}{\rho_0 * c} \tag{20}$$

This parameter controls the damping of the sound wave in the porous medium. Small values of $D < 0.5$ result in low and strongly fluctuating absorption, while high values of D result in a smooth shape with low absorption at low frequencies. An optimal value of around $D \approx 2$ leads to a curve-shape with $\alpha \approx 1$ at $\lambda/4$ and little variation for higher frequencies.

With this simple theory it is not possible to fit all the measurements. A more detailed treatment of this problem is found in [12]. An advanced theory according to Johnson [13] introduces the concept of dynamic tortuosity and effective density.

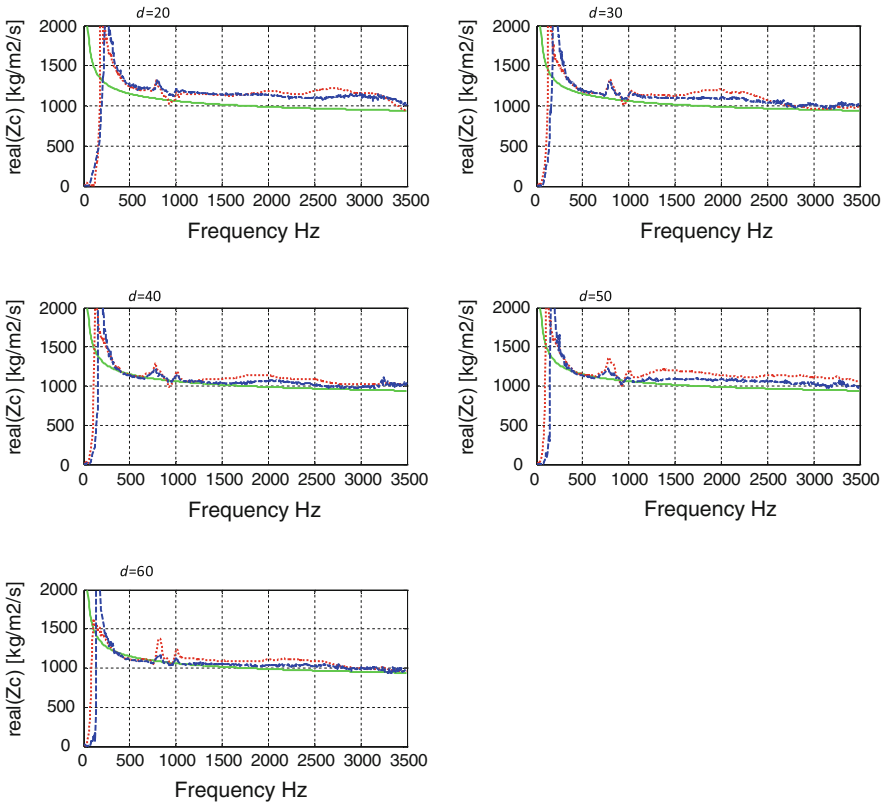


Fig. 7 MHSS 86 Real part of the impedance Z_c for different thickness d ; *full line/green* represents theory, *dashed/blue* measured values by two-load method and *dotted/red* measured values by one-load method

Compared to the simple theory, thermal effects due to the adiabatic compression and thermal exchange processes are taken into account. In addition to the parameters defined above, the tortuosity is used to account for the fact that the tubes are not straight lines and have complicated shapes. The tortuosity should be distinguished from the so-called structure form factor used in the simple theory. The exact formulae to calculate the impedance $Z_a(\omega)$, the wave number $k_a(\omega)$ and the absorption coefficient α of the porous material are given in the appendix.

3.4 Sample Preparation

The MHSS samples are built up by spheres out of steel as base material. For each sample the size of the spheres as well as the joining technique are the same. Two

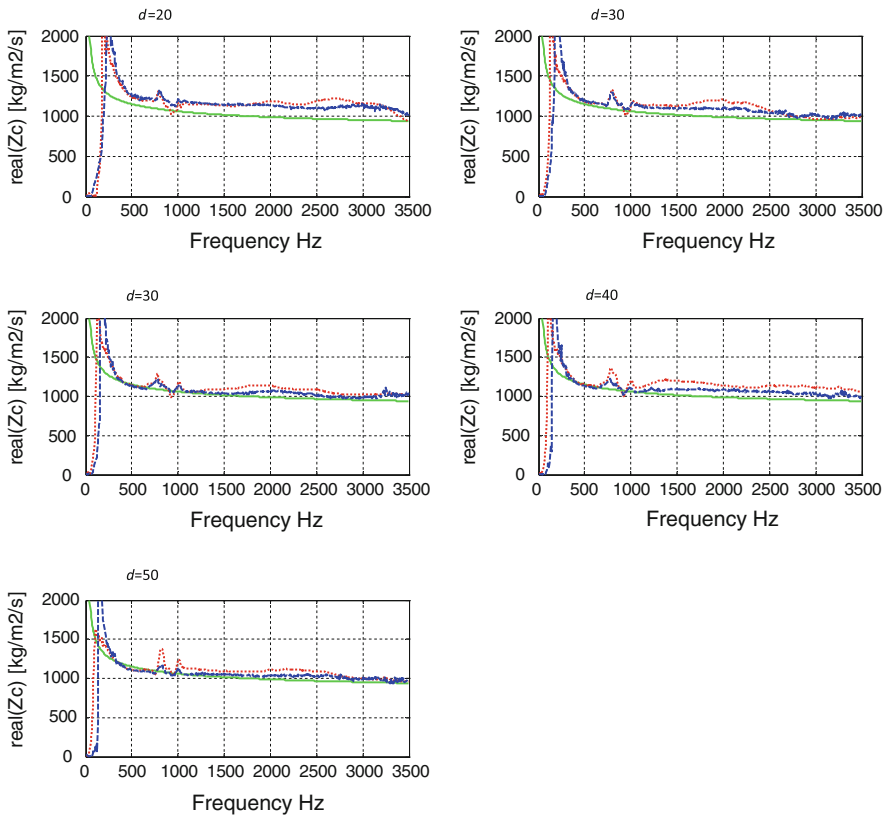


Fig. 8 MHSS 86 Imaginary part of the impedance Z_c for different thickness d ; *full line/green* represents theory, *dashed/blue* measured values by two-load method and *dotted/red* measured values by one-load method

different types of MHSS were investigated: MHSS 86 with 1.5 mm sphere diameter and MHSS 113 with 2.5 mm sphere diameter (see Fig. 3). For all samples sintering technique was used to assemble single hollow spheres to a structure. The raw MHSS plate was cut into pieces, which fit exactly in the impedance tube.

The thickness of the samples varies from 60 mm to 10 mm.

4 Results

4.1 Results for the 2-Microphone Method

In the present work the absorption coefficients for two different types of MHSS with varying thickness were measured in the frequency range from 500 Hz to 3500 Hz. In Fig. 4a resp. 4b the absorption coefficient is plotted for sample MHSS

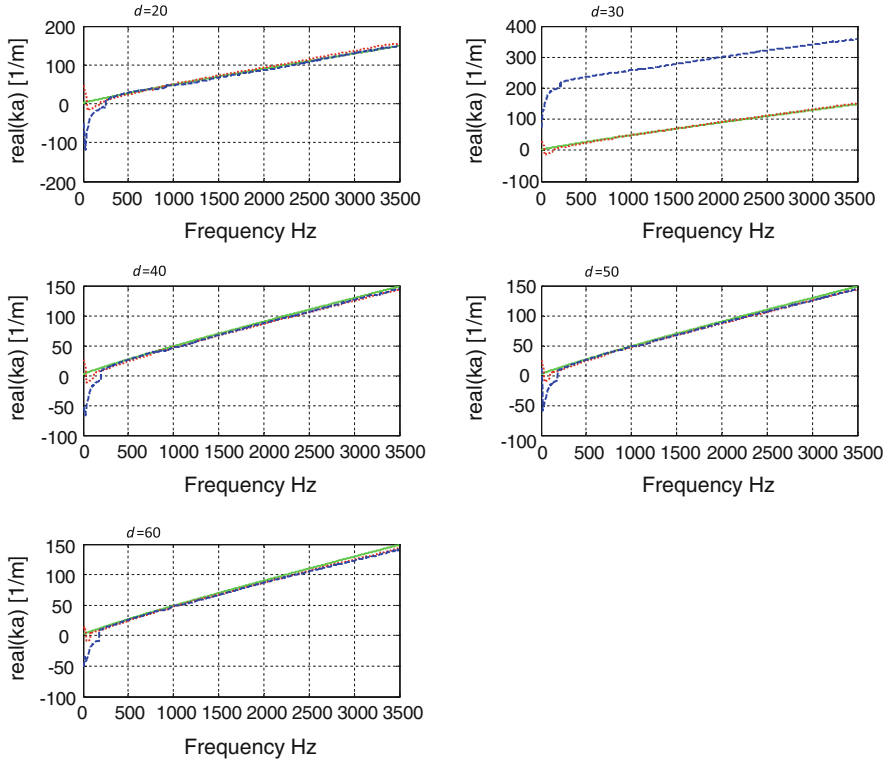


Fig. 9 MHSS 86 real part of the wave number k_a for different thickness d ; *full line/green* represents theory, *dashed/blue* measured values by two-load method and *dotted/red* measured values by one-load method

86 resp. MHSS 113. For both types of MHSS samples, we fit the measured data with the theory of Champoux and Allard [11]. In Fig. 4 one can clearly see the effect of the increasing thickness. The first maximum for the absorption is reached at lower frequencies for increasing thickness. This is the case if $\lambda/4$ is equal to the sample thickness d . The following maxima are found at odd multiples of $\lambda/4$.

Comparing the two samples with $d = 60$ mm, one can clearly see that sample MHSS 86 shows a broadband absorption above $f = 500$ Hz with little variation in frequency. The absorption is always greater than $\alpha = 0.7$. Sample MHSS 113 shows the first maximum at around $f = 800$ Hz, but in contrast it shows large variation and a decrease to $\alpha = 0.4$. One parameter—the porosity σ —was determined separately by experiments [14] and can be compared with the values, which are used to fit the data by theory. The porosity for MHSS 113 was $\sigma = 0.4$ from experiments and $\sigma = 0.37$ in the calculation. For MHSS 86 we found $\sigma = 0.6$ from experiments and $\sigma = 0.84$ in the calculation. In Table 1 the parameters used for adjusting the theory to measured data are summarized. The parameters were adjusted by a multidimensional unconstrained nonlinear minimization

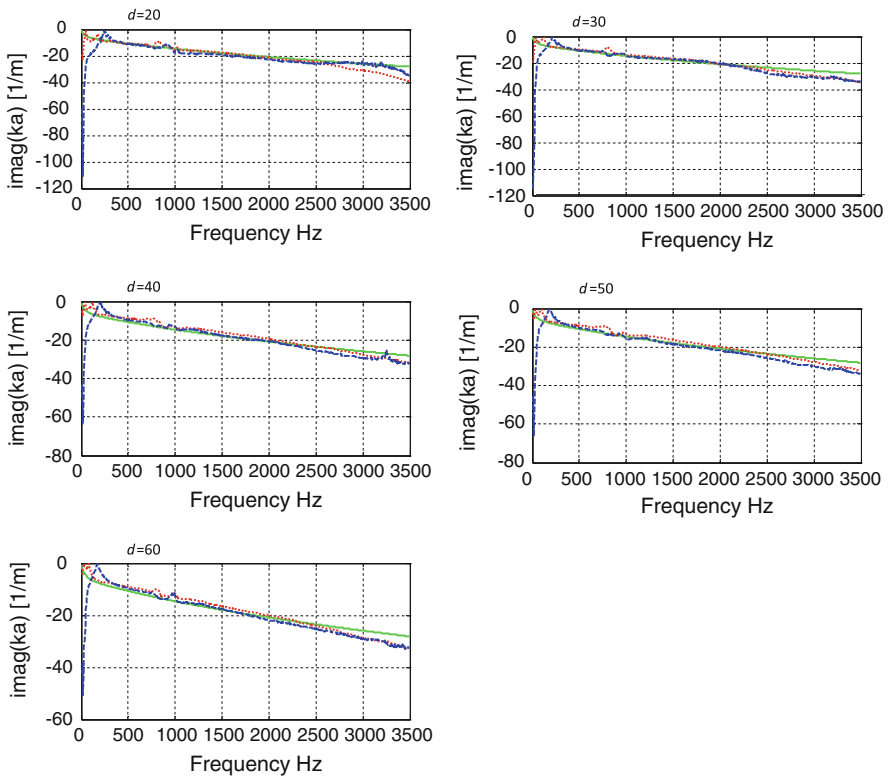


Fig. 10 MHSS 86 imaginary part of the wave number k_a for different thickness d ; *full line/green* represents theory, *dashed/blue* measured values by two-load method and *dotted/red* measured values by one-load method

(`fminsearch`), available in MatLab[®]. Because the method is not able to find the global minimum of the cost function, the calculation was started several times from very different starting points and ended at the same set of parameters. In this sense the set of parameters is unique.

Figure 5 might help to explain the differences between the measured and theoretical values of the density. The walls of the spheres clearly show pores. Even channels form inside to outside of a sphere can be seen. The theoretical model does not reflect this.

Comparing the results with absorption measurements of metal foams by several authors [4, 15, 16], similar results are found. For similar sample thickness of 20 mm, the first maximum is also found at around 2 kHz for two examples and at slightly higher frequencies in the other cases.

Thus, we can conclude that for the acoustical absorption, open celled metal foams behave very similar to MHSS.

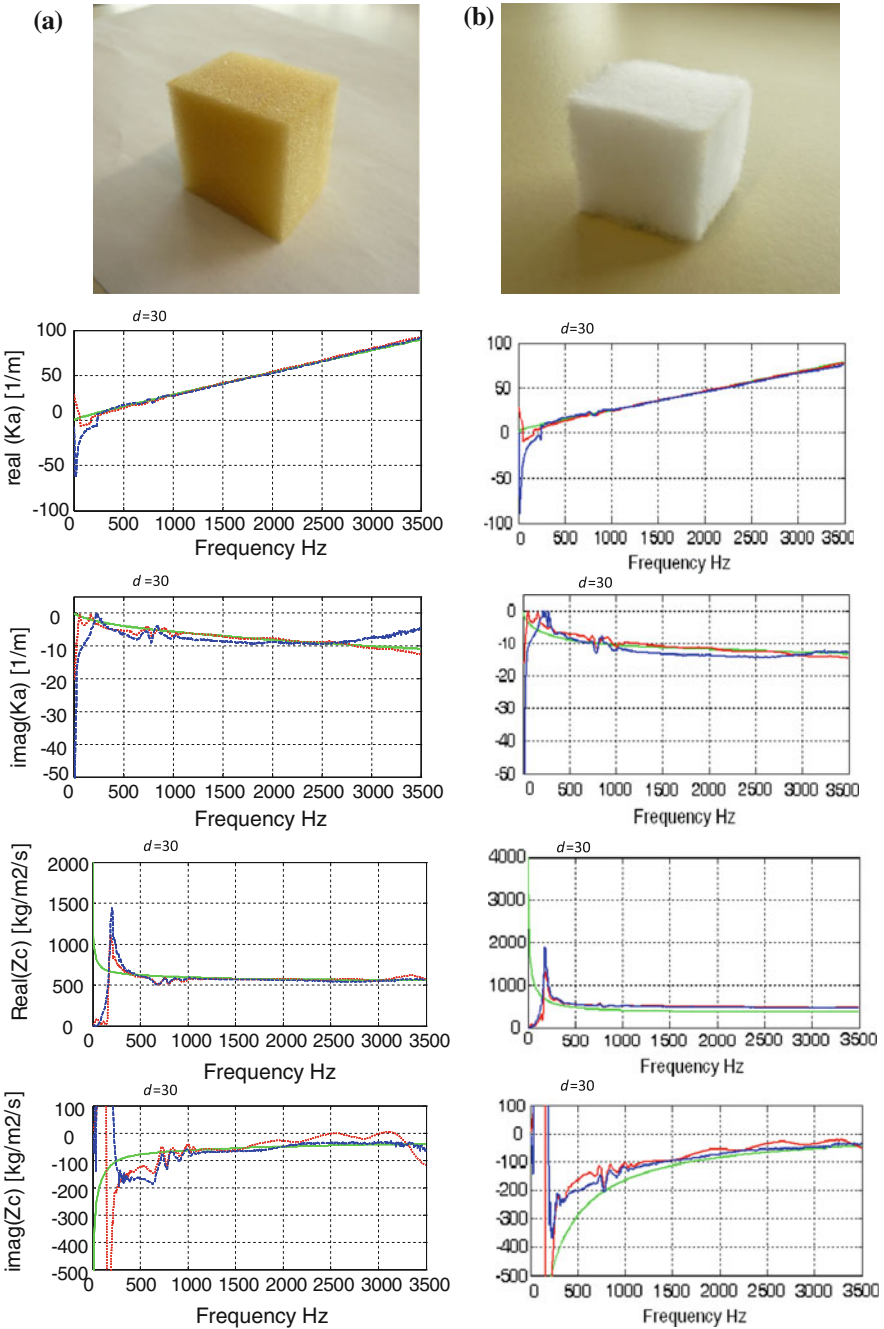


Fig. 11 a Foam and b fibre sample :Row 1: specimen Row 2 and 3: real part and imaginary part of the wave number Row 4 and 5: real part and imaginary part of the impedance

Table 2 Parameter for foam and polyester

Material	porosity	flow resistance [Ns/m ⁴]	structure form factor	shape factor of the tubes; viscous effects	shape factor of the tubes; thermal effects
Foam (yellow)	1.03	423	1.51	4.64	2.45
Polyester fibre	0.81	10289	1.08	0.04	3.77

4.2 Results for the 4-Microphone Method

For sample MHSS 86 (full line/red) and MHSS 113 (dashed line/green) we present the results for the coefficients for absorption α , for reflection r and for transmission t in Fig. 6. The thickness of the specimen is 30 mm. Because of the different experimental arrangement (no hard backing behind the sample), the coefficient of absorption α shows a different behavior in comparison to Fig. 4.

The following Figs. 7, 8, 9 and 10 show the real and the imaginary part of the two quantities which characterize the material—the characteristic impedance and the complex wave number for MHSS 86. From the results one can see the predicted independence of the sample thickness. The parameters in the theoretical calculation are the same as in Table 1. A very good agreement with the theory is achieved.

In all diagrams the colors have the following meaning: full line/green represents theory, dashed/blue measured values by two-load method and dotted/red measured values by one-load method.

In Fig. 11 we show some results of foam and fibre materials for comparison. The 2nd and 3rd row show the real resp. imaginary part of the wave number k_a . The 4th and 5th row show the real resp. imaginary part of the characteristic impedance Z_c .

A good agreement with theory is achieved by fitting the result with the following parameters given in Table 2.

5 Summary

The absorption coefficient α of MHSS was measured with the 2-microphone impedance tube in the range from 500 to 3500 Hz. The absorption coefficient shows a very typical dependence on frequency with maxima and minima that can be explained by theory as an effect of an energy loss due to frictional and thermal effects. The detailed shape and frequency dependency is influenced strongly by material parameters like sample thickness, pore size, porosity and sphere diameter, which influence the flow resistance \mathcal{E} . To reach high absorption over a wide range of frequencies, the dimensionless parameter D should have a value around $D = 2$.

With the 4-microphone impedance tube the characteristic impedance and the wave number of the material were calculated from the measurements and show the

predicted independence of the sample geometry. Good agreement with the theory of Johnson is achieved.

6 Conclusion

MHSS are broad-band sound absorbing materials. By varying different technological parameters, the ability for sound absorption can be specifically adapted to present noise spectra. These parameters include thickness, sphere diameter, packing density, mixture of different sphere diameters and others. Thus the material can be used for an efficient and new design of noise control systems.

The very good acoustical properties present one out of several characteristics of MHSS. In combination with other properties like heat-resistance up to high temperatures, low specific weight and relatively high mechanical stiffness and strength this material serves as an excellent material for multifunctional requirements. New fields of engineering applications could be defined for components for fast streaming hot media or any design where reproducible acoustic properties in humid and corrosive environments are required.

Future work should try to assign a relation between the parameters used in the theory and the microstructure of the porous material. Such an assignment would help to define a set of parameters for a microstructure which reflects requirements for a special application in an optimal way.

Appendix

Simple Rayleigh theory:

$$Z(\omega) = -j\rho_0c\frac{\sqrt{\chi}}{\sigma}\sqrt{1-j\frac{\Xi\sigma}{\omega Q_0\chi}} * \text{ctg}(k_a d) \quad (21)$$

$$Z_a(\omega) = \rho_0c\sqrt{\chi}\sqrt{1-j\frac{\Xi\sigma}{\omega Q_0\chi}} \quad (22)$$

$$k_a = k\sqrt{\chi}\sqrt{1-j\frac{\Xi\sigma}{\omega Q_0\chi}} \quad (23)$$

Definition of the parameters with units. For some parameters a typical range is added in round brackets:

d	thickness of the absorber [m]
k_a	wave number in the absorber [1/m]
ρ_0	density of air [kg/m ³]

c	speed of sound in air [m/s]
σ	porosity [%], ($\sigma < 1$)
χ	structure form factor [·], ($\chi > 1$)
ω	frequency [Hz]
Ξ	flow resistance [Ns/m ⁴], ($5,000 \text{ Ns/m}^4 < \Xi < 1,00,000 \text{ Ns/m}^4$)
$Z_a(\omega)$	characteristic Impedance [kg/m ² /s]

According to Champoux and Allard [12], who introduced the concept of characteristic dimensions, it is possible to calculate the bulk modulus and the effective density for porous media. Additional parameters arise

The meaning of the additional symbols in the following formulas is

μ	dynamic viscosity of air [Ns/m]
c_v	shape factor of the tubes; viscous effects [·]
c_t	shape factor of the tubes; thermal effects [·]
Pr	Prandtl number [·]
γ	adiabatic exponent for air [·]

Characteristic dimensions: Viscous effects:

$$\Lambda_v = \frac{1}{c_v} \sqrt{\frac{8\chi\mu}{\sigma\Xi}} \quad (24a)$$

thermal effects

$$\Lambda_t = \frac{1}{c_t} \sqrt{\frac{8\chi\mu}{\sigma\Xi}} \quad (24b)$$

$$G_v(\omega) = \sqrt{1 + \frac{j4\chi^2\mu\rho_0\omega}{\sigma^2\Lambda_v^2\Xi^2}} \quad (25a)$$

$$G_t(\omega) = \sqrt{1 + \frac{j4\chi^2\mu\rho_0\omega Pr}{c_t^4\sigma^2\Lambda_t^2\Xi^2}} \quad (25b)$$

$$\lambda_v = c_v \sqrt{\frac{8\chi\rho_0\omega}{\sigma\Xi}} \quad (26a)$$

$$\lambda_t = \frac{1}{c_t} \sqrt{\frac{8\chi\rho_0\omega}{\sigma\Xi}} \quad (26b)$$

Bulk modulus:

$$K(\omega) = \frac{\gamma P_0}{\gamma - (\gamma - 1) \left[1 + \frac{8G_t(\omega)}{jPr\lambda_t^2} \right]^{-1}} \quad (27)$$

Effective density:

$$\rho_{eff}(\omega) = \rho_0 \chi \left[1 + \frac{8c_v^2 G_v(\omega)}{j\lambda_v^2} \right] \quad (28)$$

Impedance of the medium:

$$Z_c = \sqrt{\rho_{eff}(\omega) K(\omega)} \quad (29)$$

Impedance of sample with thickness d :

$$Z = \frac{-jZ_a \cot(k_a d)}{\sigma} \quad (30)$$

Wave number in the porous medium:

$$k_a = \omega \sqrt{\frac{\rho_{eff}(\omega)}{K(\omega)}} \quad (31)$$

Coefficient of absorption:

$$\alpha = \frac{4\text{Re}\left(\frac{Z}{\rho c}\right)}{\left[\text{Re}\left(\frac{Z}{\rho c}\right) + 1\right]^2 + \left[\text{Im}\left(\frac{Z}{\rho c}\right)\right]^2} \quad (32)$$

References

1. Xie, Z., Teruyuki, I., Yoshiyuki, O., Hideo, Y.: Characteristics of sound absorption in lotus type porous magnesium. *Jpn. J. Appl. Phys.* **43**, 7315–7324 (2004)
2. Öchsner, A., Augustin, C.: *Multifunctional Hollow Sphere Structures*. Springer, Berlin (2009)
3. Ashby, M.F., Evans, A.G., Fleck, N.A., Gibson, L.J., Hutchinson, J.W., Wadley, H.N.G.: *Metal Foams: A Design Guide*. Butterworth-Heinemann, Oxford (2000)
4. Degischer, H.P., Krizst, B.: *Handbook of Cellular Metals: Production, Processing, Applications*. Wiley-VCH, Weinheim (2002)
5. Scheffler, M., Colombo, P.: *Cellular Ceramics—Structure, Manufacturing, Properties and Applications*. WILEY-VCH, Weinheim (2005)
6. Andersen, O., Hungerbach, W., Stephani, G., Studnitz, T.: Inno.zellmet—a concerted approach towards the application of non-foam type cellular metals. *Mat. Sci. Forum* **539–543**, 1892–1897 (2007)
7. Göhler, H., Kümmel, K., Hübelt, J., Hungerbach, W.: Metallic hollow sphere structures—examples for future noise reduction applications. *Proc. CELLMET* **2008**, 119–124 (2009)
8. Pannert, W., Winkler, R., Merkel, M.: On the acoustical properties of metallic hollow sphere structures (MHSS). *Mater. Lett.* **63**, 1121–1124 (2009)
9. Möser, M., Müller, H.A.: *Technische Akustik*, 3rd edn. Springer, Berlin (2004)

10. Ryu, Yunseon, Choi, Man-Rim: Transmission Loss Measurement of the Exhaust system using 4-Microphones with Impedance Tube, 18th International Congress on Acoustics, Kyoto (2004)
11. Biot, M.A.: The theory of propagation of elastic waves in a fluid-saturated porous solid. *J. Acoust. Soc. Am.* **28**, 168–178 (1956)
12. Allard, J.F.: Propagation of sound in porous media. Elsevier Applied Science, New York (1993)
13. Johnson, D.L., Koplik, J., Dashen, R.J.: Theory of dynamic permeability and tortuosity in fluid saturated porous media. *J. Fluid Mech.* **176**, 379–402 (1987)
14. Vehyl, C., Winkler, R., Merkel, M., Öchsner, A.: Structural characterisation of diffusion-bonded hollow sphere structures. *Defect Diffus. Forum* **280**, 105–113 (2008)
15. Han, F., Seiffert, G., Zhao, Y., Gibbs, B.: Acoustic absorption behavior of an open-celled aluminium foam. *J. Phys. D Appl. Phys.* **36**, 294–302 (2003)
16. Xie, Z., Teruyuki, I., Yoshiyuki, O., Hideo, Y.: Sound Absorption characteristics of lotus-type porous copper fabricated by unidirectional solidification. *Mat. Sci. Eng. A Struct. Mater.* **386**, 390–395 (2004)

Simulation of the Temperature Change Induced by a Laser Pulse on a CFRP Composite Using a Finite Element Code for Ultrasonic Non-Destructive Testing

Elisabeth Lys, Franck Bentouhami, Benjamin Campagne,
Vincent Métivier and Hubert Voillaume

Abstract Laser-ultrasonic is an innovating technique developed in aeronautics for quick and contactless inspection of composite materials. For the Non Destructive Evaluation (NDE) of composites, a short and powerful laser pulse generates ultrasonic waves. A part of the incident laser beam is absorbed by the surface and induces an elevation of the temperature of the material. This temperature increase generates local stress and thermal warping that are responsible for the generation of ultrasonic waves. This chapter of contribution describes the case of the thermal interaction between a CO₂ laser beam pulse and a carbon fibre reinforced plastic (CFRP) composite material. The laser beam is considered spatially and temporally Gaussian and the material is decomposed as two media. The first one is a 40 µm thick resin and the second is a 4 mm thick CFRP. By considering the laser beam as a volumic heat source with a 120 ns pulse duration, a 90 mJ energy and a 10 ms time range between two pulses, we have developed a finite element model using

E. Lys (✉) · V. Métivier
Laboratoire Subatech EMN-IN2P3/CNRS, Université de Nantes, 4 rue Alfred Kastler,
BP 20722 44307, Nantes, France
e-mail: elisabeth.lys@subatech.in2p3.fr

V. Métivier
e-mail: vincent.metivier@subatech.in2p3.fr

F. Bentouhami
Airbus France, Centre Technocampus EMC2, Allée du Chaffault,
44340 Bouguenais, France
e-mail: franck.bentouhami@airbus.com

B. Campagne · H. Voillaume
EADS, Centre Technocampus EMC2, Allée du Chaffault,
44340, Bouguenais, France
e-mail: benjamin.campagne@eads.net

H. Voillaume
e-mail: hubert.voillaume@eads.net

the Elmer code to simulate the transient heat equation and to evaluate the composite temperature increase. The results of the thermal analyses are applied to understand the influence of resin skin thickness and pulse rate on the ultrasound generation.

Abbreviations

EMN	Ecole des Mines de Nantes
IN2P3	Institut national de physique nucléaire et de physique des particules
CNRS	Centre national de la recherche scientifique
EMC2	Ensembles métalliques et composites complexes
NDE	Non destructive evaluation
CFRP	Carbon fibre reinforced plastic
LUIS	Laser ultrasonic inspection system
FEM	Finite element method
BiCGStab	Biconjugate gradient stabilized method
ILUT	Incomplete LU-decomposition with threshold
TSCNG	Technologies et structures composites
FCE	Fonds de compétitivité des entreprises
DGE	Direction générale des entreprises

1 Introduction

In the field of non-destructive inspection of materials, ultrasounds are considered as the reference method. Classically, a water coupling is generally used between the generator (sonotrode) and the material to propagate the ultrasonic waves. Using this water coupling could be a problem when the workpiece is porous or if its temperature is high. In the field of aeronautics, the complex shapes of CFRP materials requires the development of contactless techniques such as laser ultrasonic technology. For this contactless technique, a pulsed laser beam (with an excitation energy around 90 mJ during 120 ns) is partially absorbed by the inspected material which causes a thermal expansion of the controlled object. This thermal expansion occurs in the thermo-elastic regime and generates a local stress at the surface which creates the ultrasonic waves that propagate into the material. Defects (up to 50 μm) reflect the ultrasonic wave and are detected with a laser interferometer due to micro-strain generated on the surface [1, 2].

The laser ultrasound generation is an attractive method and presents a lot of benefits for the NDE of a material because:

- It really allows to do automated control of target without any contact.
- It avoids the use of coupling media which could create loss of signal when thickness is too important or when the thickness variation generates a change of sensibility.

- The NDE can be done at relatively high temperature in a hostile or corrosive environment.
- The complex geometry of the inspected parts is less restrictive for the non destructive testing.

In the case of composite materials, the CO₂ laser beam is partially absorbed in the resin. The ultrasonic wave is generated in the resin volume and propagates in all the sub-layers of the material.

In this chapter, we present some results issued from a collaborative research project between Airbus, EADS and Ecole des Mines de Nantes. The work consists in modelling the temperature variation in time and space in a two-body material (the first body is the isotropic resin skin and the second body is the anisotropic CFRP composite) that has been illuminated by a CO₂ pulsed laser, whose optical parameters are issued from the LUIS [3] (laser ultrasonic inspection system) device.

In a first part, we describe the heat equation used to determine the temperature distribution throughout the composite material. This equation results from a heat flux (which varies in time and space as a Gaussian distribution) applied to an anisotropic body (CFRP composite). To do this, we chose to use the open source software Elmer [4], which solves the transient heat equation in three dimensions by a finite element method (FEM). The numerical model developed to simulate the temperature changes in the material reproduces as closely as possible the experimental conditions for non-destructive evaluation of composite materials and helps, in a second part, to understand the influence of rising rates of laser pulse or change in the geometry of the material (e.g. change in skin thickness of resin) at the measured temperature.

2 Modelling of Laser Ultrasonic Inspection System of CFRP

The geometry of the laser irradiation on the CFRP composite is schematically represented in Fig. 1. When the composite (cf. Fig. 1) is illuminated by a CO₂ laser pulse, a part of the initial energy is reflected by the target material and the other part that is absorbed by the resin generates a non-uniform temperature field near the surface of the material.

The volumic heat source applied to the resin skin generates conduction, convection and radiation thermal transfers. Due to the thermoelastic mechanism induced in the resin skin, the thermal conduction equation [5] can be written (cf. Fig. 2):

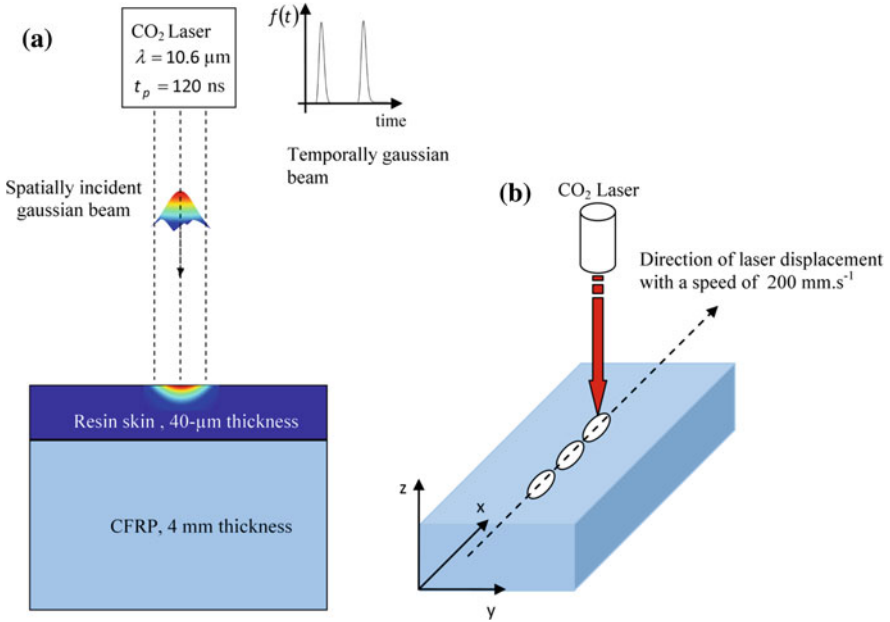


Fig. 1 Schematic diagram for a laser irradiating CFRP composite. **a** Properties of laser and composite. **b** Laser scanning description

- in the resin skin

$$\vec{\nabla} \left[\kappa_1 \vec{\nabla} T(\vec{x}, \vec{y}, \vec{z}, t) \right] - \rho_1 C_{p1} \frac{\partial T(\vec{x}, \vec{y}, \vec{z}, t)}{\partial t} + \dot{q}(\vec{x}, \vec{y}, \vec{z}, t) = 0 \quad (1)$$

- and in the CFRP

$$\vec{\nabla} \left[\kappa_2 \vec{\nabla} T(\vec{x}, \vec{y}, \vec{z}, t) \right] - \rho_2 C_{p2} \frac{\partial T(\vec{x}, \vec{y}, \vec{z}, t)}{\partial t} = 0 \quad (2)$$

where T is the temperature distribution, $\dot{q}(\vec{x}, \vec{y}, \vec{z}, t)$ is the volumic heat source, $\kappa_{1,2}$, $\rho_{1,2}$, $C_{p1,2}$ are respectively the thermal conductivity, the density and the thermal capacity of the resin skin and of the CFRP composite.

The laser beam is assumed to be spatially and temporally Gaussian distributed [6]. The volumic heat source can be estimated in the Cartesian coordinates by the equation:

$$\dot{q}(x, y, z, t) = q_{\text{laser}}(x, y) \times (1 - R) \times \alpha \times e^{-\alpha \times |z|} \times f(t) \quad [\text{Wm}^{-3}] \quad (3)$$

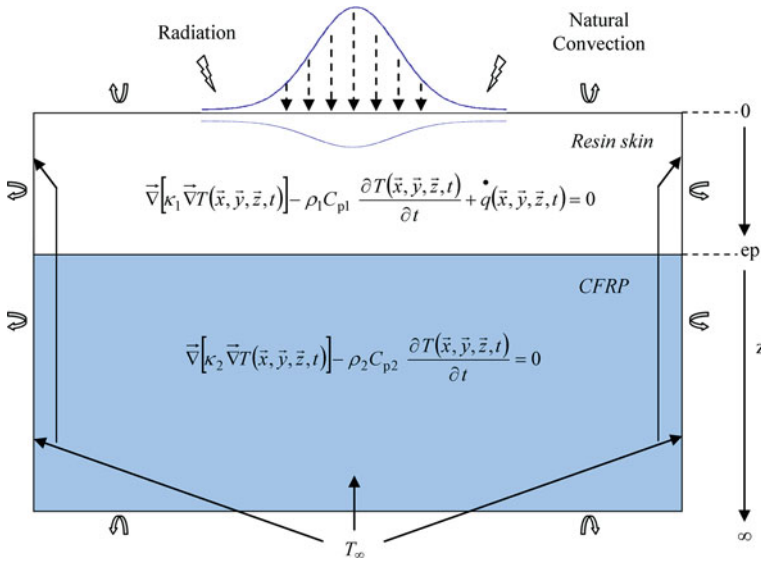


Fig. 2 Illustration of the applied mathematical model

where α is the absorption coefficient (and $1/\alpha$ is the optical penetration depth), R the reflection coefficient of resin skin, $f(t)$ a function of time for which we give expression thereafter and $q_{\text{laser}}(x, y)$ is the heat flux expressed in spatially gaussian distribution as:

$$q_{\text{laser}}(x, y) = \frac{2P_{\text{laser}}}{\pi r_{\text{spot}}^2} \times e^{-\frac{2(x^2+y^2)}{r_{\text{spot}}^2}} \quad [\text{Wm}^{-2}] \quad (4)$$

where r_{spot} is the radius of laser spot and $P_{\text{laser}} = \frac{E}{\tau_p}$ [W] is the laser power with E the energy and τ_p the pulse duration.

The volumic heat source can now be written this way:

$$\dot{q}(x, y, z, t) = \frac{2P_{\text{laser}}}{\pi r_{\text{spot}}^2} \times (1 - R) \times \alpha \times e^{-\frac{2(x^2+y^2)}{r_{\text{spot}}^2}} \times e^{-\alpha \times |z|} \times f(t) \quad [\text{Wm}^{-3}] \quad (5)$$

with the time function $f(t)$ in temporally gauss distribution [6] defined as:

$$f(t) = \left(\frac{t}{t_r}\right)^3 e^{-2\left(\frac{t}{t_r}\right)^2} \quad (6)$$

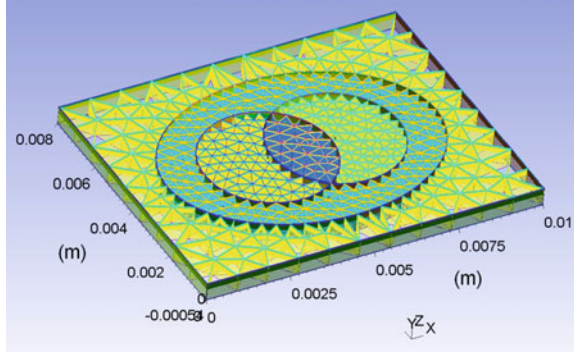
where $t_r = \tau_p/2$ is the rise time of the laser pulse.

The boundary conditions [7] are: $T(x, y, z, t = 0) = T_{\text{ambient}} = T_{\infty} = 293\text{K}$, $[T(z \rightarrow \infty)]_{\text{CFRP}} = T_{\infty}$,

Table 1 Parameters of laser LUIS

Parameters	Pulse rate 100 Hz	Pulse rate 400 Hz
Wavelength (μm)	10.6	10.6
Energy E (mJ)	90	90
Pulse duration τ_p (ns)	120	120
Velocity displacement (mm s^{-1})	200	800
Circular spot radius (mm)	1.875	1.875

Fig. 3 Typical 3D meshing used for the heat equation simulation with higher resolution into and around the laser spots



$$[T(x \rightarrow \infty, y \rightarrow \infty, z)]_{\text{Resin or CFRP}} = T_{\infty}$$

and

$$\begin{cases} [T(z = ep)]_{\text{Resin}} = [T(z = ep)]_{\text{CFRP}} \\ [-\kappa_1(\partial T/\partial z)|_{z=ep}]_{\text{Resin}} = [-\kappa_2(\partial T/\partial z)|_{z=ep}]_{\text{CFRP}} \end{cases}$$

at the interface, with a resin of ep thickness (see Fig. 2)

3 Results of the 3D Numerical Simulation

In laser-ultrasonics employed for non-destructive evaluation of the CFRP materials, the parameters such as pulse rate or/and resin thickness have a direct influence on the temperature distribution and on the ultrasonic wave generated as well. It is important to simulate the temperature distribution for two reasons:

- If the temperature of the evaluated body increases during the laser scanning, the speed of the acoustic wave may change and could introduce an error on the thickness evaluation.
- If the resin thickness is approximately equal or smaller than the optical penetration, the elevation temperature might damage the carbon fibre at the interface resin/fibre.

Table 2 Parameters of the simulated two-body material

Parameters	Resin	CFRP
Thickness	40 μm	4 mm
Density (kg m^{-3})	1,141	1,600
Conductivity κ_x ($\text{W m}^{-1} \text{K}^{-1}$)	0.22	7
Conductivity κ_y ($\text{W m}^{-1} \text{K}^{-1}$)	0.22	7
Conductivity κ_z ($\text{W m}^{-1} \text{K}^{-1}$)	0.22	0.8
Specific heat C_p ($\text{J kg}^{-1} \text{K}^{-1}$)	Function of temperature	1,200
Optical reflectivity R	0.9	–
Optical penetration depth [8] $1/\alpha$ (μm) [6]	20	–

Table 3 Resin specific heat parameters [9]

Coefficient	Value
a_1	0.00264
a_2	1.45
a_3	0.232
a_4	0.0623
a_5	0.000642

So the aim of this work is to simulate the temperature distribution in a composite material to evaluate the possible damages which could take place. From here on, we will describe the laser and the CFRP material properties which will then be used in the simulation of the transient heat equation by the Elmer FEM software.

3.1 Laser and Material Properties

The experimental settings of the LUIS that were used for simulation are shown in Table 1.

The modelled material is considered as a two-body material with isotropic resin skin and anisotropic CFRP composite. The properties of the target material are presented in Table 2.

For the resin, the specific heat varies with temperature. When the temperature is less than or equal to the vitreous temperature ($T_g \approx 490\text{K}$), the specific heat can be written as described in [9]:

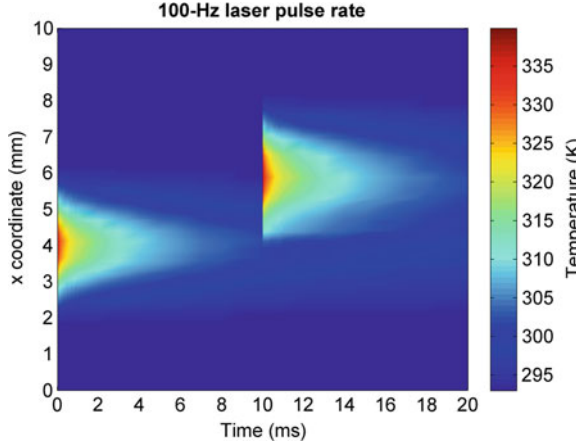
$$C_{p_1} = abs(a_1 T + a_2 + a_5(T - T_g)) + (a_3 - a_5 T_g) \tanh(m^- a_4(T - T_g)) \quad [\text{J}/(\text{kgK})] \quad (7)$$

where T is the temperature in Celsius degree, $a_{1,2,3,4,5}$ are coefficients whose values are shown in Table 3 and $m^- = \frac{-a_5 + a_4(a_3 - a_1 T_g)}{a_4(a_3 - a_1 T_g)}$.

When the temperature is more than T_g , the specific heat is written:

$$C_{p_1} = abs(a_1 T + a_2 - a_5(T - T_g)) + (a_3 - a_5 T_g) \tanh(m^+ a_4(T - T_g)) \quad [\text{J}/(\text{kgK})] \quad (8)$$

Fig. 4 Surface temperature ($x \in [0, 10 \text{ mm}]$, $y = 4 \text{ mm}$, $z = 0$) for a $40 \text{ }\mu\text{m}$ resin skin



$$\text{where } m^+ = \frac{a_5 + a_4(a_3 - a_1 T_g)}{a_4(a_3 - a_1 T_g)}.$$

3.2 Meshing Object and Elmer Program

We have used the Elmer [4] open source software for the 3D estimation of temperature profile in a dual body material which will be subject to two laser pulses. Firstly, the two considered laser pulses were separated by 10 ms and the laser displacement was 2 mm. The Elmer software allows us to simulate the heat equation with a complex heat source which is modelled as spatial and temporal Gaussian distribution, with also complex material parameters which depend, for example, of the temperature of the target.

The object was firstly meshed with the Gmsh [10] open source software and then imported in the Elmer interface. The constructed 3D model used a 2D triangular mesh extruded along the Z-axis with a fine resolution into the area of the two simulated laser spots and which decreased moving away from the two spots (along X and Y-axis), see Fig. 3.

The heat equation with heat source, material properties and boundary conditions previously described, has been solved in transient regime to determine the temperature in the material for each time step. The solver used by Elmer is used an iterative biconjugate gradient stabilized method (BiCGStab) based on the subspaces of Krylov for solving the problem [11]. To accelerate the convergence of the BiCGStab method, we used a preconditioning method (ILUT) which allows, for each iteration, to approach the inverse of the system matrix by an auxiliary matrix.

Fig. 5 Depth temperature ($x = 4 \text{ mm}$, $y = 4 \text{ mm}$, $z \in [0, -100 \text{ }\mu\text{m}]$) for a $40 \text{ }\mu\text{m}$ resin skin

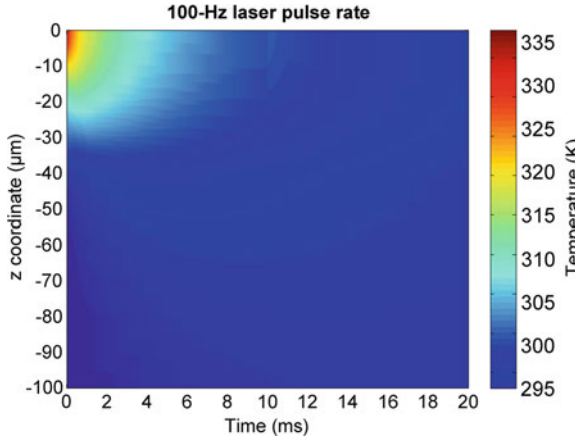
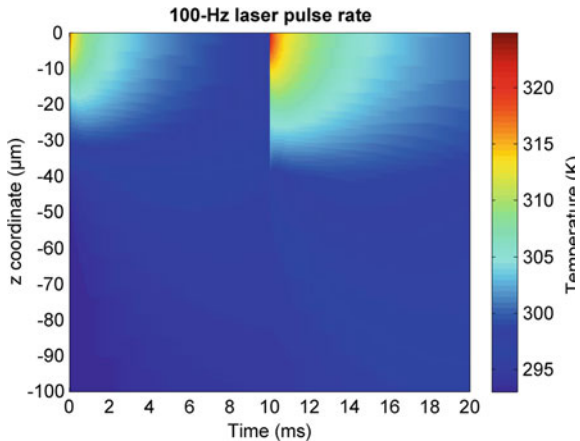


Fig. 6 Depth temperature ($x = 5 \text{ mm}$, $y = 4 \text{ mm}$, $z \in [0, -100 \text{ }\mu\text{m}]$) for a $40 \text{ }\mu\text{m}$ resin skin



3.3 Results

Using all the properties of material and settings of the LUIS system previously described in this chapter (see Tables 1, 2, 3), we have simulated the heat conduction equation in transient condition, giving a 3D model which displays the temperature in every point of the material. To illustrate the results, we have computed the temperature along a line at the surface and along the depth of the composite material.

Firstly, we have computed the temperature along a line centred between the two laser spots along the X-axis and during 20 ms, see Fig. 4. For this configuration we can observe a maximum temperature around 340 K.

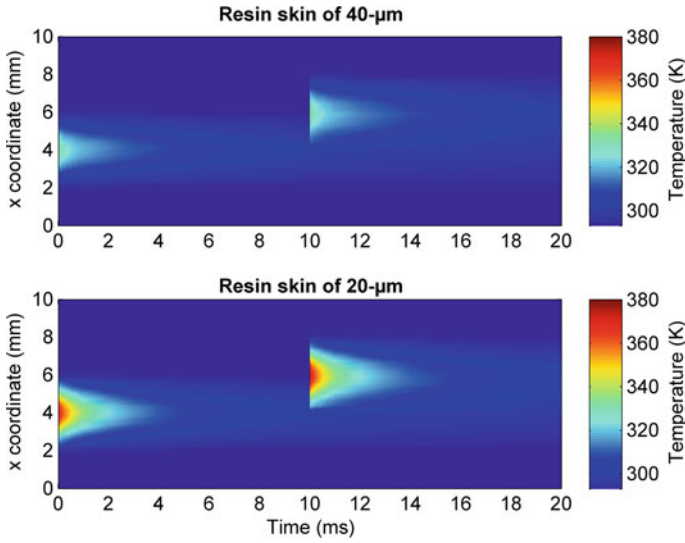


Fig. 7 Comparison of surface temperature for two resin thicknesses. Pulse rate: 100 Hz

Then, we have computed the depth temperature (along the Z-axis) firstly centred on the first laser spot (Fig. 5) and secondly at equal distance between the two laser spots centres (Fig. 6).

We can observe (Fig. 5) that there is no significant influence of the second laser pulse on the measured temperature on the first centre laser spot whereas the temperature measured from the second pulse is more important for the point centred at the middle of the two laser spots, see Fig. 6.

Besides, let us note that the influence of laser pulse is just in the area of the resin skin because the temperature does not increase significantly beyond an area of 40 μm in the first 20 ms after the pulse.

Industrial partners (EADS and Airbus) are particularly interested in the study of:

1. influence of the resin skin thickness
2. and influence of pulse rate,

on the temperature elevation at the surface and inside the material during and after scanning.

For the first point, let us note that the thermoelastic deformation is performed in the resin skin and is responsible for the ultrasound wave generation. There is probably a significant influence of the resin thickness on the ultrasound wave quality. The knowledge of the composite material temperature allows us to interpret the ultrasound wave produced.

The numerical applications indicate that when the resin skin thickness is half of the theoretical one, the maximum temperature is around 380 K which gives an increase of 40 K between the two resin thicknesses (see Figs. 7, 8).

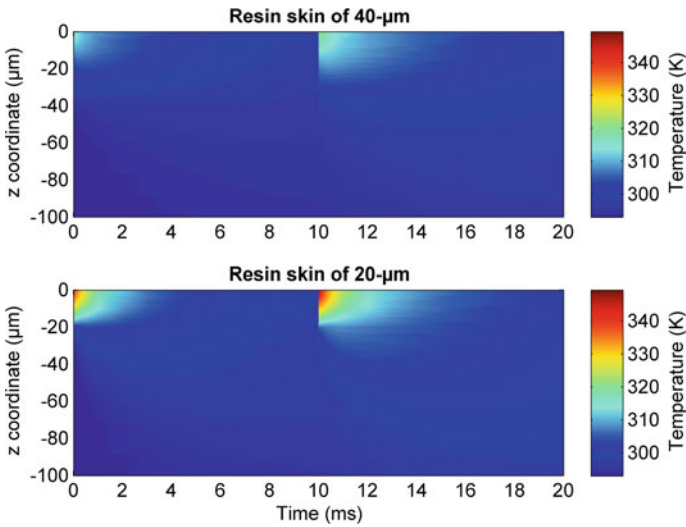


Fig. 8 Comparison of depth temperature ($x = 5$ mm, $y = 4$ mm, $z \in [0, -100 \mu\text{m}]$) for two resin thicknesses. Pulse rate: 100 Hz

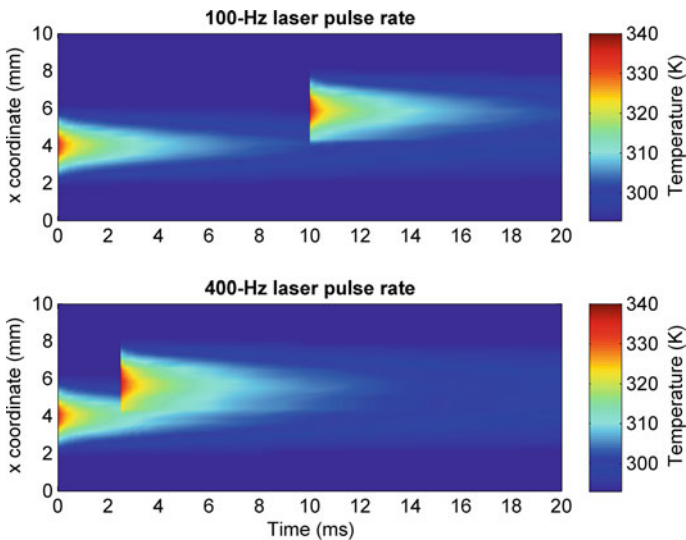


Fig. 9 Comparison of surface temperature for two laser pulse rates. Resin skin thickness of $40 \mu\text{m}$

For the second point, it is interesting to study the influence of the laser repetition rate that is directly linked to the scanning speed which will increase in the future. Here again, there is a temperature increase when the laser repetition rate increases from 100 to 400 Hz. However, the temperature variation is much less

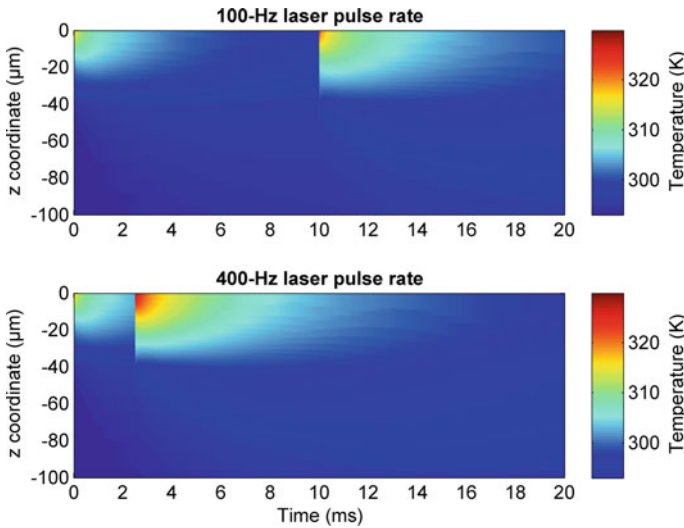


Fig. 10 Comparison of depth temperature ($x = 5$ mm, $y = 4$ mm, $z \in [0, -100 \mu\text{m}]$) for two laser pulse rates. Resin skin thickness of $40 \mu\text{m}$

important: around 6 K for a $40 \mu\text{m}$ resin skin (see Figs. 9, 10) and 8.8 K for a $20 \mu\text{m}$ resin skin.

Figure 10 shows that the heated area grows in depth and in time when the laser pulse rate increases.

4 Conclusion

In order to improve and study the non destructive evaluation of a CFRP composite, a numerical 3D transient state simulation of the propagation of a volumic heat flux generated by a spatially and temporally Gaussian laser pulse in resin skin was performed for the three dimensional temperature evaluation of a composite sample using the FEM Elmer software.

The plotted temperature profiles showed that the affected heat area is localized and the resin skin thickness influences directly the temperature results and thus affects the generated ultrasound wave. We have also studied the influence of increasing the laser repetition rate on the temperature generated in the composite. We can now say that when increasing the laser repetition rate, the temperature also increases but the temperature elevation is much less than the one obtained when the resin thickness decreases.

In order to validate our numerical model, future works will consist on the comparison of the surface temperature measurements with an infrared camera and the numerical applications in time and space of our model.

Acknowledgments This research is realized within the framework of the collaborative TSCNG project supported by the French FCE/DGE.

References

1. Scruby, C.B., Drain, L.E.: *Laser Ultrasonics: Techniques and Applications*. Taylor & Francis Group, New York (1990)
2. Zhang, L.: Development of microelectronics solder joint inspection system: modal analysis, finite element modelling and ultrasound signal processing. In partial fulfilment of the requirements for the degree Doctor of Philosophy, Georgia Institute of Technology (2006)
3. Campagne, B., Voillaume, H.: Development of laser ultrasonics: application to complex shape aeronautical parts. In: 1st International Symposium on Laser Ultrasonics: Science, Technology and Applications, Montreal, Canada (2008)
4. Råback, P.: Elmer—an open source finite element software for multiphysical problems. Elmer basic course, CSC, Espoo (2008)
5. Wang, J., Shen, Z., Xu, B., Ni, X., Guan, J., Lu, J.: Numerical simulation of laser-generated ultrasound in non-metallic material by finite element method. *Opt. Laser Technol.* **39**, 806–813 (2007)
6. Sanderson, T., Ume, C., Jarzynski, J.: Laser generated ultrasound: a thermoelastic analysis of the source. *Ultrasonics* **35**(2), 115–124 (1997)
7. Bennett, T., Kakuda, T., Kulkarni, A.: Front surface thermal property measurements of air plasma spray coatings. *J. Appl. Phys.* **105**, 083501 (2009). doi:[10.1063/1.3088897](https://doi.org/10.1063/1.3088897)
8. Dubois, M., Lorraine, P.W., Venchiarutti, B., Bauco, A.S., Filkins, R.J., Drake, T.E., Yawn, K.R.: (2000) Optimisation of temporal profile and optical penetration depth for laser-generation of ultrasound in polymer-matrix composites. In: Review of Progress in Quantitative Nondestructive Evaluation, AIP Conference Proceedings doi:[10.1063/1.1306063](https://doi.org/10.1063/1.1306063)
9. Balvers, J.M., Bersee, H.E.N., Beukers, A., Jansen, K.M.B: Determination of cure dependent properties for curing simulation of thick-walled composites. In: Proceedings of 49th AIAA Structures, Structural Dynamics, and Materials Conference, Schaumburg, IL, USA (2008)
10. Geuzaine, Ch., Remacle, J.F.: Gmsh: A 3-D finite element mesh generator with built-in pre- and post-processing facilities. *Int. J. Numer. Meth. Eng.* **79**(11), 1309–1331 (2009). doi:[10.1002/nme.2579](https://doi.org/10.1002/nme.2579)
11. Bounaim, A.: Méthodes de décomposition de domaine : Application à la résolution de problèmes de contrôle optimal. Annexe A, thèse de doctorat, Université Joseph Fourier - Grenoble I (1999)

Macroscopic Behavior and Damage of a Particulate Composite with a Crosslinked Polymer Matrix

Luboš Náhlík, Bohuslav Máša and Pavel Hutař

Abstract Particulate composites with crosslinked polymer matrix and solid fillers are one of the important classes of materials which are commonly applied as construction materials, high-performance engineering materials, sealants, protective organic coatings, dental materials, or solid explosives. This contribution is focused on the estimation of the macroscopic mechanical properties of particulate composites with a crosslinked polymer matrix. Extended numerical calculations on the base of the finite element method were performed to estimate stress–strain curves of polymer matrix composite. The numerical determination of the effective properties of particulate composites involved the calculation of the stress and strain fields for a representative volume element (RVE) that simulates the microstructure of the composite. Unit cells containing particles were used to determine the corresponding macro strength. Numerical simulations took into account the nonlinear material properties of the crosslinked polymer matrix. A simple damage model was used to simulate the matrix failure. The mechanical properties obtained from the computations are compared with experimental data and very good agreement has been found. The methodology presented can be used for estimation of mechanical properties of particulate composite with a crosslinked polymer matrix.

Keywords Polymer matrix composite • Particulate composite • Hyperelastic behaviour • Damage model • Finite element modelling

L. Náhlík (✉) · P. Hutař
CEITEC IPM, Institute of Physics of Materials, Academy of Sciences of the Czech Republic, Žižkova 22, 61662, Brno, Czech Republic
e-mail: nahlik@ipm.cz

B. Máša
Mechanical Engineering BUT, Institute of Solid Mechanics, Mechatronics and Biomechanics, Technická 2, 616 69, Brno, Czech Republic

1 Introduction

The aim of our long-term research is to find and understand the link between crosslinked matrix structures and composite properties in both the glassy and the rubbery states through modelling and verification by experiment. As a model system, crosslinked PMMA (polymethyl methacrylate) composites containing a spherical mineral filler was selected. In their application state these composites are typically glassy materials.

The paper is focused on prediction of behaviour of mentioned particulate composite with matrix in rubbery state. Results from presented study can generally contribute to a better understanding of damage mechanism of particulate composite with hyperelastic matrix subjected to tensile loading. Specifically knowledge of modeling of mechanical behaviour of such kind of composite can be used as a initial point for determination of crosslink density (elastically active network chains influenced by presence of filler particles) on macroscopic behaviour of the composite in following research.

Finite element method (FEM) was found as a suitable tool for modelling of macroscopic behaviour of studied kind of composite. Several approaches of finite element modeling of the macroscopic behavior of particular composite can be found in literature. When 2D models do not provide satisfactory results, see e.g. [1–5], 3D finite element models should be used. For an estimation of the macroscopic behavior of a particulate composite, a 3D FE model based on periodically repeated unit cells has been successfully used in many cases, see e.g. [4, 6–10]. From a macroscopic point of view, the shape of particles or clustering of particles plays an insignificant role in comparison to the influence of volume fractions of constituents [11].

2 Material Properties

The material behavior of a crosslinked PMMA matrix was determined experimentally by a standard tensile test under temperature of 180 °C. High temperature during experiments was used due to determination of crosslink density influenced by particles of filler on macroscopic behaviour of the composite (it isn't aim of presented study). This requires matrix to be in rubbery state. For experimental measurements a typical dog bone specimen was used. The material of the matrix at 180 °C was in a rubbery state. The stress–strain curve obtained by the experiment can be seen in Fig. 1. The elastic response of rubber-like materials is often described by the Mooney-Rivlin material model (e.g. [12]). On the base of experimental measurements, the hyperelastic three parameter Mooney-Rivlin material model was chosen. The strain energy density function W was considered in the form [13]:

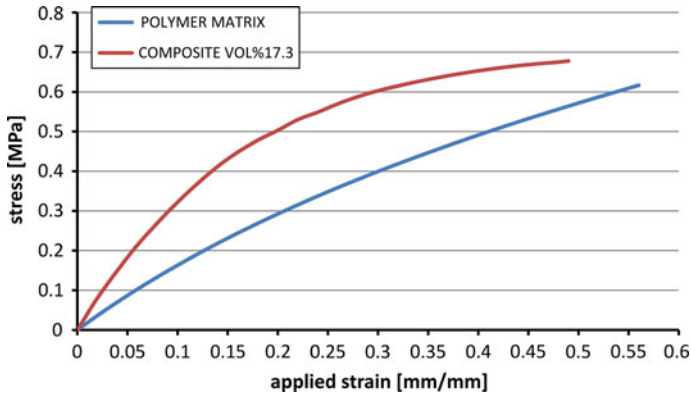


Fig. 1 Stress-strain curves of polymer matrix and particulate composite with 17.3 vol % of particles

$$W = C_{10}(\bar{I}_1 - 3) + C_{01}(\bar{I}_2 - 3) + C_{11}(\bar{I}_1 - 3)(\bar{I}_2 - 3) + \frac{1}{d}(J - 1)^2 \quad (1)$$

where \bar{I}_1 is the first deviatoric strain invariant:

$$\bar{I}_1 = J^{-2/3}I_1; \quad (I_1 = \lambda_1^2 + \lambda_2^2 + \lambda_3^2), \quad (2)$$

\bar{I}_2 , is the second deviatoric strain invariant:

$$\bar{I}_2 = J^{-4/3}I_2; \quad (I_2 = \lambda_1^2\lambda_2^2 + \lambda_2^2\lambda_3^2 + \lambda_3^2\lambda_1^2), \quad (3)$$

$\lambda_1, \lambda_2, \lambda_3$, are principal stretches, J is the determinant of the deformation gradient, C_{10}, C_{01} and C_{11} are material constants and d is the parameter of incompressibility of the material. The relationship between strains and stretches is as follows: $\varepsilon_i = \lambda_i - 1$, where $i = 1, 2, 3$.

A perfectly incompressible material (Poisson's ratio $\nu = 0.5$) is for numerical calculations unacceptable (it makes the bulk modulus infinite). The initial bulk modulus is defined as:

$$K = \frac{2}{d} \quad (4)$$

where:

$$d = \frac{1 - 2\nu}{C_{10} + C_{01}} \quad (5)$$

Due to that the value of Poisson's ratio of the matrix $\nu_m = 0.4995$ was used. The material constants of the crosslinked polymer matrix were from experimental curves identified as: $C_{10} = 0.18560$ MPa, $C_{01} = 0.12356$ MPa, $C_{11} = 0.00351$ MPa and parameter $d = 0.00500$ MPa⁻¹. Thus, the stress-strain curve of material

model of the polymer matrix is identical as a stress–strain curve obtained from experiment (Fig. 1). The maximal value of macroscopic strain at break of the matrix material was experimentally determined as $\varepsilon_{max} = 0.55$.

Alumina particles with almost spherical shape were used as a mineral filler of the particulate composite. The volume fraction of particles was chosen 17.3 % (30 weight %). A typical size of the particle was approximately 10 μm . The elastic particle properties were estimated as follows: Young’s modulus $E_p = 380$ GPa and Poisson’s ratio $\nu_p = 0.23$. The stress–strain behavior (Fig. 1) of the composite was measured to the failure with a failure strain of $\varepsilon = 0.48$.

3 Numerical Model

Three different basic types of regular particle arrangements inspired by atomic arrangement in crystal lattices were used in the numerical models: simple cubic (SC), body-centered cubic (BCC) and face-centered cubic (FCC). Three additional arrangements were considered in the numerical calculations to take into account the non-perfect particle shape or differences in particle sizes: simple cubic arrangement with ellipsoidal particles horizontally oriented (SC-HOR), simple cubic arrangement with ellipsoidal particles vertically oriented (SC-VER) and body-centered cubic arrangement with two sizes of particles: 2 and 10 μm (BCC-VAR) (Fig. 2).

The regular distributions of particles in the matrix were modeled using representative volume element (RVE) approach. The assumption of regular distribution of particles in the matrix is close to reality, because no clustering of particles was observed in the composite by studying fracture surfaces by scanning electron microscope. The size of particles varied in the composite just a little, the particle size ranged approximately from 3 to 10 μm . On the base of experimental observation, particles were considered to be of spherical shape (with exception of SC-HOR and SC-VER models). Due to symmetry of unit cells, only 1/8 of the unit cell needed to be modeled. Also, because of computing time reduction the particle was not modeled, but its influence was prescribed by boundary conditions. For finite element calculations the commercial software ANSYS was used. 3D 10-node tetrahedral elements with four integration points (SOLID 187) were used in the FE simulations and the number of elements in models exceeded 100,000. Example of mesh for SC RVE is shown in Fig. 3. A computer cluster with 8 \times 3.2 GHz processors and 24 GB RAM was used for numerical calculations.

3.1 Boundary Conditions

The boundary conditions of the models used in numerical simulations correspond to composite microstructure with regular distribution of particles. This assumption isn’t far from real microstructure of composite studied. The boundary conditions

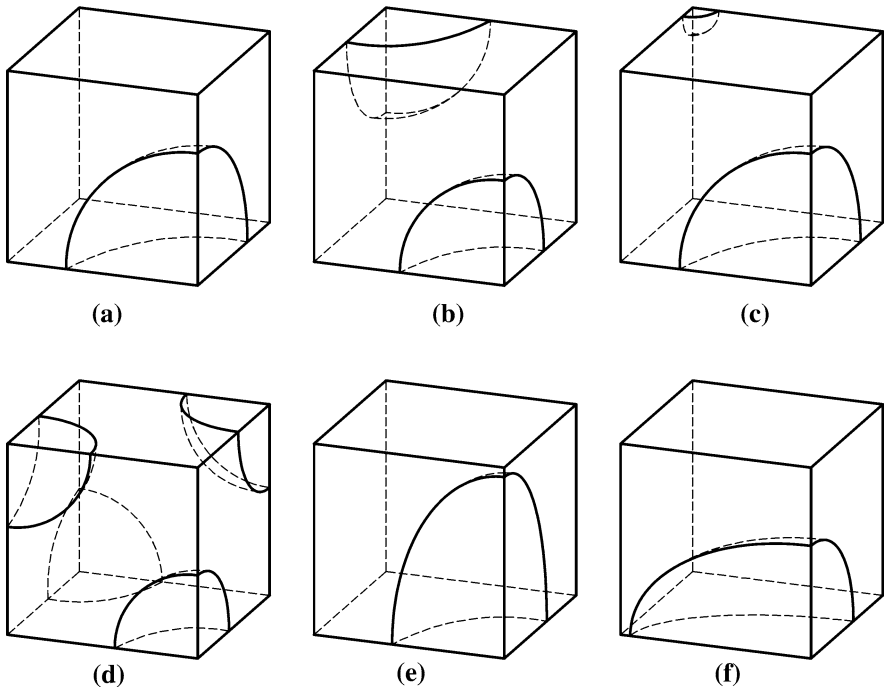


Fig. 2 Geometrical models of considered RVE: **a** simple cubic (SC), **b** body-centered cubic (BCC), **c** body-centered cubic with different size of particles (BCC-VAR), **d** face-centered cubic (FCC), **e** simple cubic with ellipsoidal particles in vertical orientation (SC-VER), and **f** simple cubic with ellipsoidal particles in horizontal orientation (SC-HOR)

Fig. 3 Mesh used for numerical solution of SC arrangement

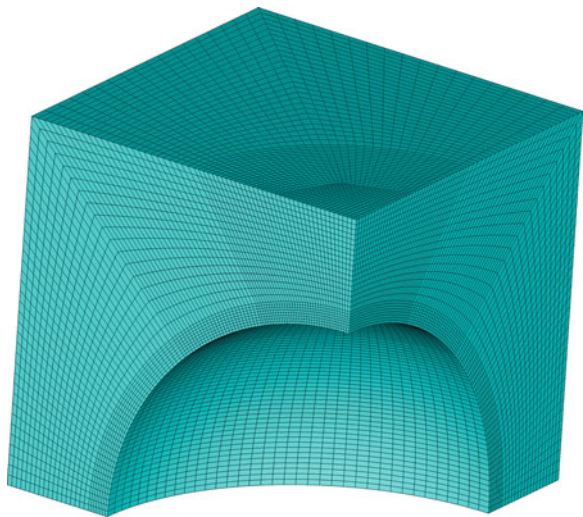
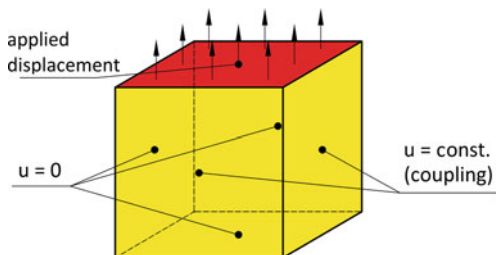


Fig. 4 Applied boundary conditions on faces of the unit cell (RVE)



of all numerical models considered were as follows: (1) normal displacements were fixed on three perpendicular faces of the cubic geometry of the model, (2) two faces were constrained to remain parallel after loading, (3) displacement normal to the cube face was applied to the top face. Ideal adhesion between particle and matrix was presumed. The applied boundary conditions are shown in Fig. 4. The maximal applied displacement in the calculations corresponded to a macroscopic strain of $\varepsilon_{\text{appl}} = 0.45$, i.e. close to the value failure strain of the composite.

3.2 Determination of Macroscopic Stress and Strain

The models were loaded by displacements, thus the macroscopic applied (engineering) strain was $\varepsilon_{\text{appl}} = u_{\text{appl}}/h$, where h was the height of the model (in all cases $h = 1$). The engineering stress was determined as a sum of particular reactions of finite elements from the top face of the model divided by the area of the top face. For common comparison, the experimental stress–strain data were expressed as engineering stresses and strains as well.

Numerical calculations were performed for all above mentioned models and the results are shown in Fig. 5. The differences in macroscopic stress–strain behavior among individual numerical models (particle arrangements) is evident as well as an overestimation of calculated stress values for higher applied strains. A good description of the stress–strain behavior of the composite is provided by the SC model and BCC-VAR model with different sizes of particles, both up to approximately $\varepsilon_{\text{appl}} = 0.2$. On the basis of the obtained numerical results, local stresses and strains were investigated in detail. The analysis showed that the maximal strain value for the matrix, ε_{max} , was exceeded in the location of stress concentration in the matrix, shown in Fig. 6a (red area). It means that in this place a microcrack can be developed in the matrix. For the subsequent analyses which was focused on matrix damage, only the SC model geometry was considered.

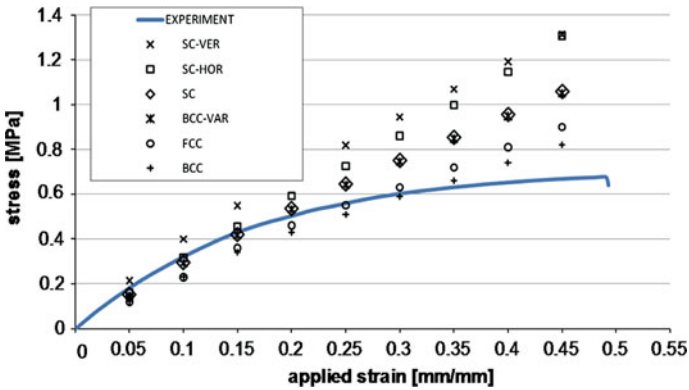


Fig. 5 Comparison of experimental data (smooth curve) and numerical results obtained by different kinds of particle arrangements in RVE: body-centered cubic (BCC), face-centered cubic (FCC), body-centered cubic with different size of particles (BCC-VAR), simple cubic (SC), simple cubic with ellipsoidal particles in horizontal orientation (SC-HOR) and simple cubic with ellipsoidal particles in vertical orientation (SC-VER)

4 Numerical Model Considering Damage of Polymer Matrix

Next, calculations were focused on the modeling of matrix damage in the case of a macroscopic applied strain higher than 0.185. Sophisticated methods for modeling of developing defects like “death and birth” elements or using contact elements (TARGET and CONTACT) did not lead to success (calculations did not converged) due to step changes in stiffness of the numerical models. Thus, “manual” approach of defect creating was used. For a given strain (higher than 0.185) the defect (crack) was modeled, see Fig. 6b. For the given macroscopic applied strain level (higher than 0.185) the right size of the defect was found by iterating. The crucial condition for defect modelling was that the strain in the matrix cannot exceed failure strain ($\epsilon_{max} = 0.55$).

The mentioned approach could be used to $\epsilon_{appl} = 0.26$, when numerical results showed that the decohesion between particle and matrix should initiate. The numerical results showed that a small decohesion at the matrix/particle interface leads to a rapid decohesion around the particle.

The maximal value of the macroscopic stress (strength of composite) was obtained at the last step before loss of cohesion between particle and matrix (particle and matrix were connected only on small area on the top of particle at that moment, see Fig. 6d). The maximal stress for the considered composite was 0.67 MPa. The state determining the matrix failure (and entire composite as well) is represented by the moment of full particle decohesion when the matrix breaks among particles perpendicularly to applied remote and microscopic cracks connect together, which leads to the macroscopic break of composite. The full decohesion of particle

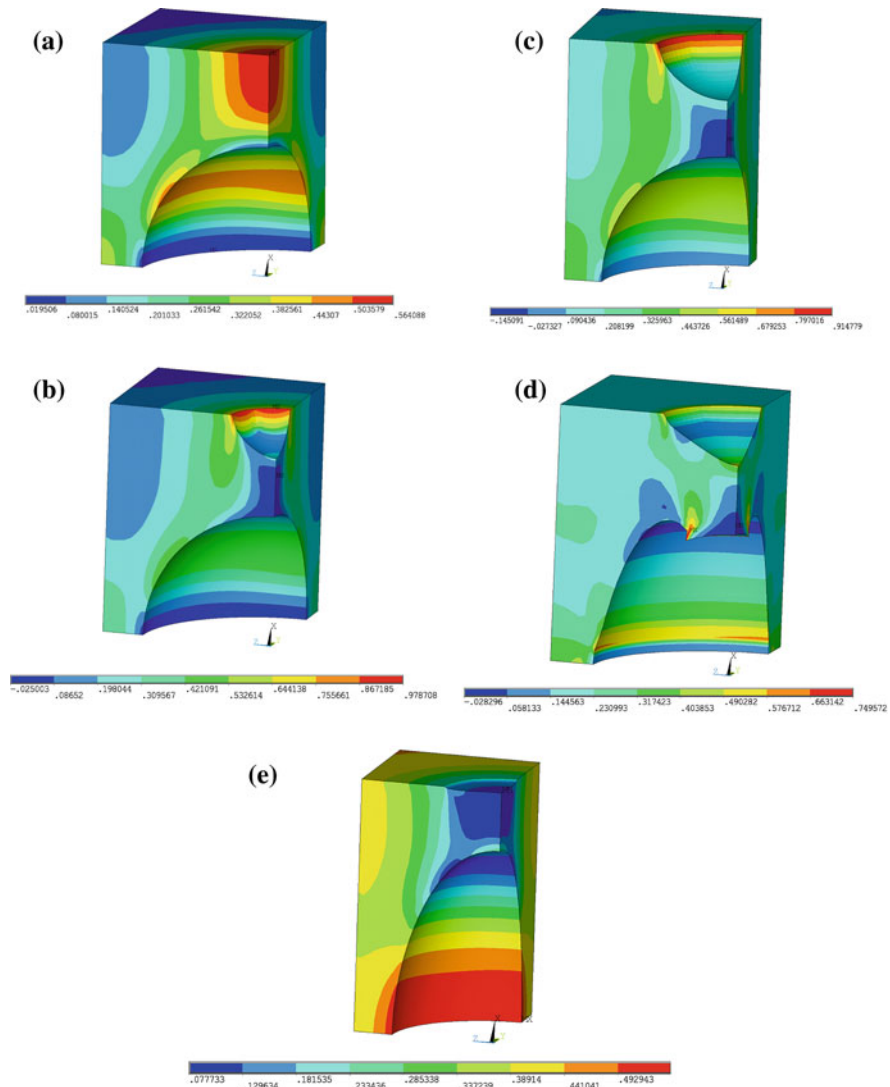


Fig. 6 Results of numerical calculations considering damage of polymer matrix **a** matrix without any damage; **b** defect in matrix ($\epsilon_{\text{appl}} = 0.19$); **c** defect in matrix ($\epsilon_{\text{appl}} = 0.26$); **d** limit state before loss of cohesion between matrix and particle; **e** full decohesion of particle leading to failure of the matrix and subsequently to failure of all composite

occurred for $\epsilon_{\text{appl}} = 0.49$ (Fig. 6e). The last point of the graph shown in Fig. 7 represents the moment before loss of cohesion. Figure 7 shows the comparison between numerically calculated and experimentally measured data. A good agreement can be found.

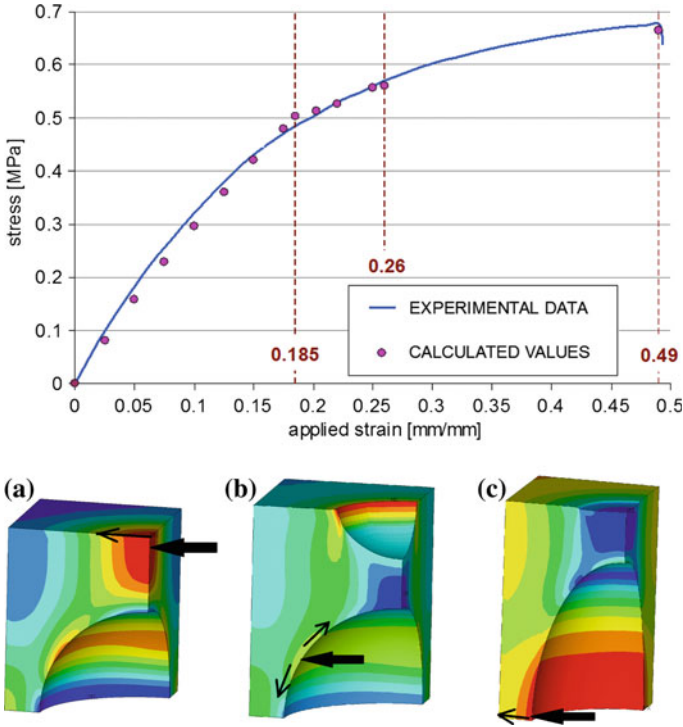


Fig. 7 Comparison of measured and calculated data and different stages of composite damage. *Dashed lines* represent damage levels of the composite: **a** 0/0.185 of macroscopic applied strain ϵ_{appl} : matrix without damage, high stress concentration in the location marked by the *bold arrow*; **b** $\epsilon_{\text{appl}} = 0.185/0.26$: microcracking of the matrix initiates in the narrow location between particles; **c** $\epsilon_{\text{appl}} = 0.26/0.49$: decohesion of the particles starts in the place marked by the *bold arrow* and goes around the particle; final failure of composite occurred at $\epsilon_{\text{appl}} = 0.49$

5 Discussion

The damage mechanism of particulate composite studied was predicted on the base of numerical modelling. The mechanism can be described as follows: high strains in the matrix cause microcracking in narrow places between particles in the material of matrix for local strain levels above 40 % of maximal macroscopic applied strain. The growth of matrix defects stops above 53 % of the maximal macroscopic applied load due to relaxation of stresses. Then the decohesion between matrix and particle occurs. Loss of cohesion between particle surfaces and matrix leads to the rapid failure of the composite.

The used numerical approach is general and can be applied with success to other kinds of particulate composites. The approach can be used for estimation of the composite behavior under static tensile loading at room temperature as well. From a practical point of view, the procedure suggested can be used for estimation

of the macroscopic stress–strain behavior of particulate composites and for safer operation of composite structures. The knowledge of damage mechanism can also be important for fatigue life of the composite. On the base of numerical calculations the limits for safe repeated operation of composite structures can be found. The results obtained contribute to a better understanding of damage of composite structures made from particulate composite with spherical particles.

6 Conclusion

Numerical models of particulate composites with a crosslinked polymer matrix were developed to simulate the macroscopic behavior of the particulate composite. Several particle arrangements in unit cells (inspired by atomic arrangements in crystal lattices) were considered and the best agreement between experimental data and calculated resultant curve was found for the simple cubic particle arrangement at lower level of macroscopic applied strain. The stress–strain behavior of the studied composite can be described in following three parts:

1. Loading of the particulate composite without any damage of matrix for macroscopic applied strain from 0 to approx. 40 % (to $\varepsilon_{\text{appl}} = 0.185$).
2. The behavior of the real composite differs from the calculated one for higher levels of applied strain. A place was found in the polymer matrix, where the calculated value of strain exceeded the maximal experimentally obtained value ε_{max} , and the damage of matrix was modeled in this place as a circular defect growing with increase of macroscopic applied load. This procedure was applied between 40 and 53 % of the maximal macroscopic applied strain ($\varepsilon_{\text{appl}} = 0.185/0.26$).
3. The conditions for decohesion between particle and polymer matrix was identified in the numerical model for macroscopic strains higher than 53 % of maximal one and the decohesion was numerically modeled as a discontinuity between particle and matrix.

Acknowledgments This contribution was supported through the Grants Nos. 106/08/1409 and 106/09/H035 of the Czech Science Foundation and through the Specific academic research grant of the Ministry of Education, Youth and Sports of the Czech Republic No. FSI-S-11-11/1190 provided to Brno University of Technology, Faculty of Mechanical Engineering. The work has been carried out at the Central European Institute of Technology (CEITEC) with research infrastructure supported by the project CZ.1.05/1.1.00/02.0068 financed from the European Structural Funds.

References

1. Iung, T., Grange, M.: Mechanical behaviour of two-phase materials investigated by the finite element method: necessity of three-dimensional modeling. *Mater. Sci. Eng.* **A201**, L8–L11 (1995)
2. Gänser, H.P., Fischer, F.D., Werner, E.A.: Large strain behavior of two-phase materials with random inclusions. *Comput. Mater. Sci.* **11**(3), 221–226 (1998)
3. Chawla, N., Sidhu, R.S., Ganesh, V.V.: Three-dimensional visualization and microstructure-based modeling of deformation in particle-reinforced composites. *Acta Mater.* **54**(6), 1541–1548 (2006)
4. Marur, P.R.: Estimation of effective elastic properties and interface stress concentrations in particulate composites by unit cell methods. *Acta Mater.* **52**(5), 1263–1270 (2004)
5. Han, W., Eckschlanger, A., Böhm, H.J.: The effects of three-dimensional multi-particle arrangements on the mechanical behavior and damage initiation of particle-reinforced MMCs. *Compos. Sci. Technol.* **61**(11), 1581–1590 (2001)
6. Wang, X., Xiao, K., Ye, L., Mai, Y.W., Wang, C.H., Rose, L.R.F.: Modelling mechanical properties of core-shell rubber-modified epoxies. *Acta Mater.* **48**(2), 579–586 (2000)
7. Zeng, X., Fan, H., Zhang, J.: Prediction of the effects of particle and matrix morphologies on Al₂O₃ particle/polymer composites by finite element method. *Computational Mater. Sci.* **40**(3), 395–399 (2007)
8. Cho, J., Joshi, M.S., Sun, C.T.: Effect of inclusion size on mechanical properties of polymeric composites with micro and nano particles. *Compos. Sci. Technol.* **66**(13), 1941–1952 (2006)
9. Hutař, P., Majer, Z., Náhlík, L., Šestáková, L., Knésl, Z.: Influence of particle size on the fracture toughness of a PP-based particulate composite. *Mech. Compos. Mater.* **45**(3), 281–286 (2009)
10. Hutař, P., Náhlík, L., Majer, Z., Knésl, Z.: The effect of an interphase on micro-crack behaviour in polymer composites. *Computational methods in applied sciences*, 1, volume 24. *Comput. Model. Adv. Simul.* **24**, 83–97 (2011)
11. Segurado, J., González, C., Llorca, J.: A numerical investigation of the effect of particle clustering on the mechanical properties of composites. *Acta Mater.* **51**(8), 2355–2369 (2003)
12. Treloar, L.R.G.: *The physics of rubber elasticity*, 3rd edn. Oxford University Press, Oxford (2005)
13. Ansys Release 12.1 Documentation.: ANSYS, Inc., USA, (2009)

Computational Simulations on Through-Drying of Yarn Packages with Superheated Steam

Ralph W. L. Ip and Elvis I. C. Wan

Abstract Industries need different types of drying technologies for their processes. The most traditional and commonly used one is to employ hot air as the drying medium. However, recent research has proved that superheated steam has higher drying capacity than hot air, because the specific heat capacity and heat conductivity of steam are higher than air. In addition, it has been found that using steam as drying medium can prevent surface hardening. Therefore, steam drying can preserve the quality of products better. This is especially important to heat-sensitive materials, like fruits and textiles. There are lots of research studies on drying process design using superheated steam, however, most of the studies were based on the jet impingement approach. In this research, an alternative approach of using steam for yarn package drying is studied. Superheated steam is generated from saturated steam and passes through the wetted yarn packages by establishing a pressure gradient between the up and down stream of the process. Computational fluid dynamics (CFD) analysis has been carried out using ANSYS 13 to model the heat and mass transfer process for the entire drying cycle, and to determine analytical solutions to quantify the residual water in the packages against cycle time. An industrial grade dryer prototype has been built to support experimental tests. Experimental results have been empirically used to assist the assignment of viscous resistance factor for CFD simulation studies. In the simulation process, the yarn packages have been assumed to be porous homogeneous. The drying rate under different pressures gradients between the up and down stream has been observed. The ultimate goals from the CFD results are to explore mathematical

R. W. L. Ip (✉) · E. I. C. Wan
Department of Mechanical Engineering, The University of Hong Kong,
Pokfulam, Hong Kong
e-mail: ralhip@hku.hk

E. I. C. Wan
e-mail: elvisgp@hku.hk

relationships in the drying process and predict the fastest drying rate with minimum amount of steam used.

Keywords Drying process • Superheated steam • Yarn packages • Viscous resistance • CFD

1 Introduction

In recent years, many industrial processes have switched to steam drying base instead of using hot air or other drying methods, such as dielectric heating. Food, paper, furniture, timber and construction material manufacturing industries are typical cases [1]. The application of steam for drying has been introduced into the textile industry for some years. The very reason behind this is the higher drying capacity of superheated steam than hot air [2]. Also, drying textile materials with superheated steam can prevent hardening of the fabric surface and give better treatment results. Chen et al. [3] have performed several laboratory-scale tests to show the improvement of the brightness and strength of silk after steam drying. Although the steam drying process has been known in the industry for some times, most applications were just for fabric drying usages [4]. Drying of yarn packages in many dye-houses still relies on the conventional hot air and microwave radiation technologies. However, hot air drying takes longer cycle time while microwave drying has introduced many technical problems yet to be resolved, such as radiation hazard. In this research, trials have been carried out to develop an industrial grade superheated steam drying machine. Experiments have been conducted to evaluate the drying cycle time under different machine control parameters, and properties of the textile materials. Experimental results were collected to form a database for further investigation, and for the building up analytical equations to describe the characteristics of the drying process precisely. In this paper, details about the experiment set-up and the dryer prototype design are given. Results from experiments were employed as references for the construction of heat transfer models in CFD studies. Concluding remarks from CFD studying results were generated to discuss the achievements of this study.

2 Prototype Design and Experiment Set-up

Figure 1 is a schematic drawing of the industrial grade yarn package dryer design, used to build up a prototype for in-house tests. Saturated steam at 550 kPa and 423 K enters the prototype via the steam valve—V4. The steam is reheated in the heat exchanger—E2 after an *isenthalpic expansion* process takes place in the steam valve—V6. The steam flow rate entering the kier, which contains the wetted

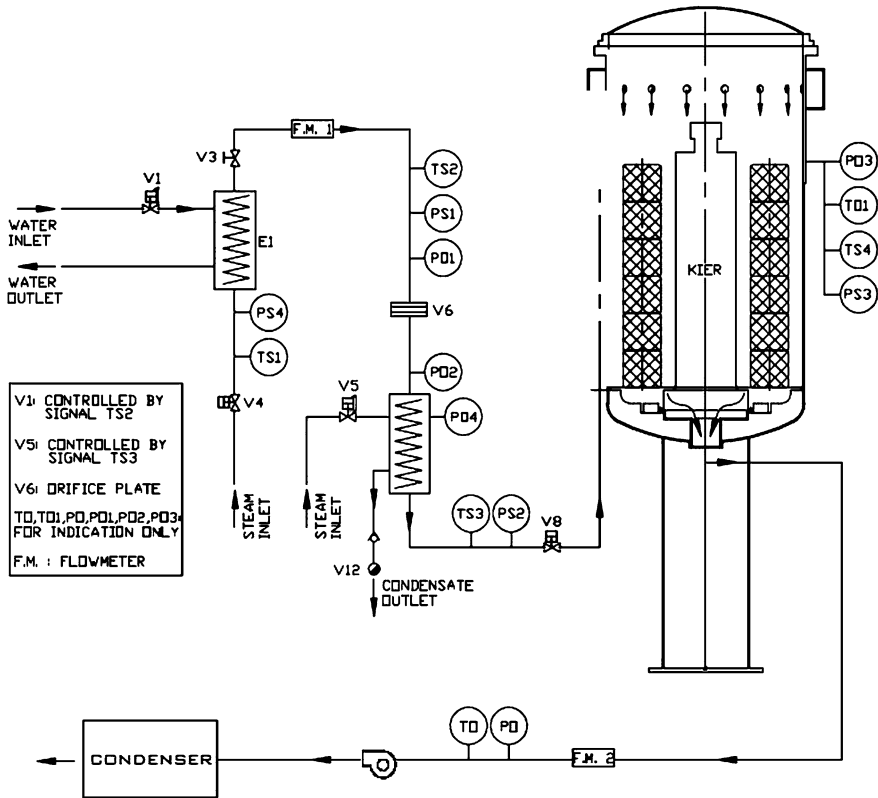


Fig. 1 Schematic sketch of the superheated steam dryer prototype

packages, can be measured from the flow-meter F.M. 1. The kier is a pressure vessel and the design working pressure is 700 kPa. Its capacity is up to 6 columns of yarn packages and 6 for each column. In the drying process, the generated superheated steam is injected into the kier. It penetrates through the yarn packages by a pressure gradient between the outer and inner surfaces. Welty [5] has stated two drying phases would occur through the entire process. One is due to thermal *conductive evaporation* and the other one is due to *diffusion*. Drying by thermal conductive evaporation takes place prior to diffusion. No matter the water in the yarn packages is dried up by conductive evaporation or diffusion, the vaporized water is forced to move into the package centre core and driven by the downstream flow current as illustrated in Fig. 2. The package columns are connected to a common steam extraction pipeline, and a steam extractor is installed at the pipe end to assist the creation of a larger pressure gradient between the outer and inner surfaces of each yarn package. Resistances of the flow of water and steam inside the yarn packages is determined from the pressure gradient between the kier internal pressure, measured by pressure gauge PO3, and the discharge pressure PO created by the blower.

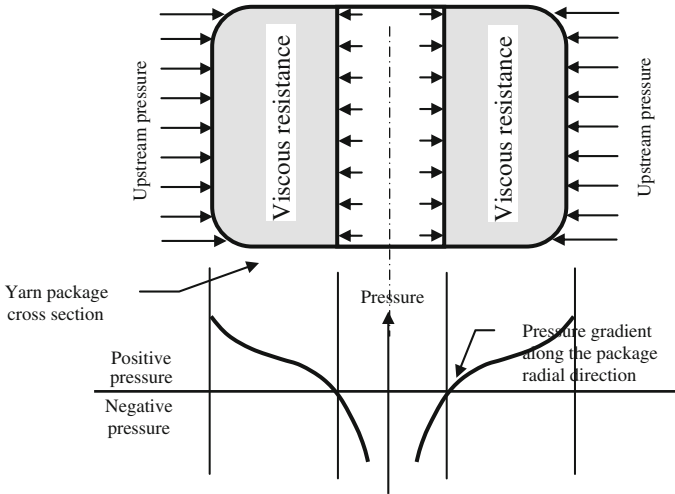


Fig. 2 Analog model of pressure gradient and viscous resistance in a yarn package for the drying process

3 Analyses of Experimental Data

In the experimental tests, 36 yarn packages were dried at various temperature and pressure gradient. The water residual weight from the packages was measured at fixed time intervals. The water reduction rate at cycle times of 0.01, 0.05, 0.1, 0.5, 1 and 5 min were measured by drawing tangential lines on the acquired drying curves. The results were further used to calculate the mean flow rate of water in the yarn packages at the conductive evaporation drying period. The pressure gradient and mean velocity of steam flow across porous materials can be obtained by the following equation:

$$P = \left(\frac{1}{2}C\rho\Delta n\right)v^2 + \left(\frac{1}{\alpha}\mu\Delta n\right)v \quad (1)$$

where P is the pressure gradient, C is the inertia resistance factor of the yarn package, $1/\alpha$ is the viscous resistance of water, ρ is the water density, μ is the water viscosity, Δn is the mean thickness of porous material, and v is the mean flow velocity of water across the porous material. C in Eq. (1) can be neglected for fibrous materials, thus Eq. (1) can be rewritten as:

$$P = \left(\frac{1}{\alpha}\mu\Delta n\right)v \quad (2)$$

In Eq. (2), the pressure gradient (P) is directly proportional to the mean flow velocity of water across the yarn packages (v). A plot of P versus v , as shown in

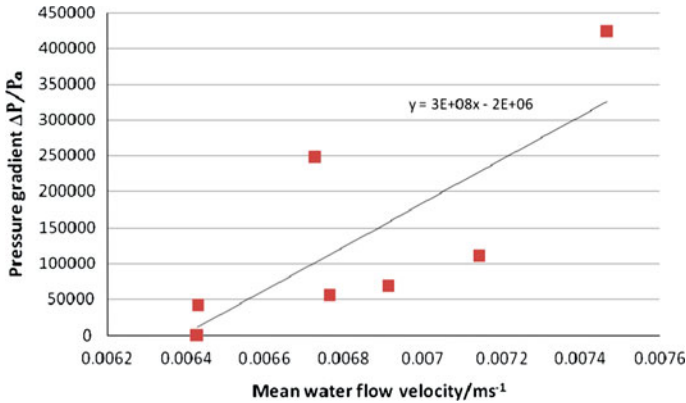


Fig. 3 Pressure gradient (P) versus mean flow velocity of water (v) passing through yarn package at a cycle time of 0.01 min

Fig. 3, can be used to estimate the viscous resistance ($1/\alpha$) at a particular cycle time. It is known that the slope of the curve in Fig. 3 is the viscous resistance.

Other curves were obtained from other cycle time (t) at 3, 6, 30, 60 and 300 s. The viscous resistance was then plotted against cycle time and is illustrated in Fig. 4. The viscous resistance of steam ($1/\beta$) across yarn package can be found in similar way and the mean flow velocity of steam is the difference between readings from flow meters F.M.1 and F.M.2.

4 Analysis of Yarn Packages Drying Using Computational Fluid Dynamics Tools

Figure 5 shows the modeled yarn package finite element meshes created from ANSYS 13. The nominal dimensions of the modeled package are 200, 50 and 200 mm for the outer diameter, inner diameter and height respectively. A total of 1.2 million rectangular finite elements have been used to create the mesh model. A pressure gradient at the outer surface of 200 kPa (absolute) and 402 K, and 100 kPa at the inner surface was set as the initial boundary conditions. The porosity factor of the yarn package was set to be 0.325. The coupling between water vaporization and steam condensation in the drying process was accounted as an *evaporation/condensation* mechanism.

Two modeling cases using ANSYS 13 to study characteristics of drying were performed from the experimental results listed in Figs. 3 and 4. They are:

1. Constant $1/\alpha$: The viscous resistance of water at the starting point of the cycle time, i.e. $t = 0$ is applied. In this condition, the packages are fully wetted and the determined resistance can be made to be the viscous resistance of purely water.

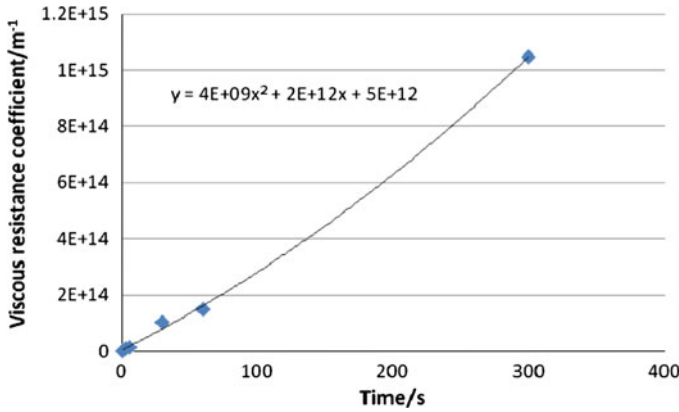
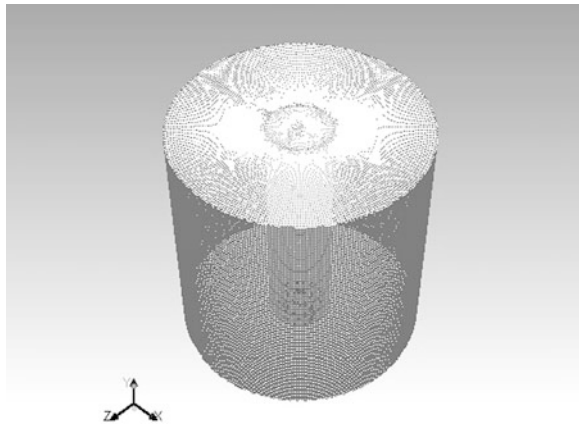


Fig. 4 Relationship of water viscous resistance ($1/\alpha$) with cycle time (t)

Fig. 5 Meshed model of a yarn package created by ANSYS 13



2. Changing $1/\alpha$: The viscous resistance increases with time, as shown in Fig. 4.

Two modeling results from each of the two cases were obtained, and are given in Fig. 6. The used viscous resistance for case 1 was $5 \times 10^{12} \text{ m}^{-2}$, and $4 \times 10^9 t^2 + 2 \times 10^{12} t + 5 \times 10^{12} \text{ m}^{-2}$ for case 2.

5 Discussion

As shown in Fig. 6, the residual water fraction in cubic volume of the yarn packages has linear and nonlinear relationship against cycle time for the conditions of constant and changing viscous resistance respectively. Kowalski [6] has stressed that a normal drying curve for porous materials can be divided into two periods: conductive evaporation (constant drying) and diffusion (falling drying). At the

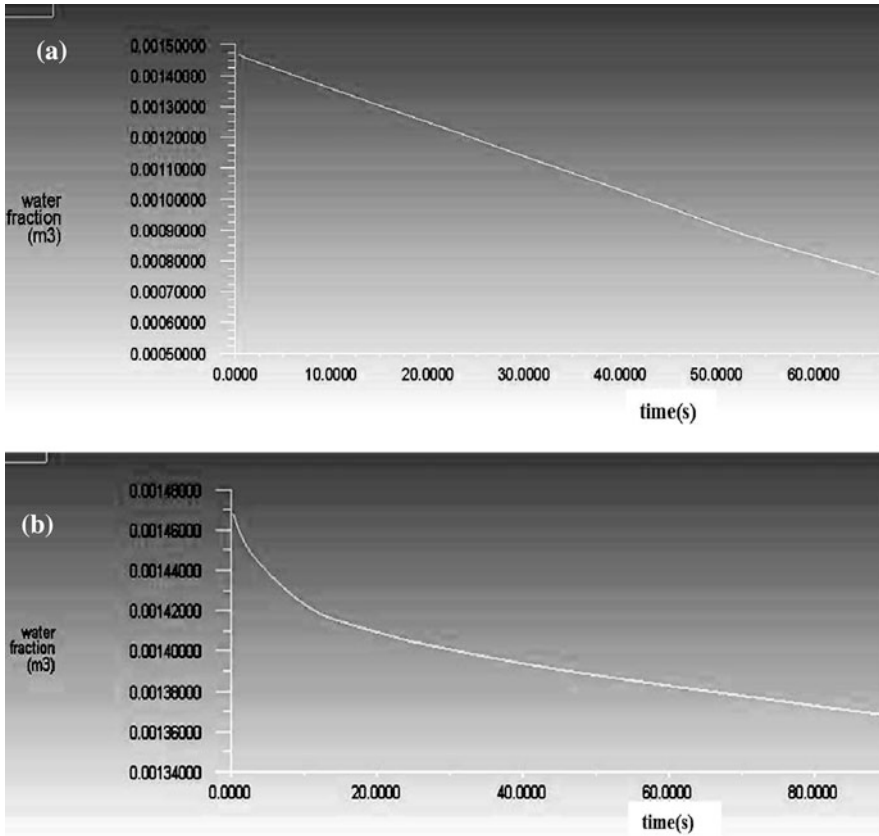


Fig. 6 CFD modeling results for (a) constant and (b) changing viscous resistance

initial state of drying, water trapped in the package surface can be easily vaporized and removed by conductive heat process. While water on the package surface has been removed, the diffusion drying mechanism replaces the conductive evaporation process. The diffusion process usually is slow, which causes a nonlinear drying behavior. Thus, the ANSYS simulation results given in Fig. 6b using a changeable viscous resistance factor could be more accurate to simulate the entire process, and a better and realistic result was obtained in comparison with the finding as given in Fig. 6a.

6 Conclusion

In conclusion, an industrial grade drying prototype was built as a working platform to support the research on the modeling of yarn package drying using superheated steam. From a series of experimental tests, the water viscous resistance in terms of

a constant value and a second order equation with respect to cycle time were separately investigated. They were subsequently employed to determine the water fraction against cycle time for through drying studies. The analysis results from ANSYS have indicated that the modeled results from the changing viscous resistance study case could give more realistic outputs than those results from the constant viscous resistance case. The deduced viscous resistance relationship against cycle time has provided analytical solutions for further modeling of others porous materials used in textile industry.

References

1. Devahastin, S., Suvarnakuta, P., Soponronnarit, S.: A comparative study of low-pressure superheated steam and vacuum drying of a heat-sensitive material. *Drying Technol.* **22**, 1845–1867 (2004)
2. Hagi, A.K.: Transport phenomena in porous media: a review. *Theor. Found Chem. Eng.* **40**, 14–26 (2006)
3. Chen, S.R., Chen, J.Y., Mujumdar, A.S.: Preliminary study of steam drying of silkworm cocoons. *Drying Technol.* **10**, 251–260 (1992)
4. van Deventer, H.C., Heijmans, R.M.H.: Drying with superheated steam. *Drying Technol.* **19**, 2033–2045 (2001)
5. Welty, J.R.: *Fundamentals of Momentum, Heat and Mass Transfer*. Wiley, New York (1976)
6. Kowalski, S.J.: *Thermo mechanics of Drying Processes*. Springer, Germany (2003)

Anisotropic Stiffened Panel Buckling and Bending Analyses Using Rayleigh–Ritz Method

Jose Carrasco-Fernández

Abstract A Rayleigh–Ritz energy method application is proposed to calculate the buckling onset and bending behavior of flat rectangular anisotropic composite stiffened panels submitted to any combination of in-plane loads (biaxial compression and shear) and pressure. Panels may consist in any kind of anisotropic laminate. Thickness, lay-up and material property changes are allowed along both longitudinal and transverse directions and transverse shear effects are considered using a first order theory. Stiffeners, idealized as offset beams, can also be placed in both directions. Simply supported edges are the assumed boundary conditions for the panel. Nevertheless, additional restrictions can be added by means of the definition of certain torsional or flexural stiffness at the edges. Therefore, clamped conditions or any other condition between clamped and simply supported can be analyzed. The consideration of all these features, together with the potentially high computational performances of the Rayleigh–Ritz method compared with the classical finite elements analyses, enables a wide application in real aircraft structures, such as CFRP (composite fiber reinforced plastic) torque box covers and spars with elevated performances and accuracy. Comparisons with finite element methods and tests in real structures are shown.

1 Introduction

Composite materials are extensively used in aerospace structures because of their high specific strength and their ability to be tailored. These structures are often designed as stiffened panels (e.g. torque boxes covers and spars, fuselage panels), where the combination of stiffeners and skin allows further weight optimization.

J. Carrasco-Fernández (✉)
Airbus Operations S.L, Getafe (Madrid), Spain
e-mail: jose.a.carrasco@airbus.com

These panels can be analyzed using finite element models, with very accurate results, but consuming significant computational resources. On the other hand, closed form results offer a faster solution, but at the expense of having a much more limited scope.

The objective of this chapter is to propose an analytical solution able to cover a wide range of anisotropic stiffened panel configurations with the accuracy level of a finite element analysis, but much faster, making possible its extensive use in parametric studies and enabling to plug it in optimization algorithms.

This method is not only able to predict the buckling and bending behavior of the structure but also to show the buckling or bending shape as it is presented at the end of the chapter.

2 Analysis Details

2.1 *Geometry, Boundary Conditions and Loads*

Figure 1 shows an example of the configurations that this method is able to analyze.

This procedure can deal with any flat anisotropic rectangular panel with longitudinal and/or transverse stiffeners submitted to in-plane loads (longitudinal and transverse tension/compression, shear and in-plane bending) and/or constant pressure (Fig. 2).

Panels may have thickness, lay-up and/or material properties changes along both longitudinal (parallel to x -axis) and transverse (parallel to y -axis) directions.

The application of additional torsion and flexural stiffness at the edges allows the use of any boundary condition between simply supported and clamped.

2.2 *Laminate Constitutive Equations*

A first order shear deformation theory is used [1], assuming therefore that the straight lines perpendicular to the middle surface before deformation remain straight after deformation but not necessarily perpendicular. This allows for a rotation due to transverse shear to be added to the usual rotation due to classical plate bending theory.

The transverse shear effects are often neglected in metallic structures or even in thin composite panels. However, these effects become much more relevant in fiber reinforced plastics because the transverse (through-the-thickness) elastic properties are, to a large extent, dependent upon the properties of the matrix material, whose properties can be very low compared with those in the direction of the reinforcing fibers. This effect is significant when the ratio thickness/short edge dimension, sometimes very small, is not so low.

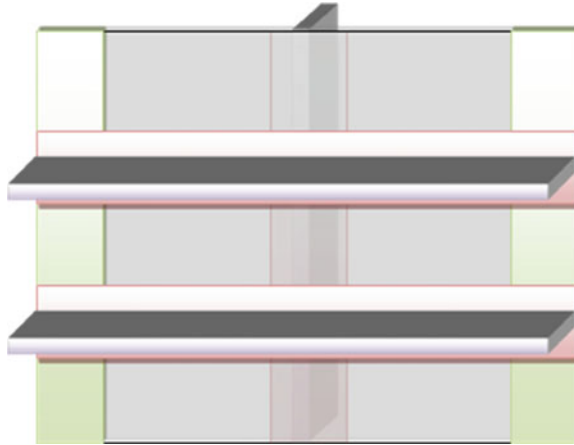


Fig. 1 Example of stiffened panel geometry

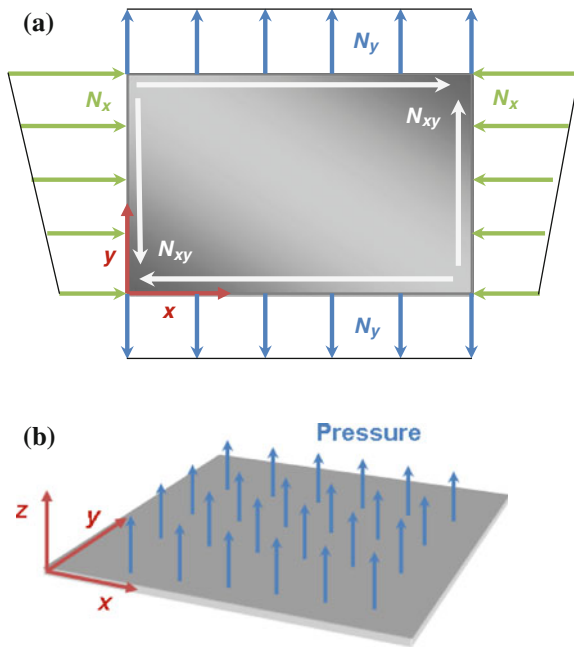


Fig. 2 Loads considered in the analysis: in-plane (a), and out-of-plane (b)

Let u , v and w be the plate displacements along axes of the Cartesian coordinate system, the displacement field can be expressed as:

$$\begin{cases} u(x, y, z) = u^0(x, y) + z \cdot \psi_x(x, y) \\ v(x, y, z) = v^0(x, y) + z \cdot \psi_y(x, y) \\ w(x, y, z) = w^0(x, y) \end{cases} \quad (1)$$

where (u^0, v^0, w^0) denote the displacements of a point in the plane $z = 0$, and ψ_x and ψ_y are respectively the rotations around the y - and x -axes.

The strains are then calculated by derivation of (1), obtaining:

$$\{\varepsilon\} = \begin{Bmatrix} \varepsilon_x \\ \varepsilon_y \\ \gamma_{xy} \\ \gamma_{yz} \\ \gamma_{xz} \end{Bmatrix} = \{\varepsilon^0\} + z \cdot \{\Gamma\} = \begin{Bmatrix} \frac{\partial u^0}{\partial x} \\ \frac{\partial v^0}{\partial y} \\ \frac{\partial u^0}{\partial y} + \frac{\partial v^0}{\partial x} \\ \psi_y + \frac{\partial w}{\partial y} \\ \psi_x + \frac{\partial w}{\partial x} \end{Bmatrix} + z \cdot \begin{Bmatrix} \frac{\partial \psi_x}{\partial x} \\ \frac{\partial \psi_y}{\partial y} \\ \frac{\partial \psi_x}{\partial y} + \frac{\partial \psi_y}{\partial x} \\ 0 \\ 0 \end{Bmatrix} \quad (2)$$

The classical laminate theory (e.g. [2]) may still be applied since it is a first order theory, and the in-plane fluxes $\{N\}$ and moments $\{M\}$ can be obtained as:

$$\begin{Bmatrix} N \\ M \end{Bmatrix} = [K] \begin{Bmatrix} \varepsilon^0 \\ \Gamma \end{Bmatrix} \rightarrow [K] = \begin{bmatrix} [A] & [B] \\ [B] & [D] \end{bmatrix} \quad (3)$$

where $[A]$, $[B]$ and $[D]$ are the laminate stiffness matrices.

Regarding the transverse shear constitutive equations, it can be noted from the expressions obtained in (2) that the transverse shear strains (γ_{xz} and γ_{yz}) are constant throughout the thickness, whereas the stress equilibrium equations predicts them to be quadratic. In order to overcome this inconvenience, two transverse shear correction factors k_1 and k_2 are introduced using the procedure described by Whitney and Pagano [3] for anisotropic laminates.

$$\begin{Bmatrix} Q_y \\ Q_x \end{Bmatrix} = \begin{bmatrix} k_2^2 A_{44} & k_1 k_2 A_{45} \\ k_1 k_2 A_{45} & k_1^2 A_{55} \end{bmatrix} \begin{Bmatrix} \gamma_{yz} \\ \gamma_{xz} \end{Bmatrix} \quad (4)$$

This approach is chosen because it avoids the complexity of other higher order theories, but having a good accuracy level in predicting the effect of the transverse shear strains on the buckling onset as it will be shown in the results presented at the end of this chapter.

2.3 Rayleigh–Ritz Method Application

The Rayleigh–Ritz method is based on the principle of minimum total potential energy.

The displacement field must be expressed as a sum of functions with undetermined coefficients, each of them satisfying the boundary conditions of the structure. For a simply supported rectangular panel, $w = 0$ at the four edges, but the natural boundary conditions (null bending moments at the four edges) are only

fulfilled if the stiffness matrix terms D_{13} and D_{23} are equal to zero. This can be overcome if the number of terms in the sum is large enough.

The total strain energy is composed of the following terms:

- Plate simply supported:

$$\begin{aligned} U_{SS} &= \frac{1}{2} \iiint_V \{\sigma\} \{\varepsilon\}^T dV \\ &= \frac{1}{2} \int_0^a \int_0^b \int_{-t/2}^{t/2} (\sigma_x \varepsilon_x + \sigma_y \varepsilon_y + \tau_{xy} \gamma_{xy} + \tau_{xz} \gamma_{zy} + \tau_{yz} \gamma_{yz}) dx dy dz \end{aligned} \quad (5)$$

- Additional boundary conditions ($y_i = 0, b; x_j = 0, a$):

$$\begin{aligned} U_{BC} &= \frac{1}{2} \int_0^a \left[GJ_i \left(\frac{\partial \psi_y}{\partial x} \Big|_{y=y_i} \right)^2 + RK_i (\psi_y|_{y=y_i})^2 \right] dx \\ &\quad + \frac{1}{2} \int_0^b \left[GJ_j \left(\frac{\partial \psi_x}{\partial y} \Big|_{x=x_j} \right)^2 + RK_j (\psi_x|_{x=x_j})^2 \right] dy \end{aligned} \quad (6)$$

- Stiffeners:

$$U_{stiffeners} = \frac{1}{2} \sum_n \iiint \{\sigma\} \{\varepsilon\}^T dV = \frac{1}{2} \sum_n \iint \{\sigma\} \{\varepsilon\}^T d\Omega dt \quad (7)$$

Let N_x , N_y and N_{xy} be the panel fluxes, where N_x can vary linearly with y :

$$N_x = N_x^0 + \frac{y}{b} (N_x^b - N_x^0) \quad (8)$$

P_{xm} is the m -longitudinal stiffener load, P_{yn} is the n -transverse stiffener load and q is a constant out-of-plane pressure.

The potential energy due to the applied loads can be expressed as:

$$\begin{aligned} V_{panel} &= - \int_0^b \lambda N_x [u(a, y, 0) - u(0, y, 0)] dy \\ &\quad - \int_0^a \lambda N_y [v(x, b, 0) - v(x, 0, 0)] dx \\ &\quad - \int_0^b \lambda N_{xy} [v(a, y, 0) - v(0, y, 0)] dy \\ &\quad - \int_0^a \lambda N_{xy} [u(x, b, 0) - u(x, 0, 0)] dx \\ &\quad - \int_0^a \int_0^b qw(x, y) dx dy \end{aligned} \quad (9)$$

$$\begin{aligned}
V_{stiffeners} = & - \sum_{m=1}^{n \text{ stiff } X} \lambda P_{xm} [u(a, y, z_m) - u(0, y, z_m)] \\
& - \sum_{m=1}^{n \text{ stiff } Y} \lambda P_{ym} [v(x, b, z_m) - v(x, 0, z_m)]
\end{aligned} \tag{10}$$

The total potential energy corresponds to the sum of the strain energy and the potential energy due to the applied loads:

$$\Pi = U_{SS} + U_{BC} + U_{stiffeners} + V_{panel} + V_{stiffeners} \tag{11}$$

This total potential energy may be calculated as a function of the undetermined coefficients by using the laminate constitutive Eqs. (2), (3) and (4) together with the chosen shape functions on the previous energy expression (11).

Following the Rayleigh–Ritz method, the total potential energy is minimized by derivation with respect to the unknown coefficients. The linear system of equations obtained can be written in matrix form as:

$$(U + \lambda T)\{X\} = \{Z\} \tag{12}$$

Where U is the matrix of the total strain energy, T corresponds to the quadratic terms of the potential energy due to the applied loads, X is a vector containing all the undetermined coefficients and Z corresponds to the linear terms of the potential energy due to the applied loads.

The linear system of Eq. (12) can either be solved to obtain the bending solution to the bending problem of the stiffened panel submitted to in-plane and/or out-of-plane loads, or be treated as an eigenvalue problem in order to assess the buckling onset.

All the terms of (12) are obtained analytically, solving all the energy integrals by regions with constant properties and loads. The final resolution of (12) is performed numerically, but the linear system is reduced in order to further improve the efficiency and minimize the required computational resources.

3 Results

A comprehensive validation of this method has been made in order to correlate with finite element models and tests. In this chapter only some of the features that the method is able to analyze will be presented as example.

Figures 3 and 4 correspond to the buckling results of a plate submitted to pure compression and pure shear for three different lay-ups, (10/80/10), (30/60/10) and (60/30/10). The total thickness of the panel varies while the rest of the parameters remain constant. The Rayleigh–Ritz (RR) results show a perfect fit with the finite elements calculations (FE), with a maximum difference below 1 %.

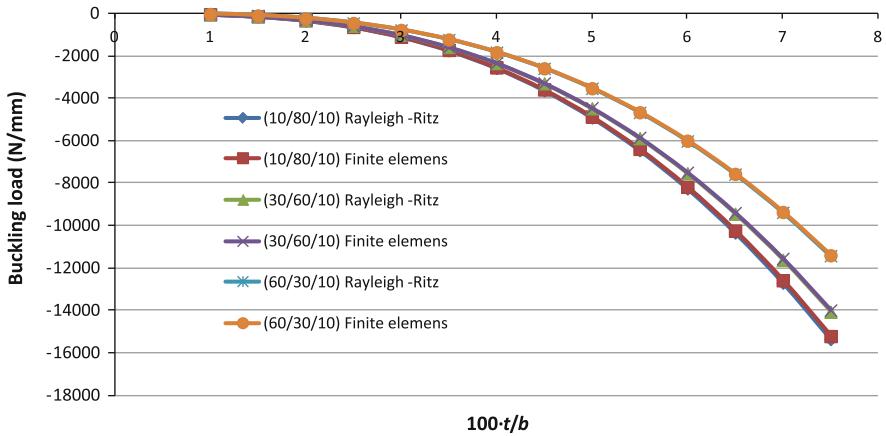


Fig. 3 Plate under compression loads

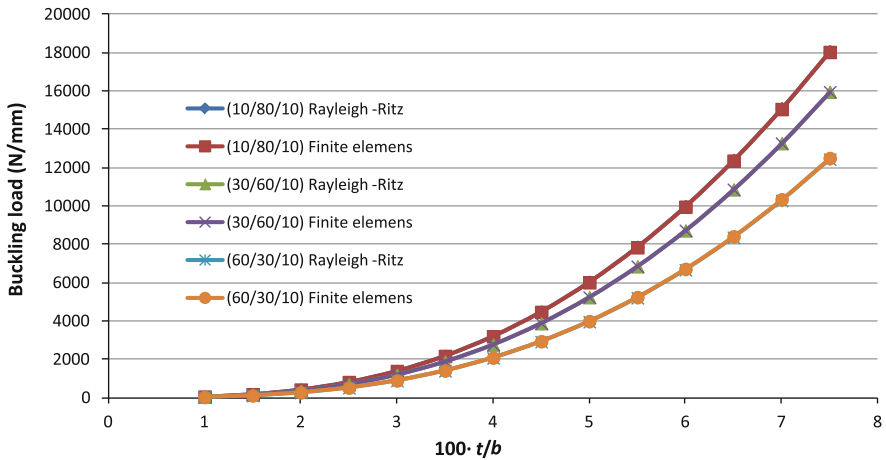


Fig. 4 Plate under shear loads

These results can be used to point out the influence of the transverse shear deformation in the buckling onset. Figure 5 shows the example of the (10/80/10) lay-up under shear load.

Other buckling parametric example is presented in Fig. 6, where a square plate (100 × 100 mm), with stacking sequence (45/-45/90/0/90/0/45/-45/45/-45)_S and intermediate modulus material, is loaded with different combinations of compression and shear. Again, there is a good correlation with finite elements results. It can be noted from the figure how the curve is not totally symmetric for positive and negative shear.

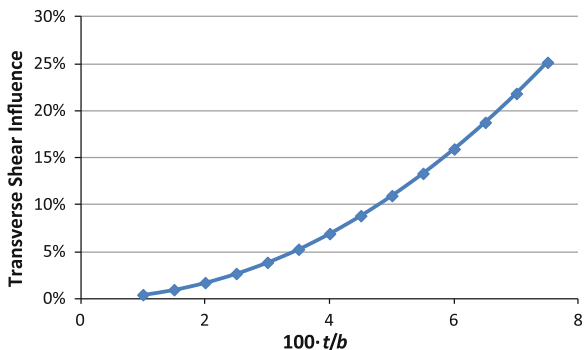


Fig. 5 Transverse shear effect on plate buckling onset

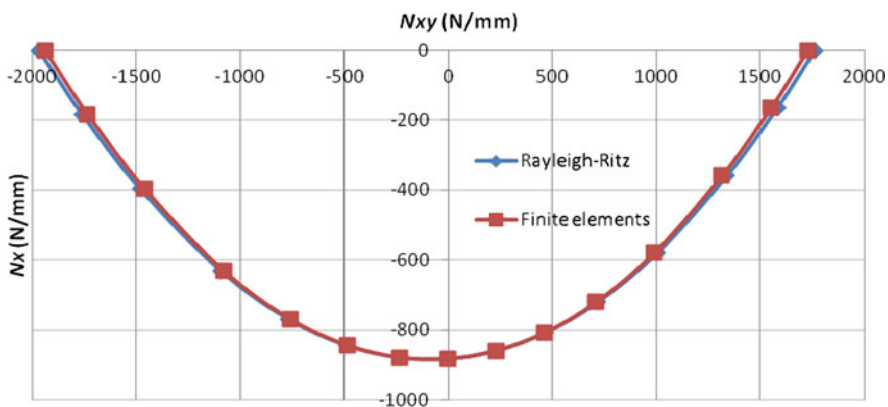


Fig. 6 Plate under different load combinations

Some examples of buckling on real aerospace structures are shown in Figs. 7, 8 and 9, where several typical configurations of a torque box spar are analyzed (Table 1).

Torque box covers are also a good example of structure that may be analyzed with this method. See, for instance, the cases provided in Table 2 and Figs. 10, 11 and 12.

Regarding the bending calculation, Table 3 contains the results of a square plate submitted to pressure and in-plane loads, and Fig. 13 shows the bending deformation calculated with both the RR method and FE (3 % difference).

Some tests have also been used to validate the method. As example: Figs. 14 and 15.

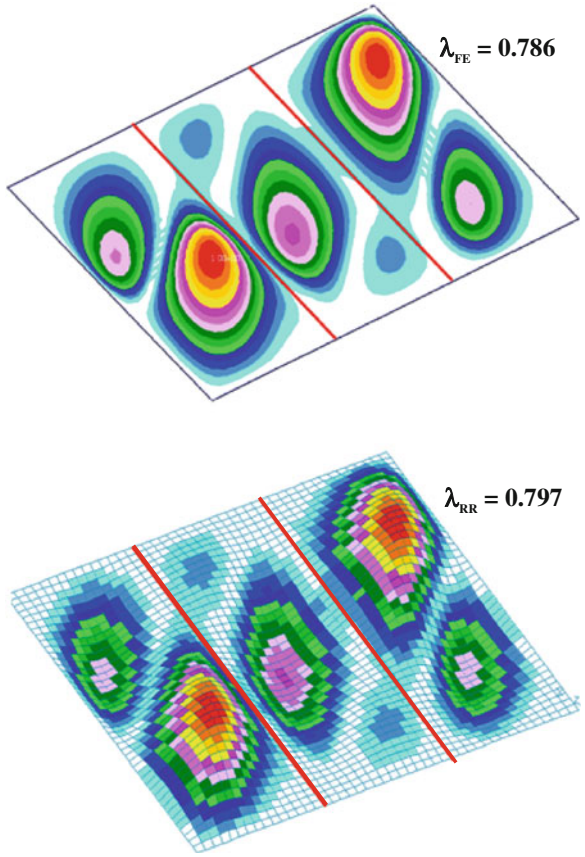


Fig. 7 Spars: finite elements (*on top*) and Rayleigh–Ritz (*at bottom*) buckling shapes

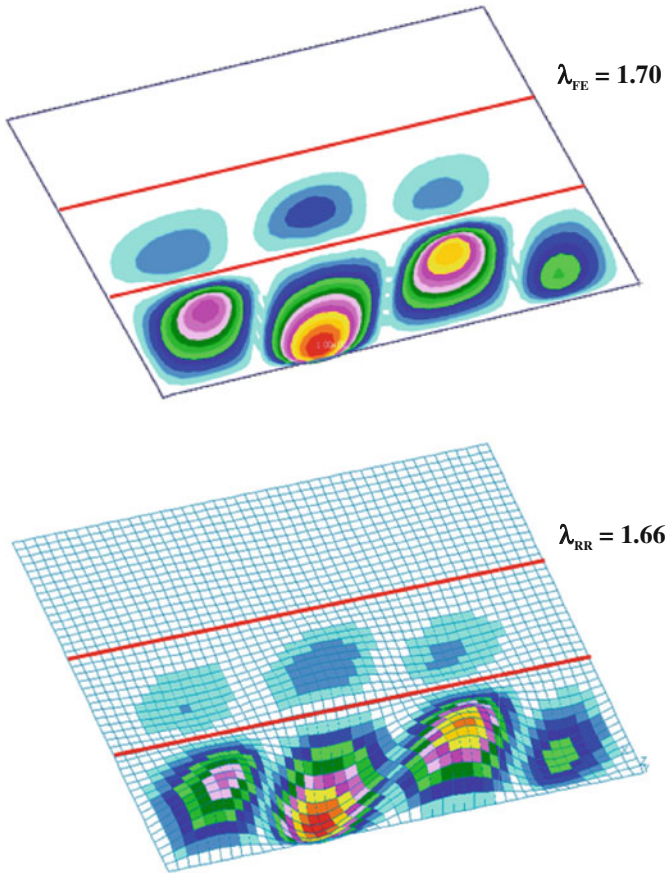


Fig. 8 Spars: finite elements (*on top*) and Rayleigh–Ritz (*at bottom*) buckling shapes

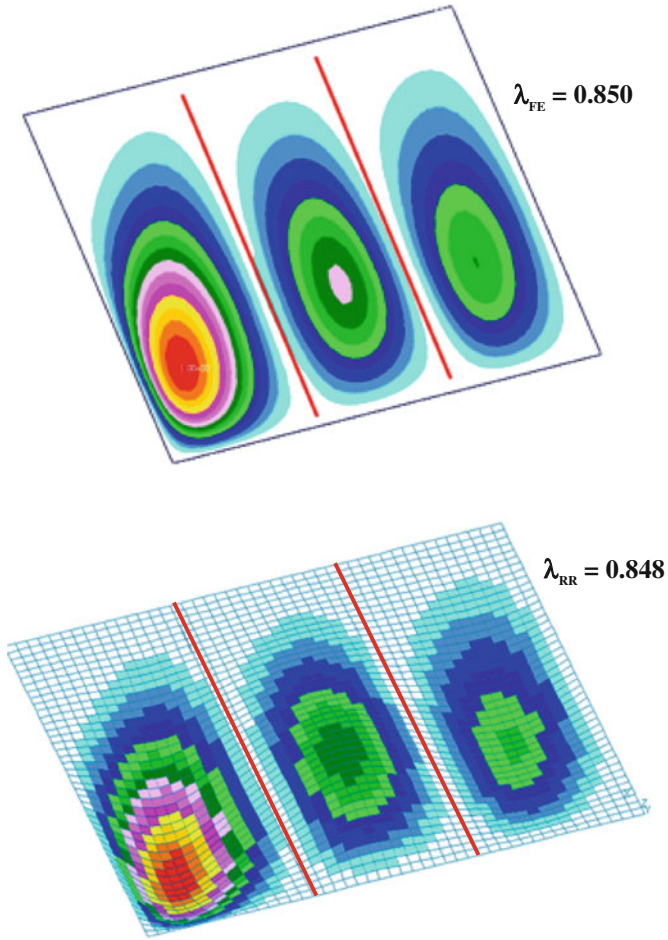


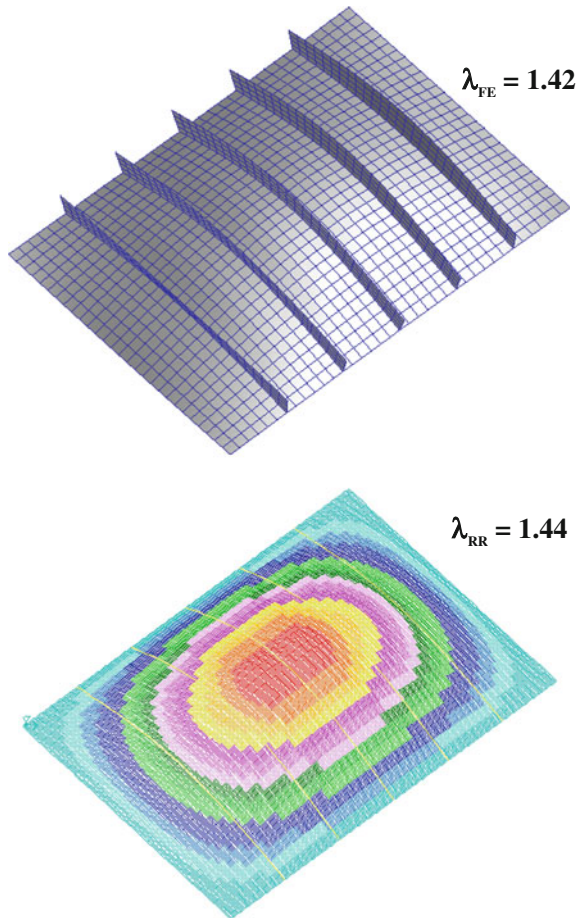
Fig. 9 Spars: finite elements (*on top*) and Rayleigh–Ritz (*at bottom*) buckling shapes

Table 1 Spar configuration results

Figures	Load	Difference Rayleigh–Ritz/finite elements (%)
Fig. 7	Shear	1.4
Fig. 8	In-plane bending + Shear	−2.3
Fig. 9	In-plane bending + Shear	−0.3

Table 2 Cover configuration results

Figures	Load	Difference Rayleigh–Ritz/finite elements (%)
Fig. 10	Longitudinal compression	1.4
Fig. 11	Transverse compression	0.0
Fig. 12	Shear	3.0

**Fig. 10** Covers: finite elements (*on top*) and Rayleigh–Ritz (*at bottom*) buckling shapes

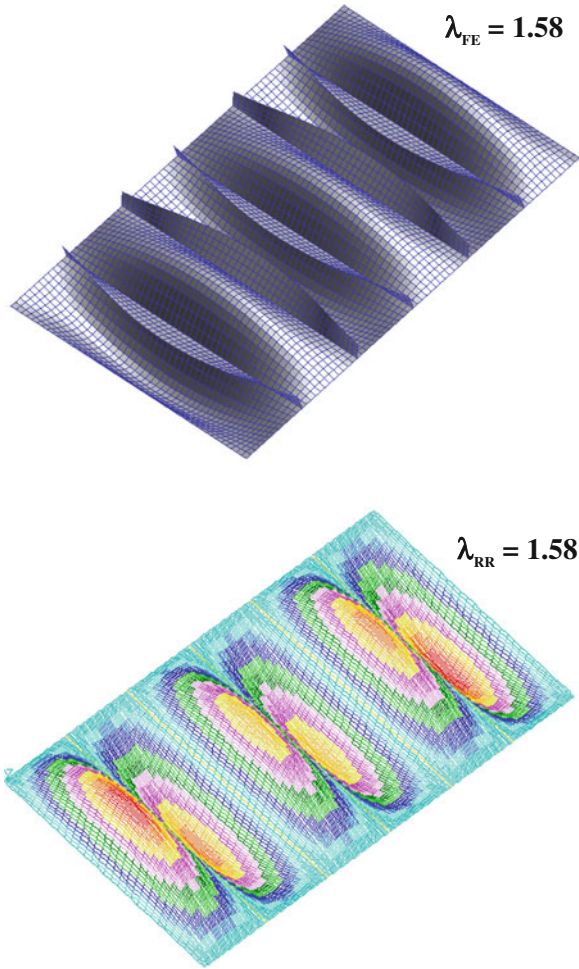


Fig. 11 Covers: finite elements (*on top*) and Rayleigh–Ritz (*at bottom*) buckling shapes

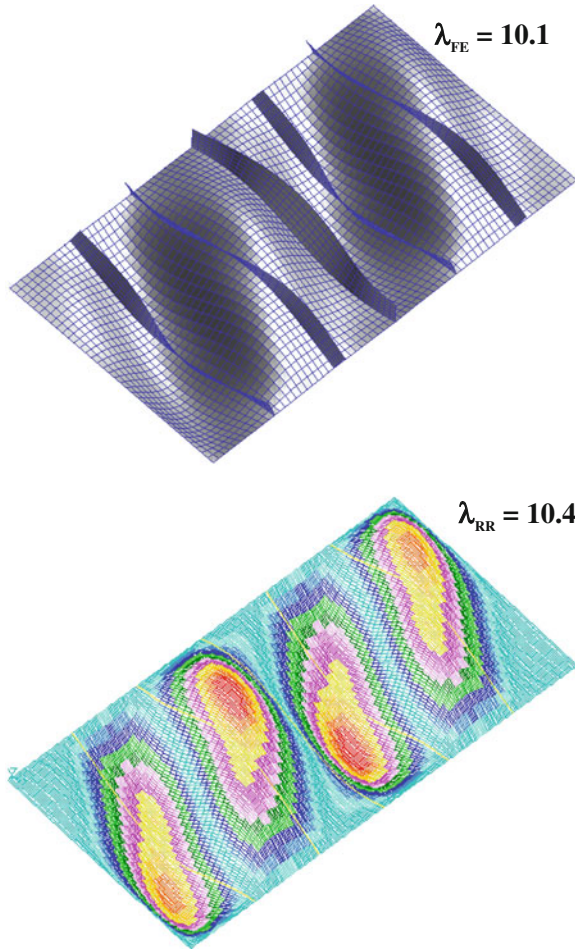


Fig. 12 Covers: finite elements (*on top*) and Rayleigh–Ritz (*at bottom*) buckling shapes

Table 3 Plate bending

Load	Difference Rayleigh–Ritz/finite elements (%)
Pressure	0.0
Pressure + Compression	1.4
Pressure + Shear	0.1
Pressure + Compression + Shear	2.4

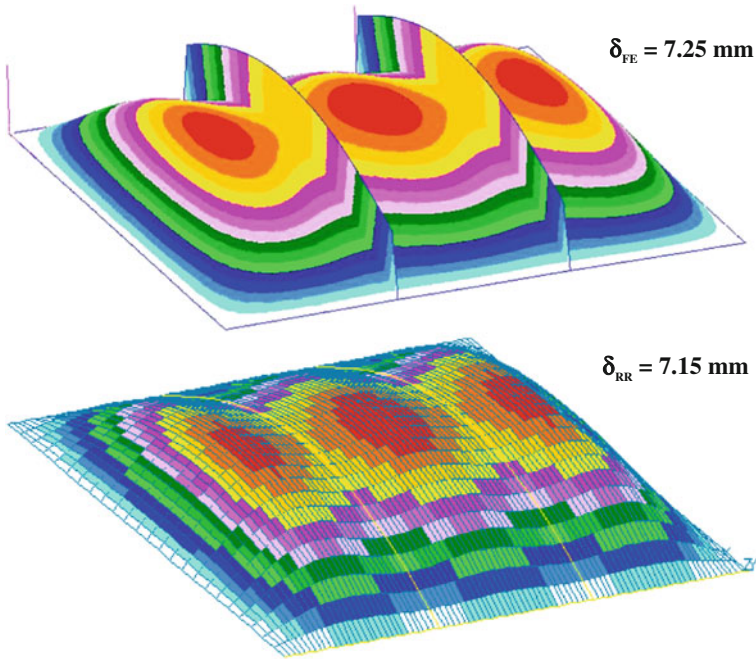


Fig. 13 Bending deformation: finite elements (on top) and Rayleigh–Ritz (at bottom)

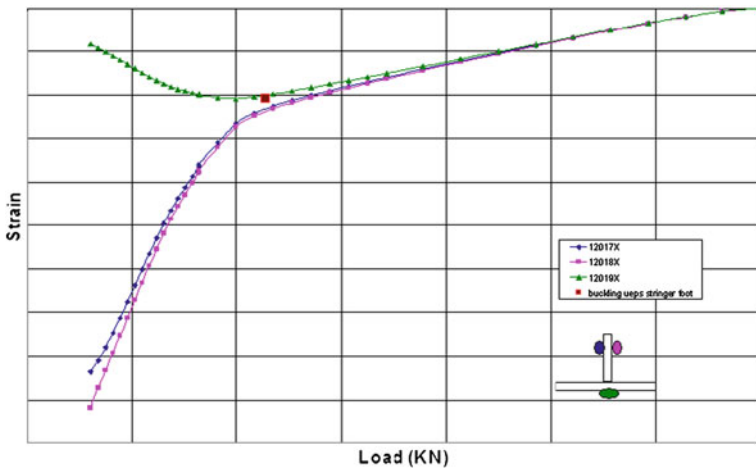


Fig. 14 Test 1

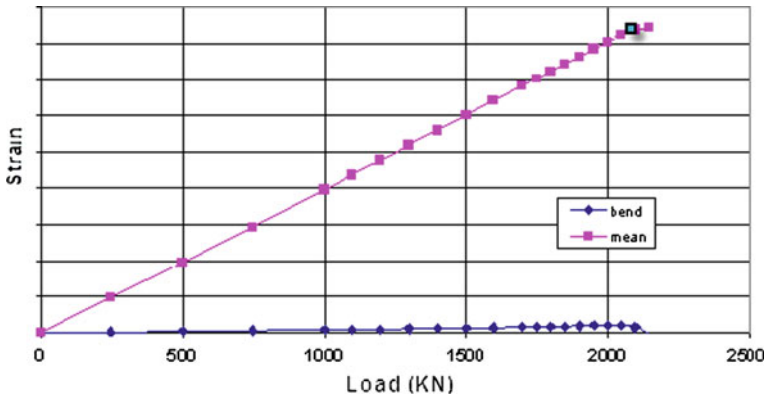


Fig. 15 Test 2

4 Conclusions

The approach proposed in this chapter has proved to be able to cover a wide range of application in real aerospace structures with a very good accuracy.

In today's aerospace structures, where the weight is a key factor, it is important to have quick but at the same time reliable and accurate methods to predict the behavior of the structure. The proposed approach provides a good balance between both factors, with much more accurate results than the closed form formulas but still very efficient, being suitable to be used for structure optimization.

Comparing the method with FE, the results are within a range of $\pm 3\%$ of difference but drastically reducing the calculation time ($\sim 10 - \sim 1,000$ times).

References

1. Mindlin, R.D.: Influence of rotatory inertia and shear on flexural motions of isotropic, elastic plates. *J. Appl. Mech.* **18**, 31–38 (1951)
2. Kollár, L.P., Springer, G.S.: *Mechanics of Composite Structures*. Cambridge University Press, Cambridge (2003)
3. Whitney, J.M., Pagano, N.J.: Shear deformation in heterogeneous anisotropic plates. *J. Appl. Mech.* **37**, 1031–1036 (1970)

Investigation of Cu–Cu Ultrasonic Bonding in Multi-Chip Package Using Non-Conductive Adhesive

Jong-Bum Lee and Seung-Boo Jung

Abstract One of the advantages of stacking active device layers, commonly known as three-dimensional integrated circuits (3-D ICs), is the ability to heterogeneously integrate various functional blocks in a given chip area. Another benefit is to shorten the intermediate interconnects length and thus reduce delay and power consumption. Since device layers are bonded in close proximity, high density and short vertical interconnections between the layers known as through silicon via (TSV) can provide much higher bandwidth. However, such 3-D packages suffer from higher power densities that will adversely affect the performance and reliability of 3-D packages by intermediate materials such as solder and conductive particles between pads. In this study, a low temperature Cu-Cu ultrasonic bonding with non-conductive film (NCF) has been developed. This bonding technique leads to high shear strength at the metal-metal contact interface, thus resulting in chemical bonding of Cu bumps, which is essential for strong bonding strength. The ultrasonic bonding is achieved by wear action induced by ultrasonic vibration that caused the interdiffusion between the Cu bump and pad. The ultrasonic power contributes to enhance the deformation of Cu bump due to ultrasonic softening effect which is then followed by the strain hardening of the Cu ultrasonic bonding.

Keywords Multi-chip package • Interconnection • Through-silicon via • Non-conductive adhesive • Electrical resistance • Reliability

J.-B. Lee · S.-B. Jung (✉)

School of Advanced Materials Science and Engineering,
Sungkyunkwan University, #300 Cheoncheon-dong, Jangan-gu,
Suwon, Gyeonggi-do, 440-746 Korea (Rep.)
e-mail: sbjung@skku.edu

1 Introduction

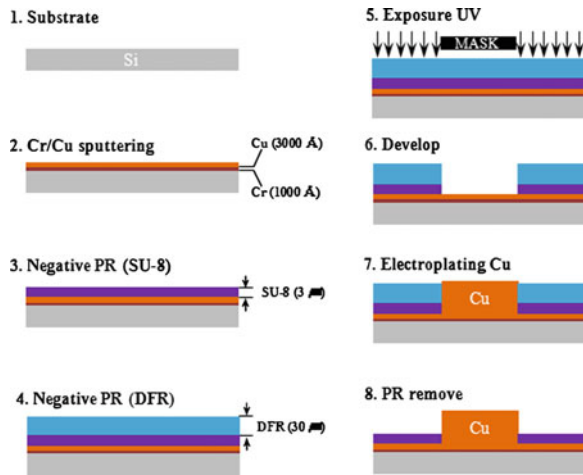
Three-dimensional (3-D) integration based on through silicon via (TSV) offers an attractive and cost effective solution as the trend towards higher electronics integration, higher speed and more functionality on portable electronic devices [1]. The high degree of technology and large amount of cost required for development of 3-D packaging make them difficult to apply to low-end products. One option of 3-D integration chips (ICs) is to stack several thinned chips by way of Cu-Cu bonding. 3-D integration of ICs using bump-less Cu-Cu bonding is one attractive bonding method because the same bonding material acts as an electrical bond to form a conductive path between the layers and as a mechanical bond to hold the layers together unfaillingly. Metallic bonding also allows TSV formation for vertical connection during bonding [2]. Cu-Cu bonding is compared to solder-based connection because: (1) an ultra-fine pitch can be achieved; (2) Cu has better electrical and thermal conductivities; and (3) Cu has much better electro-migration resistance and can endure higher current density in high speed and functional electronic devices. Advantages such as (2) and (3) are due to the absence of an intermetallic compound (IMC) and Sn layer in Cu-Cu bonding. Cu-Cu bonding has been employed using thermo-compression bonding with application of high heat and pressure (typically $\sim 350\text{--}400\text{ }^{\circ}\text{C}$ and $\sim 200\text{ kPa}$) [3]. The bonding mechanism is based on interdiffusion of Cu atoms and grain growth, and hence it is also widely known as diffusion bonding. Since a Cu surface already oxidizes in ambient air, it acts as a barrier for diffusion bonding at low temperature. However, there is strong motivation to achieve Cu-Cu bonding at low temperature for better thermal control, lower thermal stress, and improved alignment. Recently, the ultrasonic flip-chip bonding technology has become an interesting field of research due to several advantages such as short bonding time, low bonding temperature, low bonding pressure, good electrical and mechanical performance, and being environmentally friendly [4–7].

Thus, optimization of the bonding parameters could lead to a low temperature solution for Cu-Cu bonding in 3-D chip stacking. Based on this premises, we applied a low temperature Cu-Cu ultrasonic bonding approach, which is the focus of this present chapter. Die shear tests were used to optimize the shear strength between substrate and chip. The electrical resistance of joints bonded with and without non-conductive film (NCF) was investigated, and the microstructural evaluation of the joint was conducted using a scanning electron microscope (SEM). Thermal cycle (TC) and high temperature humidity (HTH) tests were carried out to elucidate the failure mechanism under environmental changes.

2 Experimental Procedures

Figure 1 shows a schematic diagram of the process flow for the fabrication of a 3-D package upper chip. As shown in Fig. 1, a photolithography process was used to make a thick mask layer for deep etching. A negative type of photoresist, SU-8

Fig. 1 Schematic diagram of the process flow for the fabrication of a 3-D package upper chip

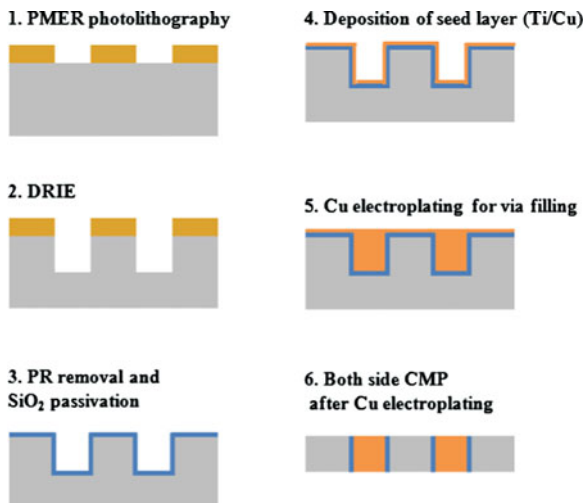


and DFR, were spin-coated to a thickness of 3 and 30 μm , respectively. SU-8 photoresist was applied for passivation layer. Cu was electroplated for the upper chip bump. The bump diameter was designed for 160 μm , because the hole size of TSV in carrier chip was manufactured for 200 μm and aspect ratio of TSV should be considered for the hole size of the opposite side. The hole diameter of the opposite side in the carrier chip was about 175 μm .

Figure 2 shows a schematic diagram of the process flow for the fabrication of a 3-D package carrier chip. As shown in Fig. 2, a photolithography process was used to make a thick mask layer for deep etching. A negative type of photoresist was spin-coated to a thickness of 12 μm . After undergoing various processes, a deep reactive ion etching (DRIE) process was carried out using an inductively coupled plasma (ICP) etcher (Multiplex ICP ASE HR, Surface Tech Sys, UK). After the TSV formation, a chemical mechanical planarization (CMP) process was employed to remove the residual Si on the backside of the wafer followed by thermal oxidation at the surface of the Si for the formation of SiO_2 passivation layer and the sputtering of seed layers for the electroplating. Cu was electroplated in the TSVs.

Si carrier and chip were bonded to the FR-4 substrate using an ultrasonic bonder (Flexible Sub-Micron Bonder, Fineplacer Lambda, Germany). There were two steps of ultrasonic bonding for 3-D packaging. The first step of ultrasonic bonding was for bonding of substrate and carrier chip, and then the second step of ultrasonic bonding was for bonding of upper flip chip and bonded package after the first step of the ultrasonic bonding. The preheating temperature for NCF bonding was 120 $^\circ\text{C}$. The frequency of vibration in the ultrasonic bonding system was 40 kHz. The FR-4 was fixed on the anvil that held the substrate in a fixed position and supported the clamping force. The bumps were bonded with increasing bonding time and input power. Die shear tests were carried out on the bonded samples using a bonding tester (PTR-1000, Rhesca, Japan) with a 5 N load cell.

Fig. 2 Schematic diagram of the process flow for the fabrication of a 3-D package carrier chip



The displacement rate, probe height, and probe width were 200 mm/s, 5 and 10 mm, respectively.

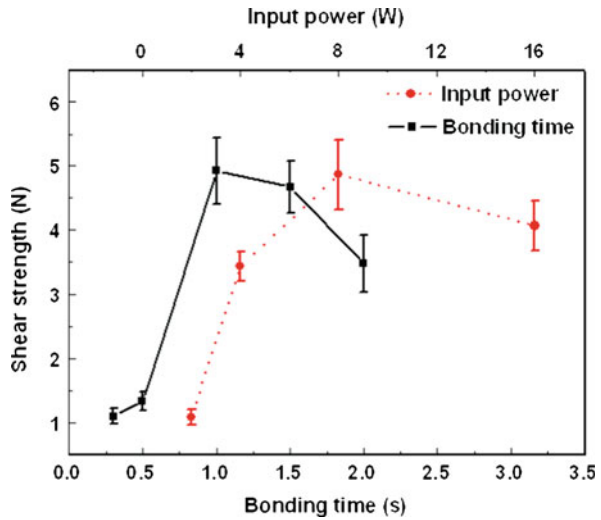
The electrical resistance of bumps located on the bonding pad was evaluated using a Kelvin structure. The resistance was evaluated by measuring the slope, i.e., the output voltage divided by input current, in the current range of 0.01–0.1 A, using a 4-point probe station. I_1 , I_2 , V_1 and V_2 denote the current input, current output, voltage input and voltage output, respectively, for measuring the electrical resistance.

To investigate the reliability of the ultrasonically bonded flip-chip and carrier, the electrical resistance of joints was monitored during the environmental test. The bonded multi-chip packages were placed in a thermal shock test chamber (TSA-101S, ESPEC, Japan) and were subjected to 500 cycles in the range -40 – 125 °C (30 min cycle time, air to air, 13.5 min dwell time) and were treated at 85 °C and 85 % RH for up to 500 h in a temperature/humidity test chamber (PL-1KPM, ESPEC, Japan). Five bonded multi-chip packages were used for each reliability test and then the contact resistance of the Kelvin structure was measured for every 100 cycles and 100 h.

3 Results and Discussion

Figure 3 shows the die shear strength variation of the joints ultrasonically bonded without NCF for various times and powers. The maximum bonding load during the ultrasonic bonding was 16 N. The shear strength of the joint reached 4.9 N at a bonding time of 1 s, and then decreased to 3.4 N as the bonding time was increased to 2 s. The input power was 8 W when the effect of bonding time was

Fig. 3 Shear strength of joints bonded without NCF with increasing bonding time and input power



evaluated. Too much bonding time caused a decrease in the shear strength due to the misaligned bonding interface between the substrate and the carrier chip caused during second ultrasonic bonding. The maximum shear strength of the joint was obtained at an input power of 8 W, and then decreased with increasing input power. The bonding time was 1 s when the effect of input power was examined. Generally, the amplitude of vibration increases as the bonding pressure decreases and the input power increases. Larger amplitude at input power of 16 W caused the chip to spin which caused misalignment of the bumps between the chip and the substrate.

Figure 4 shows the electrical resistance variations of joints bonded with NCF and without NCF. The measured electrical resistance of the joints bonded without NCF was 15.3 m Ω whereas that with NCF was 7.2 m Ω . The difference in the electrical resistance by the existing NCF was determined by second ultrasonic bonding of the upper chip to the carrier chip. The cured NCF by the first ultrasonic bonding between the substrate and the carrier chip supported the bump in a fixed position. On the other hands, in the case of the joint bonded without NCF, we could find the crack at the bonding interface between the substrate and the carrier chip which formed during second ultrasonic bonding, as shown in Fig. 5. The bumps on the substrate without NCF received a shock when the second ultrasonic energy was applied. Shocked and softened bump could shake easily and desert from its aligned position. Therefore, the crack was easily found at the bonded interface.

Figure 6 shows the shear strength and electrical resistance comparisons between Cu–Cu bonding and Sn bump bonding which was previously studied [8]. Higher shear strength was achieved after Cu–Cu ultrasonic bonding. Cu is a harder material than Sn. Thus, when Cu bumps bonded with ultrasonic energy, they formed a stronger bonding interface. On the other hand, the electrical resistance

Fig. 4 Electrical resistance variation of bumps evaluated using a Kelvin structure after ultrasonic bonding with and without NCF

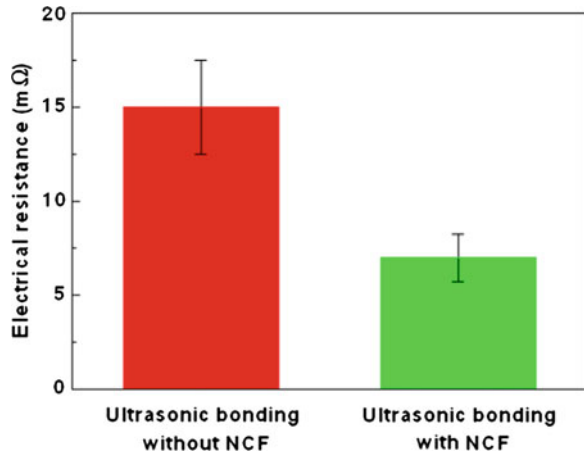


Fig. 5 SEM micrographs of ultrasonically bonded joint without NCF between substrate and carrier chip

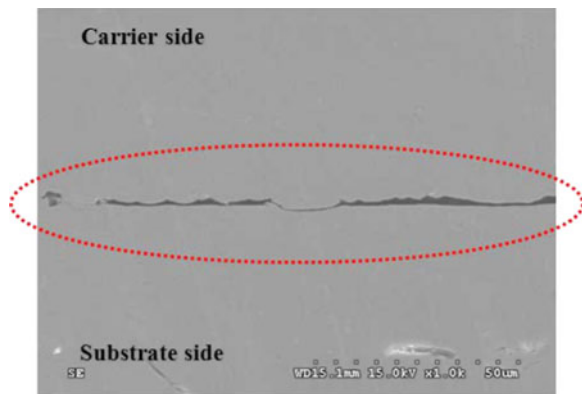
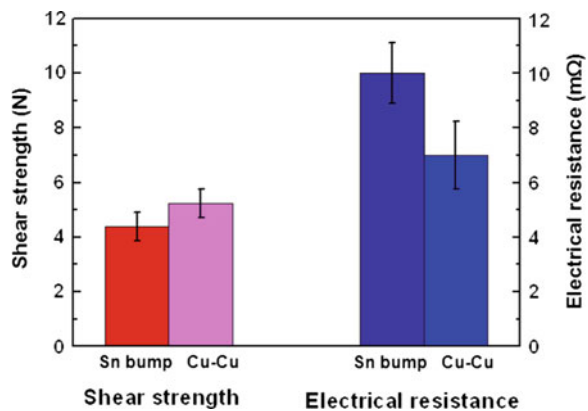


Fig. 6 The shear strength and electrical resistance changes between Cu-Cu bonding and Sn bump bonding



with Cu-Cu bonding was decreased compared to that with Sn bump bonding. These were due to the absence of medium materials such as intermetallic

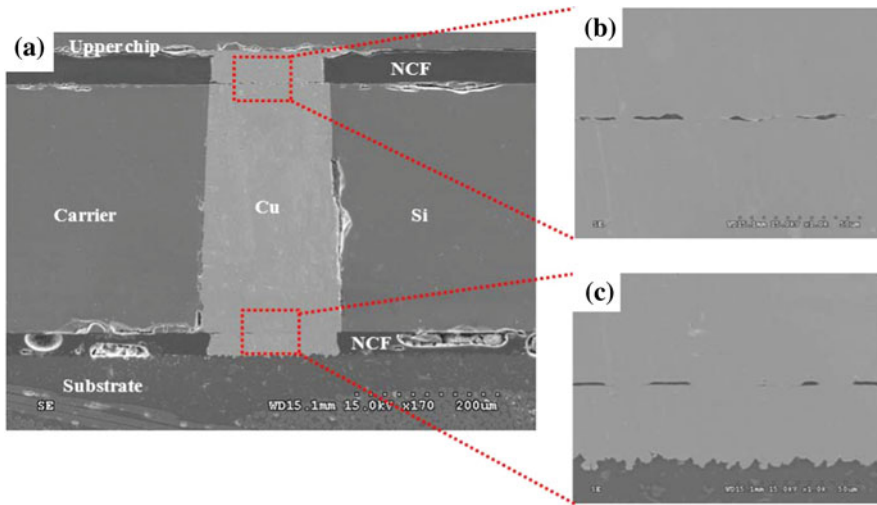


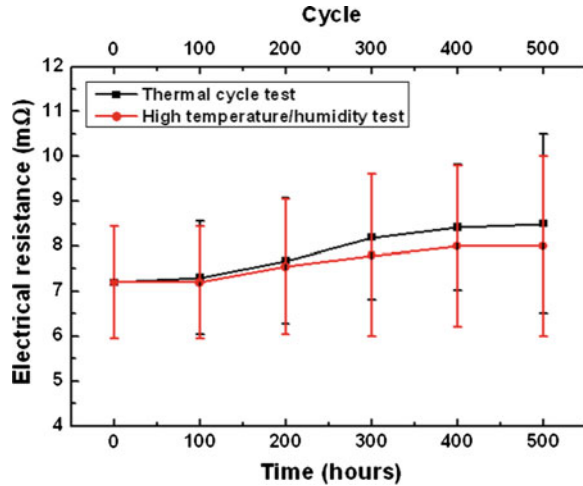
Fig. 7 Cross-sectional SEM micrographs of the joints bonded using the optimum bonding conditions

compound (IMC) and Sn layer in Cu–Cu bonding, as mentioned in the introduction section. We expect that the devices operate with higher speed and functionality when 3-D packages are applied with Cu–Cu bonding.

Figure 7 shows cross-sectional SEM micrographs of the joints bonded using the optimum bonding conditions. The bumps were almost bonded in the joint bonded with NCF. The curing degree of NCF increases as the bonding time increases. The heat was transferred to the monomers in the NCF during ultrasonic bonding and provided sufficient energy to the epoxy functional groups in the monomers to create polymer networks [9]. The heat created by friction energy started to cure the NCF adjacent to the bump. In Fig. 7b, c an un-bonded area is observed at the bonding interface. The formation of an un-bonded area is related to the initial surface smoothness and planarity. The bonding strength and electrical resistance will be improved when we can control and optimize the electro-plating condition for flat surface. Vacancies in the Cu layers can also combine and form micro-voids during ultrasonic bonding. Micro-voids act as a possible avenue for tensile stress relaxation (coefficient of thermal expansion (CTE) of Cu ~ 16 ppm/K and Si ~ 3 ppm/K) in the bonded Cu layer when they are cooled down from bonding temperature and placed in a reliability test chambers.

Figure 8 shows the electrical resistance variations of the joints ultrasonically bonded with NCF during TC and HTH tests. The electrical resistance slightly increased with increasing bonding time and cycles. The electrical resistance of joint after TC test measured higher than that of joint after HTH test. However, the multi-chip package bonded with Cu–Cu bump showed stable electrical resistance after both of the reliability test. Fully cured NCF supports the Cu bumps in fixed position and no changes are observed at the bonding interface during the reliability

Fig. 8 Electrical resistance of joints bonded with NCF during TC and HTH tests



tests. The main issue in the reliability test could be oxidation of the exposed Cu surfaces and oxidation migration along the bond interface. Even though this effect may not cause to immediate failure by existing NCF, it presents a reliability issue for Cu-Cu bonding.

4 Conclusion

Cu-Cu non thermo-compression bonding technology has been presented in this chapter. Ultrasonic power and bonding time are control parameters for bonding in 3D packaging applications. This study was focused on the optimization of bonding time and input power for the transverse ultrasonic bonding. The shear strength was influenced significantly by the bonding conditions, such as bonding time and input power. The Si carrier and chip were stacked at a bonding time of 1 s and an input power of 8 W. The electrical resistance of joint after TC test measured higher than that of joint after HTH test. However, the multi-chip package bonded with Cu-Cu bump showed stable electrical resistance after both of the reliability test.

The assembly process flow for Cu-Cu bonding was simpler than that for Cu/Sn-Cu bonding (no pre-coining and plasma treatment required prior to Cu-Cu bonding) and, thus, would have a higher throughput for manufacturing. The Cu-Cu system is more likely to scale down to smaller pitch dimensions.

Acknowledgements The present work was carried out with the support of a Next Generation New Technology Development Program (Project No. 10030049) of the Korea Ministry of Commerce, Industry and Energy (MOCIE).

References

1. Tan, C.S., Gutmann, R.J., Reif, R.: Wafer level 3-D ICs process technology. Springer, New York (2008)
2. Patti, R.: Three-dimensional integrated circuits and the future of system-on-chip designs. Proc. IEEE **94**, 1214–1224 (2006)
3. Tan, C.S., Reif, R.: Microelectronics thin films handling and transfer using low temperature wafer bonding. Electrochem. Solid State Lett. **8**, 362–366 (2005)
4. Hongoh, M., Miura, H., Ueoka, T., et al.: Temperature rise and welding characteristics of various-frequency ultrasonic plastic welding systems. Jpn. J. Appl. Phys. **45**, 4806–4811 (2006)
5. Tanida, K., Umemoto, M., Tomita, Y., et al.: Au bump interconnection with ultrasonic flip-chip bonding in 20 μm pitch. Jpn. J. Appl. Phys. **42**, 2198–2203 (2003)
6. Tsujino, J., Ueoka, T., Asada, Y., et al.: Measurement of the temperature rise at the welding surface of different metal specimens joined by a 15 kHz ultrasonic butt welding system. Jpn. J. Appl. Phys. **37**, 2996–3000 (1998)
7. Naruse, K., Watanabe, Y.: Ultrasonic plastic welding at 1.2 MHz using a surface acoustic wave device. Jpn. J. Appl. Phys. **45**, 4812–4815 (2006)
8. Lee, J.B., Lee, J.G., Ha, S.S., et al.: Effect of non-conductive film on the reliability of multi-chip package bonded using ultrasonic energy. J. Adhes. Sci. Technol. **25**, 2475–2482 (2011)
9. Tan, S.C., Chan, Y.C., Chiu, Y.W., et al.: Thermal stability performance of anisotropic conductive film at different bonding temperatures. Microelectron. Rel **44**, 495–503 (2004)

Natural Vibration Analysis of Soft Core Corrugated Sandwich Plates Using Three-Dimensional Finite Element Method

Mohammad Mahdi Kheirikhah, Vahid Babaghasabha, Arash Naeimi Abkenari and Mohammad Ehsan Edalat

Abstract Nowadays, corrugated plates, sandwich panels, and thin plates stiffened by ribs are commonly available structural materials which allow stiffening flat panels against applied loads and structural vibrations. Response to natural vibration of a soft core corrugated composite skin sandwich plate was investigated in this paper, and the natural frequency of the presented model was obtained using finite element method (FEM). The FEM of the problem has been constructed in the commercial software ANSYS 12.0. A trapezoid corrugated shape was studied on the face sheets of the sandwich structure. The model included a wavy soft core which was located between two wavy trapezoid-shaped skins. The core was assumed as a soft orthotropic material and skins are assumed generally as unequally laminated composites. Comparing the present numerical results with values taken from literature demonstrate the accuracy of the proposed model. The numerical results show that using a trapezoid composite skins increase the natural frequency of the structures.

Keywords Vibration analysis · Corrugated sandwich plate · Finite element · Composite skin

M. M. Kheirikhah (✉) · V. Babaghasabha · A. N. Abkenari · M. E. Edalat
Faculty of Industrial and Mechanical Engineering, Qazvin Branch, Islamic Azad University,
Qazvin, Iran
e-mail: kheirikhah@qiau.ac.ir

V. Babaghasabha
e-mail: babaghasabhavahid108@gmail.com

A. N. Abkenari
e-mail: arash.naeimi_f@yahoo.com

M. E. Edalat
e-mail: mechanicaleng.mee@gmail.com

Nomenclature

θ	Angle of trapezoidally model
φ	Angle of layer layup ($0/\varphi/C/0/\varphi$)
h_t	Plate thickness
h_s	Skin thickness
h_c	Core thickness
E	Elastic modulus
E_x, E_y, E_z	Orthotropic elastic modulus
G	Shear modulus
G_{xy}, G_{xy}, G_{xz}	Orthotropic shear modulus
ν	Poisson's ratio
$\nu_{xy}, \nu_{yz}, \nu_{xz}$	Poisson's ratio in the x -, y - and z - direction, respectively
a, b	Panel dimension in the x -(length) and y -directions (width), respectively
ρ	Material density
$F/2$	Trapezoidally corrugation amplitude
$2C$	Rotation period
σ_x, σ_y	Stress in the x, y direction
U	Displacement in the x -direction
V	Displacement in the y -direction
W	Displacement in the z -direction

1 Introduction

Sandwich plates are stiffened by corrugations which are used in many engineering applications such as automotive, aerospace, marine, and building constructions due to their high strength to weight ratios, and ease of manufacturing. Plates generally consist of two thin high strength face sheets and a soft thick low strength core, which are adhesively bonded together. In most cases, the core consists of a polymer foam or honeycomb material, while composite laminates are commonly used as the face sheets.

Timoshenko [1, 2] has done an analysis on the simple and flat plates under uniformly distributed load. Seydel et al. [3] extended to corrugated panels. Early work on the wrinkling and buckling of sandwich panels can be attributed to Gough et al. [4]. Presented analysis of buckling and free vibration in [5, 6] and the analysis of bending and buckling of sandwich panels in [7].

In [1999], Liew and Teo [8] presented a one kind of essential boundary condition in ANSYS design. In [2009], Liew et al. [9] presented an analysis of trapezoidal and sinusoidal wave corrugated skins using a mesh-free Galerkin method. In [2009], Reany and Grenestedt [10] presented an analysis of the sandwich core with ANSYS.

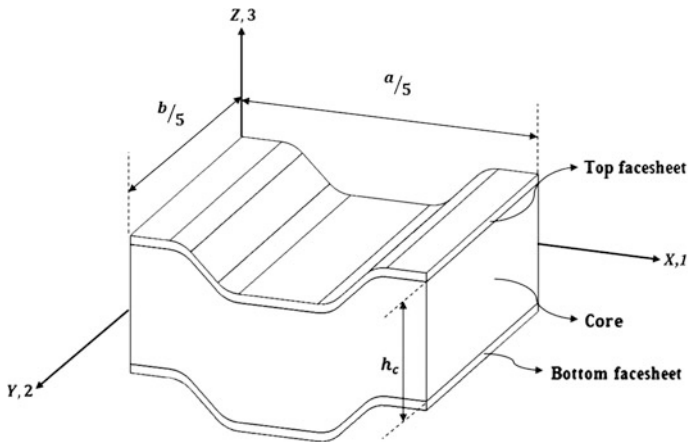


Fig. 1 Geometry of the present corrugated sandwich plate

In the present chapter of contribution, free vibration of corrugated sandwich plates with trapezoidal shape was investigated. The FEM of the sandwich plate was constructed in the commercial finite element software ANSYS 12.0. The effects of many geometrical and physical parameters such as angle of the trapezoidal shape, boundary conditions and layup angle of the composite face sheets were also regarded in this paper.

A simple and valid way to study corrugated plates is to analyze them as orthotropic skin plates of uniform thickness and equivalent rigidities (Fig. 1).

By changing the geometrical parameters of the sinusoidal and trapezoidal corrugated plates, different mode shapes and frequencies were obtained. The present analysis demonstrated that trapezoidal corrugated plates are more useful in compare to plates with sinusoidal corrugation.

2 Finite Element Modeling

The 3D FEM is used to analyze the vibration behavior of sandwich plates with trapezoidal corrugated face sheets. Figures 1 and 2 give a schematic view of the present sandwich plate with the composite face sheets and its dimensions and coordinate system.

Intermediate areas of the upper and lower face sheets were constructed with 8-node Shell 93 elements in the X-Y plane as shown in Fig. 3. These areas have the distance h_c along the Z-axis. Then, in order to construct the upper and lower face sheets, the top and bottom areas were extruded along the positive and negative direction of the Z-axis using 8-node 3D Solid 46 brick elements, respectively. These extrusions have a length h_f .

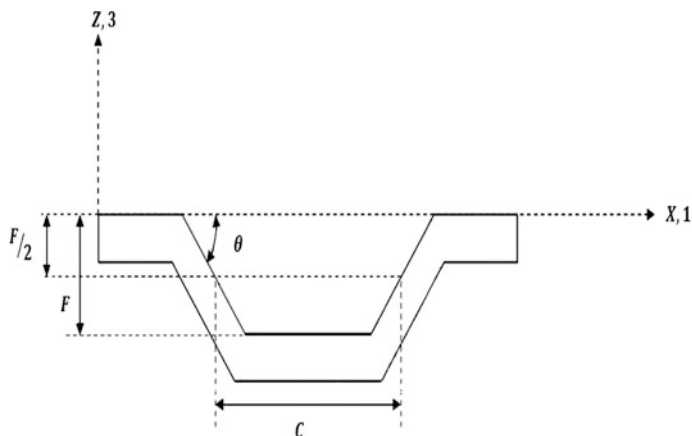
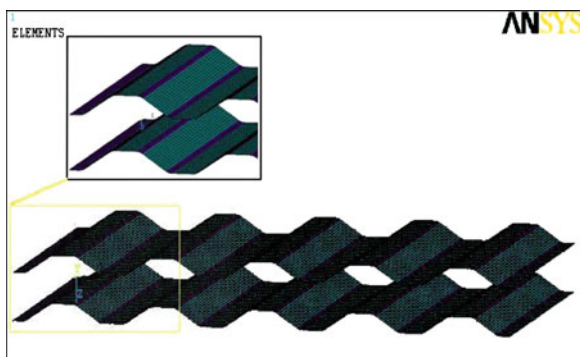


Fig. 2 Dimensions of the present trapezoidal shape

Fig. 3 Temporary meshed area of the upper and lower face sheets



In the next step, for constructing the core section, the top and bottom areas were extruded along the negative and positive directions of the Z-axis with a length of $h_c/2$, respectively. Figure 4 clarifies the above steps. In this figure, half of the core section was constructed by extruding the top area along the negative direction of the Z-axis. The intermediate mesh of the mentioned areas should be deleted during the extrusion process of the core. The 8-node 3D Solid 185 elements were employed to construct the core section of the present sandwich plate.

By following the above steps, the constructed core section of the sandwich plate was divided into two sections, including the upper-half and lower-half. In addition, there are two layers of Solid 185 elements at the middle interface of the core volume that should be merged as one. Figure 5 shows the complete 3D FEM of the sandwich plate which is studied in the present chapter.

As mentioned before, the effects of different boundary conditions such as all edges clamped (CCCC) and all edges simply supported (SSSS) on the free vibrations of the sandwich plates were analyzed in the present FEM.

Fig. 4 Upper-half finite element model of the core section

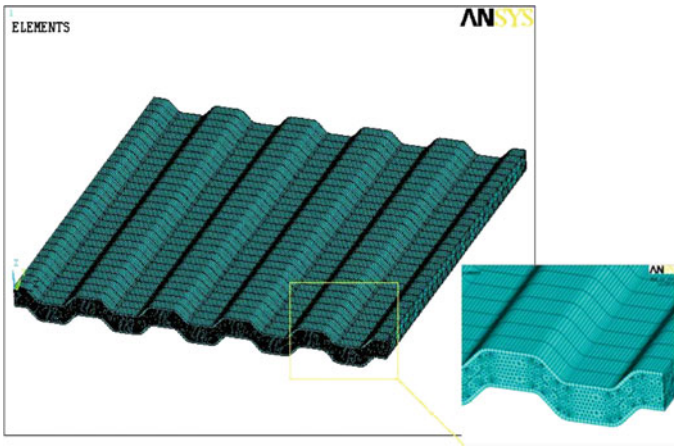
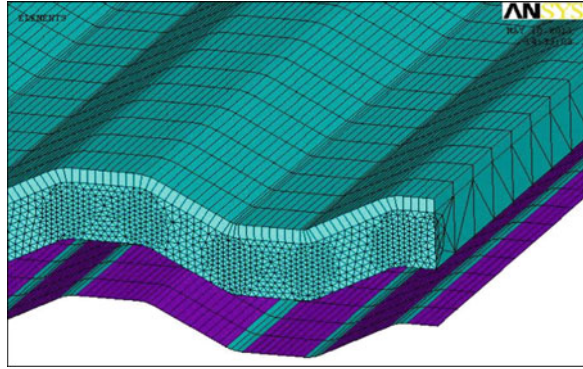


Fig. 5 Three-dimensional finite element model of a trapezoidal corrugated square sandwich plate

The boundary conditions which were applied to the edges can be defined as follows:

Edges parallel to Y -axis:

$$SSSS : v = w = \sigma_x = 0$$

$$CCCC : u = v = w = 0.$$

Edges parallel to X -axis:

$$SSSS : u = w = \sigma_y = 0$$

$$CCCC : u = v = w = 0.$$

Table 1 Numerical frequencies (Hz) of the simply supported trapezoidally corrugated plate

No. Mode	Analysis	Results of reference theory [9]	Relative errors [9] (%)
1	13.39	13.74 (13.14)	2.50 (4.30)
2	24.22	24.54 (23.90)	1.20 (2.570)
3	44.57	45.35 (44.05)	1.70 (2.80)
4	45.38	47.19 (44.38)	3.80 (8.51)
5	54.48	54.84 (53.44)	0.65 (2.51)
6	72.23	71.19 (71.05)	-1.40 (0.18)
7	73.84	75.32 (73.00)	1.90 (3.00)
8	98.02	97.54 (95.82)	-0.48 (1.70)
9	99.45	103.31 (98.03)	3.70 (5.10)
10	107.79	109.76 (105.47)	1.79 (3.90)
11	111.56	114.17 (110.32)	2.20 (3.30)
12	125.48	122.83 (122.90)	-2.10 (-0.05)
13	135.96	133.83 (134.17)	-1.60 (-0.25)
14	152.13	144.51 (149.17)	-5.20 (-3.20)
15	157.46	161.34 (155.96)	2.40 (3.30)
16	169.41	175.97 (165.69)	3.70 (5.80)
17	180.75	179.28 (176.77)	-0.82 (1.30)
18	181.26	181.23 (179.18)	-0.01 (1.10)
19	188.19	187.11 (184.77)	-0.57 (1.20)
20	200.37	198.41 (195.90)	-0.98 (1.20)

3 Verification

To verify the accuracy of the present FEM and analysis, natural frequencies of the trapezoidal corrugated plate have been computed. Tables 1 and 2 show the calculated frequencies and those of previous published results by Liew et al. [9]. The first set of material constants are given in Table 3 is used to verify the accuracy of the proposed model. As can be seen, the obtained numerical results are in very good agreement with maximum relative error of 5 %.

4 Results and Discussion

In this section, an orthotropic material with different constants has been considered for analyzing the corrugated square sandwich plate. Material set 2 [11, 12] was used for constructing the core and face sheets in ANSYS 12.0

The square ($a/b = 1$) sandwich plate which is considered here has the dimension of $1 \times 1 \text{ m}^2$. The parameter h_f is the thickness of the top and bottom face sheets and has a value of $0.1 h$. Where h is the total thickness of the sandwich plate. Also, the core is assumed as a soft isotropic material with thickness h_C which is equal to $0.8 h$. As already shown in Fig 2, a trapezoidal shape with amplitude of $F/2$ ($F = 0.03 \text{ m}$) and an alternation period of $2C$ ($C = 0.1 \text{ m}$) were

Table 2 Numerical frequencies (Hz) of the clamped trapezoidally corrugated plate

No. Mode	Analysis	Results of reference theory [9]	Relative errors [9] (%)
1	27.97	28.58 (27.18)	2.10 (4.90)
2	38.96	40.46 (39.45)	3.70 (2.49)
3	61.41	63.27 (62.12)	2.93 (1.82)
4	69.06	72.59 (67.96)	4.80 (6.39)
5	78.72	80.88 (78.51)	2.67 (2.94)
6	92.71	95.94 (94.35)	3.37 (1.60)
7	97.48	98.05 (98.28)	0.58 (-0.23)
8	122.55	125.51 (128.04)	2.35 (-2.01)
9	136.79	137.85 (135.22)	0.77 (1.90)
10	137.54	139.07 (139.28)	1.10 (-0.15)
11	157.14	159.47 (159.03)	1.46 (0.27)
12	164.14	163.37 (167.51)	-0.47 (-2.50)
13	180.25	181.66 (184.56)	0.76 (-1.60)
14	188.77	187.85 (188.30)	-0.49 (-0.24)
15	206.02	210.49 (205.38)	2.08 (2.43)
16	214.35	213.77 (216.23)	-0.27 (-1.15)
17	219.63	226.71 (217.92)	3.10 (3.87)
18	226.65	232.79 (227.42)	2.63 (2.31)
19	233.27	244.35 (239.38)	4.53 (2.03)
20	235.84	246.23 (239.98)	4.22 (2.54)

Table 3 The elastic properties for skin and core

Density (Kg/m ³)	Shear modulus (GPa)			Poisson's ratio			Young's modulus (GPa)			Location	Material set no.
	G _{yz}	G _{xz}	G _{xy}	ν_{yz}	ν_{xz}	ν_{xy}	E _z	E _y	E _x		
7830	11.54			0.30			30			Face sheet	1
1800	3.28	4.14	4.14	0.26	0.26	0.26	8.27	8.27	38.6	Face sheet	2
250	0.108			0.39			0.30			Core	

Set 1. [9]
Set 2. [11, 12]

considered here. Different quantities for the angle of trapezoidal shape ($\theta = 30^\circ, 45^\circ$ and 60°) were also considered in order to design an optimum shape of the corrugation against vibration of the sandwich structure. Also, the variations of the layup angle in the composite face sheets (φ) is regarded in this paper. Tables 4 and 5 give the vibration modes of a simply supported and clamped anti-symmetric (0/90/C/0/90) corrugated sandwich plate, respectively.

The corrugated sandwich panel which is considered in the present study has the thickness ratio of $h/a = 0.1$. Tables 6, 7 and 8 give the obtained vibration modes for a clamped sandwich plate (0/ φ /C/0/ φ) with the trapezoidal angle of ($\theta = 30^\circ, 45^\circ$ and 60°), respectively. Layup angle for the corrugated face sheets

Table 4 Numerical frequencies (Hz) of the simply supported trapezoidally sandwich panel for a layup (0/90/C/0/90) (0/90/C/0/90)-(SSSS)

NO. mode	$\theta = 30^\circ$	$\theta = 45^\circ$	$\theta = 60^\circ$
1	196.37	194.21	195.77
2	310.26	289.33	296.28
3	460.90	438.30	451.64
4	483.42	463.29	462.73
5	483.52	473.76	471.61
6	484.00	474.12	471.76
7	540.69	534.63	538.86
8	683.31	616.50	637.98
9	674.78	645.71	661.46
10	683.46	652.73	664.08
11	749.83	752.89	747.30
12	817.07	803.27	815.15
13	844.61	808.86	819.04
14	891.25	814.89	835.48
15	931.14	920.29	922.20
16	957.76	938.61	938.53
17	959.59	946.94	942.08
18	966.70	965.85	1003.80
19	1043.10	983.29	1012.50
20	1048.90	992.75	1030.60

varies between 0° and 90° with a step size of 15° , as can be seen in the mentioned tables. A corrugated sandwich plate with simply supported boundary conditions is considered in Tables 9, 10 and 11.

In order to investigate the effects of layup angle on the vibration behavior of the corrugated sandwich plates in a better manner, the obtained vibration modes are plotted against layup angles of the composite face sheets for the sandwich plates with trapezoidal angle of ($\theta = 30^\circ$, 45° and 60°). A figs. 6 and 7 shows these variations for the clamped and simply supported sandwich plates, respectively.

5 Conclusion

According to the obtained numerical results, the sandwich plate with a trapezoidal angle of 30° has the best to resist against higher vibration modes in modes compared to the sandwich plates with trapezoidal angles of 45° and 60° . This is because according to the geometrical shape, sandwich plates with a trapezoidal angle of 30° have less volume and thus less weight compared to the sandwich plates with trapezoidal angles of 45° and 60° in a same width.

Table 5 Numerical frequencies (Hz) of the clamped trapezoidally sandwich panel for a layup (0/90/C/0/90) (0/90/C/0/90)-(CCCC)

NO. mode	$\theta = 30^\circ$	$\theta = 45^\circ$	$\theta = 60^\circ$
1	266.64	262.41	263.18
2	384.12	363.45	370.31
3	503.81	504.70	502.45
4	555.47	518.48	530.04
5	595.30	587.19	589.49
6	675.17	671.01	690.72
7	737.16	705.51	721.23
8	756.09	716.14	722.04
9	783.00	785.58	778.55
10	858.51	854.71	853.07
11	906.82	872.45	884.13
12	936.11	887.13	910.79
13	980.68	968.78	967.97
14	1025.50	1021.40	1063.70
15	1069.70	1056.30	1071.40
16	1073.80	1059.30	1071.40
17	1104.40	1063.40	1073.50
18	1108.40	1076.90	1099.30
19	1132.90	1109.10	1113.20
20	1142.20	1137.90	1131.30

Table 6 Natural vibration frequencies [HZ] of corrugated sandwich plates with boundary condition (CCCC) and $= 30^\circ 0/\varphi/C/0/\varphi$

Mode Φ [deg]	1	2	3	4
0	262.02	381.96	495.97	549.98
15	260.95	381.94	495.22	550.61
30	259.22	381.92	493.57	551.77
45	259.11	382.16	493.58	552.95
60	261.31	382.79	496.83	554.13
75	264.80	383.66	501.58	555.09
90	266.64	384.12	503.81	555.47

As can be seen in the Figs. 6 and 7, vibration modes vary parabolic against the layup angle and the minimum quantity for the vibration mode belongs to sandwich plates with a layup angle of 45° . Also, the numerical results demonstrated that sandwich plates with the trapezoidal angle of 30° and layup angle of 90° have a higher frequency compare to the other sandwich plates. For sandwich plates with composite angle layup between 0 and 75° and simply support boundary conditions, the trapezoidal corrugated sandwich plate with trapezoidal angle of 60 has largest natural frequency. Also, for sandwich plates with composite angle layup between

Table 7 Natural vibration frequencies [HZ] of corrugated sandwich plates with boundary condition (CCCC) = 45° $0/\varphi/C/0/\varphi$

Mode Φ [deg]	1	2	3	4
0	257.32	361.65	496.81	514.41
15	256.13	361.62	494.45	515.19
30	254.30	361.65	492.09	516.56
45	254.28	361.99	492.22	517.69
60	256.72	362.56	496.21	518.41
75	260.46	363.18	501.94	518.61
90	262.41	363.45	504.70	518.48

Table 8 Natural vibration frequencies [HZ] of corrugated sandwich plates with boundary condition (CCCC) = 60° , $0/\varphi/C/0/\varphi$

Mode Φ [deg]	1	2	3	4
0	263.68	368.23	503.28	525.77
15	262.09	368.32	501.14	526.50
30	259.42	368.58	497.23	527.8
45	258.35	368.96	495.58	529.07
60	259.59	369.53	497.36	529.88
75	261.94	370.09	500.82	530.12
90	263.18	370.31	502.45	530.04

Table 9 Natural vibration frequencies [HZ] of corrugated sandwich plates with boundary condition (SSSS) = 30° , $0/\varphi/C/0/\varphi$

Mode Φ [deg]	1	2	3	4
0	189.43	307.84	478.22	547.72
15	188.30	308.26	446.07	539.31
30	187.44	309.78	481.17	537.82
45	188.12	310.88	482.78	537.28
60	190.23	310.58	483.27	537.40
75	193.92	310.12	483.30	539.07
90	196.37	310.26	483.47	540.70

Table 10 Natural vibration frequencies [HZ] of corrugated sandwich plates with boundary condition (SSSS) = 45° $0/\varphi/C/0/\varphi$

Mode Φ [deg]	1	2	3	4
0	187.15	287.28	434.46	532.57
15	185.74	287.72	435.66	531.11
30	184.40	289.28	438.10	529.49
45	184.94	290.34	439.61	529.25
60	187.35	289.88	439.47	530.17
75	191.53	289.26	438.46	532.74
90	194.21	289.33	438.30	534.63

Table 11 Natural vibration frequencies [HZ] of corrugated sandwich plates with boundary condition (SSSS) = 60° , $0/\varphi/C/0/\varphi$

Mode Φ [deg]	1	2	3	4
0	193.26	293.74	448.02	536.12
15	191.37	294.36	449.18	535.25
30	189.80	294.8	449.9	534.34
45	189.09	297.34	453.26	534.65
60	190.6	297.22	454.88	535.18
75	193.74	296.24	452.02	537.34
90	195.77	296.28	451.64	538.86

Fig. 6 Vibration natural frequency mode graph base on the change the layer layup for boundary (CCCC), $0/\varphi/C/0/\varphi$

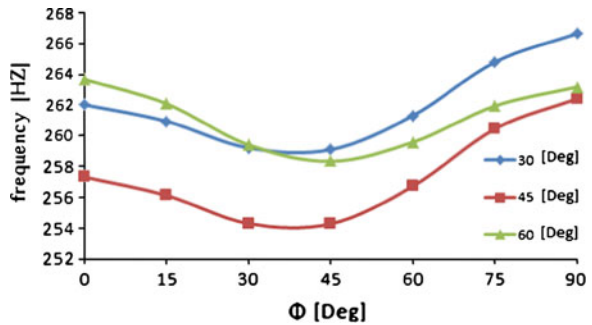
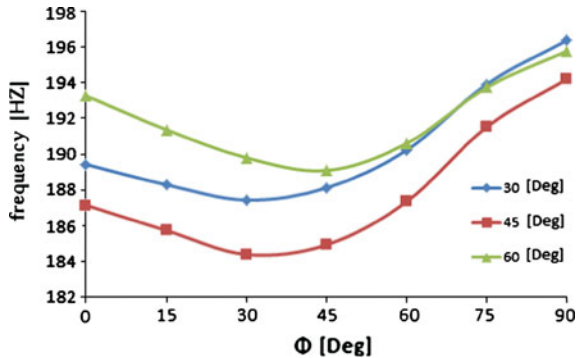


Fig. 7 Vibration natural frequency mode graph base on the change the layer layup for boundary (SSSS), $0/\varphi/C/0/\varphi$



75 and 90° and simply support boundary conditions, the trapezoidal corrugated sandwich plate with trapezoidal angle of 30 has largest natural frequency.

Acknowledgments The work that is described in this chapter was supported by the Islamic Azad University of Qazvin.

References

1. Timoshenko, S.: Theory of elastic stability. McGraw-Hill Book Co., New York (1936)
2. Timoshenko, S., Woinowski-Krieger, S.: Theory of plates and shells. McGraw-Hill Book Co., New York (1959)
3. Seydel, E.B.: Schubkinckversuche mit wellblechtafeln, Jahrbuch d. deutsch.Versuchsanstaltfürluftfahrt. e.V. München und Berlin, p 233–5 (1931)
4. Gough, G.S., Elam, C.F., DeBruyne, N.A.: The stabilization of a thin sheet by continuous supporting medium. J. Roy. Aero. Soc. **44**, 12–43 (1940)
5. Frostig, Y., Baruch, M.: Buckling of simply-supported sandwich beams with transversely flexible core a high order theory. J. ASCE. EM. Div. **119**(3), 476–495 (1993)
6. Frostig, Y., Baruch, M.: Free vibration of sandwich beams with a transversely flexible core: a high order approach. J. Sound Vib. **176**(2), 195–208 (1994)
7. Frostig, Y., Baruch, M.: Localized load effects in high-order bending of sandwich panels with transversely flexible core. J. ASCE. EM. Div. **122**(11), 1069–1076 (1996)
8. Liew, K.M., Teo, T.M: Three-dimensional vibration analysis of rectangular plates based on differential quadrature method. **220**(4), 577–599 (1999)
9. Liew, K.M., Peng, L.X., Kitipornchai, S.: Vibration analysis of corrugated Reissner-Midline plates using a mesh-free Galerkin method. **51**, 642–652 (2009)
10. Reany, J., Grenestedt, J.L.: Corrugated skin in a foam core sandwich panel. Compos. Struct. **89**(3), 345–355 (2009)
11. KAW Autar, K.: Mechanics of composite materials. Edition by Tylor (2006)
12. Birman, V., Bert, CH.W., Wrinkling of composite-facing sandwich panels under biaxial loading. **6**, 217 (2004)

A New High Strength 0–3 PZT Composite for Structural Health Monitoring

Mohammad Ehsan Edalat, Mohammad Hadi Behboudi,
Alireza Azarbayjani and Mohammad Mahdi Kheirikhah

Abstract Lead Zirconate Titanate (PZT) cement-based composites are used in structural health monitoring. These composites are fabricated from Portland cement matrix and PZT powder under high pressure by steam curing to potential applications in civil engineering. Some researchers proposed different PZT cement-based composites for structural health monitoring (Zhang, *J Cement Concrete Res* 32:825, 2002; Li et al. *J Cement Concrete Res* 27:27, 2005; Xin et al. *J Eur Ceram Soc* 25:3223–3228, 2005; Shifeng et al. *J Ferroelectr* 187, 2006) , which all of them do not have acceptable tensile and compressive strengths. Therefore these cement-based composites cannot be used as structural members. In this study, to eliminate this disadvantage, a new 0–3 Nano-PZT cement based composite is proposed which has excellent high tensile and compressive strengths and good vibration signal sensing ability. This composite contains quartz aggregates and mentioned materials. 96 standard specimens were constructed and tested according to ASTM C-39 and ASTM C-1583 standard codes requirements under different terms and conditions. The results show that the tensile and compressive strengths of this new proposed composite are about 12 times higher than the recent 0–3 Nano-PZT cement-based composites which were proposed by Zhang (J

M. E. Edalat (✉) · M. M. Kheirikhah
Islamic Azad University, Qazvin Branch, Faculty of Industrial and Mechanical Engineering,
Qazvin, Iran
e-mail: mechanicaleng.mee@gmail.com

M. M. Kheirikhah
e-mail: kheirikhah@qiau.ac.ir

M. H. Behboudi · A. Azarbayjani
Islamic Azad University, Qazvin Branch, Faculty of Architecture and Civil Engineering,
Qazvin, Iran
e-mail: civileng.hadi2006@gmail.com

A. Azarbayjani
e-mail: ali.civileng11@gmail.com

Cement Concrete Res 32:825, 2002), Li et al. (J Cement Concrete Res 27:27, 2005), Shifeng et al. (J Ferroelectr 187, 2006). Also experimental tests indicated that the piezoelectric properties of the present new PZT composite are in good agreement with theoretical and experimental results (Banno, *Advanced Ceramics*, p. 8, Oxford University Press, Oxford, 1988; Mazur, *Ferroelectric Polymers: Chemistry, Physics and Applications*, p. 539, New York: Inc., New York, 1995).

Keywords Cement-based composite · Nano-PZT powder · Quartz aggregate · Compressive strength · Piezoelectric strain factor

1 Introduction

By the modern development of civil engineering, the health monitoring of structures is being introduced. Real-time structural health monitoring systems can provide instantaneous information on the condition of a specified structure such as huge bridges and towers. This will result in a significant increase of safety margin and reductions in maintenance cost [7–9].

Also recent advances in smart sensor technologies have provided various tools for structural health monitoring of civil engineering structures and introduced a concept of smart structures [10]. So, different types of sensors have been designed and used according to these applications. It is noted that the sensors suitable for application in other engineering fields, such as mechanical engineering, may not be applicable in civil engineering due to the differences in the properties between sensor and the host. Thus, a new kind of sensor should be developed to meet the requirements of civil engineering applications.

Piezoelectric materials have attracted great attention in research activities towards the applications of sensors and actuators [11–14]. Smart materials, especially piezoceramics, find a wide range of applications in many industries for active vibration control, shape control and health monitoring of structures. These piezoceramics have been extensively studied in recent years for actuator and sensor applications because of their high electro- mechanical coupling coefficient and it is well known that the mechanical and electrical responses of a piezoelectric material are coupled.

By composition the piezoceramics such as lead zirconatetitanate (PZT) and cement-based composites can provide a suitable and reliable new cement-based composite with sensory effect [15].

Different kind of PZT cement-based composites have been designed and fabricated by many different connectivity patterns, among which the 0–3 connectivity is the simplest. A 0–3 cement-based piezoelectric composite consists of a three dimensionally connected cement load with active piezoelectric ceramic particles connected in zero dimensions [16].

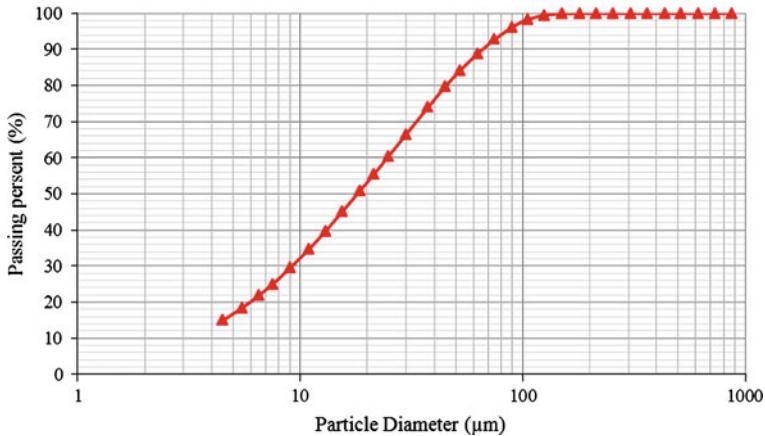


Fig. 1 Cement particles diameter (m)

The fabrication and the sensory effect of 0–3 and 2–2 cement matrix piezoelectric composites have been presented in earlier reports. But it seems that they do not have any especial mechanical strength.

In this study, at first the strength reported in previous studies has been surveyed. Then, a novel high strength 0–3 Nano-PZT cement-based composite which consists of Portland cement as a matrix, homogenously distributed either PZT Nanoparticles or quartz aggregates as a ferroelectric phase is proposed and tested. The influences of quartz aggregates on the dielectric and piezoelectric properties of the composites are then examined.

2 Experiments

It has been reported that the ceramic particle size can affect the ferroelectric properties of 0–3 piezoelectric composites. The composites with larger piezoelectric particles had higher d_{33} values, but also higher dielectric losses. So, in this study, for the first time, in addition to using nano-PZT powder, quartz aggregates were used to achieve high strength beside a suitable d_{33} value.

Also in the present study, PZT powders were obtained by ball milling commercial PZT ceramic pieces (SAHRA LTD CO) and sieved through nylon meshes to get the particle size fraction.

As the results of tests, the mean diameter of PZT powder is 19.63 nm. Figure 1 shows that the mean diameter of Portland cement is 27.15 m and Fig. 2 shows that quartz aggregates after sieving through meshes reveal a particle size fraction from 0 to 4.75 mm.

To prepare this composite, quartz aggregates, nano-PZT powder and cement paste (9) were mixed in eight different ratios. Table 1 presents these eight different

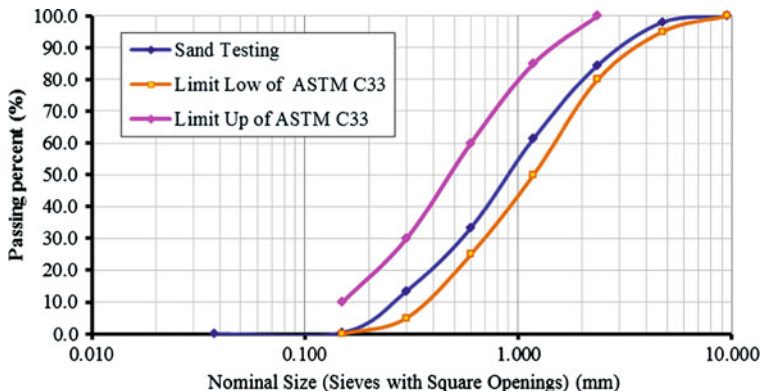


Fig. 2 Particle size distribution of quartz aggregates

Table 1 Volume fraction of used materials of 8 different mix design (%)

	MD ^a -1	MD-2	MD-3	MD-4	MD-5	MD-6	MD-7	MD-8
Ratio of sand to nano-PZT	97.5/2.5	95/5	92.5/7.5	90/10	87.5/12.5	85/15	82.5/12.5	80/20
Sand aggregates	68.39	67.02	65.65	64.28	62.91	61.53	60.16	58.79
Nano-PZT powder	1.37	2.74	4.11	5.48	6.85	8.23	9.60	10.97
Cement	12	12	12	12	12	12	12	12
Water	17.5	17.5	17.5	17.5	17.5	17.5	17.5	17.5
Carbon black	0.7	0.7	0.7	0.7	0.7	0.7	0.7	0.7
Super-plasticizer	0.04	0.04	0.04	0.04	0.04	0.04	0.04	0.04

^a MD is abbreviation of mix design

mixing ratios and attention should be given to the different volume ratios of used aggregates to the value of ceramics powder.

It is noted in this study, for all of the constructed specimens that the ratio of cement to water (c/w) is 50 which is a common normal value to produce a normal concrete.

To achieve a uniform mixture, cement and ceramics powder and quartz particles were mixed thoroughly first, then water and super-plasticizer were added into the mixture. The mixing process was continued until the mixture became uniform. Then the mixture was compacted into the metal (or plastic) 50 × 50 × 50 mm cubic model which produced 96 specimens according to the experimental requirements.

After casting, the specimens were put in the curing room with a temperature of 23 °C and relative humidity of 90 % for 3, 7 and 28 days, respectively.

Then after curing, specimens could be placed under an electrical field undergo a polarization process. To this end, after each mentioned aging time, the different specimens were placed under a 45 kV/mm electrical field. A key technique for fabrication of piezoelectric materials is the polarizing procedure. As this process

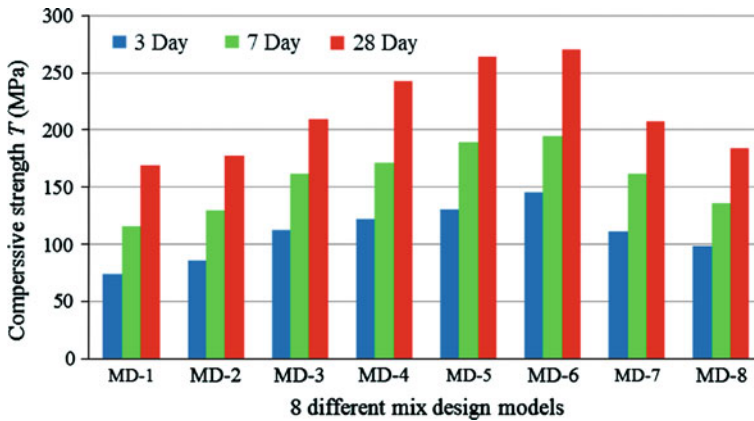


Fig. 3 Compressive strength of 3, 7 and 28 days aged mix design models

should be done at high temperature, this can produce some problems to achieve the main research goal. Hongyu et al. presented that by adding a small amount of carbon black can facilitate the polling process [17]. So by kindly attention to that, 0.7 % of volume carbon black was added to the mixture. Thereby polarizing was carried out at room temperature too.

After the preparation procedures, the compressive strength T and piezoelectric strain factor d_{33} of specimens were measured by a 300 ton and a Model ZJ-3A d_{33} meter, respectively. The entire tests were carried out at 23 °C and 45 % relative humidity.

3 Results and Analysis

As mentioned before, the main goal of this research is to achieve a new kind of cement based composite which has in addition a high strength and piezoelectric properties (Fig. 3).

The main goal in this study is to investigate the effect of quartz aggregates PZT nano-powder contents on the compressive strength T and the piezoelectric strain factor d_{33} .

These factors have been determined and analyzed, respectively, and the results presented blow:

3.1 Effect of Quartz Aggregates and PZT Nano-Powder Contents on Compressive Strength T

The difference between eight mixing designs is in the used aggregate content and PZT powder content. These content, cf. Table 1. It can be seen in Fig. 4 that the compressive strength is improved by relative increasing of the used nano-PZT

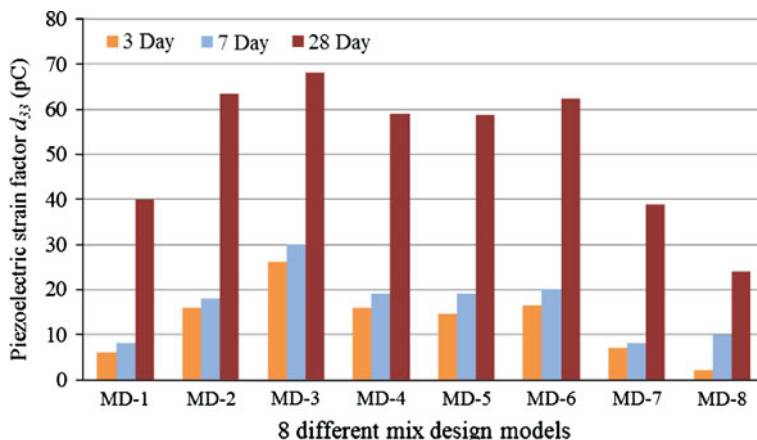


Fig. 4 Piezoelectric strain factor of 3, 7 and 28 days aged mix design models

powder up to the 15 % of the total volume and decreasing the content of aggregates up to 85 % of the total volume. However, this procedure is not permanent. This Means that increasing the PZT powder and decreasing quartz aggregates will cause strength by a deduction in compressive strength; so that the strength of MD-7 by ratio of 82.5/17.5 is lower than MD-3 by a ratio of 92.5/7.5.

So, the highest value of compressive strength was belonged to MD-6 specimen by ratio of 85/15.

3.2 Effect of Quartz Aggregates and PZT Nano-Powder Contents on Piezoelectric Strain Factor d_{33}

As well as quartz has a high piezoelectric capacity, it can have a great effect on the piezoelectric strain factor d_{33} of composite, in addition of nano-PZT powder. This can be proven by attention to Fig. 4 which shows d_{33} values of different 3, 7 and 8 days aged specimens.

As shown in Fig. 4, sample MD-3 has the highest d_{33} value. After that, samples MD-2 and MD-6 were allocated the maximum values.

This figure shows that medial compounds in Table 1 are the most appropriate combination of powder and sand aggregates which have greater values than the initial and final mix design models in Table 1.

According to this, it is not possible to consider a linear relation for the effect of quartz aggregates and Nano-PZT powder contents on the piezoelectric strain factor of composites.

So, considering all the mentioned findings it can be concluded that model MD-6 is the best model; because its high compressive strength and d_{33} values are in high position.

Although, MD-5 and MD-3 have a great values in compressive strength and d_{33} respectively; but they do not have an acceptable amounts of d_{33} and strength respectively. Since both factors must be considered together, no one of them can be considered as an eligible model.

4 Conclusions

The following conclusions can be drawn from the current study:

- (1) A new kind of cement based composite showing good performance has been prepared using quartz aggregates and Nano-PZT powder.
- (2) Different amount of mixing of quartz sand and PZT powder had different effects on strength and piezoelectric behavior of the composite.
- (3) The piezoelectric strain coefficient d_{33} and compressive strength T were determined as a function of volume fraction of quartz aggregates and nano-PZT powder in the composite. It was found that a limited amount of quartz sand of about 85.0 vol. % and nano-PZT powder of about 15.0 vol. % was optimum for enhancing the high compressive strength and piezoelectric properties of the composite.
- (4) Because of its high strength, it can be easily used as an intelligent member structure which has vibration sensing properties.

References

1. Zhang, D., Li, Z., Wu, K.: 2-2 Piezoelectric cement matrix composite: Part II. Actuator effect. *J. Cement Concrete Res.* **32**, 825 (2002)
2. Li, Z., Dong, B., Zhang, D.: Influence of polarization on properties of 0–3 cement-based PZT composites. *J. Cement Concrete Res.* **27**, 27 (2005)
3. Xin, C., Shifeng, H., Jun, C., Ronghua, X., Futian, L., Lingchao, L.: Piezoelectric and dielectric properties of piezoelectric ceramic–sulphoaluminate cement composites. *J. Eur. Ceram. Soc.* **25**, 3223–3228 (2005)
4. Shifeng, H., Lingchao, L., Jun, C., Dongyu, X., Futian, L., Xin, C.: Influence of Ceramic Particle Size on Piezoelectric Properties of Cement-Based Piezoelectric Composites. *J. Ferroelectr.* 187 (2006)
5. Banno, H.: *Advanced Ceramics*, p. 8. Oxford University Press, Oxford (1988)
6. Mazur, K.: *Ferroelectric Polymers: Chemistry, Physics and Applications*, p.539. New York: Inc., New York (1995)
7. Chang, F.K.: Lancaster. Technomic Publishing Co. Inc., Pennsylvania (1999)
8. Tzou, H.S., Guran, A.: *Structronics systems: smart structures, devices and systems (Parts I & II)*. World Scientific, Singapore (1998)
9. Aizawa, S., Kakizawa, T., Higasino, M.: Case studies of smart materials for civil structures. *Smart Mater. Struct.* **7**(5), 617–626 (1998)

10. Liu, S.C., Tomizuka, M., Ulsoy, G.: Strategic issues in sensors and smart structures. *Struct. Control Health Monit.* **13**(6), 946–957 (2006)
11. Wetherhold, R.C., Panthalingal, N.: Smart structures and materials. SPIE. P 266–274 (1993)
12. Xu, Y.: *Ferroelectric materials and their applications*. Amsterdam: North-Holland (1991)
13. Furukawa, T.: Piezoelectricity and pyroelectricity in polymers. *IEEE Trans. Electrical Insul.* **24**(3), 375–394 (1989)
14. Okazaki, K.: Developments in fabrication of piezoelectric ceramics. In: Taylor, G.W., Gagnepain, J.J., Meeker, T.R., Nakamura, T., Shuvalov, L.A. (eds.) *Piezoelectricity*, pp. 131–150. Gordon and Breach Science Publishers, Switzerland (1985)
15. Li, Z., Zhang, D., Wu, K.R.: Cement-based 0-3 piezoelectric composites. *J. Am. Ceram. Soc.* **85** (2), 305–313 (2002)
16. Newnham, R.E., Skinner, D.P., Cross, L.E.: *Mater. Res. Bull.* **13**, 525–536 (1978)
17. Hongyu, G., Zongjin, L., Yujun, Z., Runhua, F.: Piezoelectric and dielectric behavior of 0-3 cement-based composites mixed with carbon black. *J. Eur. Ceram. Soc.* **29**, 2013–2019 (2009)

Free Vibration Analysis of Sandwich Plates with Temperature-Dependent Properties of the Core Materials and Functionally Graded Face Sheets

Y. Mohammadi and S. M. R. Khalili

Abstract In the present chapter, the free vibration of sandwich plates with power-law functionally graded face sheets in different thermal environments is performed. The material properties of the core, such as Young's modulus, density, thermal expansion coefficient and Poisson's ratio, are assumed to be temperature dependent by a nonlinear function of temperature and the material properties of the face sheets are assumed to vary continuously through the thickness according to a power-law distribution in terms of the volume fractions of the constituents. Both un-symmetric and symmetric sandwich plates are considered in this analysis. A new approach is used to reduce the equations of motion from twenty three equations to eleven equations and then solve them. The new solution approach consists of isolating six of the unknowns in the displacements of the face sheets using the compatibility equations, followed by isolating the additional six Lagrange multipliers using the equations of the face sheets. Finally, the isolated unknowns are substituted into the eleven equations of the core. Good agreement is found between theoretical predictions of the fundamental frequency parameters and the results obtained from other references for simply supported sandwich plates with FG face sheets. The results also reveal that as the side-to-thickness

Y. Mohammadi
Qazvin Branch, Faculty of Industrial and Mechanical
Engineering, Islamic Azad University, Qazvin, Iran
e-mail: u.mohammadi@gmail.com

S. M. R. Khalili
Center of Excellence for Research in Advanced Materials and Structures,
Faculty of Mechanical Engineering, K. N. Toosi University of Technology,
Tehran, Iran

S. M. R. Khalili (✉)
Faculty of Engineering, Kingston University, London, UK
e-mail: smrkhalili2005@gmail.com

ratio, the core-to-face sheet thickness ratio and temperature changes, affect the fundamental frequency parameters significantly.

1 Introduction

Most of the classical models ignore the effects of the transversely flexible core, such as changes of the height of the sandwich plate, non-linearity of the section plane after deformation, and different boundary conditions at the upper and the lower face sheets. Hence, when using these models for the free vibration response, the through thickness modes of the core cannot be detected. The classical linear and non-linear analytical approaches, see for example Allen [1], Plantema [2], and some recent comprehensive reviews, such as Librescue [3], emphasize on traditional sandwich panels made of metallic, anti-plane, incompressible honeycomb cores and fully bonded face sheet-core interfaces. These models assume that the face sheets have only bending rigidity, while the core has only shear rigidity. For the prediction of the overall load response of sandwich plates subjected to bending, shearing and buckling loads, as well as undergoing free or forced vibrations, most analyses adopt the so-called “equivalent single layer” approach based on the first-order shear deformable model, see Mindlin [4], or based on a high-order approach, see Reddy [5].

The non-planar deformed cross-section of the sandwich beam, observed experimentally by Petras and Sutcliffe [6], suggest the need for a model which allows non-linear variations of in-plane and vertical displacement fields through the core. But, the simple beam theory where the core in-plane displacements are assumed to vary in a linear way through the depth, and the out-of-plane displacements are assumed to be constant. Frostig and Baruch [7, 8] used variational principles and then introduced the high-order sandwich panel theory (HSAPT), which includes the transverse flexibility of the core. This theory has been successfully used by different authors for the analysis of various linear and non-linear applications. Frostig and Thomsen [9] used the HSAPT to analysis the vibration of sandwich plates; Malekzadeh et al. [10] analysed the local and global damped vibrations of sandwich plates by an improved HSAPT. But in the HSAPT model, they always neglected the in-plane stresses of the core, because in their analysis the core in the sandwich structures has only out-of-plane strength.

The improved model used in the present chapter considers both in-plane and out-of-plane strength for the core and assumes that the distribution of the in-plane and vertical displacements of the core can be represented as cubic and quadratic polynomials, respectively [11]. The variational principle of minimum of the total potential energy is used to derive the field equations along with the appropriate boundary conditions. Here, the high-order stress resultants of the non-uniform core are determined using a direct integration process, and since, the core in-plane stresses considered in this improved model, twelve in-plane high-order stress

resultants as well as eight out-of-plane high-order stress resultants are available. It should be noticed that this improved model which involves high-order core stress resultants, has no physical interpretation and the model yields high-order modes that involve vibrations through the depth of the core that the HSAPT model cannot detect. Therefore, in this chapter, the “displacements formulation” model is extended to the case of free vibration of sandwich plates with power-law FG face sheets and temperature dependent properties of the face sheets material properties, considering the core in-plane stresses. Also, it should be noticed here that both unsymmetric and symmetric sandwich plates are considered.

Functionally graded materials (FGMs) are presently in the forefront of material research receiving worldwide attention [12]. The considerable advantages offered by FGMs over conventional materials and the need of overcoming the technical challenges involving high temperature environments have prompted an increased use of sandwich structures, and incorporation in their construction of FGMs as face sheets [12, 13]. A typical advanced construction of a sandwich plate consists of two FG face sheets, not necessarily identical, is considered in the present chapter.

An extensive literature review reveals that only a limited research works are available that take into account the temperature-dependent properties of the core material properties in their analysis. For example, Frostig and Thomsen [11] analysed the free vibration of sandwich beams with temperature dependent core material properties.

Another novel contribution of the present work is the use of a new approach to reduce the equations of motion from twenty three equations which are the functions of core constants, face sheets constants and Lagrange constants to eleven equations that are just the functions of eleven core constants. Finally, the numerical results are used to show the effects of temperature changes, volume fraction distribution of FG face sheets, side-to-thickness ratio and core-to-face sheet thickness ratio on the free vibration characteristics of the defined sandwich plate.

2 Formulation

The equations of motions of the free vibration response of sandwich plate are derived through the Hamilton’s principle which extremists the Lagragian that consists of the kinetic and the internal potential energy as follows [5]:

$$\int_{t_1}^{t_2} (\delta T + \delta U) dt = 0 \quad (1)$$

where T and U are kinetic energy and internal potential energy, respectively; t is the time coordinate that varies between the times t_1 and t_2 ; and δ denotes the variational operator.

Consider a sandwich plate of length a and width b , consisting of a core with thickness h_c , Young’s and shear modulus E_c and G_c , respectively, and two FG face sheets with thicknesses h_t and h_b , Young’s modulus $E_i (i = t, b)$ and Poisson’s ratio $\nu_i (i = t, b)$. Subscripts t and b denote upper and lower face sheets, respectively. The first variation of the kinetic energy for the sandwich plates with FG face sheets and temperature dependent properties of the core materials reads [5]:

$$\int_{t_1}^{t_2} \delta T dt = - \int_{t_1}^{t_2} \left\{ \int_{t_1}^a \int_{t_1}^b \int_{0}^{h_t/2} \rho_t(z_t) (\ddot{u}_t \delta u_t + \ddot{v}_t \delta v_t + \ddot{w}_t \delta w_t) dz_t dy dx \right. \\ + \int_{t_1}^a \int_{t_1}^b \int_{0}^{h_b/2} \rho_b(z_b) (\ddot{u}_b \delta u_b + \ddot{v}_b \delta v_b + \ddot{w}_b \delta w_b) dz_b dy dx \quad (2) \\ \left. + \int_{t_1}^a \int_{t_1}^b \int_{0}^{h_c/2} \rho_c(T_c) (\ddot{u}_c \delta u_c + \ddot{v}_c \delta v_c + \ddot{w}_c \delta w_c) dz_c dy dx \right\} dt$$

where T_c is the temperature variation of the core; $\rho_t(z_t)$ and $\rho_b(z_b)$ are the density of the upper and lower FG face sheets, respectively, that vary in the thickness direction with z_t and z_b by power-law function of FGMs; and $\rho_c(T_c)$ is the density of the core that varies with temperature; Subscript c corresponds to the core; z_t, z_b and z_c are the vertical coordinates of the upper and lower face sheets and the core, respectively, and are measured downward from the mid-plane of each constituents; u_i, v_i and $w_i (i = t, b, c)$ are the displacements in the x, y and vertical directions, respectively, for the sandwich plate constituents; \ddot{u}_i, \ddot{v}_i and $\ddot{w}_i (i = t, b, c)$ are the accelerations in the x, y and vertical directions, respectively, for the sandwich plate constituents.

The material properties for the core, P , such as Young’s modulus, density, thermal expansion coefficient and Poisson’s ratio, can be expressed as a nonlinear third-order function of temperature as follows [14]:

$$P = C_0 (C_{-1} T^{-1} + 1 + C_1 T + C_2 T^2 + C_3 T^3) \quad (3)$$

where C_0, C_{-1}, C_1, C_2 and C_3 are unique to the constituent materials; and $T = T_0 + \Delta T$ where $T_0 = 300$ K.

Considering small deformations and rotations, the kinematic relations for the face sheets are based on Bernoulli’s assumptions. In this model, the displacement fields in the core are assumed a priori, using the quadratic and cubic polynomial distributions [11]. Here, the coefficients of these polynomials are the unknowns, and they are determined through the variational principle. The pre-assumed displacement field of the core is as follows:

$$u_c(x, y, z_c, t) = u_0(x, y, t) + u_1(x, y, t)z_c + u_2(x, y, t)z_c^2 + u_3(x, y, t)z_c^3 \quad (4)$$

$$v_c(x, y, z_c, t) = v_0(x, y, t) + v_1(x, y, t)z_c + v_2(x, y, t)z_c^2 + v_3(x, y, t)z_c^3 \quad (5)$$

$$w_c(x, y, z_c, t) = w_0(x, y, t) + w_1(x, y, t)z_c + w_2(x, y, t)z_c^2 \quad (6)$$

Where u_k and v_k ($k = 0, 1, 2, 3$) are the unknowns of the in-plane displacements of the core, and w_l ($l = 0, 1, 2$) are the unknowns of the core vertical displacements. The compatibility conditions, assuming perfect bonding between the core and the face sheets, at the upper and the lower face sheet–core interfaces, are as follows:

$$u_t(z_t = h_t/2) = u_c(z_c = -h_c/2) \quad (7)$$

$$v_t(z_t = h_t/2) = v_c(z_c = -h_c/2) \quad (8)$$

$$w_t = w_c(z_c = -h_c/2) \quad (9)$$

$$u_c(z_c = h_c/2) = u_b(z_b = -h_b/2) \quad (10)$$

$$v_c(z_c = h_c/2) = v_b(z_b = -h_b/2) \quad (11)$$

$$w_c(z_c = h_c/2) = w_b \quad (12)$$

The compatibility conditions at the upper and the lower face sheet–core interfaces are enforced through the use of six Lagrange multipliers. Thus, the first variation of the internal potential energy is as follows:

$$\begin{aligned} \delta U = & \int_{V_t} \left(\sigma'_{xx} \delta \varepsilon'_{xx} + \sigma'_{yy} \delta \varepsilon'_{yy} + \tau'_{xy} \delta \gamma'_{xy} \right) dV + \int_{V_b} \left(\sigma^b_{xx} \delta \varepsilon^b_{xx} + \sigma^b_{yy} \delta \varepsilon^b_{yy} + \tau^b_{xy} \delta \gamma^b_{xy} \right) dV \\ & + \int_{V_{core}} \left(\tau^c_{xz} \delta \gamma^c_{xz} + \tau^c_{yz} \delta \gamma^c_{yz} + \sigma^c_{zz} \delta \varepsilon^c_{zz} + \sigma^c_{xx} \delta \varepsilon^c_{xx} + \sigma^c_{yy} \delta \varepsilon^c_{yy} + \tau^c_{xy} \delta \gamma^c_{xy} \right) dV \\ & + \delta \int_0^a \int_0^b \left[\lambda_{xt} (u_t(z_t = h_t/2) - u_c(z_c = -h_c/2)) + \lambda_{yt} (v_t(z_t = h_t/2) - v_c(z_c = -h_c/2)) \right. \\ & + \lambda_{zt} (w_t - w_c(z_c = -h_c/2)) + \lambda_{xb} (u_c(z_c = h_c/2) - u_b(z_b = -h_b/2)) \\ & \left. + \lambda_{yb} (v_c(z_c = h_c/2) - v_b(z_b = -h_b/2)) + \lambda_{zb} (w_c(z_c = h_c/2) - w_b) \right] dx dy \end{aligned} \quad (13)$$

where σ^j_{xx} and σ^j_{yy} ($j = t, b, c$) are the in-plane normal stresses and ε^j_{xx} and ε^j_{yy} ($j = t, b, c$) are the in-plane normal strains of the upper and lower face sheets and the core; τ^j_{xy} and γ^j_{xy} ($j = t, b, c$) are the in-plane shear stresses and strains in the face sheets and the core; σ^c_{zz} and ε^c_{zz} are the normal stress and strain in the vertical direction of the core; τ^c_{xz} and γ^c_{xz} are the vertical shear stress and shear strain in the core; V_t , V_b and V_{core} are the volumes of the upper and the lower face sheets and the core, respectively; λ_{xi} , λ_{yi} and λ_{zi} ($i = t, b$) are the Lagrange multipliers at the upper and the lower face sheet–core interfaces. Notice that the effects of the core in-plane stresses are considered in this formulation.

Using the Hamilton's principle, the expression of the kinetic energy and the internal potential energy, along with the acceleration distribution, the displacements distributions of the face sheets, the kinematic relations of the face sheets and the core, the compatibility conditions, the stress resultants of the face sheets, the high-order stress resultants of the core, and after some algebraic manipulation, the

twenty three equations of motion are as follows: Three equations for the upper FG face sheet:

$$N_{xx,x}^t + N_{xy,y}^t - \lambda_{xt} - I_{0t}\ddot{u}_{0t} + I_{1t}\ddot{w}_{t,x} = 0 \quad (14)$$

$$N_{yy,y}^t + N_{xy,x}^t - \lambda_{yt} - I_{0t}\ddot{v}_{0t} + I_{1t}\ddot{w}_{t,y} = 0 \quad (15)$$

$$\begin{aligned} M_{xx,xx}^t + M_{yy,yy}^t + 2M_{xy,xy}^t - \frac{h_t}{2}\lambda_{xt,x} - \lambda_{zt} - \frac{h_t}{2}\lambda_{yt,y} \\ - I_{1t}\ddot{u}_{0t,x} + I_{2t}\ddot{w}_{t,xx} - I_{1t}\ddot{v}_{0t,y} + I_{2t}\ddot{w}_{t,yy} - I_{0t}\ddot{w}_t = 0 \end{aligned} \quad (16)$$

Three equations for the lower FG face sheet:

$$N_{xx,x}^b + N_{xy,y}^b + \lambda_{xb} - I_{0b}\ddot{u}_{0b} + I_{1b}\ddot{w}_{b,x} = 0 \quad (17)$$

$$N_{yy,y}^b + N_{xy,x}^b + \lambda_{yb} - I_{0b}\ddot{v}_{0b} + I_{1b}\ddot{w}_{b,y} = 0 \quad (18)$$

$$\begin{aligned} M_{xx,xx}^b + M_{yy,yy}^b + 2M_{xy,xy}^b - \frac{h_b}{2}\lambda_{xb,x} + \lambda_{zb} - \frac{h_b}{2}\lambda_{yb,y} \\ - I_{1b}\ddot{u}_{0b,x} + I_{2b}\ddot{w}_{b,xx} - I_{1b}\ddot{v}_{0b,y} + I_{2b}\ddot{w}_{b,yy} - I_{0b}\ddot{w}_b = 0 \end{aligned} \quad (19)$$

Eleven equations for the core:

$$R_{x,x}^c + Q_{xy,y}^c + \lambda_{xt} - \lambda_{xb} - I_{0c}\ddot{u}_0 - I_{1c}\ddot{u}_1 - I_{2c}\ddot{u}_2 - I_{3c}\ddot{u}_3 = 0 \quad (20)$$

$$\begin{aligned} -Q_{xc} + M_{x1,x}^c + M_{Q1xy,y}^c - \frac{h_c}{2}\lambda_{xt} - \frac{h_c}{2}\lambda_{xb} - I_{1c}\ddot{u}_0 - I_{2c}\ddot{u}_1 - I_{3c}\ddot{u}_2 - I_{4c}\ddot{u}_3 = 0 \\ (21) \end{aligned}$$

$$\begin{aligned} -2M_{Q1xc} + M_{x2,x}^c + M_{Q2xy,y}^c + \frac{h_c^2}{4}\lambda_{xt} - \frac{h_c^2}{4}\lambda_{xb} - I_{2c}\ddot{u}_0 - I_{3c}\ddot{u}_1 - I_{4c}\ddot{u}_2 - I_{5c}\ddot{u}_3 = 0 \\ (22) \end{aligned}$$

$$\begin{aligned} -3M_{Q2xc} + M_{x3,x}^c + M_{Q3xy,y}^c - \frac{h_c^3}{8}\lambda_{xt} - \frac{h_c^3}{8}\lambda_{xb} - I_{3c}\ddot{u}_0 - I_{4c}\ddot{u}_1 - I_{5c}\ddot{u}_2 - I_{6c}\ddot{u}_3 = 0 \\ (23) \end{aligned}$$

$$R_{y,y}^c + Q_{xy,x}^c + \lambda_{yt} - \lambda_{yb} - I_{0c}\ddot{v}_0 - I_{1c}\ddot{v}_1 - I_{2c}\ddot{v}_2 - I_{3c}\ddot{v}_3 = 0 \quad (24)$$

$$\begin{aligned} -Q_{yc} + M_{y1,y}^c + M_{Q1yx,x}^c - \frac{h_c}{2}\lambda_{yt} - \frac{h_c}{2}\lambda_{yb} - I_{1c}\ddot{v}_0 - I_{2c}\ddot{v}_1 - I_{3c}\ddot{v}_2 - I_{4c}\ddot{v}_3 = 0 \\ (25) \end{aligned}$$

$$\begin{aligned} -2M_{Q1yc} + M_{y2,y}^c + M_{Q2yx,x}^c + \frac{h_c^2}{4}\lambda_{yt} \\ - \frac{h_c^2}{4}\lambda_{yb} - I_{2c}\ddot{v}_0 - I_{3c}\ddot{v}_1 - I_{4c}\ddot{v}_2 - I_{5c}\ddot{v}_3 = 0 \end{aligned} \quad (26)$$

$$\begin{aligned}
& -3M_{Q2yc} + M_{y3,y}^c + M_{Q3xy,x}^c - \frac{h_c^3}{8}\lambda_{yt} - \frac{h_c^3}{8}\lambda_{yb} \\
& - I_{3c}\ddot{v}_0 - I_{4c}\dot{v}_1 - I_{5c}\ddot{v}_2 - I_{6c}\ddot{v}_3 = 0
\end{aligned} \tag{27}$$

$$Q_{xc,x} + Q_{yc,y} + \lambda_{zt} - \lambda_{zb} - I_{0c}\ddot{w}_0 - I_{1c}\ddot{w}_1 - I_{2c}\ddot{w}_2 = 0 \tag{28}$$

$$M_{Q1xc,x} + M_{Q1yc,y} - R_{zc} - \frac{h_c}{2}\lambda_{zt} - \frac{h_c}{2}\lambda_{zb} - I_{1c}\ddot{w}_0 - I_{2c}\ddot{w}_1 - I_{3c}\ddot{w}_2 = 0 \tag{29}$$

$$M_{Q2xc,x} + M_{Q2yc,y} - 2M_{zc} + \frac{h_c^2}{4}\lambda_{zt} - \frac{h_c^2}{4}\lambda_{zb} - I_{2c}\ddot{w}_0 - I_{3c}\ddot{w}_1 - I_{4c}\ddot{w}_2 = 0 \tag{30}$$

and six compatibility conditions corresponding to perfect bonding:

$$u_{0t} - \frac{h_t}{2}w_{t,x} - u_0 + u_1\frac{h_c}{2} - u_2\frac{h_c^2}{4} + u_3\frac{h_c^3}{8} = 0 \tag{31}$$

$$v_{0t} - \frac{h_t}{2}w_{t,y} - v_0 + v_1\frac{h_c}{2} - v_2\frac{h_c^2}{4} + v_3\frac{h_c^3}{8} = 0 \tag{32}$$

$$w_t - w_0 + w_1\frac{h_c}{2} - w_2\frac{h_c^2}{4} = 0 \tag{33}$$

$$u_0 + u_1\frac{h_c}{2} + u_2\frac{h_c^2}{4} + u_3\frac{h_c^3}{8} - u_{0b} - \frac{h_b}{2}w_{b,x} = 0 \tag{34}$$

$$v_0 + v_1\frac{h_c}{2} + v_2\frac{h_c^2}{4} + v_3\frac{h_c^3}{8} - v_{0b} - \frac{h_b}{2}w_{b,y} = 0 \tag{35}$$

$$w_0 + w_1\frac{h_c}{2} + w_2\frac{h_c^2}{4} - w_b = 0 \tag{36}$$

where N_{xx}^j , N_{yy}^j , N_{xy}^j , M_{xx}^j , M_{yy}^j , M_{xy}^j ($j = t, b$) are the stress resultants and the moment resultants of the upper and the lower face sheets; I_{kt} , I_{kb} ($k = 0, 1, 2$) are the inertia terms of the upper and the lower face sheets, respectively; I_{lc} ($l = 0, 1, 2, 3, 4, 5, 6$) are the inertia terms of the core. The high-order stress resultants due to out-of-plane stresses of the core are equal to:

$$\{Q_{xc}, M_{Q1xc}, M_{Q2xc}\} = \int_{-h_c/2}^{h_c/2} (1, z_c, z_c^2)\tau_{xz}^c dz_c \tag{37}$$

$$\{Q_{yc}, M_{Q1yc}, M_{Q2yc}\} = \int_{-h_c/2}^{h_c/2} (1, z_c, z_c^2)\tau_{yz}^c dz_c \tag{38}$$

$$\{R_{zc}, M_{zc}\} = \int_{-h_c/2}^{h_c/2} (1, z_c)\sigma_{zz}^c dz_c \tag{39}$$

and since the effects of in-plane stresses of the core are considered in the present analysis, twelve high-order stress resultants due to in-plane stresses of the core also exist which are equal to:

$$\left\{ Q_{xy}^c, M_{Q1xy}^c, M_{Q2xy}^c, M_{Q3xy}^c \right\} = \int_{-h_c/2}^{h_c/2} (1, z_c, z_c^2, z_c^3) \tau_{xy}^c dz_c \quad (40)$$

$$\left\{ R_x^c, M_{x1}^c, M_{x2}^c, M_{x3}^c \right\} = \int_{-h_c/2}^{h_c/2} (1, z_c, z_c^2, z_c^3) \sigma_{xx}^c dz_c \quad (41)$$

$$\left\{ R_y^c, M_{y1}^c, M_{y2}^c, M_{y3}^c \right\} = \int_{-h_c/2}^{h_c/2} (1, z_c, z_c^2, z_c^3) \sigma_{yy}^c dz_c \quad (42)$$

The governing equations of motion are derived by substituting the stress resultants of the face sheets into the governing equations for the face sheets, and the high-order stress resultants of the core into the core equations. These equations are formulated in terms of the following twenty three unknowns: the six in-plane and vertical displacements of the face sheets, the six Lagrange multipliers and the eleven polynomial coefficients of the core. Notice that the solution of the set equations can be achieved numerically for general type of boundary conditions, but does not have a general closed-form analytical solution. However, for the particular case of a simply-supported sandwich plate, a closed-form solution exists.

3 Simply Supported Sandwich Plate

An analytical solution exists in the case of a simply supported sandwich plate where the upper and the lower face sheets are simply supported and the vertical displacements through the depth of the core at the edges of the plate are prevented. Furthermore, the face sheets are assumed to be functionally graded and the core is assumed to be isotropic. For this case, an analytical closed-form solution in the form of an infinite series of trigonometric functions, which satisfy the boundary conditions exist. The solution can be expressed as:

$$u_{0j}(x, y, t) = \left[\sum_{n=1}^N \sum_{m=1}^M C_{uj} \cos(\alpha_m x) \sin(\beta_n y) \right] e^{i\omega t}, \quad (j = t, b) \quad (43)$$

$$v_{0j}(x, y, t) = \left[\sum_{n=1}^N \sum_{m=1}^M C_{vj} \sin(\alpha_m x) \cos(\beta_n y) \right] e^{i\omega t}, \quad (j = t, b) \quad (44)$$

$$w_j(x, y, t) = \left[\sum_{n=1}^N \sum_{m=1}^M C_{wj} \sin(\alpha_m x) \sin(\beta_n y) \right] e^{i\omega t}, (j = t, b) \tag{45}$$

$$u_k(x, y, t) = \left[\sum_{n=1}^N \sum_{m=1}^M C_{uk} \cos(\alpha_m x) \sin(\beta_n y) \right] e^{i\omega t}, (k = 0, 1, 2, 3) \tag{46}$$

$$v_k(x, y, t) = \left[\sum_{n=1}^N \sum_{m=1}^M C_{vk} \sin(\alpha_m x) \cos(\beta_n y) \right] e^{i\omega t}, (k = 0, 1, 2, 3) \tag{47}$$

$$w_l(x, y, t) = \left[\sum_{n=1}^N \sum_{m=1}^M C_{wl} \sin(\alpha_m x) \sin(\beta_n y) \right] e^{i\omega t}, (l = 0, 1, 2) \tag{48}$$

$$\lambda_{xj}(x, y, t) = \left[\sum_{n=1}^N \sum_{m=1}^M C_{\lambda_{xj}} \cos(\alpha_m x) \sin(\beta_n y) \right] e^{i\omega t}, (j = t, b) \tag{49}$$

$$\lambda_{yj}(x, y, t) = \left[\sum_{n=1}^N \sum_{m=1}^M C_{\lambda_{yj}} \sin(\alpha_m x) \cos(\beta_n y) \right] e^{i\omega t}, (j = t, b) \tag{50}$$

$$\lambda_{zj}(x, y, t) = \left[\sum_{n=1}^N \sum_{m=1}^M C_{\lambda_{zj}} \sin(\alpha_m x) \sin(\beta_n y) \right] e^{i\omega t}, (j = t, b) \tag{51}$$

where $C_{uj}, C_{vj}, C_{wj}, C_{uk}, C_{vk}, C_{wl}, C_{\lambda_{xj}}, C_{\lambda_{yj}}$ and $C_{\lambda_{zj}}$ are the twenty three unknown constants of the series solution. Also, $\alpha_m = \frac{m\pi}{a}$ and $\beta_n = \frac{n\pi}{b}$ where m and n are the wave numbers, M and N are the number of terms in the truncated series, ω is the eigenfrequency of the plate, and i is the imaginary unit.

After substitution of the general term of the series into the equations of motion, along with the stress resultants of functionally graded face sheets and the high-order stress resultants of the core, the solution is determined by the use of a new approach to solve these twenty three equations of motion.

The new solution approach consists of isolating six unknown constants of the face sheets as a function of the eleven core constants using the six compatibility equations, followed by isolating the additional six Lagrange constants as a function of face sheets constants using the six equations of the face sheets. Then, the isolated unknown constants are substituted into the eleven equations of the core. Finally, there are eleven equations in terms of the eleven core constants. Thus, although the full set of the governing equations consist of twenty three equations, the actual number of eigenfrequencies is only eleven. This yields a set of homogeneous algebraic equations for each wave numbers m and n that may be described by a mass and a stiffness matrix, where the eigenfrequency equals the eigenvalue and the series constants for each wave numbers m and n are the corresponding eigenvectors as follows:

$$(\mathbf{K}_{mn} - \omega_{mn}^2 \mathbf{M}_{mn}) \mathbf{C}_{mn} = 0 \quad (52)$$

where \mathbf{K}_{mn} and \mathbf{M}_{mn} are the stiffness and the mass matrices, respectively, that correspond to the m th and n th harmonic term in the series and are not presented for the sake of brevity; ω_{mn} is the eigenfrequency that corresponds to the m th and n th term; $\mathbf{0}$ is a null vector; and \mathbf{C}_{mn} is the eigenvector and its components are equal to eleven core constants:

$$\mathbf{C}_{mn} = [C_{u0} C_{u1} C_{u2} C_{u3} C_{v0} C_{v1} C_{v2} C_{v3} C_{w0} C_{w1} C_{w2}] \quad (53)$$

4 Verification and Numerical Results

The numerical examples of rectangular simply supported sandwich plates with power-law FG face sheets are used for validation of the new approach. The example used by Li et al. [15] is considered for validation. Considering FG sandwich plate, as shown in Fig. 1, the Young's modulus and mass density in the lower face sheet at $z = h_c/2$ and in the upper face sheet at $z = -h_c/2$ are 380 GPa and 3,800 kg/m³, respectively (the properties of alumina). In the lower face sheet at $z = (h_c/2 + h_b)$ and in the upper face sheet at $z = -(h_c/2 + h_t)$, the Young's modulus and mass density are 70 GPa and 2,707 kg/m³, respectively (the properties of aluminum). Young's modulus and mass density in each face sheet vary according to the power-law function. The sandwich plate has a hard core made of alumina. Poisson's ratio is equal to 0.3 throughout the analysis. For simplicity, the non-dimensional natural frequency parameter is defined as [15]:

$$\bar{\omega} = \frac{\omega b^2}{h_b + h_c + h_t} \sqrt{\frac{\rho_0}{E_0}}, (\rho_0 = 1 \text{ kg/m}^3, E_0 = 1 \text{ GPa}) \quad (54)$$

Table 1 shows the comparison of flexural vibration frequency parameter $\bar{\omega}$ of the present study and the results obtained in Ref. [15] for square 2-1-2 sandwich plates with power-law functionally graded face sheets and homogeneous hard core with volume fraction index $\kappa = 1$ and two thickness ratios ($h/b = 0.01, 0.1$). 2-1-2 sandwich plate is a symmetric sandwich plate with the face sheet thickness twice of the core thickness. The maximum discrepancy in results of Table 1 is 0.63 %, which indicates a very good agreement between the results of the present study and the results of Ref. [15]. These discrepancies are indicated in Table 1.

The results of simply supported square sandwich plates with functionally graded face sheets and homogeneous hard core are compared in Table 2 with the results from Ref. [15] for four different face sheets and core thicknesses. Young's modulus and mass density in the FG face sheets are based on the power-law distribution. The maximum discrepancy in results of Table 2 is 6.57 %, that is related to 2-1-2 sandwich plate and for $\kappa = 5$. Consequently, Table 2 shows a

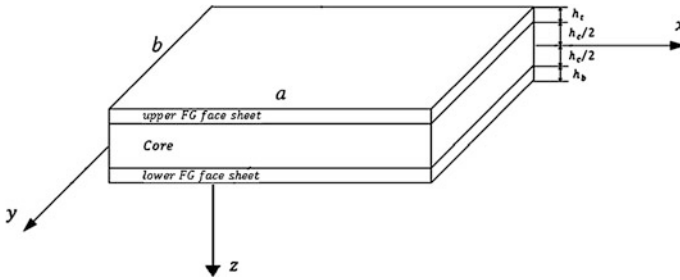


Fig. 1 Geometry of a simply supported sandwich plate with FG face sheets

Table 1 Comparison of flexural vibration frequency parameter $\bar{\omega}$ of the present study for 2-1-2 hard core sandwich FG plates with results of Ref. [15], ($\frac{a}{b} = 1, \kappa = 1$)

$h/b = 0.01$			$h/b = 0.1$		
Li et al. [15]	Present	Dis. percent	Li et al. [15]	Present	Dis. percent
1.32974	1.32748	0.17 %	1.30186	1.31011	0.63 %

Table 2 Comparison of fundamental frequency parameter $\bar{\omega}$ with results of Ref. [15], for square hard core sandwich plates, ($\frac{h}{b} = 0.01$)

κ	2-1-2		1-1-1		2-2-1		1-2-1	
	Li et al. [15]	Present						
1	1.32974	1.32748	1.38511	1.37485	1.42992	1.40626	1.47558	1.44351
5	0.99903	1.06465	1.06309	1.10095	1.13020	1.14883	1.19699	1.18585
10	0.95934	1.00676	1.01237	1.03671	1.08065	1.08746	1.14408	1.12336

good agreement by comparisons of FG sandwich plates for three different volume fraction indices $\kappa = 1, 5, 10$ with results of Ref. [15].

A square soft core sandwich plate with side-to-thickness ratio $b/h = 10$ is considered. Note that the core of the plate is fully stainless steel, while the upper and the lower face sheets of the plate are silicon nitride/stainless steel FGM and properties distribution in thickness direction of the FG face sheets vary by power-law function.

Figure 2 depicts the fundamental frequency parameter ω versus temperatures for 1-8-1 and 1-1-1 simply supported FG sandwich plates for five values of power-law index ($\kappa = 0, 0.1, 1, 10, \infty$). $\kappa = 0$ and $\kappa = \infty$ mean metal and ceramic, respectively. It is seen that the fundamental frequency parameter $\bar{\omega}$ increases with increase in the face sheet thickness rather than core thickness in 1-8-1(Fig. 2a) and 1-1-1(Fig. 2b) FG sandwich plates, respectively. This is because the amount of ceramic and so the structural stiffness increases with increase in the face sheet

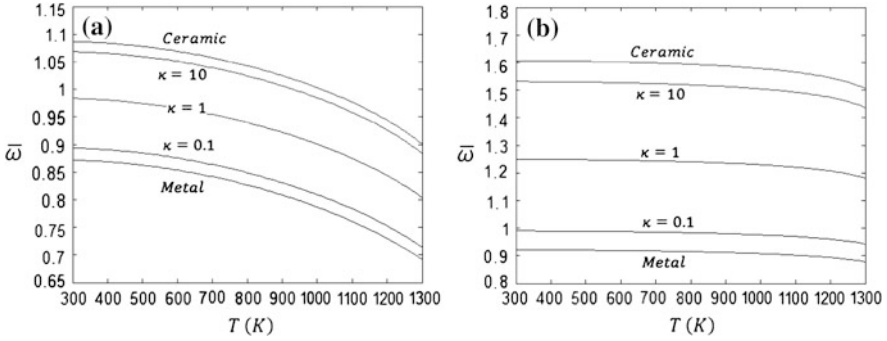


Fig. 2 Variation of fundamental frequency parameter $\bar{\omega}$ with temperature, for **a** 1-8-1 and **b** 1-1-1 FG sandwich plates at different power-law indices κ . ($a/b = 1, b/h = 10$)

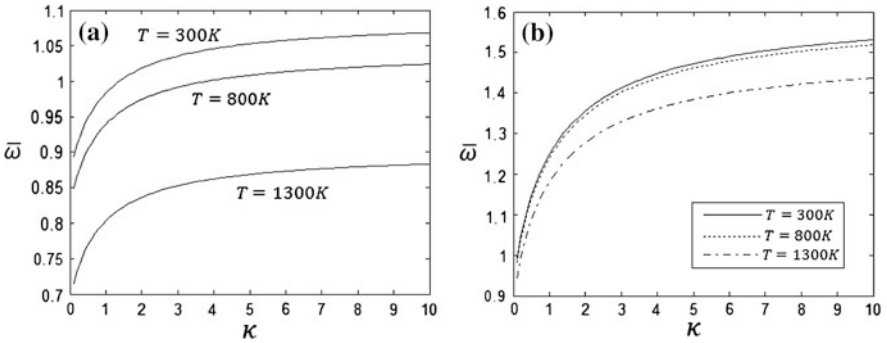


Fig. 3 Variation of fundamental frequency parameter $\bar{\omega}$ with power-law index κ , for **a** 1-8-1 and **b** 1-1-1 FG sandwich plates at different temperatures. ($a/b = 1, b/h = 10$)

thickness. Figure 2a and b indicate that the effect of temperature on the fundamental frequency parameter decreases with decreasing core thickness, because, in the present chapter only the core material properties are temperature dependent. It is also shown in Fig. 2 that for lower temperatures and for higher power-law indices, the amounts of fundamental frequency parameter are higher as expected.

Figure 3 indicates the variation of the fundamental frequency parameter at different temperatures versus power-law index for 1-8-1 and 1-1-1 FG sandwich plates. It is shown that the effect of temperature on the value of the fundamental frequency parameter decreases with increase in the FG face sheets thickness, because, the sandwich plates with thicker FG face sheets have more silicon nitride than the sandwiches with thin FG face sheets, and with respect to Table 3, the effect of temperature on the metal (stainless steel) properties is more significance than the effect of temperature on the ceramic (silicon nitride) properties.

The fundamental frequency parameter ($\bar{\omega}$) versus side-to-thickness ratio (b/h) for square sandwich plates is plotted in Figs. 4 and 5. These figures are plotted for 1-8-1 and 1-1-1 sandwich plates, for different temperatures and power law indices.

Table 3 Temperature effect on amount of elasticity modulus for silicon nitride and stainless steel

Temperature	Elasticity modulus	
	Silicon Nitride	Stainless steel
300 K	322.27 GPa	207.79 GPa
1300 K	268.08 GPa	59.51 GPa
Change percent:	16.81 %	71.36 %

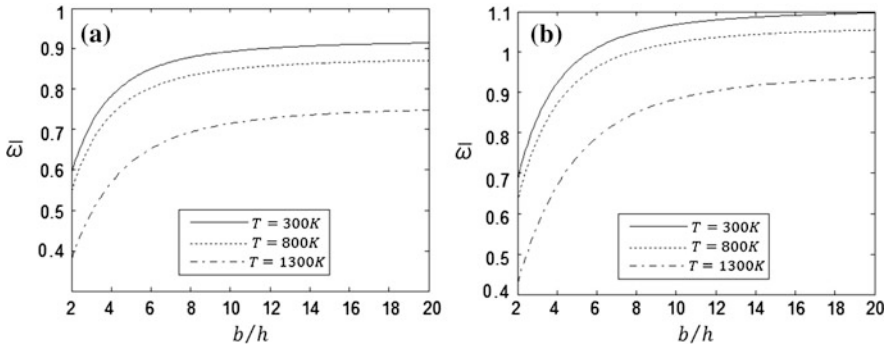


Fig. 4 Fundamental frequency parameter ($\bar{\omega}$) as a function of side-to-thickness ratio (b/h), for 1-8-1 and (Silicon Nitride/Stainless Steel/Silicon Nitride) FG square sandwich plates at different temperatures. **a** $\kappa = 0.1$ **b** $\kappa = 10$

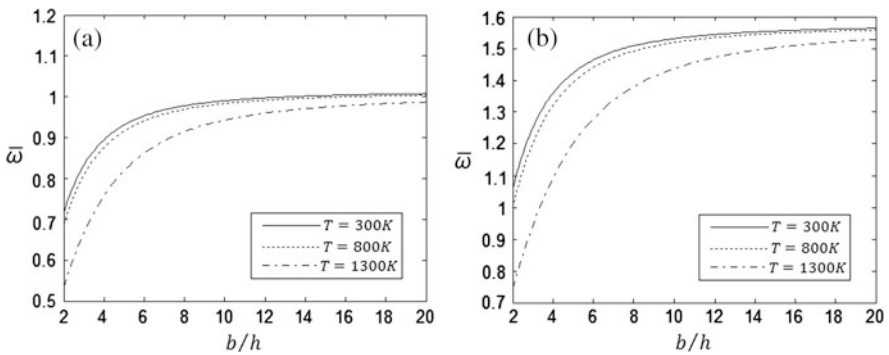


Fig. 5 Fundamental frequency parameter ($\bar{\omega}$) as a function of side-to-thickness ratio (b/h), for 1-1-1 and (Silicon Nitride/Stainless Steel/Silicon Nitride) FG square sandwich plates at different temperatures. **a** $\kappa = 0.1$ **b** $\kappa = 10$

In these figures, the fundamental frequency parameter increases with increasing side-to-thickness ratio. It should be notice that for the side-to-thickness ratio greater than approximately twelve ($b/h > 12$), the variation of fundamental frequency parameter is very small. This result indicates that $\bar{\omega}$ is almost constant for

high aspect ratio FG sandwich plates. Furthermore, increase in the face sheet thickness from Fig. 4 to Fig. 5, is caused to increase in the fundamental frequency parameter. Also, these figures show that the effect of temperature on the fundamental frequency parameter decreases with decreasing the core thickness, too, because, in Fig. 5 the curves of different temperatures are nearest to each other than the same curves in Fig. 4.

5 Conclusion

An improved high-order sandwich plate theory is used to analyze the free vibration of sandwich plates with FG face sheets and temperature dependent properties of the core materials. The second model of Frostig [11] that assumes the through-the thickness displacements distributions of the core to be quadratic and cubic for the vertical and horizontal displacements, respectively, is used in present chapter. Hence, the unknowns in this model consist of the coefficients of these polynomials together with the face sheet displacements. This model implicates the existence of high-order stress resultants in the core, which cannot be associated with any meaningful physical interpretation. This model is improved by considering the in-plane stresses of the core, and the equations of motion are solved using a new approach. The capabilities of the improved high-order sandwich plate theory for free vibration analysis of sandwich plates with FG face sheets and isotropic soft or hard core are verified by results in open literature. There is a good agreement with the references results. Based on the results obtained, the following conclusions can be drawn:

The fundamental frequency parameter increases with increase in the face sheet-to-core thickness ratio, for a soft core FG sandwich plate.

The effect of temperature on the value of fundamental frequency parameter decreases with decreasing the core thickness.

The fundamental frequency parameter increases for soft core FG sandwich plates with increase in the power-law index (κ).

The fundamental frequency parameter decreases for hard core FG sandwich plates with increase in the power-law index (κ).

Increase in temperature decrease the fundamental frequency parameters.

The fundamental frequency parameter increases with increasing the side-to-thickness ratio (b/h).

The fundamental frequency parameter is almost constant for soft core (Silicon Nitride/Stainless Steel/Silicon Nitride) FG sandwich plates with side-to-thickness ratio greater than about twelve.

The fundamental frequency parameter is almost constant for different temperatures in core-to-face sheet thickness ratio approximately zero.

References

1. Allen, H.G.: Analysis and design of structural sandwich panels. Pergamon Press, London (1969)
2. Plantema, F.J.: Sandwich Construction. Wiley, New York (1966)
3. Librescu, L., Hause, T.: Recent developments in the modeling and behavior of advanced sandwich constructions: a survey. *Compos. Struct.* **48**(1), 1–17 (2000)
4. Mindlin, R.D.: Influence of transverse shear deformation on the bending of classical plates. *Trans. ASME J. Appl. Mech.* **8**, 18–31 (1951)
5. Reddy, J.N.: Energy Principles and Variational Methods in Applied Mechanics. Wiley, New York (1984)
6. Petras, A., Sutcliffe, M.P.F.: Indentation resistance of sandwich beams. *J. Compos. Struct.* **46**, 413–424 (1999)
7. Frostig, Y., Baruch, M., Vilnay, O., Sheinman, I.: A high order theory for the bending of sandwich beams with a flexible core. *J. ASCE EM Div.* **118**(5), 1026–1043 (1992)
8. Frostig, Y., Baruch, M.: Localized load effects in high-order bending of sandwich panels with flexible core. *J. Engrg. Mech.* **122**(11), 1069–1076 (1996)
9. Frostig, Y., Thomsen, O.T.: High-order free vibration of sandwich panels with a flexible core. *Int. J. Solids Struct.* **41**(5–6), 1697–1724 (2004)
10. Malekzadeh, K., Khalili, M.R., Mittal, R.K.: Local and global damped vibrations of sandwich plates with a viscoelastic soft flexible core: an improved high-order approach. *J. Sandwich Struct. Mater.* **7**(5), 431–456 (2005)
11. Frostig, Y., Thomsen, O.T.: On the free vibration of sandwich panels with a transversely flexible and temperature-dependent core material—Part I: Mathematical formulation. *J. Compos. Sci. Technol.* **69**, 856–862 (2009)
12. Shen, H., Li, S.: Postbuckling of sandwich plates with FGM face sheets and temperature-dependent properties. *Compos. Part B* **39**, 332–344 (2008)
13. Zhao, J., Li, Y., Ai, X.: Analysis of transient thermal stress in sandwich plate with functionally graded coatings. *Thin Solid Films* **516**, 7581–7587 (2008)
14. Reddy J.N: Thermo mechanical behavior of functionally graded materials. Texas, (1998)
15. Li, Q., Iu, V.P., Kou, K.P.: Three-dimensional vibration analysis of functionally graded material sandwich plates. *J. Solid Vib.* **311**, 498–515 (2008)